

Springer Proceedings in Physics 254

Jutta Escher · Yoram Alhassid
Lee A. Bernstein · David Brown
Carla Fröhlich · Patrick Talou
Walid Younes *Editors*

Compound-Nuclear Reactions

Proceedings of the 6th International
Workshop on Compound-Nuclear
Reactions and Related Topics CNR*18

 Springer

Springer Proceedings in Physics

Volume 254

Indexed by Scopus

The series Springer Proceedings in Physics, founded in 1984, is devoted to timely reports of state-of-the-art developments in physics and related sciences. Typically based on material presented at conferences, workshops and similar scientific meetings, volumes published in this series will constitute a comprehensive up-to-date source of reference on a field or subfield of relevance in contemporary physics. Proposals must include the following:

- name, place and date of the scientific meeting
- a link to the committees (local organization, international advisors etc.)
- scientific description of the meeting
- list of invited/plenary speakers
- an estimate of the planned proceedings book parameters (number of pages/articles, requested number of bulk copies, submission deadline).

More information about this series at <http://www.springer.com/series/361>

Jutta Escher • Yoram Alhassid • Lee A. Bernstein
David Brown • Carla Fröhlich • Patrick Talou
Walid Younes
Editors

Compound-Nuclear Reactions

Proceedings of the 6th International
Workshop on Compound-Nuclear Reactions
and Related Topics CNR*18

 Springer

Editors


Jutta Escher
Lawrence Livermore National Laboratory
Livermore, CA, USA

Yoram Alhassid
Department of Physics
Yale University
New Haven, CT, USA

Lee A. Bernstein
Lawrence Berkeley National Laboratory
Berkeley, CA, USA

David Brown
National Nuclear Data Center
Brookhaven National Laboratory
Upton, NY, USA

Carla Fröhlich
North Carolina State University
Raleigh, NC, USA

Patrick Talou 
Los Alamos National Laboratory
Los Alamos, NM, USA

Walid Younes
Lawrence Livermore National Laboratory
Livermore, CA, USA

ISSN 0930-8989

ISSN 1867-4941 (electronic)

Springer Proceedings in Physics

ISBN 978-3-030-58081-0

ISBN 978-3-030-58082-7 (eBook)

<https://doi.org/10.1007/978-3-030-58082-7>

© This is a U.S. government work and not under copyright protection in the U.S.; foreign copyright protection may apply 2021

All rights are reserved by the Publisher, whether the whole or part of the material is concerned, specifically the rights of translation, reprinting, reuse of illustrations, recitation, broadcasting, reproduction on microfilms or in any other physical way, and transmission or information storage and retrieval, electronic adaptation, computer software, or by similar or dissimilar methodology now known or hereafter developed.

The use of general descriptive names, registered names, trademarks, service marks, etc. in this publication does not imply, even in the absence of a specific statement, that such names are exempt from the relevant protective laws and regulations and therefore free for general use.

The publisher, the authors, and the editors are safe to assume that the advice and information in this book are believed to be true and accurate at the date of publication. Neither the publisher nor the authors or the editors give a warranty, expressed or implied, with respect to the material contained herein or for any errors or omissions that may have been made. The publisher remains neutral with regard to jurisdictional claims in published maps and institutional affiliations.

This Springer imprint is published by the registered company Springer Nature Switzerland AG
The registered company address is: Gewerbestrasse 11, 6330 Cham, Switzerland

Preface

This volume contains the Proceedings of the 6th International Workshop on Compound-Nuclear Reactions and Related Topics (CNR*18), held at the Lawrence Berkeley National Laboratory, in Berkeley, California, on September 24–28, 2018.

The CNR* series began in 2007 with a meeting near Yosemite National Park. It has since been held in Bordeaux (2009), Prague (2011), Sao Paulo (2013), and Tokyo (2015). The workshop series focuses on improving our understanding of



reactions that involve compound nuclei. Even though the concept of the compound nucleus dates back to the 1930s, interest in compound-nuclear reactions, which exhibit a rich set of phenomena, remains strong. Statistical, semi-classical, and quantum mechanical approaches are employed to describe the static properties of the many-body systems and the dynamics of their collisions and decays. Traditional stable-beam and state-of-the-art radioactive-beam experiments, innovative indirect methods, and decay experiments are utilized to shed light on the reaction dynamics and relevant structural properties. Compound-nuclear reactions play a crucial role for applications in various areas, such as nuclear astrophysics, medicine, nuclear energy, and national security. An overarching goal of the series is to establish a comprehensive, quantitative picture of the processes involved in the formation and decay of a compound nucleus, informed and tested by appropriate experiments, and to formulate accurate predictions for the associated cross sections.

The CNR*18 workshop brought together experts in nuclear theory, experiment, and data evaluation. A broad range of topics was discussed: A number of presentations were dedicated to nuclear structure properties needed for the description of compound-nuclear reactions, such as level densities and gamma-ray strength functions. Other presentations addressed the reaction mechanisms associated with the formation and decay of compound nuclei, including pre-equilibrium processes, fluctuation effects, and possible deviations from standard statistical descriptions. Widely used codes for the description of compound-nuclear reactions were compared. Current efforts in improving optical models, R-matrix descriptions, and *ab initio* reaction theory were presented. Recent progress in developing indirect approaches for determining compound-nuclear cross sections, including the surrogate reactions method and the Oslo method, was reviewed. Theoretical approaches to fission, as well as experimental fission studies, were covered. Several presentations focused on nuclear astrophysics and on isotope production for medical applications. Overviews of existing and planned facilities for experimental studies of compound-nuclear reactions were presented. These Proceedings, edited by the CNR*18 organizing committee, contain summaries of the individual contributions presented at the workshop.

CNR*18 was organized by Jutta Escher and Walid Younes (Lawrence Livermore National Laboratory, LLNL), Yoram Alhassid (Yale University), Lee A. Bernstein (Lawrence Berkeley National Laboratory, LBNL), David Brown (Brookhaven National Laboratory, BNL), Carla Fröhlich (North Carolina State University), and Patrick Talou (Los Alamos National Laboratory, LANL). We thank Tom Gallant (LBNL) for his dedication and outstanding administrative assistance before, during, and after the workshop. We acknowledge support for the organization of the workshop and the publication of these Proceedings, provided by LLNL, LANL, BNL, LBNL, and the Nuclear Science and Security Consortium (NSSC). We would like to express our appreciation to the members of the international advisory committee for valuable suggestions regarding the program and to the session chairs

and panel members for providing a framework for inspiring discussions. We thank the participants for their positive response to the workshop, their extensive work and excellent presentations during the meeting, and their contributions to this volume.

Livermore, CA, USA

New Haven, CT, USA

Berkeley, CA, USA

Upton, NY, USA

Raleigh, NC, USA

Los Alamos, NM, USA

Livermore, CA, USA

Jutta Escher

Yoram Alhassid

Lee A. Bernstein

David Brown

Carla Fröhlich

Patrick Talou

Walid Younes

Organization

Organizing Committee

Jutta Escher	Lawrence Livermore National Laboratory
Yoram Alhassid	Yale University
Lee A. Bernstein	Lawrence Berkeley National Laboratory
David Brown	Brookhaven National Laboratory
Carla Fröhlich	North Carolina State University
Patrick Talou	Los Alamos National Laboratory
Walid Younes	Lawrence Livermore National Laboratory

International Advisory Committee

G. Bertsch	INT
C. Brune	Ohio U
R. Capote	IAEA
B. Carlson	ITA
S. Chiba	Tokyo Tech
M. Dupuis	CEA, DAM, DIF
S. Goriely	ULB
A. Hayes	LANL
M. Heffner	LLNL
K. Jones	UTK
B. Jurado	CENBG
T. Kawano	LANL
P. Koehler	LANL
A. Koning	IAEA

M. Krticka	Charles U
G. Perdikakis	CMU
R. Raifarth	GU Frankfurt
S. Siem	U Oslo
M. Wiescher	Notre Dame
V. Zelevinsky	MSU/NSCL

Contents

Part I Modeling Compound-Nuclear Reactions	
Towards More Predictive Nuclear Reaction Modelling	3
S. Hilaire and S. Goriely	
Modeling Compound Nuclear Reactions with EMPIRE	17
M. Herman, R. Capote, B. V. Carlson, M. Sin, and A. Trkov	
CoH₃: The Coupled-Channels and Hauser-Feshbach Code	27
Toshihiko Kawano	
Part II Beyond Statistical Descriptions	
Recent Advances in R-matrix Data Analysis	37
Ian J. Thompson	
The Transition from Isolated Resonances to the Continuum	45
Carl R. Brune	
Cross Section Correlation Functions and Deviations from the Porter-Thomas Distribution	53
Edward D. Davis	
Moldauer's Sum Rule Implies Superradiance in Compound Nuclear Reactions	57
David Brown, Mike Herman, and Gustavo Nobre	
Multi-step Direct Reaction Models Including Collectivity in Nucleon Induced Reactions	65
E. V. Chimanski, R. Capote, B. V. Carlson, and A. J. Koning	
New Symmetry-Adapted ab initio Approach to Nuclear Reactions for Intermediate-mass Nuclei	73
Alexis Mercenne, Kristina D. Launey, Jutta E. Escher, Tomas Dytrych, and Jerry P. Draayer	

Part III Optical Models

Linking Nuclear Reactions and Nuclear Structure to Study Exotic Nuclei Using the Dispersive Optical Model	83
W. H. Dickhoff	
Microscopic Optical Potential from Chiral Effective Field Theory	91
T. R. Whitehead, Y. Lim, and J. W. Holt	

Part IV Level Densities

Nuclear Level Densities: From Empirical Models to Microscopic Methods	97
Y. Alhassid	
Problem of Level Densities in Compound Nuclear Reactions	113
Alexander Voinov	
Nuclear Shell Model and Level Density	123
Vladimir Zelevinsky and Sofia Karampagia	
Constraining Level Densities Using Spectral Data	133
Gustavo P. A. Nobre, David A. Brown, and Michal W. Herman	
Rotational Enhancement Factor for Nuclear Level Density	139
S. M. Grimes	
Role of Fluctuations on the Pairing Properties of Nuclei in the Random Spacing Model	145
M. A. A. Mamun, C. Constantinou, and M. Prakash	

Part V Gamma-Ray Strength Functions

Gamma Strength Functions and the Brink-Axel Hypothesis	155
Peter von Neumann-Cosel	
γ-Ray Strength Functions and GDR Cross Sections in the IAEA Photonuclear Data Project	165
H. Utsunomiya, I. Gheorghe, D. M. Filipescu, K. Stopani, S. Belyshev, T. Renstrøm, G. M. Tveten, G. Fan, H. Wang, S. Goriely, Y.-W. Lui, T. Ari-izumi, S. Miyamoto, V. Varlamov, B. Ishkhanov, A. C. Larsen, and S. Siem	
Neutron Capture on Actinides Studied with DANCE	173
J. L. Ullmann, B. Baramsai, T. A. Bredeweg, A. J. Couture, R. C. Haight, M. Jandel, T. Kawano, A. L. Keksis, S. Mosby, J. M. O'Donnell, C. Prokop, R. S. Rundberg, G. Rusev, D. J. Vieira, C. Walker, J. B. Wilhelmy, C.-Y. Wu, J. A. Becker, A. Chyzch, R. A. Henderson, G. E. Mitchell, and M. Krlicka	

Deconvolution of the Photon Strength Function 179
 Richard B. Firestone

Part VI Oslo Method

**Attempting to Close the Loop on the Oslo Technique at ^{198}Au :
 Constraining the Nuclear Spin Distribution** 187
 Paul Koehler, John Ullmann, Aaron Couture, and Shea Mosby

**Impact of Restricted Spin-Ranges in the Oslo Method: The
 Example of $(d,p)^{240}\text{Pu}$** 195
 F. Zeiser, G. Potel, G. M. Tveten, A. C. Larsen, M. Guttormsen,
 T. A. Laplace, S. Siem, D. L. Bleuel, B. L. Goldblum, L. A. Bernstein,
 F. L. B. Garrote, L. C. Campo, T. K. Eriksen, A. Gorgen,
 K. Hadynska-Klek, J. E. Midtbo, T. Renstrom, E. Sahin, T. Tornyi,
 A. Voinov, and M. Wiedeking

Systematics of γ -Ray Strength Functions Within the Shell Model 203
 J. E. Midtbo, A. C. Larsen, T. Renstrom, F. L. B. Garrote, and E. Lima

Part VII Surrogate Nuclear Reactions

Future Perspectives for Surrogate-Reaction Studies at Storage Rings..... 209
 A. Henriques, B. Jurado, D. Denis-Petit, T. Chiron, L. Gaudefroy,
 J. Glorius, M. Grieser, C. Langer, Y. A. Litvinov, L. Mathieu, V. Meot,
 R. Perez-Sanchez, J. Pibernat, R. Reifarh, O. Roig, B. Thomas,
 B. A. Thomas, J. C. Thomas, and I. Tsekhanovich

**Prospects for Surrogate Neutron Capture Measurements
 with Radioactive Ion Beams and GODDESS** 217
 Jolie A. Cizewski, Andrew Ratkiewicz, Alexandre Lepaillieur,
 Steven D. Pain, Heather Garland, Harrison Sims, and David Walter

**Surrogate Reaction Method for Neutron Capture and Other
 Reactions on Unstable Isotopes** 221
 J. E. Escher, J. T. Burke, R. O. Hughes, N. D. Scielzo, and R. J. Casperson

**Neutron Capture Cross Sections from Surrogate Reaction Data and
 Theory: Connecting the Pieces with a Markov-Chain Monte Carlo
 Approach** 229
 Oliver Gorton and Jutta E. Escher

**Describing Neutron Transfer Reactions for Deformed Nuclei with a
 Sturmian Basis** 233
 V. G. Gueorguiev, J. E. Escher, F. S. Dietrich, and P. D. Kunz

Part VIII Fusion, Isotope Production, and Superheavy Nuclei

P_{CN} Calculations for $Z = 111$ to $Z = 118$ 239
 W. Loveland and Liangyu Yao

On the Role of the Curvature Corrections in the Surface Tension Coefficient upon the Orientation Effects in the Fusion Reactions	247
Kostyantyn Cherevko, Leonid Bulavin, Laszlo Jenkovszky, and Volodymyr Sysoev	
Excitation Function Measurements of Alpha-Induced Reaction on Natural Copper and Titanium Up To 46 MeV	251
Hiroshi Yashima, Masayuki Hagiwara, Toshiya Sanami, and Shunsuke Yonai	
Measurement of the Excitation Function of $^{96}\text{Zr}(\alpha,x)^{99}\text{Mo}$ Reaction up to 32 MeV	255
Masayuki Hagiwara, Hiroshi Yashima, Toshiya Sanami, and Shunsuke Yonai	
Part IX Fission	
A Grand Tour of Nuclear Fission Physics	261
W. Younes	
Microscopic Calculation of Fission Fragment Mass Distributions at Increasing Excitation Energies	275
Nicolas Schunck, Zachary Matheson, and David Regnier	
Microscopic Description of Fission for the r-Process in Neutron Star Mergers	285
J.-F. Lemaître, S. Goriely, S. Hilaire, and N. Dubray	
Event-by-Event Fission Modeling with FREYA	293
R. Vogt, J. Randrup, J. T. Van Dyke, and L. A. Bernstein	
Capabilities of the NIFFTE FissionTPC	301
R. J. Casperson	
Part X Experimental Techniques and Facilities	
Resonance Measurements at Rensselaer Polytechnic Institute	309
Ezekiel Blain, Greg Leinweber, Michael Rapp, and Yaron Danon	
Experimental Facilities at iThemba LABS and Measurements to Constrain Astrophysical Processes	315
Mathis Wiedeking	
Late Gamma Rays from Neutron-Induced Fission and Capture from ^{235}U	323
G. Rusev, J. M. O'Donnell, I. Stetcu, M. Jandel, P. Talou, B. Baramsai, T. A. Bredeweg, E. Bond, A. Couture, S. Mosby, C. J. Prokop, J. L. Ullmann, and C. L. Walker	
Index	327

Part I
Modeling Compound-Nuclear Reactions

Towards More Predictive Nuclear Reaction Modelling



S. Hilaire and S. Goriely

1 Introduction

Nuclear reaction models, beyond the fundamental quest for understanding processes taking place when a nuclear reaction occurs, are necessary to produce nuclear data for various applications. Depending on the targeted goal, the accuracy of the predictions as well as the type of data predicted might be very different. For nuclear reactors, for instance, the accuracy is clearly a key issue for specific nuclei and specific types of data. At the other extreme, one finds nuclear astrophysics for which the accuracy is less crucial than the ability of the model to produce data for all possible interacting systems. Even for the most important nuclei, for which many measurements have been performed, the need for better nuclear reaction models is still relevant since one still have to deal with processes for which data are not available or not precise enough. Within this context, nuclear reaction models have to be as robust and predictive as possible. This is why during the last 40 years at least, many nuclear reaction codes have been developed and used to answer the question: “what happens when a projectile hits a target nucleus?”

It is clear that the answer to this question depends on the nature of the projectile, on the target and on the projectile energy. In what follows, we restrict ourselves to the case where light projectiles (gamma, neutron, protons . . . up to ^4He) interact with a target nucleus heavy enough (typically with a mass $A > 10$) with an incident energy between 1 keV and 200 MeV, a framework enabling the implementations of the so-called statistical models. Within this framework, several models come

S. Hilaire (✉)
CEA, DAM, DIF, Arpajon, France
e-mail: stephane.hilaire@cea.fr

S. Goriely
Institut d’Astronomie et d’Astrophysique, Université Libre de Bruxelles, Brussels, Belgium

into play. We will first describe in Sect. 2, general features observed when a nuclear reaction occurs at energies below 200 MeV, features that have motivated the introduction of several models that will be discussed in Sect. 3. In Sect. 4, we will discuss current developments on specific ingredients required by the reaction models as those related to fission, for instance. Finally, Sect. 5 will draw conclusions and prospects.

2 General Features About Nuclear Reactions

For incident projectiles with energy between a few keV and 200 MeV impinging on a target nucleus, the typical outgoing particle spectrum displays three main domains as illustrated in Fig. 1. Two extreme regimes can be distinguished. For high outgoing energies, and forward angles, discrete peaks are observed and dominate the outgoing spectrum. Such processes correspond to fast interactions, also called “direct interactions”, which take place in a timescale comparable to the time the

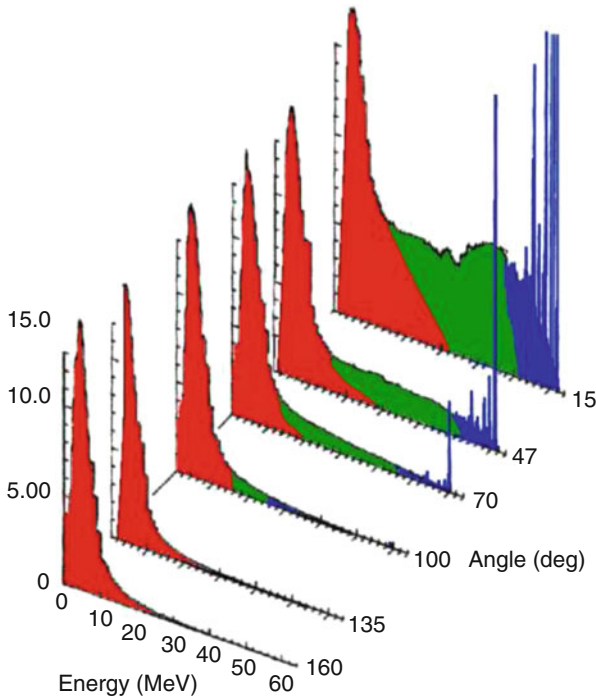


Fig. 1 Outgoing proton spectrum for a 62 MeV incident proton on a ^{56}Fe target. Colours are used to distinguish the three regions corresponding to the direct reactions described by the optical model (blue), the pre-equilibrium model (green) and the compound nucleus model (red)

projectile takes to cross the nucleus. For low outgoing energies, a typical evaporation spectrum is observed. In this case, it is usually assumed that the projectile has been absorbed in the target with which it has shared all its energy to form a compound system. This process, described by the so-called compound nucleus (CN) model, assumes to the first order of approximation, that the formation and decay of the CN are independent processes. This assumption explains that the emission spectrum looks very similar whatever the angle of emission is: the compound nucleus has lost memory of the way it has been created! This feature is characterized by angular distribution of emitted particle symmetric around 90° . Between these two extreme situations, one finds, if the projectile energy is high enough, an intermediate process whose frontiers are less well defined: the so-called pre-equilibrium process. This last process has been historically less studied than the two others (mainly because contrary to the two previous ones, it can be neglected for low incident energies) and, therefore, the formalism which is employed to describe it is still subject to important debates and still offers room for significant improvements. To these three types of processes, correspond in practice three types of models which are linked together, as illustrated in Fig. 2, in order to produce many different types of nuclear data: the “optical model (OM)”, the “pre-equilibrium model (PE)” and the “CN model”. All these models need to be implemented in a nuclear reaction code aiming at producing useful information. As can be observed, the optical and pre-equilibrium models both yield an output (elastic, fission or inelastic data) and also provide the CN model with an input data (σ_{Reaction} , T_{ij} or σ_{NC}).

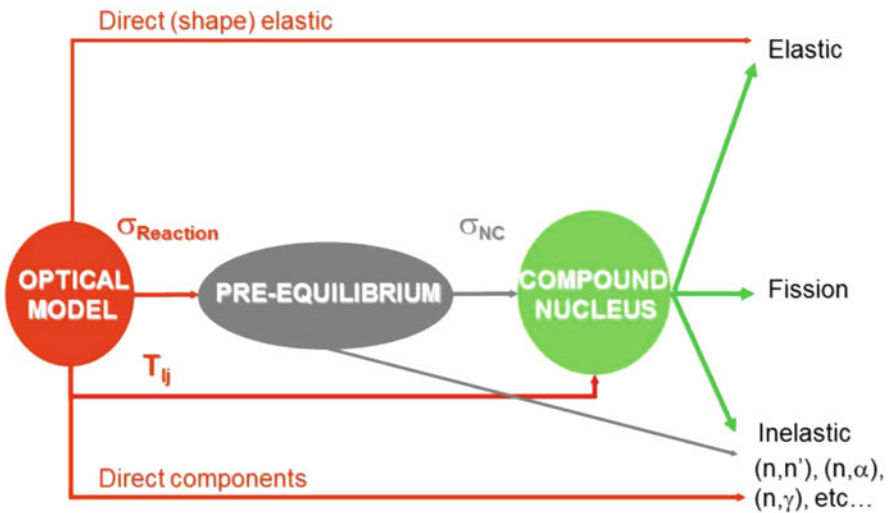


Fig. 2 Sequence of nuclear models required to describe a nuclear reaction

3 Nuclear Models for Nuclear Reactions

The three nuclear reaction models whose qualitative features have been discussed above rely on various input data. The latter can either be directly measured or have to be deduced from other models. Two types of approaches can be distinguished. The first one, traditionally employed, is generally based on empirical expressions which can be easily fine-tuned to reproduce data. The more recently developed ones have benefited from the increase in computing power which enables today to provide microscopic models able to compete with the traditional approaches.

3.1 *Basic Nuclear Structure Information*

The most fundamental data required for a nuclear reaction is the mass of the various nuclei that can appear during a decay process. This knowledge is necessary to determine reaction thresholds and to compute the kinematic relations enabling laboratory to centre of mass frame transformations. Other quantities such as nucleus levels' excitation energies, spins and parities are also welcome and govern features such as angular distribution or decay selection rules. Another feature also interesting though not mandatory is the deformed or spherical nature of the target. This information is particularly useful to adopt the proper treatment of the OM. Experimental nuclear masses are available today for nearly 2500 nuclei [1]. This set constitutes the reference data that nuclear mass models try to reproduce at best. Many different mass models have been developed during the last decades and the most advanced ones are able today to reach a root mean square (rms) deviation from experiment close to 500 keV [2], a remarkable level of accuracy with respect to the mass of a nucleus of the order of a GeV. Generally speaking, the more the nuclear mass models are based on first principle physics, the higher the predictive power should be. This has been recently demonstrated by analysing the predictive power of various mass models adjusted on the 2003 atomic mass evaluation [3] with respect to the update of 2012 [4] and 2016 [1]. One of the big advantages of the microscopic models is that on top of the nuclear masses, they can also provide spectroscopic data, as well as all detailed input which can be used in other models, thus improving the coherence in an attempt to predict microscopically a nuclear reaction.

3.2 *The Optical Model*

The OM is very important since it determines the reaction cross section that the PE and CN models are then going to spread in the different outgoing open channels. It also provides the direct elastic, total and inelastic cross sections as well as various

angular distributions. Historically, the OM has been first determined postulating functional forms whose parameters have to be adjusted until a good agreement with data is obtained. This type of approach is still currently used [5] in particular because of its ability to allow very accurate description of experimental data (less than 1% accuracy on total cross sections). However, it depends very much on experimental data availability. An alternative to the pure phenomenological approach is the microscopic approach. Such approaches enable to determine the OM without any a priori knowledge of any related experimental data. Therefore, it enables predictions even for nuclei far from the valley of stability. The disadvantage of such microscopic approaches is of course a lower accuracy. One of the most employed one is the so-called JLM approach [6] which is based on nuclear matter data obtained from mean field or beyond mean field nuclear structure descriptions. Such structure methods generally provide a nuclear structure description which is hoped to be precise enough to guaranty that predictions far from the valley of stability should not be too far from the reality.

The choice between phenomenology and microscopy is guided by the goal one has in mind. Within the framework of nuclear data evaluation where accuracy is one of the key issues, availability of experimental data will make it preferable to use the first option because of its fitting power. For more fundamental research or when there is a lack of data, the microscopic option is preferred.

3.3 The Pre-equilibrium Model

Once the OM has treated the various direct processes, the remaining cross section, corresponding to all processes which have not been explicitly accounted for, is “feeding” the second model of Fig. 2, the PE model. This reaction cross section reflects the probability that the projectile be captured in the continuum of the target to form a “composite” system. At this stage, the system still remembers the way it was formed and is going to de-excite either by re-emitting a particle or by distributing step by step the incident projectile energy between one or several nucleons of the target. In the latter case, several particles and holes are going to be created sequentially, holding on towards more complex configurations, to reach, after sufficient time, a situation corresponding to the CN approximation, where the projectile energy has been shared among all the constituents of the composite system. At each step of this process, the probability to emit a particle has to be accounted for. Again, one has the choice between more or less refined models. The most employed one is the so-called exciton model, introduced in the seventies, which has been successively improved to account for more and more physical features either because the appearance of new experimental data evidenced a lack of predictive power or simply because initially missing, though important, features were introduced [7]. Quantum mechanical approaches have also been developed but they are clearly more complex and less flexible and do not provide results of better quality as those obtained with the exciton model. However,

recent experimental measurements seem to show that such quantum mechanical approaches are unavoidable if one aim at improving the predictive power [8].

3.4 The Compound Nucleus Model

Beyond the fact that optical and pre-equilibrium models contribute to the emission of particles, they are also those which determine the initial conditions of the last model of the chain of Fig. 2: the CN model. Starting from such initial conditions, the CN model then uses the statistical hypothesis stating that the decay in a given outgoing channel depends on the ratio of the probability to decay in this specific channel with respect to all possible decay probabilities. This approximation, which consists in considering that the decay of the CN does not keep track of the CN formation (the Bohr hypothesis), is formally translated into the so-called Hauser–Feshbach equation,

$$\sigma_{ab} = \sum_{J,\pi} \sigma_a^{NC}(E^*, J, \pi) \frac{\langle \Gamma_b(E^*, J, \pi) \rangle}{\sum_c \langle \Gamma_c(E^*, J, \pi) \rangle}$$

In this equation, σ_{ab} , corresponding to the cross section for the decay in channel b (particle type, energy, outgoing angular momentum) from the compound nucleus formed in the entrance channel a , is given by the product of the CN formation cross section σ_a^{NC} at a given energy, spin and parity (E^*, J, π) by the probability to decay in channel b given all open channels c . The question, therefore, consists in estimating all possible average decay widths Γ_c . The Hauser–Feshbach approximation enables to write, to the first-order approximation, that

$$\frac{\langle \Gamma_b(E^*, J, \pi) \rangle}{\sum_c \langle \Gamma_c(E^*, J, \pi) \rangle} = \frac{\langle T_b^{J\pi}(E^*) \rangle}{\sum_c \langle T_c^{J\pi}(E^*) \rangle},$$

where the transmission coefficients $\langle T_c \rangle$, which will be further discussed in Sect. 4, correspond to the decay probability in outgoing channel c (note that this expression becomes much more complicated when spin and parity conservation rules are explicitly written). Soon, it was realized that this first-order approximation had to be corrected at low energy, or, more precisely when the number of competing channel is relatively low. In such situations, indeed, interferences, either constructive or destructive, occur between entrance and exit channels. These interferences are accounted for introducing a width fluctuation correction factor, which, generally enhances the elastic channel and accordingly decreases the other competing channels [9], but can also, in very particular situation, enhance the first inelastic channel [10].

4 Nuclear Reaction Model Ingredients

The models described in the previous section require specific ingredients depending on the outgoing channel under consideration. To be more precise, the OM only provides transmission coefficient for outgoing particle decay to a well-defined level of the residual nucleus. However, it does not enable to deal with the particle decay in the residual nucleus levels' continuum, with photon emission, and does not provide either any fission decay probability. These three situations require supplementary particular approximations that we now discuss.

4.1 Particle Decay in the Continuum

When the projectile energy is large enough, the compound nucleus can decay by emitting a particle in the residual levels' continuum. This continuum has to be accounted for because it is well known that beyond a given excitation energy it is impossible to describe nuclear excited levels individually. In such cases, a nuclear level density (NLD) has to be introduced and the transmission coefficients entering the Hauser–Feshbach expression are given by the integral

$$\left\langle T_c^{J\pi}(E_c) \right\rangle = \int_{E_c - \Delta}^{E_c + \Delta} \rho(\varepsilon) T_c^{J\pi}(E_c) d\varepsilon$$

in which E_c is the excitation energy of the residual nucleus once a particle has been emitted in a channel c , $\rho(\varepsilon)$ the residual nucleus level density in which we have omitted, for simplicity, the spin and parity labels which are implicitly included in the definition of the channel c and Δ is the width of the excitation energy bin into which the emission occurs. An extensive literature exists on nuclear level densities, where both analytical and microscopic approaches are considered. Analytical approaches, because of the free parameters they contain allow one to fit both low energy levels and experimental s-wave mean spacings rather well [11]. Concerning the microscopic alternatives, one has to find a compromise between accuracy and completeness. The most advanced approaches [12] are usually limited to local mass regions, and, so far only few approaches have been used to provide complete sets of data for all nuclei [13, 14]. The main advantage of the microscopic approaches is that they usually go beyond the assumed statistical hypothesis used in analytical expressions, a feature that can have a significant impact when comparing theoretical and experimental cross sections [15].

As illustrated in Fig. 3, for instance, the combinatorial level density approach predicts much more high spin levels than the statistical approach (right panel), and such differences strongly modify the isomer production by photo-neutron reaction on ^{181}Ta (left panel).

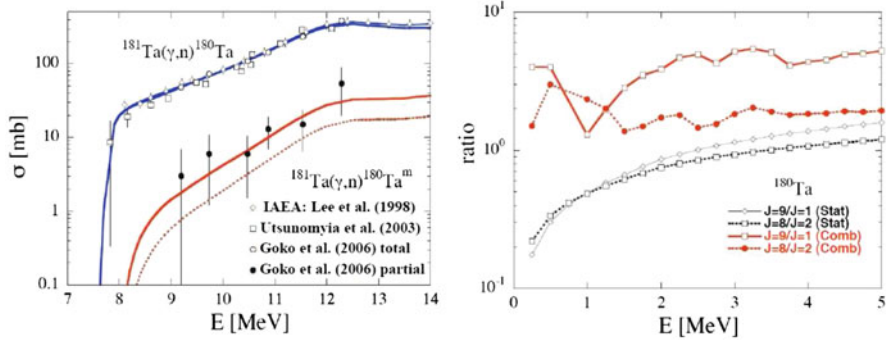


Fig. 3 (Left) $^{181}\text{Ta}(\gamma, n)$ and $^{181}\text{Ta}(\gamma, n)^{180}\text{Ta}^m$ cross sections. (Right) Level density ratio for specific spins. In the left panel, the use of the combinatorial level density predictions (full line) improves the description of the isomer production with respect to the results obtained using the statistical (dotted line). See Ref. [15] for more details

4.2 Photon Emission

Whatever the projectile energy, γ emission is always an open decay channel for which the residual nucleus turns out to be the compound system with a lower excitation energy, the difference being the energy of the emitted photon. To determine a γ transmission coefficient, one assumes that photo-absorption and photoemission cross sections associated with a given decay type X ($X = E$ or M for electric or magnetic transition) and a given multipolarity are related one with the other, thanks to the same so-called photon strength function (PSF). Experimentally, the PSF follows a Lorentzian shape, whose parameterization can be more or less complicated [16]. A specific feature of the capture process is due to the fact that the γ decay occurs from the continuum of the CN to a very large number of levels, therefore requiring, the use of a NLD to be modelled, and, on top of that, the PSF concerns low-energy photons in the tail of the Lorentzian which cannot be constrained by photo data. One has then two sources of uncertainty which are combined to produce a total γ -ray transmission coefficient. For this reason, the theoretical γ -ray width is often quite different from the measured one, and a renormalization factor is introduced in the PSF to improve the agreement with either the measured γ -ray width or the experimental capture cross section data. Microscopic alternatives have been developed [17, 18] and have shown significant deviations from the Lorentzian shape as far as the PSF is concerned, in particular for nuclei far from the valley of stability [17]. Quite recently, attempts to solve the normalization problem have also been undertaken [19, 20]. The current situation reached within the Gogny-QRPA framework is illustrated in Fig. 4. As can be observed, the agreement with experimental radiative widths is much better with the microscopic approach provided a phenomenological correction is used to describe the de-excitation PSF at low γ -emission energies [20]. It is worth adding that on

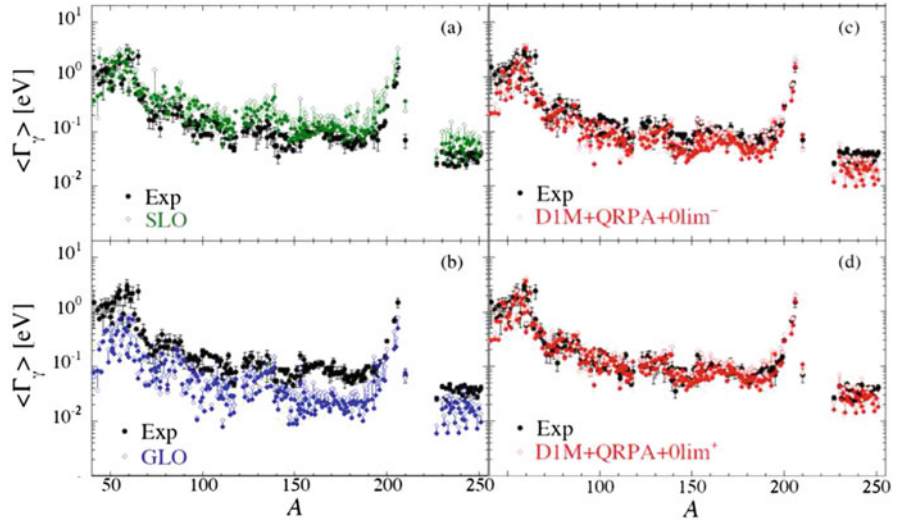


Fig. 4 Average radiative widths as function of the mass number. Comparison between theoretical predictions and experiment. The (a) and (b) panels correspond to the traditional analytical expression SLO and GLO [16], while panels (c) and (d) display the HFB-Gogny QRPA predictions with two options for the low energy M1 phenomenological correction [20]

top of its ability to reproduce experimental radiative width, the HFB-Gogny QRPA model has also been tested successfully with respect to other experimental data [21, 22].

4.3 Fission

Despite its fundamental role in nuclear applications as a source of energy, as well as the fact that it has been discovered many decades ago and intensively studied since, fission remains probably the least well-understood process in nuclear reaction modelling. Qualitatively speaking, fission is modelled by a gradual transition of the nucleus from an initial compact shape to such an elongated shape that the nucleus breaks into fragments. This evolution is governed by a potential energy landscape corresponding to nuclear shapes more or less probable depending on the excitation energy required to reach them. This landscape exhibits features such as valleys and peaks which help in understanding the major characteristics of the fission process, and, in particular the fission fragments distributions observed experimentally. For cross section calculation, one reduces the multidimensional landscape to an effective one-dimensional (1D) approach. This 1D landscape suggests the concept of fission barriers through which quantum tunnelling probabilities are computed to determine fission transmission coefficients.

Given an initial compound nucleus state, fission occurs by tunnelling through all accessible fission barriers. Therefore, for a single barrier, the fission transmission coefficient is given by

$$T_f(E, J, \pi) = \sum_{d(J, \pi)} T_{hw}(E - \varepsilon_d) + \int_{E_c}^{E+B_n} \rho(\varepsilon, J, \pi) T_{hw}(E - \varepsilon) d\varepsilon$$

in which ε corresponds to the transition states' energies. These transition states are discrete up to a given arbitrary threshold E_c , and, as for the compound nucleus at normal deformation, are then described by a NLD, $\rho(\varepsilon, J, \pi)$, beyond E_c .

The potential energy surface often displays several barriers and the fission transmission coefficient used in the Hauser–Feshbach model takes more complicated forms [23–25]. For multiple humped fission barriers, one also accounts for the fact that there exist potential wells between the barriers in which quantum states can be located, usually called class-II or class-III states depending upon whether they are located between the first and second barrier or between the second and the third. If these class-II/III states have a spin and parity corresponding to that of the compound nucleus from which fission occurs, they induced a resonance effect in the fission transmission coefficient for which more or less refined treatments are possible [23–25].

When one uses traditional (i.e. based on analytical expressions) methods to compute fission cross section, a large number of parameters have to be adjusted to reproduce at best experimental data. One can adjust the fission barrier heights and widths, the transition states and their corresponding NLD parameters as well as the eventual class-II/III states. With increasing kinetic energy of the projectile, several residual nuclei come into play. For a 10 MeV neutron incident on ^{238}U , for instance, both ^{239}U (first-chance fission) and ^{238}U (second-chance fission) fission barrier parameters have to be simultaneously fine-tuned and the higher the incident energy, the larger the number of fissioning nuclei. If this makes the fine-tuning more complicated, it also provides a way to get more constraints than the single ^{238}U neutron-induced fission cross section, provided one wants to coherently model the several fission chances.

To be more precise, the fact that the fourth chance of ^{238}U fission is governed by the fission barriers of ^{236}U implies that the latter should also provide a good description of the first chance of ^{235}U since in both cases the nucleus which undergoes fission is the same. Another constraint can also be obtained by noticing that the fission barriers parameters enabling a proper description of photo-induced fission on ^{238}U should also provide a good second-chance fission of neutron-induced fission of ^{238}U . Therefore, a coherent modelling of fission means that the same set of input parameters should provide simultaneously the various fission chances of the various fissioning systems encountered within a given isotopic chain. An illustration of the results obtained within such a modelling framework is given in Fig. 5. If the price to pay by considering all these constraints is an important amount of work,

the reward is a simultaneous description of a whole isotopic chain. In the case of ^{238}U neutron-induced fission indeed, fitting experimental fission cross section data up to 40 MeV requires to adjust the fission parameters for all Uranium isotopes between ^{239}U (first-chance fission) and ^{235}U (fifth chance) as well as other fission chances due to the opening of proton emission and ^4He emission (see Fig. 5). Semi-microscopic alternatives to such a modelling framework have been studied and have shown promising results [26, 27]. Even though the accuracy reached is not at the level required for practical applications, this is a direction to follow in particular if one aims at studying fission for nuclei far from experimentally accessible regions.

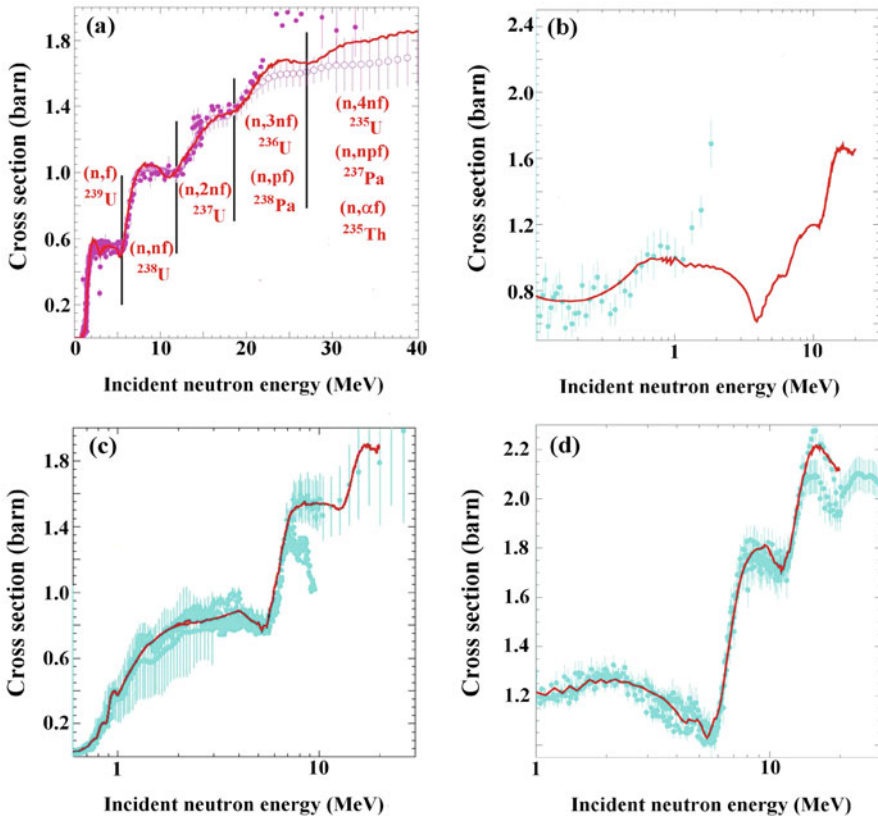


Fig. 5 Illustrations of the coherent modelling of fission cross sections. (a) Neutron-induced fission cross section on ^{238}U . (b) Neutron-induced fission cross section on ^{237}U . (c) Neutron-induced fission cross section on ^{236}U . (d) Neutron-induced fission cross section on ^{235}U . In panel (a), the vertical lines indicate for which incident neutron energy new fissioning nuclei have to be accounted for (see text for more explanations). These fissioning systems are indicated in red as well as the emission process they are involved in

5 Conclusions

The modelling of a nuclear reaction is a complicated task, sometimes challenging. Several models and nuclear ingredients have to be linked together to be able to predict the outcome of a nuclear reaction. Although significant improvements have been made during the last decades, there are still many challenges to face. Pre-equilibrium and fission modelling are certainly among these. In the case of pre-equilibrium, the main reason is that the flexibility of semi-classical approaches makes it possible to obtain at small computational price results which satisfy the quality required for applications. It is only recently that the need for better models has become timely, in particular while studying “subtle” processes such as $(n, xn\gamma)$ transitions in actinides [8]. For fission, the problem is more complicated. The models used are far too simple compared to the most fundamental approaches which evidence a need to account for multidimensional energy landscapes. If future developments consist, without any doubt, in adding more and more microscopic approaches in the nuclear reaction models, this will be a very long-term project. For now, such microscopic approaches can only provide guidelines for nuclear data evaluations but offer the only alternative to empirical expressions whose predictive power far from the valley of stability cannot be trusted given the number of phenomenological parameters they rely on.

References

1. G. Audi et al., The NUBASE 2016 evaluation of nuclear properties. *Chin. Phys. C* **41**(3), 030001 (2017)
2. A. Sobczewski, Y. Litvinov, Predictive power of nuclear-mass models. *Phys. Rev. C* **90**, 017302 (2014)
3. G. Audi et al., The AME2003 atomic mass evaluation. *Nucl. Phys. A* **729**, 337–676 (2003)
4. G. Audi et al., The Ame2012 atomic mass evaluation. *Chin. Phys. C* **36**(12), 1287–1602 (2012)
5. A.J. Koning, J.P. Delaroche, Local and global nucleon optical models from 1 keV to 200 MeV. *Nucl. Phys. A* **713**, 231–310 (2003)
6. E. Bauge et al., Lane-consistent semi-microscopic nucleon-nucleus optical model. *Phys. Rev. C* **63**, 024607 (2001)
7. A.J. Koning, J.M. Akkermans, in *Workshop on Nuclear Reaction Data and Nuclear Reactors: Physics, Design and Safety*, ed. by P. Obložinsky, A. Gandini, (ICTP, Trieste, 1998), p. 143, Feb 23–March 27 1998
8. M. Dupuis et al., Microscopic modeling of direct pre-equilibrium emission from neutron induced reactions on even and odd actinides. *EPJ Web Conf.* **146**, 12002 (2017)
9. S. Hilaire et al., Comparison between various width fluctuation correction factors for compound nucleus reactions. *Ann. Phys.* **306**, 209 (2003)
10. T. Kawano et al., Statistical Hauser-Feshbach theory with width fluctuation correction including direct reaction channels for neutron induced reaction at low energy. *Phys. Rev. C* **94**, 014612 (2016)
11. A.J. Koning et al., Global and local level density models. *Nucl. Phys. A* **810**, 13–76 (2008)
12. Y. Alhassid, The shell model Monte Carlo approach to level densities: Recent developments and perspectives. *Eur. Phys. J. A* **51**, 171 (2015)

13. S. Hilaire et al., Temperature-dependent combinatorial level densities with the DIM Gogny force. *Phys. Rev. C* **86**, 064317 (2012)
14. S. Goriely et al., Microscopic nuclear level densities for practical applications. *Nucl. Phys. A* **695**, 95–108 (2001)
15. S. Goko et al., Partial photoneutron cross sections for the isomeric state $^{180}\text{Ta}^m$. *Phys. Rev. Lett.* **96**, 192501 (2006)
16. R. Capote et al., Reference input parameter library for calculation of nuclear reactions and nuclear data evaluations. *Nucl. Data Sheets* **110**, 3107–3214 (2009)
17. S. Goriely et al., Microscopic HFB + QRPA predictions of dipole strength for astrophysics applications. *Nucl. Phys. A* **739**, 331–352 (2004)
18. M. Martini et al., Large-scale deformed quasiparticle random-phase approximation calculations of the gamma-ray strength function using the Gogny force. *Phys. Rev. C* **94**, 014304 (2016)
19. M.R. Mumpower et al., Estimation of M1 scissors mode strength for deformed nuclei in the medium- to heavy-mass region by statistical Hauser-Feshbach model calculations. *Phys. Rev. C* **96**, 024612 (2017)
20. S. Goriely et al., Gogny-HFB+QRPA dipole strength function and its application to radiative nucleon capture cross section. *Phys. Rev. C* **98**, 014327 (2018)
21. S. Goriely et al., Reference database for photon strength functions. *Eur. Phys. J. A* **55**, 172 (2019)
22. M. Krticka et al., Constraints on the dipole photon strength functions from experimental multistep cascade spectra. *Phys. Rev. C* **99**, 044308 (2019)
23. M.J. L Lopez Jiménez et al., Triple-humped fission barrier model for a new ^{238}U neutron cross-section evaluation and first validations. *Ann. Nucl. Energy* **32**, 195 (2005)
24. P. Romain et al., Bruyères-le-Châtel neutron evaluations of actinides with the TALYS code: The Fission Channel. *Nucl. Data Sheets* **131**, 222 (2016)
25. M. Sin et al., Fission of light actinides: $^{232}\text{Th}(n, f)$ and $^{231}\text{Pa}(n, f)$ reactions. *Phys. Rev. C* **74**, 014608 (2006)
26. S. Goriely et al., Towards a prediction of fission cross sections on the basis of microscopic nuclear inputs. *Phys. Rev. C* **79**, 024612 (2009)
27. S. Goriely et al., Towards an improved evaluation of neutron-induced fission cross sections on actinides. *Phys. Rev. C* **83**, 034601 (2011)

Modeling Compound Nuclear Reactions with EMPIRE



M. Herman, R. Capote, B. V. Carlson, M. Sin, and A. Trkov

1 Introduction

The description of low-energy nucleon-induced reactions in the continuum region requires, at the very least, calculations of elastic scattering within the optical model and of statistical emission of photons and light particles from the compound nucleus formed from the fusion of the projectile and target. If actinide targets are to be described, a reasonably sophisticated model of fission should also be included in the statistical emission calculation. At very low energies, width fluctuation corrections must be included, while at energies above about 10 MeV, pre-equilibrium effects should be taken into account.

The EMPIRE code, [36] first released in 1980, calculated both elastic scattering and the cross sections and spectra of statistical equilibrium and pre-equilibrium decay processes. It was later extended to include width fluctuation corrections to low-energy cross sections. A version for heavy-ion induced reactions was also introduced.

In its second release, EMPIRE-2, the code was entirely rewritten using a modular structure, as well as taking advantage of more relaxed memory limitations, to obtain an increase in execution speed of about a factor of 20. The new code was projected

M. Herman

Theoretical Division, Los Alamos National Laboratory, Los Alamos, New Mexico, USA

R. Capote · A. Trkov

NAPC-Nuclear Data Section, International Atomic Energy Agency, Vienna, Austria

B. V. Carlson (✉)

Instituto Tecnológico da Aeronáutica, São José dos Campos, SP, Brazil

M. Sin

Faculty of Physics, University of Bucharest, Bucharest, Romania

© This is a U.S. government work and not under copyright protection in the U.S.; foreign copyright protection may apply 2021

J. Escher et al. (eds.), *Compound-Nuclear Reactions*, Springer Proceedings in Physics 254, https://doi.org/10.1007/978-3-030-58082-7_2

to be general and flexible. Each module was designed to perform a well-defined task and to communicate with other modules through a set of global COMMON blocks. This assured access to all the resources throughout the code and facilitated the addition of new features and mechanisms. The third release of the code, EMPIRE-3, maintains and extends this structure.

The current version, EMPIRE-3.2, is named Malta, after Napoleon's capture of the island on the way to Egypt. Although a minor release, it features a number of significant improvements such as: (1) prompt fission neutron spectra, including automatic adjustment to experimental data, (2) anisotropic angular distributions for compound elastic and inelastic excitations, (3) simulation of the Engelbrecht-Weidenmüller transformation, and (4) new IO subroutines for the manipulation of ENDF-6 formatted files.

2 Basic Objectives and Scope

The basic objectives of the EMPIRE code are:

- to provide the state-of-the-art modeling of nuclear reactions for basic science and data evaluation;
- to ensure reasonably comprehensive coverage of incident particles, targets, incident energies, and observables;
- To unify (1) reaction models, (2) model parameters, (3) nuclear structure data, and (4) experimental results;
- to provide a full set of tools for evaluators to enable efficient production of high quality nuclear data files;
- to be as general, flexible, and easy to use as possible.

The present scope of the code includes:

- A broad range of incident energies (up to 150 MeV) and projectiles (n, p, d, t, ^3He , ^4He , photons, and heavy ions);
- The low-energy range for neutron reactions covered by an interface to the Atlas of Neutron Resonances [1];
- Default input parameters for targets of mass number $A \geq 20$ [2];
- Direct, pre-equilibrium, and statistical model reaction mechanisms—with width fluctuations and a full gamma cascade;
- Observables: cross sections, angular distributions, spectra (including prompt fission neutron spectra), energy-angular distributions;
- Outgoing channels: multi-particle emission, γ -emission (including discrete lines), discrete levels (including isomers), fission, several exclusive channels.

To a large extent, the present scope of the EMPIRE code permits it to fulfill its objectives. However, it should also be clear that the objectives are an evolving target that will never be completely met.

3 Reaction Modeling

A low-to-intermediate-energy nuclear reaction can be approximately divided into an initial stage, during which direct reactions occur or the projectile (or a part of it) fuses with the target, and a subsequent stage, during which the compound nucleus fissions or de-excites by particle and gamma-ray emission. Pre-equilibrium emission, which consists predominantly of multistep direct reactions, tends to blur the distinction between the two stages, but is traditionally considered as part of the emission rather than the formation stage of the reaction. We discuss below the models and codes used in EMPIRE to describe each of the stages.

3.1 *Fusion and Direct Reactions*

EMPIRE uses the optical model to calculate transmission coefficients and absorption cross sections for light particles. Spherical optical model calculations are performed using ECIS-2006 [3, 4], while deformed optical model calculations are performed using ECIS-2006 or OPTMAN [5–7]. For heavy-ion induced reactions, the simplified coupled channels code CCFUS [8] or a distributed barrier model can be used. The photoabsorption cross section is used to initiate a gamma-induced reaction. If desired, absorption cross sections or transmission coefficients can also be input directly.

Direct reaction cross sections can be calculated using coupled channels with the codes ECIS-2006 or OPTMAN or the distorted wave Born approximation (DWBA) using ECIS-2006. The two methods can be mixed when ECIS-2006 is used. That is, strongly coupled channels can be calculated using coupled channels, while weaker channels can be calculated using the DWBA.

Deuteron breakup and its incomplete fusion have recently been included in EMPIRE [9]. The breakup is calculated in the DWBA approximation and the formation and decay of the compound nuclei involving the remaining deuterons and the breakup protons and neutrons are taken into account consistently.

3.2 *Compound Nucleus and Pre-equilibrium Emission*

The basic compound nucleus decay model in EMPIRE is a multi-emission Hauser-Feshbach decay model [10] with a full γ -cascade and dynamical deformation effects. Width fluctuations can be included using the HRTW [11, 12] or Moldauer [13] formalisms. Direct channel coupling can be included in the statistical emission through the Engelbrecht-Weidenmüller transformation [14]. Both cross sections and angular distributions can be calculated for elastic and resolved inelastic states. Cross sections, spectra, angular distributions, and double differential energy-angular

distributions can be calculated for emissions in the continuum region. Exclusive quantities can also be calculated for simple emission channels (xn, xp, np).

Level densities can be described by three phenomenological models—the Gilbert–Cameron model [15], the generalized superfluid model [16], or the enhanced generalized superfluid model [17]—or by a model based on Hartree–Fock–Bogoliubov levels [18]. The level densities are parametrized or normalized to reproduce the average parameters of the neutron resonances and the data on the cumulative number of low-lying nuclear levels.

Several options exist for the gamma-ray strength functions in the statistical decay. These include the enhanced generalized Lorentzian [19], several modified Lorentzians [20, 21], the generalized Fermi-liquid model [22], the standard Lorentzian [23], and single-particle Weisskopf estimates. These are normalized internally to experimental gamma-ray strength functions, when available.

At higher incident energies, pre-equilibrium emission becomes important. Models available in EMPIRE for the description of these reactions are:

- the Tamura-Udagawa-Lenske multistep direct reaction model, as implemented in ORION + TRISTAN [24, 25];
- the Nishioka-Verbaarschot-Weidenmüller-Yoshida multistep compound model with γ -emission [26];
- the standard single-emission exciton model, as implemented in PCROSS;
- the Iwamoto-Harada model for complex particle emission [27, 28], also implemented in PCROSS; and
- the hybrid Monte Carlo simulation model, which permits multiple pre-equilibrium emissions, as implemented in the code DDHMS [29–31].

These models need not be executed exclusively. Thus, for example, it is possible to calculate pre-equilibrium neutron emission using ORION + TRISTAN and the pre-equilibrium emission of light charged particle using PCROSS, among other possible combinations.

3.3 *Fission*

EMPIRE contains both simple and sophisticated models of fission.

- The Sierk model can be used for light particle or heavy-ion induced fission [32].
- For incident light particles or photons, one can use an optical model for transmission through multi-humped fission barriers parametrized analytically or defined numerically, as well as multi-modal fission [33].
- Finally, prompt fission neutron spectra can be calculated using either the Madland–Nix [34] or the Kornilov [35] model.

4 Cross Section Calculations Using EMPIRE-3.2

In the following, we compare EMPIRE calculations with experimental data for several different reactions. We begin with the cross sections for neutron-induced reactions on ^{56}Fe and ^{238}U , shown in Figs. 1 and 2. The cross sections for the various emission channels of each target were calculated simultaneously and display very good agreement with the experimental data. The elastic, inelastic, capture, and $2n$ cross sections make important contributions to the total cross section in both cases. Proton emission is also an important channel for the iron target but is strongly suppressed in uranium. In the latter, the fission channel plays an important role.

EMPIRE-3.2 can also describe photon-induced reactions. The photabsorption cross section is modeled as a sum of giant dipole resonance and quasi-deuteron terms, leading to initial one-particle one-hole and two-particle two-hole configurations, respectively. The particle emission is calculated as a pre-equilibrium + equilibrium statistical decay process. Cross sections for photoabsorption on ^{181}Ta and its multiple neutron emission channels are shown in Fig. 3.

The $^{124}\text{Te}(d,2n)^{124}\text{I}$ reaction, shown in Fig. 4, provides a good example of the importance of breakup in a deuteron-induced reaction. All optical model calculations all overestimate the cross section due to the fact that they do not discount the large (d,p) contribution from the breakup. The direct breakup model

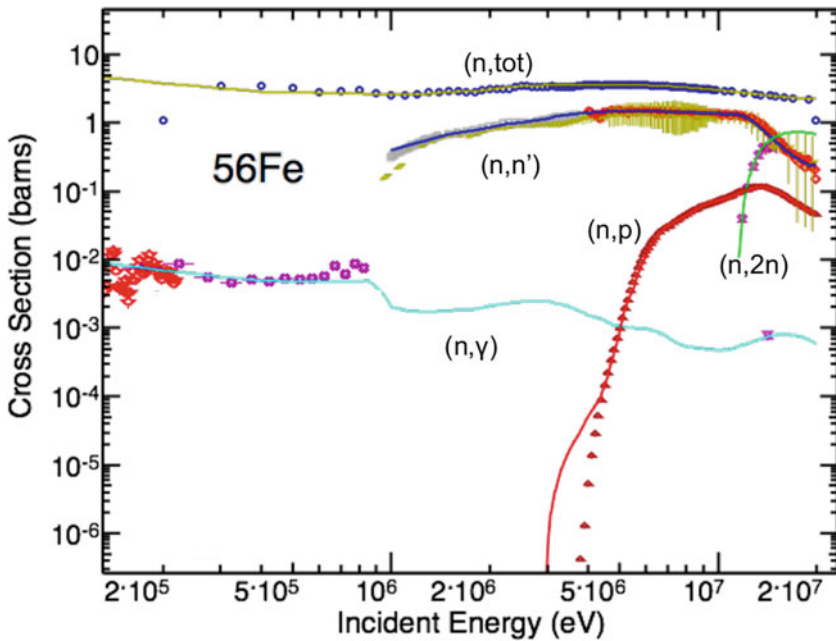


Fig. 1 Experimental data and cross sections calculated with EMPIRE-3.2 for several neutron-induced reactions on ^{56}Fe as a function of the incident energy

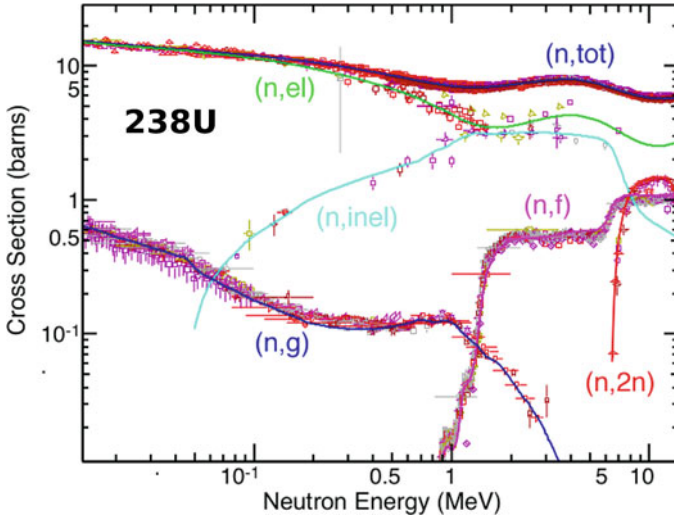


Fig. 2 Experimental data and cross sections calculated with EMPIRE-3.2 for several neutron-induced reactions on ^{238}U as a function of the incident energy

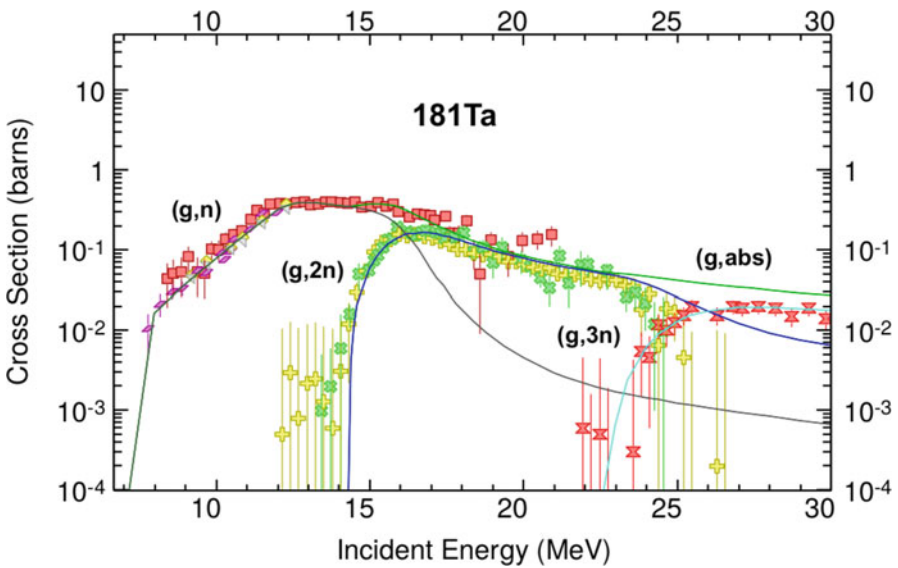


Fig. 3 Experimental data and cross sections calculated with EMPIRE-3.2 for photoabsorption and neutron emission channels of the photon-induced reaction on ^{181}Ta as a function of the incident energy

calculation of EMPIRE-3.2, shown as the red triangles in the figure, is also high compared to the experimental data, but will decrease when the calculation of stripping to bound states is improved.

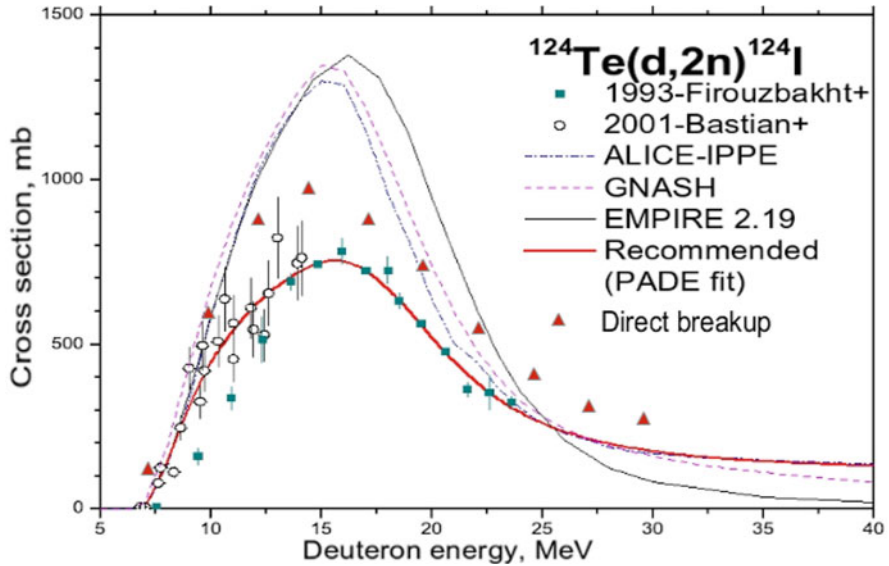


Fig. 4 Experimental data and several cross section calculations for the reaction $^{124}\text{Te}(d,2n)^{124}\text{I}$. The calculation taking into account deuteron breakup (red triangles) was performed with EMPIRE-3.2.

5 Summary

In closing, we want to point out a few of the highlights of the EMPIRE code, not all of which were mentioned above. In our opinion, among these are:

- inclusion of most important nuclear reaction mechanisms;
- a large choice of models and parametrizations;
- use of the Reference Input Parameter Library, RIPL-3 [2];
- automatic retrieval of experimental data from EXFOR;
- interactive plots of calculated and experimental results;
- highly automated fits of optical model parameters;
- automatic adjustment of all model parameters;
- determination of covariances (Monte Carlo, KALMAN);
- a resonance module with a link to the Atlas of Neutron Resonances [1];
- ENDF-6 formatting and verification;
- NJOY support.

In short, EMPIRE provides a complete path from experiment to evaluation to validation.

Versions of EMPIRE for Windows, Linux, and Mac OSX are available on the EMPIRE webpage at www-nds.iaea.org/empire/. More details of the code can be found in Ref. [36] and the EMPIRE manual, available at www-nds.iaea.org/publications/indc/indc-nds-0603/.

Acknowledgments EMPIRE is the result of an international cooperation towards open source software, as so successfully promoted by the General Public License. A number of authors contributed to the development of the code and it would be next to impossible to list all names. We mention here several important EMPIRE developers, D. Brown (BNL, Upton), S. Hoblit (deceased), G. Nobre (BNL, Upton), H. Wienke (deceased), and V. Zerkin (IAEA, Vienna), as well as a number of important contributors to the code, E. Betak (SAS, Bratislava), Young-Sik Cho (KAERI, Daejeon), T. Kawano (LANL, Los Alamos), C. Mattoon (LLNL, Livermore), S. Mughabghab (deceased), P. Oblozinsky (Bratislava), M. Pigni (ORNL, Oak Ridge), V. Plujko (University of Kiev), and A. Ventura (ENEA, Bologna).

BVC acknowledges support from grant 2017/05660-0 of the São Paulo Research Foundation (FAPESP), grant 306433/2017-6 of the CNPq, the INCT-FNA project 464898/2014-5 and Research Project 17440 of the IAEA. Part of this work was performed under the auspices of the National Nuclear Security Administration of the U.S. Department of Energy at Los Alamos National Laboratory under Contract No. 89233218CNA000001.

References

1. S. F. Mughabghab, *Atlas of Neutron Resonances: Thermal Cross Sections and Resonance Parameters* (Elsevier, Amsterdam, 2006)
2. R. Capote et al., Nucl. Data Sheets **110**, 3107 (2009)
3. J. Raynal, Technical Report No. SMR-9/8, IAEA (unpublished)
4. J. Raynal, Computing as a language of physics, in *ICTP International Seminar Course* (IAEA/ICTP, Trieste, Italy, 1972), p. 281
5. E. Soukhovitskiĭ, G. Morogovski, S. Chiba, T. Fukahori, Technical report, JAERI-Data/Code 2004-002, Japan Atomic Energy Research Institute (unpublished).
6. E. Soukhovitskiĭ et al., Technical Report No. JAERI-Data/Code 2005-002, Japan Atomic Energy Research Institute (unpublished).
7. E. Soukhovitskiĭ et al., Technical report, JAERI-Data/Code 2008-025, Japan Atomic Energy Research Institute (unpublished).
8. C. H. Dasso, S. Landowne, Comput. Phys. Commun. **46**, 187 (1987)
9. B.V. Carlson, R. Capote, M. Sin, Few-Body Syst. **57**, 307 (2016)
10. W. Hauser, H. Feshbach, Phys. Rev. **87**, 366 (1952)
11. H.M. Hofmann, J. Richert, J.W. Tepel, H. A. Weidenmüller, Ann. Phys. **90**, 403 (1975)
12. H.M. Hofmann, T. Mertelmeier, M. Herman, J.W. Tepel, Z. Physik A **297**, 153 (1980)
13. P.A. Moldauer, Phys. Rev. C **12**, 744 (1975)
14. C.A. Engelbrecht, H.A. Weidenmüller, Phys. Rev. C **8**, 859 (1973)
15. A. Gilbert, A.G.W. Cameron, Can. J. Phys. **43**, 1446 (1965)
16. A.V. Ignatyuk, G.N. Smirenkin, A.S. Tishin, Sov. J. Nucl. Phys. **21**, 255 (1975)
17. A. D'Arrigo et al., J. Phys. G **20**, 365 (1994)
18. S. Goriely, M. Samyn, J.M. Pearson, Phys. Rev. C **75**, 064312 (2007)
19. J. Kopecky, M. Uhl, R.E. Chrien, Phys. Rev. C **47**, 312 (1993)
20. V.A. Plujko, Acta Phys. Pol. B **31**, 435 (2000)
21. V.A. Plujko, S.N. Ezhov, M.O. Kavatsyuk, in *International Conference on Nuclear Data for Science and Technology*, vol. 1, ed. by K. Shibata (Atomic Energy Society of Japan, Tsukuba, 2001), p. 811
22. S.F. Mughabghab, C.L. Dunford, Phys. Lett. B **487**, 155 (2000)
23. D.M. Brink, Ph.D. thesis (Oxford University, Oxford, 1955)
24. T. Tamura, T. Udagawa, H. Lenske, Phys. Rev. C **26**, 379 (1982)
25. H. Lenske, H.H. Wolter, TRISTAN and ORION codes, private communication to M. Herman.
26. H. Nishioka, J.J.M. Verbaarschot, H.A. Weidenmüller, S. Yoshida, Ann. Phys. **172**, 67 (1986)
27. A. Iwamoto, K. Harada, Phys. Rev. C **26**, 1821 (1982)

28. K. Sato, A. Iwamoto, K. Harada, *Phys. Rev. C* **28**, 1527 (1983)
29. M. Blann, *Phys. Rev. C* **54**, 1341 (1996)
30. M. Blann, M. Chadwick, *Phys. Rev. C* **57**, 233 (1998)
31. M.B. Chadwick, DDHMS code, private communication to M. Herman
32. A.J. Sierk, *Phys. Rev. C* **33**, 2039 (1986)
33. M. Sin, R. Capote, M.W. Herman, A. Trkov, *Phys. Rev. C* **93**, 034605 (2016)
34. D.G. Madland, J.R. Nix, *Nucl. Sci. Eng.* **81**, 213 (1982)
35. N.V. Kornilov, A.B. Kagalenko, F.-J. Hamsch, *Phys. At. Nucl.* **62**, 173 (1999)
36. M. Herman, R. Capote, B.V. Carlson, P. Obložinský, M. Sin, A. Trkov, H. Wienke, V. Zerkin, *Nucl. Data Sheets* **108**, 2655 (2007)

CoH₃: The Coupled-Channels and Hauser-Feshbach Code



Toshihiko Kawano

1 Introduction

The statistical Hauser-Feshbach (HF) codes with width fluctuation correction are the main tool for calculating compound nuclear reactions when an individual resonance structure no longer persists. Typically this situation is satisfied when a nucleon or a light charged particle having more than a few hundred keV energy interacts with a medium to heavy ($A > 20$) target. These codes provide complete information of nuclear reactions, not only the reaction cross sections but also the energy and angular distributions of secondary particles, γ -ray production cross sections, isomeric state productions, and so on.

In the 1990s, the Los Alamos HF code, GNASH [1], was widely utilized to calculate nuclear reaction cross sections, together with an optical model code such as ECIS or ELIESE-3 [2] for generating the particle transmission coefficients. Although GNASH is a powerful code to study nuclear reaction mechanisms, the mainframe-age technology makes upgrading and maintaining the source code extremely difficult. Under such the circumstances, development of a new optical and HF code, CoH, began at Kyushu University. Originally it was written in C, and later whole the source code was rewritten in C++. The most recent version, CoH₃, possesses more functionality than GNASH, and it is fully capable for calculating various nuclear reactions.

T. Kawano (✉)

Theoretical Division, Los Alamos National Laboratory, Los Alamos, NM, USA
e-mail: kawano@lanl.gov

© This is a U.S. government work and not under copyright protection in the U.S.; foreign copyright protection may apply 2021
J. Escher et al. (eds.), *Compound-Nuclear Reactions*, Springer Proceedings in Physics 254, https://doi.org/10.1007/978-3-030-58082-7_3

2 CoH₃ Code

2.1 *Quick Glance*

Each version of CoH₃ has a unique nickname taken from the moons of Uranus. The current version of 3.5 Miranda consists of about 140 C++ source codes and 60 header files. The total line number is about 45,000. The code is written in a semi-OOP (Object-Oriented Programming) style, and there are about 80 classes defined. Unlike the other HF codes currently available in the market, such as EMPIRE [3] or TALYS [4], CoH₃ includes its own optical model solver to generate the transmission coefficients internally. This feature is the same as in the CCONE code [5].

Another noticeable difference is that CoH₃ runs both in the deterministic and stochastic (Monte Carlo) modes [6]. In the Monte Carlo mode, the compound nucleus decay is tracked by a random sampling technique in order to preserve all correlated information. Albeit this feature is not yet widely used in practical calculations for now, an accurate estimate of the exclusive particle emission spectra can be examined.

CoH₃ is designed to calculate nuclear reactions at relatively low energies. Although it is capable of calculating a 100-MeV nucleon induced reaction, it is not so efficient. We will revisit this issue later.

2.2 *Models and Modules*

Spherical and Deformed Optical Models In the deformed nucleus case, a rotational or vibrational model is employed for the coupled-channels (CC) calculation. These models yield a channel transmission coefficient T_a , which defines the probability of forming a compound nucleus from a channel a . The optical model scattering wavefunction is also used in the DWBA (Distorted Wave Born Approximation) method for the direct inelastic scattering process.

Compound Reaction Properties of excited states in a compound nucleus are determined by reading the nuclear structure database [7]. At higher excitation energies, we use the Gilbert–Cameron level density formula [8] with updated parameters [9]. CoH₃ allows to overlap the discrete level and continuum regions, and some of the levels can be embedded in the continuum. This is particularly important when some γ transitions from highly excited states are observed experimentally. This often impacts the isomeric state production.

The width fluctuation correction is calculated by applying the method of Moldauer [10] with LANL updated parameters [11], which gives very similar correction factors to the GOE (Gaussian Orthogonal Ensemble) results [12]. When strongly coupled channels exist, the inelastic scattering process is calculated with

the CC method, and the Engelbrecht-Weidenmüller transformation is invoked to diagonalize the S -matrix [13].

Pre-equilibrium Reaction The two-component exciton model [14, 15] is used to calculate the pre-equilibrium process. The quantum mechanical pre-equilibrium models, such as FKK (Feshbach-Kerman-Koonin) [16, 17] or NWY (Nishioka-Weidenmüller-Yoshida) [18, 19], are also available, yet provided as external codes. See Ref. [20], for example.

Prompt Fission Neutron Spectrum For fissioning nuclei, the prompt fission neutron spectrum is calculated with the Madland–Nix model [21] including pre-fission neutron emissions.

Direct/Semidirect (DSD) Neutron Capture The direct/semidirect (DSD) neutron capture process is calculated with the DSD model [22–26]. A standard option is to use the spherical Woods–Saxon potential for calculating the single-particle wavefunctions. In the deformed nucleus case, two mean-field models can be used [27]; FRDM (Finite-Range Droplet Model) [28, 29] and HF-BCS (Hartree-Fock BCS) [30].

3 Transmission Coefficients for the Excited States

CoH₃ is designed to combine tightly the CC optical model and the statistical HF theory, in which the generalized transmission coefficients for the excited states are calculated from the CC S -matrix [31]. This is especially important for calculating nuclear reaction process on a deformed nucleus, such as actinides. The transmission coefficient for the n -th excited state with orbital angular momentum l and spin j is calculated as

$$T_{lj}^{(n)} = \sum_{J\Pi} \sum_c g_{Jc} \left(1 - \sum_{c' \in n} |S_{cc'}^{J\Pi}|^2 \right), \quad (1)$$

where c labels the channel, and g_{Jc} is the spin factor. Here the flux going into the directly coupled channels is eliminated from the total absorption probability, such that the sum of $T_{ij}^{(n)}$ gives a correct compound formation cross section from the n -th level. In contrast to this, other HF codes often replace $T_{lj}^{(n)}$ by the one for the ground state $T_{lj}^{(0)}$, and shift the energy by the level excitation energy $E_x^{(n)}$,

$$T_{lj}^{(n)}(E) \simeq T_{lj}^{(0)}(E - E_x^{(n)}). \quad (2)$$

This approximation has never been validated. The calculated neutron transmission coefficients of Eqs. (1) and (2) are compared in Fig. 1. These are for the first excited

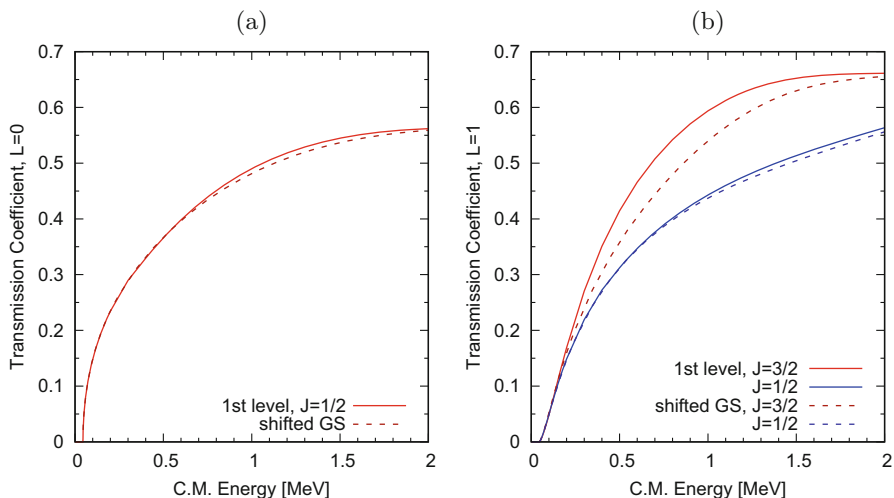


Fig. 1 Calculated transmission coefficients for the neutron induced reaction on ^{238}U . The solid curves are the correct transmission coefficients for the excited states, while the dashed curves are approximations using results for the ground state. **(a)** s -wave. **(b)** p -wave

state of ^{238}U . The CC calculation was performed by coupling the first five levels in the ground state rotational band with the optical potential of Soukhovitskii et al. [32]. The right side panel for the s -wave well supports the approximation of the replacement, while an obvious difference is seen for the p -wave case. Since the impact is not so significant, the calculated cross section might not be so discrepant. However, we should keep this in our mind that the uncertainty in the model calculation adds up due to the actual implementation of the HF formula. A code comparison performed among EMPIRE, TALYS, CCONE, and CoH₃ showed the inelastic scattering cross section by CoH₃ tends to be slightly higher than from the other codes [33].

When the Engelbrecht-Weidenmüller transformation is applied to the width fluctuation correction, the CC S -matrix is converted into Satchler's penetration matrix [34] and diagonalized to eliminate the off-diagonal elements. This is an exact calculation of the combined CC and HF models, although the computation will take a few times longer than the approximated calculation. Details are explained elsewhere [13].

4 Multiparticle Emission and Exclusive Cross Section

A compound nucleus at a given excited state decays to another nucleus by emitting several particles when the excitation energy is high enough, and different reaction chains sometimes end up with the same residual nucleus. For example, the residual

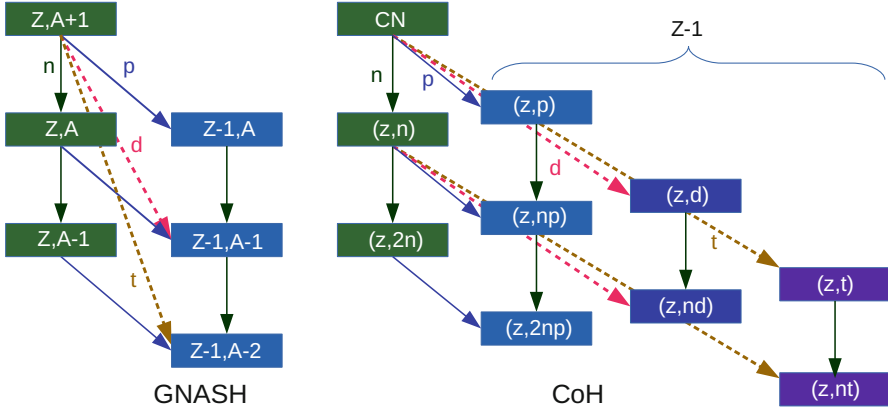


Fig. 2 Schemes of compound nucleus decay. The left hand side shows an inclusive algorithm employed by GNASH, where all information having the same Z, A enters into the same memory space. CoH₃ adopts an exclusive algorithm, in which different reaction paths are explicitly tracked

nucleus of $(n, n+p)$ reaction is the same as that of (n, d) . When a common memory space is allocated to these residual nuclei, it is difficult to separate cross sections into the $(n, n+p)$ and (n, d) reactions. This happens to the regular HF codes like GNASH, which is schematically shown in the left panel of Fig. 2. In order to distinguish these reaction paths, in other words, to seek an exclusive reaction cross section, CoH₃ allocates independent objects for different reaction channels, as shown in the right panel of Fig. 2. For example, information of the $(n, n+p)$ reaction is stored in an object, while that of (n, d) is elsewhere.

Indeed this technique allows us to split a residual nucleus production cross section into the exclusive reaction channels, the extra cost incurred is in the computational resources. When the excitation energy of a compound nucleus increases, the number of objects necessary to keep all the information increases rapidly, and the computational time becomes very long. For high energy applications, one might need to stay on the traditional inclusive algorithm. Anyway, with the exclusive algorithm adopted by CoH₃, the compound nuclear reaction cross section and its energy spectrum are easily divided into individual reaction channels.

5 Satellite Tools

CoH₃ includes some subsidiary codes to expand its capability and to explore a wider area of nuclear reaction physics. In the stable branch of the package, a subset of CoH₃, called BeoH, is included. The BeoH code just calculates the statistical decay of a given compound state. Application of this code includes the emission of neutron and γ -ray in both β -decay [35, 36] and the fission process [37]. In the fission case,

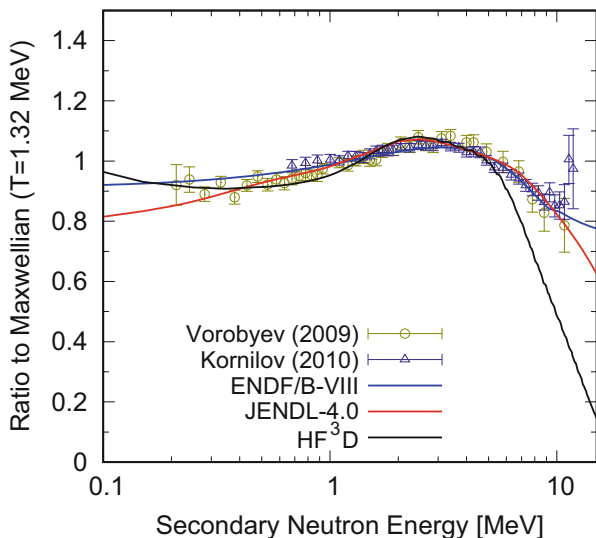


Fig. 3 The calculated prompt fission neutron spectrum for the thermal neutron induced fission on ^{235}U with the HF^3D model. The spectrum is shown as the ratio to the Maxwellian at the temperature of 1.32 MeV

we follow the decay of two excited fragments formed by a fission process by using the HF theory, called HF^3D (Hauser-Feshbach Fission Fragment Decay) [37]. Such calculation produces the fission product yields and the prompt fission observables (neutron and γ -ray spectra and multiplicities) in a consistent manner. An example of a calculated prompt fission neutron spectrum for the thermal neutron induced fission on ^{235}U is shown in Fig. 3. The HF^3D spectrum is distinct from the Madland–Nix model calculation in the two energy domains; the spectrum tends to be higher than the Madland–Nix prediction at low energies, while it drops quickly above 6 MeV. We are still investigating why the HF^3D spectrum is softer than the evaluated data.

Two more modules are provided in the development branch; the microscopic level density [19] based on the random matrix theory, and the FRLDM (Finite-Range Liquid Drop Model) [38]. Despite these experimental modules have not been fully merged yet with the main reaction calculation stream, they offer a better connection between the nuclear structure and reaction models [39].

6 Conclusion

As demonstrated the CoH_3 code is designed mainly to predict reliable nuclear reaction cross sections at low energies, where many nuclear applications exist such as the fission energy systems and the nuclear astrophysics. We outlined that CoH_3 includes careful modeling of the coupled-channels optical model and the Hauser-

Feshbach theory with the width fluctuation correction. It should be emphasized that CoH₃ is the first code that fully implements the Engelbrecht-Weidenmüller transformation of the coupled-channels *S*-matrix, which is particularly important for calculating neutron inelastic scattering off very deformed nuclei.

Acknowledgments The author thanks to P. Talou and M.R. Mumpower of LANL, S. Chiba of Tokyo Institute of Technology, S. Okumura of IAEA for valuable discussions. This work was carried out under the auspices of the National Nuclear Security Administration of the U.S. Department of Energy at Los Alamos National Laboratory under Contract No. 89233218CNA000001.

References

1. P.G. Young, E.D. Arthur, Tech. Rep. LA-6947 (Los Alamos National Laboratory, New Mexico, 1977)
2. S. Igarasi, Tech. Rep. JAERI-1224 (Japan Atomic Energy Research Institute, Japan, 1972)
3. M. Herman, R. Capote, M. Sin, A. Trkov, B.V. Carlson, P. Obložinský, C.M. Mattoon, H. Wienke, S. Hoblit, Y.S. Cho, G. Nobre, V. Plujko, V. Zerkin, Tech. Rep. INDC(NDS)-0603 (International Atomic Energy Agency, Vienna, 2013)
4. A.J. Koning, S. Hilaire, M.C. Duijvestijn, EPJ Web of Conferences, in *Proceedings of the International Conference on Nuclear Data for Science and Technology, 22–27 April 2007, Nice, France*, ed. by O. Bersillon, F. Gunsing, E. Bauge, R. Jacqmin, S. Leray (2008), pp. 211–214
5. O. Iwamoto, J. Nucl. Sci. Technol. **44**(5), 687–697 (2007)
6. T. Kawano, P. Talou, M.B. Chadwick, T. Watanabe, J. Nucl. Sci. Technol. **47**(5), 462–469 (2010)
7. R. Capote, M. Herman, P. Obložinský, P.G. Young, S. Goriely, T. Belgya, A.V. Ignatyuk, A.J. Koning, S. Hilaire, V.A. Plujko, M. Avrigeanu, O. Bersillon, M.B. Chadwick, T. Fukahori, Z. Ge, Y. Han, S. Kailas, J. Kopecky, V.M. Maslov, G. Reffo, M. Sin, E.S. Soukhovitskii, P. Talou, Nucl. Data Sheets **110**(12), 3107–3214 (2009)
8. Gilbert, A.G.W. Cameron, Can. J. Phys. **43**, 1446–1496 (1965)
9. T. Kawano, S. Chiba, H. Koura, J. Nucl. Sci. Technol. **43**(1), 1–8 (2006)
10. P.A. Moldauer, Nucl. Phys. A **344**(2), 185–195 (1980)
11. T. Kawano, P. Talou, Nucl. Data Sheets **118**, 183–186 (2014)
12. T. Kawano, P. Talou, H.A. Weidenmüller, Phys. Rev. C **92**, 044617 (2015)
13. T. Kawano, R. Capote, S. Hilaire, P. Chau Huu-Tai, Phys. Rev. C **94**, 014612 (2016)
14. C. Kalbach, Phys. Rev. C **33**, 818–833 (1986)
15. A.J. Koning, M. Duijvestijn, Nucl. Phys. A **744**, 15–76 (2004)
16. H. Feshbach, A. Kerman, S. Koonin, Ann. Phys. **125**(2), 429–476 (1980)
17. T. Kawano, Phys. Rev. C **59**, 865–875 (1999)
18. H. Nishioka, H. Weidenmüller, S. Yoshida, Ann. Phys. **193**(1), 195–205 (1989)
19. T. Kawano, S. Yoshida, Phys. Rev. C **64**, 024603 (2001)
20. T. Kawano, T. Ohsawa, M. Baba, T. Nakagawa, Phys. Rev. C **63**, 034601 (2001)
21. D.G. Madland, J.R. Nix, Nucl. Sci. Eng. **81**(2), 213–271 (1982)
22. G.B. Brown, Nucl. Phys. **57**, 339–344 (1964)
23. C.F. Clement, A.M. Lane, J.R. Rook, Nucl. Phys. **66**(2), 273–292 (1965)
24. J.P. Boisson, S. Jang, Nucl. Phys. A **189**(2), 33–352 (1972)
25. H. Kitazawa, T. Hayase, N. Yamamuro, Nucl. Phys. A **307**(1), 1–21 (1978)
26. W.E. Parker, M.B. Chadwick, F.S. Dietrich, J.E. Kammeraad, S.J. Luke, K.E. Sale, R.M. Chasteler, M.A. Godwin, L.H. Kramer, G.J. Schmid, H.R. Weller, A.K. Kerman, Phys. Rev. C **52**, 252–266 (1995)

27. T. Kawano, *Eur. Phys. J. A* **51**, 164–170 (2015)
28. P. Möller, J.R. Nix, W.D. Myer, W. Swiatecki, *At. Data Nucl. Data Tables* **59**(2), 185–381 (1995)
29. P. Möller, A.J. Sierk, T. Ichikawa, H. Sagawa, *At. Data Nucl. Data Tables* **109–110**, 1–204 (2016)
30. L. Bonnaeu, T. Kawano, T. Watanabe, S. Chiba, *Phys. Rev. C* **75**, 054618 (2007)
31. T. Kawano, P. Talou, J.E. Lynn, M.B. Chadwick, D.G. Madland, *Phys. Rev. C* **80**, 024611 (2009)
32. E.S. Soukhovitskii, R. Capote, J.M. Quesada, S. Chiba, *Phys. Rev. C* **72**, 024604 (2005)
33. R. Capote, S. Hilaire, O. Iwamoto, T. Kawano, M. Sin, *EPJ Web Conf.* **146**, 12034 (2017)
34. G. Satchler, *Phys. Lett.* **7**(1), 55–56 (1963)
35. T. Kawano, P. Möller, W.B. Wilson, *Phys. Rev. C* **78**, 054601 (2008)
36. M.R. Mumpower, T. Kawano, P. Möller, *Phys. Rev. C* **94**, 064317 (2016)
37. S. Okumura, T. Kawano, P. Jaffke, P. Talou, S. Chiba, *J. Nucl. Sci. Technol.* **55**(9), 1009–1023 (2018)
38. P. Möller, A.J. Sierk, T. Ichikawa, A. Iwamoto, R. Bengtsson, H. Uehlenholt, S. Åberg, *Phys. Rev. C* **79**, 064304 (2009)
39. T. Kawano, *EPJ Web Conf.* **146**, 12004 (2017)

Part II
Beyond Statistical Descriptions

Recent Advances in R-matrix Data Analysis



Ian J. Thompson

1 R-matrix Theory

R-matrix theory is designed to describe individual resonances in two-body scattering even when overlapping, and the non-resonant background between them. It describes all the asymptotic properties of the relative wave function outside some fixed radius a in terms of pole energies e_p and reduced width amplitudes $\gamma_{p\alpha}$ for each partial-wave channel α and pole p . The $\gamma_{p\alpha}$ can be calculated from some structure theory, or fitted to data.

R-matrix theory is the starting point for compound-nucleus models. It is the basis for making statistical approximations, such as the Reich–Moore approximation, and Hauser-Feshbach models. It can be used to check the accuracy of those approximate models, as well as models for the width-fluctuation corrections.

The foundation of R-matrix theory is summarized in the landmark paper of Lane and Thomas [1]. In that paper is the foundational “R-matrix Theorem”: For Hermitian $H = T + V + \hat{B}$ with Bloch operator $\hat{B} = \delta(r-a)(\frac{d}{dr} - \frac{B}{r})$, with $V \neq 0$ only for $r \in [0, a]$ and E -independent, then the exact scattering solution $H\psi = E\psi$ can be represented by a R-matrix at $r = a$ with a set of pole energies e_p and reduced width amplitudes $\gamma_{p\alpha}$ as

$$R_{\alpha\alpha'}(E) = \sum_{p=1}^{\infty} \frac{\gamma_{p\alpha}\gamma_{p\alpha'}}{e_p - E}. \quad (1)$$

I. J. Thompson (✉)

Lawrence Livermore National Laboratory, Livermore, CA, USA

e-mail: I-Thompson@llnl.gov; thompson97@llnl.gov

© This is a U.S. government work and not under copyright protection in the U.S.; foreign copyright protection may apply 2021

J. Escher et al. (eds.), *Compound-Nuclear Reactions*, Springer Proceedings in Physics 254, https://doi.org/10.1007/978-3-030-58082-7_4

2 Phenomenological R-matrix

The “phenomenological R-matrix method” that is followed in the remainder of this paper does not start from a Hamiltonian and does not have an infinite series of poles. Rather it uses a finite number P of R-matrix pole energies e_p , with reduced width amplitudes $\gamma_{p\alpha}$ as parameters in the familiar *finite* sum

$$R_{\alpha\alpha'}(E) = \sum_{p=1}^P \frac{\gamma_{p\alpha}\gamma_{p\alpha'}}{e_p - E}, \quad (2)$$

to be adjusted to fit experimental scattering data. Positive-energy poles are again aligned with scattering resonances. Other poles are “background poles” at higher positive energies to attempt to represent the effects of all the remaining terms missing in comparison with expression (1).

Both the exact and phenomenological R-matrix expressions yield (a) unitary S-matrix at each energy, and (b) orthogonal scattering wave functions at different energies. When we come to the approximations often used in R-matrix theory, they should only be accepted if at least they still yield those features. Both conditions derive from having a Hermitian and energy-independent Hamiltonian.

The Reich–Moore approximation [2], by contrast, has imaginary damping widths for missing channels, so condition (a) is not satisfied. It is perhaps satisfactory if a specific meaning is given to the missing flux, e.g., capture or fusion.

Another convenient approximation changes the boundary conditions in the Bloch operator, so B is not constant but is set equal to the shift function at each energy: $B = S(E)$. But now condition (b) is not satisfied since $H = T + V + \hat{B}$ is energy-dependent.

The “alternative parametrization” of Brune [3] is much better than using $B = S(E)$ for making R-matrix pole energies close the energies of cross-section peaks and resonances, since the Brune basis is transformable to and from the Lane and Thomas formalism.

3 Verification of R-matrix Codes

An inter-comparison of the capabilities of the R-matrix codes AMUR [4], AZURE2 [5], EDA (LANL), FRESCOX [6], GECCOS (TU Vienna), SAMMY [7], and CONRAD [8] was performed [9] following a series of IAEA consultants meetings since 2015 [10–13]. As the codes were developed initially for the solution of different problems, each one has its particular features, strengths, and weaknesses, an inter-comparison is particularly valuable.

I have written a python program FERDINAND.PY, to translate between most of the input and output formats of these codes, using GNDS [14] as the intermediate structure. It is also able to make ENDF output sections in the MT= 151 format for evaluations. This kind of interchangeability makes it much easier to track down discrepant details, and to verify and build on each other’s work.

4 Example in A = 7 Scattering

As an example of R-matrix fits, Fig. 1 shows the FRESCOX results for ${}^4\text{He}+{}^3\text{He}$ elastic scattering, with the $p+{}^6\text{Li}$ channel also included. A code-to-code comparison for this data “based on fixed R-matrix parameters” is shown by ratios in Fig. 2. Agreement is almost all better than 0.5%, the level of accuracy needed for R-matrix standard cross-sections. The original fit was done with $B = -L$ boundary conditions, but we can easily and reversibly transform to the Brune basis.

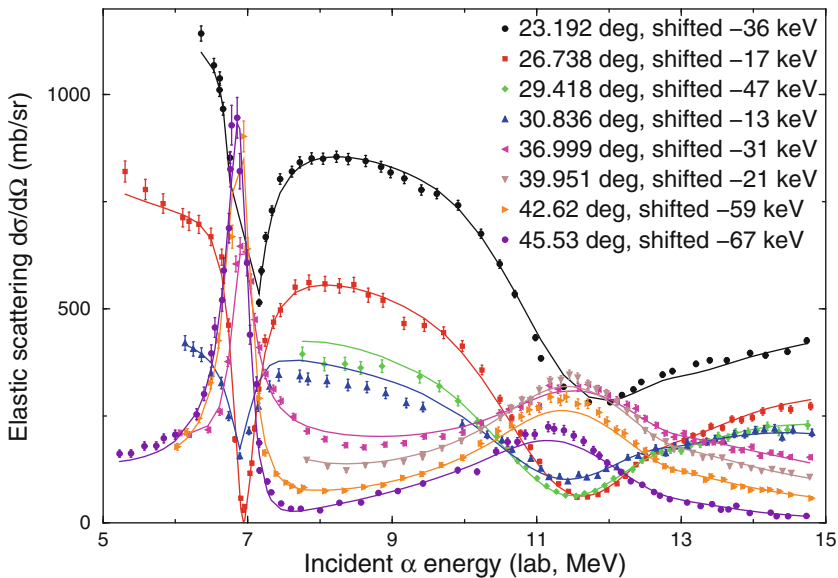


Fig. 1 Fitted cross-sections ${}^3\text{He}(\alpha, \alpha){}^3\text{He}$ reaction to the data of [15]. The separate curves are for each scattering laboratory angle, with preferred data shifts shown by the listed keV values. Tombrello quoted a systematic uncertainty of 5%. Taking this as a 1σ value, the overall fit preferred a systematic increase of the data by 8%

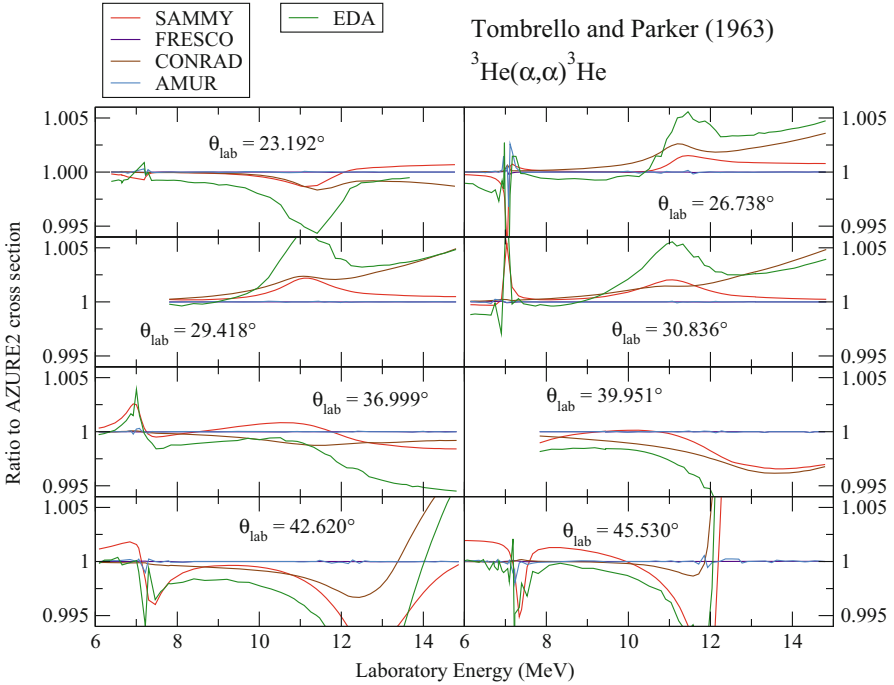


Fig. 2 Comparison of calculations to AZURE2 results for the ${}^3\text{He}(\alpha, \alpha){}^3\text{He}$ reaction using the energies and angles of the [15] data

5 An “Optical” R-matrix Model

At higher incident energies, there are more and more inelastic or transfer two-body channels. Numbers of partial waves increase, but this is still manageable using standard R-matrix theory. But when breakup channels begin to open, these are more difficult to model as they need three-body dynamics. Sometimes these can be well approximated by cascaded two-body channels [16], or by using hyper-spherical harmonics to model the three-body kinematics in full detail. In the meantime, we could perhaps settle for using damping widths Γ_α to describe loss of flux to outside the two-body model space in generalization of the Reich–Moore approximation.

Such damping widths Γ_α describe loss of flux to outside the model space like an optical model, generalizing Reich–Moore for missing particle channels, as in

$$R_{\alpha\alpha'}(E) = \sum_{p=1}^P \frac{\gamma_{p\alpha}\gamma_{p\alpha'}}{e_p - E + i\Gamma_\alpha/2}. \quad (3)$$

This could be allowed, as mentioned earlier, if there are specific physical channels missing from the model (never for bound states). Then the missing flux (from the

unitarity defect) could (for example) be fed into a Hauser-Feshbach decay model built only on the missing physics channels.

But if the total width of a damped resonance is large, then the flux will be missing at lower energies, even below the known threshold for the excluded channels! In that case, absorption would still be present below the threshold of the missing channels, and that would be unphysical.

I therefore consider energy-dependent damping widths, which allows me to describe the energy dependence of flux going to an excluded channel with known threshold E_0 . This makes the damping width energy-dependent, $\Gamma_\alpha(E)$. Ideally, we would like the energy dependence to mimic a set of missing level widths, each behaving as the formal R-matrix widths $\Gamma = 2\gamma^2 P_L(E - E_0)$. So I used, for each R-matrix level p above threshold, a formula which cuts off the width below threshold:

$$\Gamma_\alpha(E) = \tilde{\Gamma}_\alpha \frac{P_L(E - E_0)}{P_L(e_p - E_0)}, \quad (4)$$

for penetrability functions $P_L(E - E_0)$. This cuts off the damping for $E < E_0$, and gives $\Gamma_\alpha(e_p) = \tilde{\Gamma}_\alpha$ as a parameter to be fitted. Making this work depends on having good experimental data for angular distributions above the E_0 threshold. We may also need to choose the e_p energy in the Brune basis in order to keep it at the right energy above the threshold.

If we know the physics of missing channels we can estimate L and Coulomb barriers in the penetrability functions. This would even allow many-body exit channels, in particular three-body ($M = 3$) channels such as (p, pn). If these are described by hyper-spherical harmonics, then there is a new quantum number $K \geq 0$ that describes the ratios of the new three-body coordinates for given moment of inertia ρ . For each value of K there is a centrifugal barrier $L(L + 1)/\rho^2$ where $L = K + (3M - 6)/2$. For 3-body breakup channels this gives $L = K + 3/2$. If a particular K dominates in an exit channel, then the corresponding L -value should be used in Eq. (4).

As an example fit with energy-dependent damping, I refitted ${}^4\text{He}+{}^3\text{He}$ data from Tombrello [15] with only the elastic channel, and no explicit $\text{p}+{}^6\text{Li}$ channel which should open above 10 MeV. The effect of the missing channel is to be represented by the new fitted damping parameters. I fitted the e_p energy in the Brune basis, keeping $L = 0$. The result is shown in Fig. 3, with a fit quality of $\chi^2/\text{df} = 4.25$ compared with 2.63 in the full R-matrix fit.

This first attempt at least gives (blue line on the right) transfer cross-sections that are close to the average of the more complete model (black line). It has no absorption below 10 MeV, unlike what we would get from fixed damping widths (red line).

This kind of treatment is reminiscent of optical models for elastic scattering, where energy-dependent imaginary terms are added even though the total Hamiltonian is no longer Hermitian or even energy-dependent. It is available as a resort above the energy range of a strict Lane and Thomas model, by generalizing the Reich–Moore approximation to particle channels.

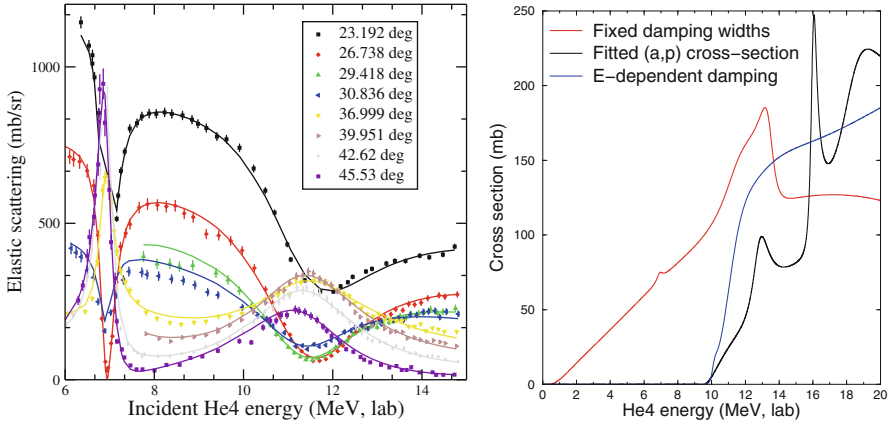


Fig. 3 (Left) Fitted cross-sections ${}^3\text{He}(\alpha, \alpha){}^3\text{He}$ reaction to the data [15], without an explicit $p+{}^6\text{Li}$ channel, but with energy-dependent damping. (Right) Absorption cross-sections from the elastic channel, with red, black, and blue lines from Eqs. (3), (2), and (4), respectively

Acknowledgments This work was performed under the auspices of the U.S. Department of Energy by Lawrence Livermore National Laboratory under Contract DE-AC52-07NA27344

References

1. A.M. Lane, R.G. Thomas, *Rev. Mod. Phys.* **30**, 257 (1958). <https://doi.org/10.1103/RevModPhys.30.257>. <http://link.aps.org/doi/10.1103/RevModPhys.30.257>
2. C.W. Reich, M.S. Moore, *Phys. Rev.* **111**, 929 (1958). <https://doi.org/10.1103/PhysRev.111.929>. <https://link.aps.org/doi/10.1103/PhysRev.111.929>
3. C.R. Brune, *Phys. Rev. C* **66**, 044611 (2002). <https://doi.org/10.1103/PhysRevC.66.044611>
4. S. Kunieda, *EPJ Web Conf.* **146**, 12029 (2017). <https://doi.org/10.1051/epjconf/201714612029>
5. E. Uberseder, R.J. deBoer, *AZURE2 User Manual* (2015). azure.llnl.gov
6. I.J. Thompson, *Comput. Phys. Rep.* **7**(4), 167 (1988). [http://dx.doi.org/10.1016/0167-7977\(88\)90005-6](http://dx.doi.org/10.1016/0167-7977(88)90005-6). <http://www.sciencedirect.com/science/article/pii/0167797788900056>
7. N.M. Larson, Updated users' guide for SAMMY: multilevel R-matrix fits to neutron data using Bayes' equations. Tech. Rep. ORNL/TM-9179/R8 (Oak Ridge National Laboratory, Oak Ridge, 2008)
8. P. Archier, C. De Saint Jean, O. Litaize, G. Noguère, L. Berge, E. Privas, P. Tamagno, *Nucl. Data Sheets* **118**, 488 (2014). <https://doi.org/10.1016/j.nds.2014.04.114>. <http://www.sciencedirect.com/science/article/pii/S0090375214001446>
9. I. Thompson, R. deBoer, P. Dimitriou, S. Kunieda, A. Pigni, G. Arbanas, H. Leeb, T. Srdinko, G. Hale, P. Tamagno, P. Archier, *Eur. Phys. J. A* **55**(6), 92 (2019). <https://doi.org/10.1140/epja/i2019-12753-y>
10. P. Dimitriou, R.J. DeBoer, S. Kunieda, H. Leeb, M. Paris, T. Srdinko, I.J. Thompson, Summary Report of Consultants' Meeting about "R-matrix codes for charged-particle reactions in the resolved resonance region". Tech. Rep. INDC(NDS)-0703 (International Atomic Energy Agency, Vienna, 2016). <https://www-nds.iaea.org/publications/indc/indc-nds-0703.pdf>

11. H. Leeb, P. Dimitriou, I.J. Thompson, Summary Report of 2nd Consultants' Meeting about "R-matrix codes for charged-particle reactions in the resolved resonance region". Tech. Rep. INDC(NDS)-0726 (International Atomic Energy Agency, Vienna, 2017). <https://www-nds.iaea.org/publications/indc/indc-nds-0726.pdf>
12. H. Leeb, P. Dimitriou, I.J. Thompson, Summary Report of 3rd Consultants' Meeting about "R-matrix codes for charged-particle reactions in the resolved resonance region". Tech. Rep. INDC(NDS)-0737 (International Atomic Energy Agency, Vienna, 2017). <https://www-nds.iaea.org/publications/indc/indc-nds-0737.pdf>
13. H. Leeb, P. Dimitriou, I.J. Thompson, Summary Report of 4th Consultants' Meeting about "R-matrix codes for charged-particle reactions in the resolved resonance region". Tech. Rep. INDC(NDS)-0767 (International Atomic Energy Agency, Vienna, 2018). <https://www-nds.iaea.org/publications/indc/indc-nds-0767.pdf>
14. C. Mattoon, B. Beck, N. Patel, N. Summers, G. Hedstrom, D. Brown, Nucl. Data Sheets **113**(12), 3145 (2012). <https://doi.org/10.1016/j.nds.2012.11.008>. <http://www.sciencedirect.com/science/article/pii/S0090375212000944>. Special Issue on Nuclear Reaction Data
15. T.A. Tombrello, P.D. Parker, Phys. Rev. **130**, 1112 (1963). <https://doi.org/10.1103/PhysRev.130.1112>. <http://link.aps.org/doi/10.1103/PhysRev.130.1112>
16. C.R. Brune, J.A. Caggiano, D.B. Sayre, A.D. Bacher, G.M. Hale, M.W. Paris, Phys. Rev. C **92**, 014003 (2015). <https://doi.org/10.1103/PhysRevC.92.014003>. <https://link.aps.org/doi/10.1103/PhysRevC.92.014003>

The Transition from Isolated Resonances to the Continuum



Carl R. Brune

1 Introduction

Many nuclear reactions of astrophysical importance are modeled by Hauser-Feshbach (HF) calculations, the well-established approach for computing average cross sections when many resonant levels are involved. For this approach to be successful it is necessary that the parameters of the model (optical potentials, level densities, etc.) be reasonably well understood *and* that number of resonant states involved be sufficiently large. The latter point is one of the questions we would like to address. A rule of thumb of at least 10 levels in the energy window of interest has been given but many caveats apply [1]. In principle a HF reaction rate should have a temperature-dependent theoretical statistical uncertainty associated with the finite number of contributing levels. A quantitative understanding of this statistical uncertainty can in turn be used to quantify the applicability of the model and to assess the uncertainty in the derived reaction rate. These considerations also have important implication for the planning and interpretation of experiments. Because measurements are performed with a finite energy resolution due to target thickness and other factors, energy average is also present in experimental data.

C. R. Brune (✉)

Edwards Accelerator Laboratory, Department of Physics and Astronomy, Ohio University,
Athens, OH, USA

e-mail: brune@ohio.edu

© This is a U.S. government work and not under copyright protection
in the U.S.; foreign copyright protection may apply 2021

J. Escher et al. (eds.), *Compound-Nuclear Reactions*, Springer Proceedings in
Physics 254, https://doi.org/10.1007/978-3-030-58082-7_5

2 Astrophysical Scenarios

The transition from isolated resonances to the continuum will be important when the level density is modest. This situation is most easily realized in lighter nuclei, in the range $20 \lesssim A \lesssim 50$. In nuclear astrophysics, this leads us to consider proton- and α -induced reactions in the rapid proton capture process (rp-process) and in type-II supernovae. The rp-process primarily consists of a sequence of (p, γ) reactions, (α, p) reactions, and β^+ decays which occur on the surface of an accreting neutron star, with a relevant temperature range of 0.5–2.0 GK. In the type-II (core-collapse) supernova scenario, these reactions may occur during the oxygen and silicon burning phase before the explosion, or in the α -rich freeze-out immediately afterward. Here, the relevant temperature range is 1.5–5 GK.

We focus here on the $^{34}\text{Ar}(\alpha, p)^{37}\text{K}$ reaction which is thought to be an important reaction for regulating flow to higher masses in the rp-process [2, 3]. The time-reversed reaction has recently been measured at the ATLAS facility at Argonne National Laboratory [4]. An indirect study of the compound-nuclear levels in ^{38}Ca has been performed using the $^{40}\text{Ca}(p, t)^{38}\text{Ca}$ reaction at iThemba [5]. The properties of ^{38}Ca levels have also been studied using the elastic scattering of protons from ^{37}K [6]. Finally, measurements of the $^{34}\text{Ar}(\alpha, p)^{37}\text{K}$ reaction have been performed for $E_{c.m.} = 5.7$ and 6.1 MeV with the ReA3 facility at the National Superconducting Cyclotron Laboratory (K. Schmidt, K. Chipps, private communication). The reaction rate in the rp process is determined by the cross section for $1 \lesssim E_{c.m.} \lesssim 4$ MeV, considering the aforementioned temperature range. It should be noted that none of the direct measurements to date have been performed in the astrophysically relevant energy range.

3 Overview of Our Approach

The Breit–Wigner formula for the cross section connecting channels c and c' is given by

$$\sigma_{cc'} = \frac{\pi}{k^2} \omega_J \frac{\Gamma_c \Gamma_{c'}}{(E - E_R)^2 + \Gamma^2/4}, \quad (1)$$

where k is the incoming wavenumber, E is the incoming energy, ω_J is a statistical factor, Γ_c are the partial widths, E_R is the resonance energy, and $\Gamma = \sum_c \Gamma_c$ is the total width. The channel label c represents the particle pair type, the total angular momentum J , the orbital angular momentum, and channel spin. The corresponding HF (energy-averaged) result is [7]

$$\sigma_{cc'} = \frac{\pi}{k^2} \omega_J \frac{T_c T_{c'}}{\sum_c T_c}, \quad (2)$$

where T_c is the transmission coefficient. Here, we have neglected the width fluctuation correction, which is unimportant for the case we consider below.

The Monte Carlo simulations of the reaction cross section of interest are based on discrete levels sampled from distributions consistent with the HF parametrization. This approach builds on the ideas Mohr et al. [8] who have estimated the $^{18}\text{Ne}(\alpha, p)^{21}\text{Na}$ reaction rate using experimental data for level positions and some spectroscopic properties, while using Monte Carlo for the unknown spins, parities, and partial widths. Although not performed for reaction rate calculations, there have been several previous Monte Carlo studies of compound-nuclear reactions; see, e.g., Moldauer [9] and the recent work of Kawano et al. [10].

The transmission coefficient T_c for channel c in the HF formula is related to the mean partial width $\langle\Gamma_c\rangle$ and level density ρ via [11, 12]

$$T_c = 1 - \exp(-2\pi\langle\Gamma_c\rangle\rho), \quad (3)$$

which reduces to $T_c = 2\pi\langle\Gamma_c\rangle\rho$ when $T_c \ll 1$. If the T_c and ρ are assumed to be known, the level positions, spins, and parities can be sampled from the level density allowing for the Wigner distribution of level spacings [10]. Likewise, the reduced level widths can be sampled from the Porter-Thomas distribution [8, 10]. Finally, the reaction rate can be calculated by taking the usual Maxwell-Boltzmann average. By repeating the Monte Carlo process, the statistical uncertainty in the reaction rate can be determined.

4 Details of the Calculation

We limit our consideration to $E_{c.m.} < 5\text{ MeV}$, where $\Gamma_\alpha \ll \Gamma_p$ and in the HF approach only the α transmission factor is important. Since ^{34}Ar and the α particle both have $J^\pi = 0^+$, the entrance channel label may be identified by $c = J$ and the statistical factor is $\omega_J = 2J + 1$. Since the total width is dominated by the outgoing proton widths, the cross section for $^{34}\text{Ar}(\alpha, p)^{37}\text{K}$ resulting from Eq. (2) is

$$\sigma = \frac{\pi}{k^2} \sum_{J=0}^{\infty} (2J + 1) T_J, \quad (4)$$

where in practice only the few lowest J values contribute appreciably. Following previous work [13–15], we utilize the McFadden and Satchler α optical potential [16]. Our result for the $^{34}\text{Ar}(\alpha, p)^{37}\text{K}$ cross section, presented as an astrophysical S factor, is shown in Fig. 1. We find that the cross section at low energies is sensitive to the tail of the Woods Saxon potential out to a distance of about 18 fm. We note that this part of the potential is certainly not constrained by any of the higher-energy elastic scattering data considered in Ref. [16]. Also shown in Fig. 1 is a calculation using the Non-Smoker code [13–15] using the same α optical

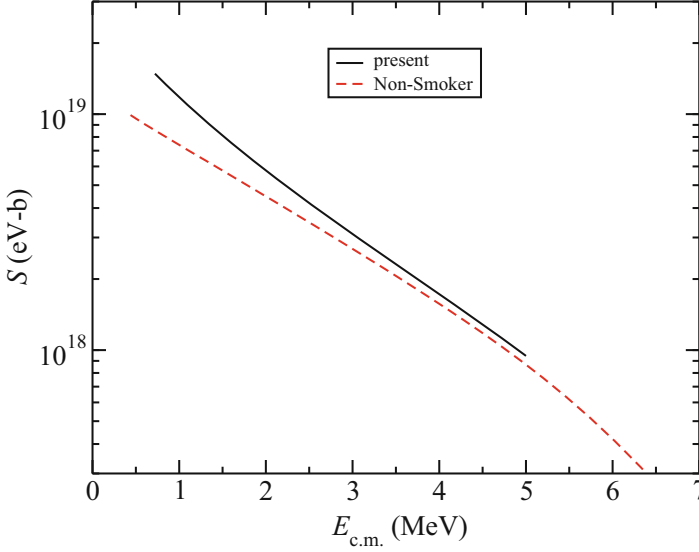


Fig. 1 Astrophysical S factor for the $^{34}\text{Ar}(\alpha, p)^{37}\text{K}$ reaction. The solid black curve shows the present calculation and the dashed red curve shows the Non-Smoker result

potential. It is seen to be somewhat lower than the present result for low energies. However, a more recent calculation using the SMARAGD code (the successor to Non-Smoker) is in excellent agreement with the present calculation (T. Rauscher, private communication).

Our Monte Carlo approach also requires knowledge of the level density in the compound nucleus ^{38}Ca . Note that the threshold for $\alpha+^{34}\text{Ar}$ is located at an excitation energy of 6.1 MeV, which implies the astrophysically important excitation energies are between 7 and 10 MeV. We have taken the level density from the mirror nucleus ^{38}Ar , where two studies are available. In Fig. 2 we show the result of Beckerman [17] and the constant temperature result of von Egidy and Bucurescu [18]. The two curves are seen to be in reasonably good agreement; we have adopted the latter for the calculations described below. It is parametrized as

$$\rho(U, J, \pi) = \frac{1}{2} \rho(U) f(J), \quad \text{with} \quad (5)$$

$$f(J) = \exp\left(-J^2/2\sigma^2\right) - \exp\left[-(J+1)^2/2\sigma^2\right] \quad \text{and} \quad (6)$$

$$\rho(U) = \frac{1}{T} \exp[(U - E_0)/T], \quad (7)$$

where U is the excitation energy, J is the level spin, π is the level parity, and σ is the spin-cutoff parameter, T is the temperature, and E_0 is the backshift. For our case, we have $\sigma = 0.98A^{0.29}$, $T = 1.51$ MeV, $E_0 = 1.30$ MeV, and $A = 38$.

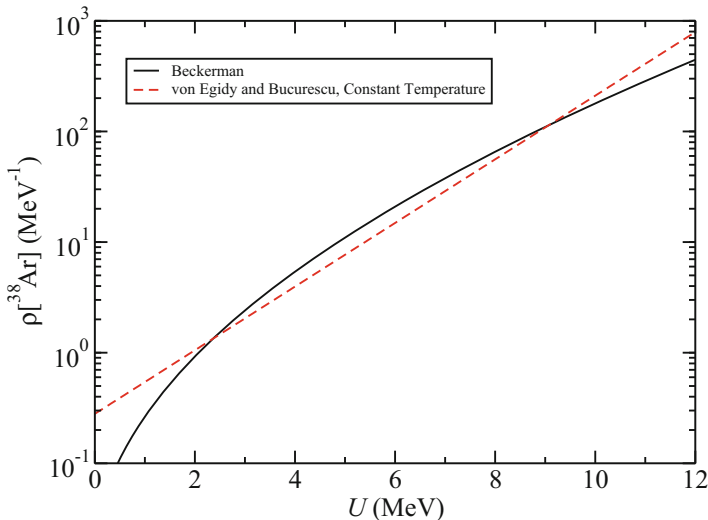


Fig. 2 The level density for the nucleus ^{38}Ar , as a function of excitation energy. The solid black curve is from Beckerman [17] and the red dashed curve is the constant temperature result from von Egidy and Bucurescu [18]

The Monte Carlo sampling of the energy levels assumes the distribution of level spacings for a given J^π is given by the Wigner distribution

$$P_W(s) = \frac{\pi}{2} s \exp\left(-\frac{\pi s^2}{4}\right), \quad (8)$$

where $0 \leq s < \infty$ and s is the ratio of the actual spacing to the average spacing defined by the level density. The widths were sampled from the Porter-Thomas distribution

$$P_{PT}(t) = \frac{1}{\sqrt{2\pi}} \exp\left(-\frac{t^2}{2}\right), \quad (9)$$

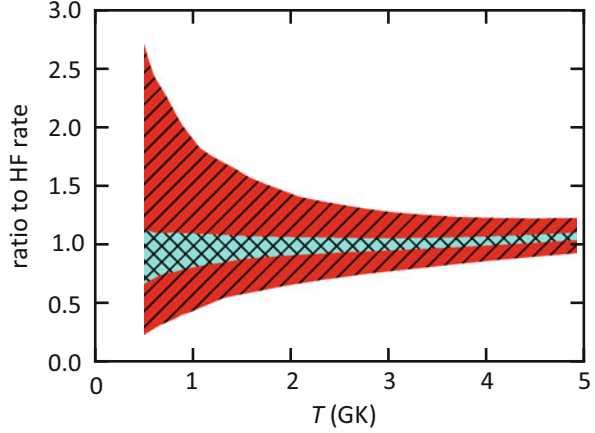
where $-\infty < t < \infty$ and $\Gamma_c = t^2 \langle \Gamma_c \rangle$. The average partial width $\langle \Gamma_c \rangle$ is determined from the transmission coefficient and level density using Eq. (3).

The two-body thermonuclear reaction rate is in general given by

$$\langle \sigma v \rangle = \left(\frac{8\pi}{\mu}\right)^{1/2} (kT)^{-3/2} \int_0^\infty E \sigma(E) \exp\left(-\frac{E}{kT}\right) dE, \quad (10)$$

where μ is the reduced mass of the reactants and kT is the temperature in units of energy. This formula may be used together with the HF cross section to determine the HF reaction rate. Alternatively, the cross section may be represented by narrow

Fig. 3 The variance in the calculated reaction rate as a function of temperature. The results are normalized by the HF reaction rate. The cross-hatched light blue region contains 68% of the simulations. This region together with the single-hatched red region contains 95% of the simulations



resonances. For the case of $^{34}\text{Ar}(\alpha, p)^{37}\text{K}$, where $\Gamma_\alpha \ll \Gamma_p$, the reaction rate due to a single narrow resonance described by Eq. (1) is given by

$$\langle \sigma v \rangle = c(\hbar c)^2 \left(\frac{2\pi}{\mu c^2 k T} \right)^{3/2} (2J+1)\Gamma_\alpha \exp\left(-\frac{E_R}{kT}\right), \quad (11)$$

where Γ_α is the entrance channel width of the level, c is the speed of light, and \hbar is Planck's constant.

For each iteration of the Monte Carlo simulation, a set of levels and partial widths is generated. The reaction rate as a function of temperature is then calculated using the narrow resonance formula, Eq. (11), for each resonance. We repeated the cross section simulation 5×10^5 times using this procedure. For a grid of temperatures between 0.5 and 5 GK, we accumulated histograms of the reaction rate. The average reaction rate was observed to be very close the HF rate for all temperatures, which provides a cross-check on our methodology. Information about the variance of the reaction rate is presented in Fig. 3. It is seen that the 68% confidence region is reasonably well constrained to be within about 25% of the HF rate for astrophysically relevant temperatures. However, the 95% region does exceed a factor of two deviation from the HF rate at low temperatures. These results suggest that an accurate determination of the $^{34}\text{Ar}(\alpha, p)^{37}\text{K}$ reaction rate will require that the energies and α widths of individual resonances be determined.

5 Future Directions and Conclusions

In the future, we will look at the effects of energy averaging on experiments. The fact that the cross section is composed of narrow resonances will also give rise to a variance here which will need to be considered. We can also include experimental

information on specific resonances, if it becomes available, using the methods of Ref. [8].

We plan to implement a full R -matrix description of the cross section, which will take interference between resonances into account. Using the approach described in Ref. [19], this is straightforward, as level shift effects are removed. Including interference effects will allow additional phenomena, such as Ericson fluctuations, to be revealed. This extension will require that the reaction rate be calculated by the numerical integration of Eq. (10), which will be more computationally intensive. It should be noted that these type of interference effects are not expected to be significant for the case of $^{34}\text{Ar}(\alpha, p)^{37}\text{K}$.

In conclusion, the variance in the $^{34}\text{Ar}(\alpha, p)^{37}\text{K}$ reaction rate due to the finite number of contributing resonances has been calculated. It is found to be a non-trivial consideration. We also note that the $\alpha + ^{34}\text{Ar}$ optical potential, which is used in this and other works to predict the $^{34}\text{Ar}(\alpha, p)^{37}\text{K}$ cross section, is poorly known at astrophysically relevant energies.

Acknowledgments It is a pleasure to thank K.A. Chipps, S.M. Grimes, M.A.A. Mamun, T. Rauscher, K. Schmidt, and A. Voinov for providing useful discussions and information. This work was supported in part by the U.S. Department of Energy, under Grants No. DE-FG02-88ER40387, DE-NA0002905, and DE-NA0003883.

References

1. T. Rauscher, The path to improved reaction rates for astrophysics. *Int. J. Mod. Phys. E* **20**, 1071–1169 (2011). <https://doi.org/10.1142/S021830131101840X>. <http://www.worldscientific.com/doi/abs/10.1142/S021830131101840X>
2. J.L. Fisker, F.K. Thielemann, M. Wiescher, The nuclear reaction waiting points: ^{22}Mg , ^{26}Si , ^{30}S , and ^{34}Ar and bolometrically double-peaked type I x-ray bursts. *Astrophys. J. Lett.* **608**, L61 (2004). <https://doi.org/10.1086/422215>
3. A. Parikh, J. José, F. Moreno, C. Iliadis, The effects of variations in nuclear processes on type I x-ray burst nucleosynthesis. *Astrophys. J. Suppl. Ser.* **178**, 110 (2008). <https://doi.org/10.1086/589879>
4. C. Deibel et al.: Radioactive ion beam studies of αp process waiting points in x-ray bursts. *PoS (NIC XII)* **146**, 044 (2013). <https://doi.org/10.22323/1.146.0044>. <https://pos.sissa.it/146/044/>
5. A.M. Long et al.: Indirect study of the stellar $^{34}\text{Ar}(\alpha, p)^{37}\text{K}$ reaction rate through $^{40}\text{Ca}(p, t)^{38}\text{Ca}$ reaction measurements. *Phys. Rev. C* **95**, 055803 (2017). <https://link.aps.org/doi/10.1103/PhysRevC.95.055803>
6. A.C. Lauer, Studying the reaction $^{34}\text{Ar}(\text{ALPHA},\text{P})^{37}\text{K}$ and its impact on XRB nucleosynthesis and observables. Ph.D. thesis (Louisiana State University, Louisiana, 2017). http://digitalcommons.lsu.edu/gradschool_dissertations/4118
7. P.E. Hodgson, Compound nucleus reactions. *Rep. Prog. Phys.* **50**, 1171–1228 (1987). <https://doi.org/10.1088/0034-4885/50/9/002>
8. P. Mohr, R. Longland, C. Iliadis, Thermonuclear reaction rate of $^{18}\text{Ne}(\alpha, p)^{21}\text{Na}$ from Monte Carlo calculations. *Phys. Rev. C* **90**, 065806 (2014). <https://doi.org/10.1103/PhysRevC.90.065806>
9. P.A. Moldauer, Why the Hauser-Feshbach formula works. *Phys. Rev. C* **11**, 426–436 (1975). <https://doi.org/10.1103/PhysRevC.11.426>. <http://link.aps.org/doi/10.1103/PhysRevC.11.426>

10. T. Kawano, P. Talou, H.A. Weidenmüller, Random-matrix approach to the statistical compound nuclear reaction at low energies using the Monte Carlo technique. *Phys. Rev. C* **92**, 044,617 (2015). <https://doi.org/10.1103/PhysRevC.92.044617>. <http://link.aps.org/doi/10.1103/PhysRevC.92.044617>
11. P.A. Moldauer, Average resonance widths in single-channel scattering. *Phys. Rev.* **177**, 1841–1842 (1969). <https://doi.org/10.1103/PhysRev.177.1841>. <https://link.aps.org/doi/10.1103/PhysRev.177.1841>
12. M. Simonius, Unitarity and the energy averaged S -matrix. *Phys. Lett. B* **52**(3), 279–281 (1974). [https://doi.org/10.1016/0370-2693\(74\)90040-9](https://doi.org/10.1016/0370-2693(74)90040-9). <http://www.sciencedirect.com/science/article/pii/0370269374900409>
13. T. Rauscher, F.K. Thielemann, Astrophysical reaction rates from statistical model calculations. *At. Data Nucl. Data Tables* **75**(1), 1–351 (2000). <https://doi.org/10.1006/adnd.2000.0834>. <http://www.sciencedirect.com/science/article/pii/S0092640X00908349>
14. T. Rauscher, F.K. Thielemann, Tables of nuclear cross sections and reaction rates: an addendum to the paper “Astrophysical reaction rates from statistical model calculations”. *At. Data Nucl. Data Tables* **79**(1), 47–64 (2001). <https://doi.org/10.1006/adnd.2001.0863>. <http://www.sciencedirect.com/science/article/pii/S0092640X01908630>
15. T. Rauscher, *Nuclear Astrophysics Results*. Accessed: 8 June 2016. <http://nucastro.org>
16. L. McFadden, G. Satchler, Optical-model analysis of the scattering of 24.7 MeV alpha particles. *Nucl. Phys.* **84**(1), 177–200 (1966). [https://doi.org/10.1016/0029-5582\(66\)90441-X](https://doi.org/10.1016/0029-5582(66)90441-X). <http://www.sciencedirect.com/science/article/pii/002955826690441X>
17. M. Beckerman, Level densities for $23 \leq A \leq 40$. *Nucl. Phys. A* **278**(2), 333–356 (1977). [https://doi.org/10.1016/0375-9474\(77\)90243-3](https://doi.org/10.1016/0375-9474(77)90243-3). <http://www.sciencedirect.com/science/article/pii/0375947477902433>
18. T. von Egidy, D. Bucurescu, Systematics of nuclear level density parameters. *Phys. Rev. C* **72**, 044311 (2005). <https://link.aps.org/doi/10.1103/PhysRevC.72.044311>
19. C.R. Brune, Alternative parametrization of R -matrix theory. *Phys. Rev. C* **66**, 044,611 (2002). <http://link.aps.org/doi/10.1103/PhysRevC.66.044611>

Cross Section Correlation Functions and Deviations from the Porter-Thomas Distribution



Edward D. Davis 

Given the importance of the Porter-Thomas distribution [1] to statistical models of the compound nucleus, the identification [2] of resonance data sets that are almost certainly statistically inconsistent with the PTD has prompted several attempts to account for these findings within standard models of CN processes (for recent overviews, see [3, 4]). The only issue on which theorists seem to concur at present is that more data is needed to guide their considerations.

With a few exceptions (viz., Ref. [5]), autocorrelation function studies of nuclear reactions have previously been confined to the regime of strongly overlapping resonances, but, in this short contribution, I want to advocate that the autocorrelation function involving the total cross section

$$R_{\text{tot}}(\varepsilon) = \frac{\langle \sigma_{\text{tot}} \left(E + \frac{1}{2}\varepsilon \right) \sigma_{\text{tot}} \left(E - \frac{1}{2}\varepsilon \right) \rangle}{\langle \sigma_{\text{tot}} \rangle^2} - 1, \quad (1)$$

be investigated in the unresolved but not strongly overlapping resonance regime.¹ Via the optical theorem, $R_{\text{tot}}(\varepsilon)$ is a linear superposition of (two-point) measures $C_{ab}(\varepsilon) = \left\langle S_{aa}^{\text{fl}*} \left(E + \frac{1}{2}\varepsilon \right) S_{bb}^{\text{fl}} \left(E - \frac{1}{2}\varepsilon \right) \right\rangle$ of fluctuations in elastic elements of the S -matrix ($S^{\text{fl}} \equiv S - \langle S \rangle$). The relation between $R_{\text{tot}}(\varepsilon)$ and the $C_{ab}(\varepsilon)$'s has two desirable consequences. First, for neutron-induced reactions, there are contributions to $R_{\text{tot}}(\varepsilon)$ sensitive to a key statistic of neutron partial width amplitudes, namely the

¹In (1), the angle brackets denote an average over the scattering energy E .

E. D. Davis (✉)
North Carolina State University, Raleigh, NC, USA
e-mail: dedavis4@ncsu.edu

kurtosis. Second, the integral representation of $C_{ab}(\varepsilon)$ derived by Verbaarschot et al. [6] permits, in principle, the exact evaluation of $R_{\text{tot}}(\varepsilon)$ within the stochastic CN model introduced by these authors (the VWZ model).

It is the VWZ model which is the starting point for the majority of the investigations into the origin of deviations from the PTD. De facto, it is the capacity of the VWZ model to describe CN phenomena which is under scrutiny. A comparison of its predictions for $R_{\text{tot}}(\varepsilon)$ with data in the unresolved (but weakly overlapping) resonance regime would constitute another test, and any discrepancies found could not be attributed to the method of evaluation of $R_{\text{tot}}(\varepsilon)$.

Is there any reason to expect that data on $R_{\text{tot}}(\varepsilon)$ for unresolved but weakly overlapping resonances may display sensitivity to non-generic dynamics? Previous investigations [7, 8], in which results deduced from the VWZ model have been compared with microwave resonator and CN data in the regime of weakly overlapping resonances, do not address this point. To this end, it is helpful to consider the approximation of $C_{ab}(\varepsilon)$ in the statistical Breit–Wigner (SBW) model, using the scheme of calculation laid out in [9].

In the SBW model, guided by the empirical characterization of data on partial widths [10], it can be assumed that partial widths are drawn from a χ^2 distribution of ν degrees of freedom. In the weakly overlapping resonance regime, the dominant contribution to $C_{ab}(0)$ is then

$$C_{ab}^{(d)}(0) = \left(1 + \frac{2}{\nu}\delta_{ab}\right) T_a T_b I_{ab}^{(\nu)}, \quad (2)$$

where the transmission coefficients $T_c = 1 - |\langle S_{cc} \rangle|^2$, and

$$I_{ab}^{(\nu)} = \int_0^\infty \frac{\prod_c \left(1 + \frac{2}{\nu} T_c \tau\right)^{-\nu/2}}{\left(1 + \frac{2}{\nu} T_a \tau\right) \left(1 + \frac{2}{\nu} T_b \tau\right)} d\tau. \quad (3)$$

(The product in the integrand above is over all open channels c .)

The ν dependence in (2) is encouraging. Figure 1 displays the relative change $\delta \equiv C_{aa}^{(d)}(0) / C_{aa}^{(d)}(0) [\nu = 1] - 1$ in the dominant contribution to $C_{aa}(0)$ as ν ranges from its value in the Porter-Thomas limit ($\nu = 1$) through values implied by the analysis of Pt neutron width data ($\nu \approx \frac{1}{2}$). [In δ , the value of the dominant contribution to $C_{aa}(0)$ for arbitrary ν is divided by its value for $\nu = 1$.] In generating Fig. 1, all transmission coefficients have, for simplicity, been taken to be equal in all Λ open channels, meaning that δ is a function of only ν and Λ .

For values of ν comparable to those found in the statistical analysis of reduced neutron widths in [10], Fig. 1 suggests that $R_{\text{tot}}(0)$ could deviate from its value in the VWZ model by more than 20%. This should be a large enough signal to warrant determination of $R_{\text{tot}}(0)$ with high quality total cross section data for weakly overlapping resonances in the unresolved resonance regime.

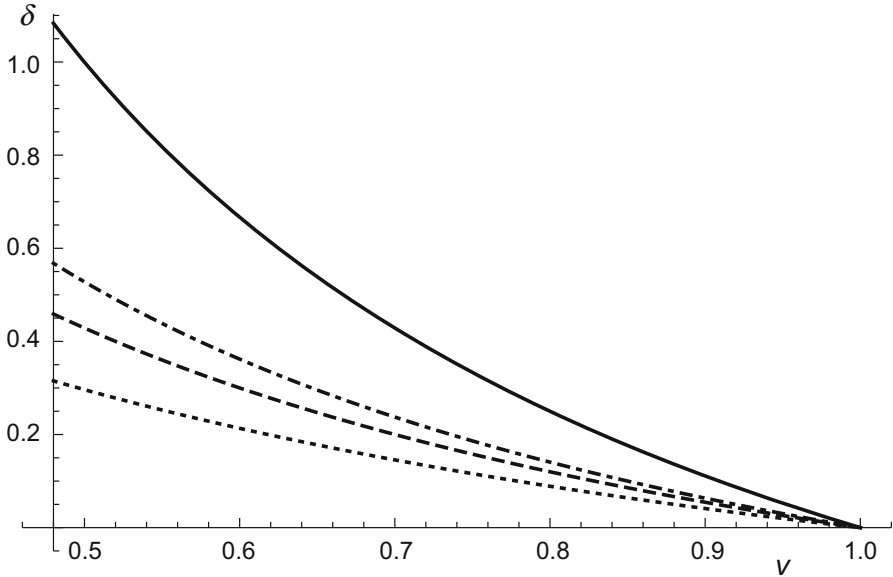


Fig. 1 The relative change δ of the dominant contribution to $C_{aa}(0)$ in the SBW model versus ν for different choices of the number Λ of open channels: $\Lambda = 5$ (dotted line), $\Lambda = 10$ (dashed line), $\Lambda = 20$ (dot-dashed line), and $\Lambda = \infty$ (solid line)

In summary, a test of the VWZ model involving fluctuations in neutron-induced CN reactions has been identified. For weakly overlapping resonances, $R_{\text{tot}}(0)$ is sensitive to fluctuations in reduced neutron widths but insensitive to correlations between levels (beyond level repulsion) [5]. These properties make the study of $R_{\text{tot}}(0)$ for weakly overlapping resonances in the unresolved resonance regime a test, in effect, of the Porter-Thomas distribution.

Acknowledgments This work was supported in part by the US Department of Energy under Grant No. DE-FG02-97ER41042.

References

1. C.E. Porter, R.G. Thomas, Phys. Rev. **104**, 483 (1956). <https://doi.org/10.1103/PhysRev.104.483>
2. P.E. Koehler, F. Bečvář, M. Krtička, K.H. Guber, J.L. Ullmann, Fortschr. Phys. **61**, 80 (2013). <https://doi.org/10.1002/prop.201200067>
3. H.A. Weidenmüller, AIP Conf. Proc. **1912**, 020021 (2017). <https://doi.org/10.1063/1.5016146>
4. P. Fanto, G.F. Bertsch, Y. Alhassid, Phys. Rev. C **98**, 014604 (2018). <https://doi.org/10.1103/PhysRevC.98.014604>
5. G.F. Bertsch, D. Brown, E.D. Davis, Phys. Rev. C **98**, 014611 (2018). <https://doi.org/10.1103/PhysRevC.98.014611>

6. J.J.M. Verbaarschot, H.A. Weidenmüller, M.R. Zirnbauer, Phys. Rep. **129**, 367 (1985). [https://doi.org/10.1016/0370-1573\(85\)90070-5](https://doi.org/10.1016/0370-1573(85)90070-5)
7. B. Dietz, T. Friedrich, H.L. Harney, M. Miski-Oglu, A. Richter, F. Schäfer, H.A. Weidenmüller, Phys. Rev. E **78**, 055204 (2008). <https://doi.org/10.1103/PhysRevE.78.055204>
8. S. Kumar, B. Dietz, T. Guhr, A. Richter, Phys. Rev. Lett. **119**, 244102 (2017). <https://doi.org/10.1103/PhysRevLett.119.244102>
9. T.E.O. Ericson, B. Dietz, A. Richter, Phys. Rev. E **94**, 042207 (2016). <https://doi.org/10.1103/PhysRevE.94.042207>
10. P.E. Koehler, F. Bečvář, M. Krtička, J.A. Harvey, K.H. Guber, Phys. Rev. Lett. **105**, 072502 (2010). <https://doi.org/10.1103/PhysRevLett.105.072502>

Moldauer's Sum Rule Implies Superradiance in Compound Nuclear Reactions



David Brown, Mike Herman, and Gustavo Nobre

1 Background

For neutron-induced reactions, the unresolved resonance region (URR) interpolates between the fast neutron range and the resolved resonance region (RRR). The fluctuations in the neutron cross sections in the URR are not fully resolvable yet the URR in a typical nucleus is in the 100 keV–2 MeV window, where fission spectra peak, therefore introducing substantial uncertainty in practical applications. As the cross section fluctuates strongly in the URR, at best we can describe the probability distribution of the cross section in terms of the average resonance spacing D , the average channel widths \overline{V}_c , and the number of degrees of freedom ν_c for each channel c . Here “channel” denotes the two incoming/outgoing particles and all the quantum numbers needed to specify their state (for our purposes only the orbital angular momentum L and total angular momentum J).

We focus on the energy average cross sections in the URR as a first step toward determining the full probability distribution. The Gaussian Orthogonal Ensemble (GOE) triple integral result of Verbaarschot, Weidenmüller, and Zirnbauer [1] is believed to provide an exact solution for the energy averaged cross section, but it is both difficult to interpret physically and numerically expensive to use in practice. Given this, we consider the Hauser-Feshbach equation with Moldauer's Width Fluctuation Correction [2] as it is both easier to use and simpler to interpret. The Hauser-Feshbach equation is

D. Brown (✉) · G. Nobre
National Nuclear Data Center, Brookhaven National Laboratory, Upton, NY, USA
e-mail: dbrown@bnl.gov

M. Herman
National Nuclear Data Center, Brookhaven National Laboratory, Upton, NY, USA
Los Alamos National Laboratory, Los Alamos, NM, USA

$$\sigma_{ab}^{\text{cn}} = \sigma_a^{\text{abs}} \frac{\bar{\Gamma}_b}{\sum_c \bar{\Gamma}_c} \mathcal{W}_{ab}(\mathbf{\Gamma}) \quad \text{with} \quad \sigma_a^{\text{abs}} = \frac{\pi g_a \bar{\Gamma}_a}{Dk_a^2}. \quad (1)$$

Here the absorption cross section for channel a is σ_a^{abs} and $\mathcal{W}_{ab}(\mathbf{\Gamma})$ is the Width Fluctuation Correction (WFC). The WFC is a function of the average widths of all relevant channels written as the vector $\mathbf{\Gamma}$.

The WFC was originally derived under the assumption that $D \gg \bar{\Gamma}$ so resonances are widely spaced and interference between them can be ignored. The cross sections then simplify to the single level Breit–Wigner approximation [3]. Under these conditions, one assumes that the resonance widths Γ_c follow a χ^2 distribution with ν_c degrees of freedom, giving

$$\mathcal{W}_{ab}(\mathbf{\Gamma}) = \left(1 + \delta_{ab} \frac{2}{\nu_a}\right) \int_0^\infty dx \prod_c \left(1 + \frac{2\bar{\Gamma}_c}{\nu_c \sum_i \bar{\Gamma}_i} x\right)^{-\delta_{ac} - \delta_{bc} - \nu_c/2}. \quad (2)$$

Improvements to this, such as Moldauer’s approach [2], are based on phenomenological fits of transmission coefficient dependent $\nu_c(T_c)$.

The Hauser-Feshbach equation given in most textbooks [4] is written in terms of the transmission coefficient $T_c = 1 - |\langle S_{cc} \rangle|^2$ that can, for example, be computed using the optical model. Noting that in the weak coupling limit $T_c \approx 2\pi \bar{\Gamma}_c / D$, one usually replaces

$$\frac{\bar{\Gamma}_b}{\sum_c \bar{\Gamma}_c} \rightarrow \frac{T_b}{\sum_c T_c}. \quad (3)$$

In the Sect. 3, we argue that this conventional form is incomplete and must be modified, giving rise to a form that predicts superradiance. Even so, a prescription that can connect the average resonance widths $\bar{\Gamma}_c$ and level spacings D to transmission coefficients T_c and extends beyond the weak coupling limit would allow for a unified framework that connects the average cross sections in the RRR, URR, and fast regions.

2 Transmission Coefficients

Moving beyond the weak coupling limit requires us to understand the connection between the transmission coefficients T_c used in the fast region and the D , $\bar{\Gamma}_c$, and ν_c used in the URR. The authors of this contribution investigated three parameterizations of T_c in Ref. [5]: the SPRT method [6], Moldauer’s “optical model” form which (we call the Moldauer–Simonijs form) [7], and the result that is implied by Moldauer’s “sum rule for resonance reactions” [8]. These parameterizations are summarized in Table 1.

Table 1 Summary of transmission coefficients T_c under consideration in this contribution

Parameterization	Equation	Derivation
SPRT [6]	$T_c^{\text{SPRT}} = \frac{2x_c}{(1 + x_c/2)^2 + (P_c R_c^\infty)^2}$	Replace R-matrix with energy average \bar{R}
Sum rule [8]	$T_c^{\text{SR}} = 2x_c \left[\sqrt{x_c^2 + 1} - x_c \right]$	Compute energy average \bar{S} using Moldauer's sum rule of the S-matrix
Moldauer-Simonius [7]	$T_c^{\text{MS}} = 1 - \exp(-2x_c)$	Phenomenological
Weak coupling limit	$T_c^{\text{weak}} = 2x_c(1 - x_c)$	The other three parameterizations reduce to this in limit $x_c \ll 1$

Here $x_c = \pi \bar{\Gamma}_c / D = 2\pi P_c s_c$

To better visualize the different parameterizations, we turn to ^{90}Zr , recently re-evaluated by S.F. Mughabghab [9]. Using the URR parameters of ^{90}Zr we computed the neutron transmission coefficients using the prescriptions in Table 1. We also computed the transmission coefficients using the coupled-channel code ECIS [10] and a Lane consistent dispersive soft rotor coupled-channel optical model potential (RIPL OMP #612) [11]. In Fig. 1 we show these transmission coefficients. For s -, p -, and d - wave neutrons impinging on the 0^+ ground state of ^{90}Zr , only the given J shown in Fig. 1 are possible.

In Fig. 1, all of the transmission coefficient parameterizations are consistent at low energies but the two weak coupling approximations diverge from the rest above 500 keV. The other three parameterizations (SPRT, Moldauer-Simonius (MS), and sum rule (SR)) agree over the entire range of the URR and with the RRR at low energy. The transmission coefficients computed by ECIS are roughly consistent with the resolved and unresolved resonances, but disagree in detail. The spin orbit coupling in the optical model potential generates a J dependence which is clearly visible in the plots, especially in the p -wave ($L = 1$) channels. We note that the neutrons in Fig. 1 approach the strong coupling limit already at 1 MeV in the p -wave channels. A coupled-channel calculation with a realistic optical model potential should not allow $T = 1$ as this would violate unitarity when combined with the other channels in the problem.

Above 1 MeV, the optical model potential predicts a turnover in T_c . Were we to extend the URR parameters to higher energies, we would see this behavior in the SPRT parameterization (see the SPRT equation in Table 1), but not in the sum rule or Moldauer-Simonius parameterizations. We speculate that this is a result of an implicit neglect of interference effects in the sum rule and Moldauer-Simonius parameterizations. We note that Ref. [12] describes a numerical study using stochastically generated scattering matrices which strongly supports the SPRT parameterization over either the sum rule or Moldauer-Simonius parameterizations.

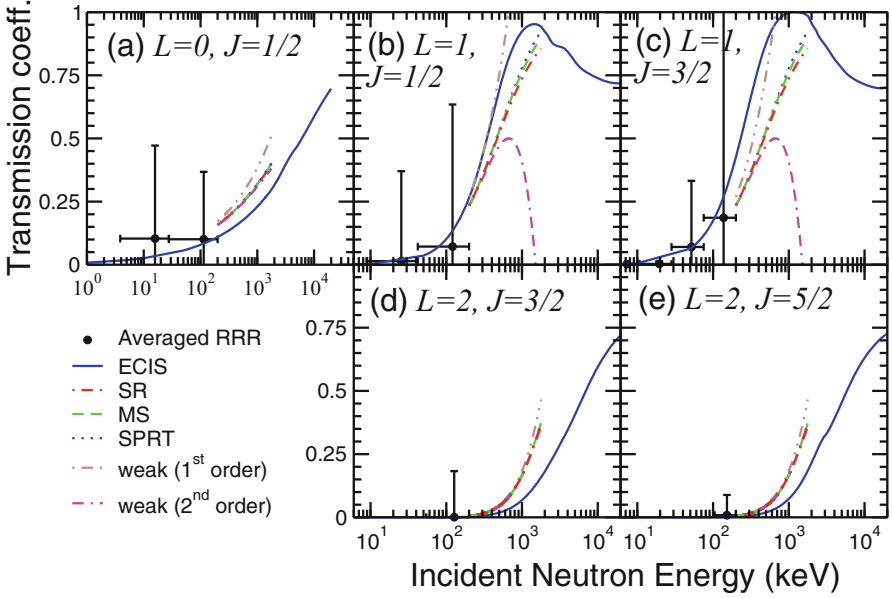


Fig. 1 Neutron transmission coefficients of ^{90}Zr , computed using ECIS and RIPL optical model potential #612 [11] and computed directly from the resolved and unresolved resonance parameters in the ENDF/B-VIII.0 file. Figure from Ref. [5]

3 Superradiance

The WFC in Eq. (2) was derived in the weak coupling limit ($x_c = \pi \bar{\Gamma}_c / D \ll 1$) but it is regularly applied outside its region of validity. Both Eqs. (1) and the WFC (2) contain factors $\bar{\Gamma}_b / \sum_c \bar{\Gamma}_c$ which, by substituting the sum rule parameterization in Table 1, give

$$\left. \frac{\bar{\Gamma}_b}{\sum_c \bar{\Gamma}_c} \right|_{\text{SR}} = \frac{T_b / \sqrt{1 - T_b}}{\sum_c T_c / \sqrt{1 - T_c}}. \quad (4)$$

There is an additional factor of $\bar{\Gamma}_a$ in σ_a^{abs} which we will return to. If instead one used the Moldauer–Simonius parameterization, we find a similar expression. Both of these substitutions reduce to the one shown in Eq. (3) in the weak coupling limit. The SPRT parameterization does not provide a unique mapping between $x_c = \pi \bar{\Gamma}_c / D$ and T_c due to its behavior at large x_c , so we do not know how to make an equivalent substitution for it.

Both Eq. (4) and the equivalent Moldauer–Simonius parameterization have potentially dramatic implications. When we reach the strong coupling limit in only one channel (so $T_c \rightarrow 1$), that channel dominates the cross section, an effect known as superradiance [13]. This might happen if there are many close resonances

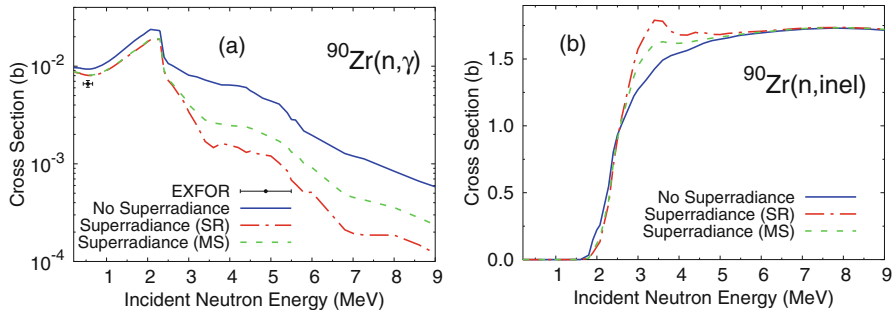


Fig. 2 Plots of ^{90}Zr cross sections, computed with and without the superradiance-modified Hauser-Feshbach equation. Cross sections computed with the sum rule and Moldauer-Simonius parameterizations are labeled “SR” and “MS,” respectively. Experimental data from the EXFOR library are also shown [16]. Figure from Ref. [5]

(causing $D \rightarrow 0$) or a few very strong resonances (causing $\bar{T}_c \rightarrow \infty$) acting incoherently [14]. The superradiant effect has been seen in many other mesoscopic systems [13, 14] and because compound nuclear reactions are only treated in the weak coupling limit, the effect is neglected.

The peaks in the p -wave transmission coefficients suggest that we might see superradiance in ^{90}Zr cross sections. We calculated the ^{90}Zr cross sections using the EMPIRE [15] reaction code, modified with the substitution in Eq. (4). The results are shown in Fig. 2 for the capture and total inelastic cross sections. The effects of superradiance are not obvious either at low energy (where we are in the weak coupling limit) or at high energy (where there are a large number of open channels and the effects of pre-equilibrium emission become evident). In the region around 2–4 MeV, we see noticeable differences between the cross sections computed with and without superradiance. While the most dramatic changes are in the total inelastic and capture cross sections, the elastic cross section shows an effect as well. Superradiance appears to cause an interesting modification to the shape of the inelastic cross section just above threshold. A measurement of $^{90}\text{Zr}(n, n'\gamma)$ between 2 and 4 MeV would be very helpful by providing experimental evidence for (or lack of) superradiance.

4 Conclusion and Outlook

In Ref. [5], we investigated the consequences of different formulations of the neutron transmission coefficient, enabling a rigorous connection between the RRR, URR, and fast neutron regions. This work suggests that predictions of the mean level spacing coupled with an optical model potential can allow one to predict the average neutron widths even in the strong coupling regime. This provides a tool for predicting neutron widths far off stability.

Our work also shows how and where superradiance may impact nuclear reactions. The effects of superradiance in the compound nuclear cross section appear to be small in most cases and are only evident in systems with a small number of open channels with large transmission coefficients. In practice, there are many effects that could mask superradiance: (a) direct reactions will lower the effective transmission coefficient because of the Englebrecht-Weidenmueller transform, (b) strong level repulsion prevents small D , (c) $\bar{F}_c \rightarrow \infty$ is unphysical, and (d) odd cross section behavior may be washed out by the cross section fluctuations. However, the right optical model potential could lead to $T_c \approx 1$ as in Fig. 1.

The effects of superradiance might be easier to see in the incoming channel because it is easier to control this channel experimentally. Blindly substituting the sum rule transmission coefficient into the absorption cross section we have $\sigma_a^{\text{abs}} \rightarrow \frac{2\pi^2 g_a}{k_a^2} \frac{T_a}{\sqrt{1-T_a}}$, which clearly is singular when $T_a \rightarrow 1$. The Moldauer-Simonius transmission coefficient is also singular as $T_a \rightarrow 1$. As the results of Ref. [12] strongly disfavor both and favor the SPRT parameterization, we think a possible resolution requires a detailed re-examination of how the WFC must be modified to account for level repulsion. Such a study might also help us understand the variance of the cross section in the URR.

Acknowledgments Work at Brookhaven National Laboratory was sponsored by the Office of Nuclear Physics, Office of Science of the U.S. Department of Energy under Contract No. DE-AC02-98CH10886 with Brookhaven Science Associates, LLC. Work at Los Alamos National Laboratory was carried out under the auspices of the National Nuclear Security Agency of the U.S. Department of Energy under Contract No. DE-AC52-06NA25396.

References

1. J.J.M. Verbaarschot, H.A. Weidenmüller, M.R. Zirnbauer, Phys. Rep. **129**, 367 (1985)
2. P.A. Moldauer, Phys. Rev. C **11**, 426 (1975)
3. A.M. Lane, J.E. Lynn, Proc. Phys. Soc. **A70**, 557 (1957); F.H. Fröhner, JEFF Report 18 (2000)
4. G.R. Satchler *Introduction to Nuclear Reactions* (Wiley, New York, 1980); P. Fröbrich, R. Lipperheide, *Theory of Nuclear Reactions (Oxford Studies in Nuclear Physics)* (Clarendon Press, Oxford, 1996) ISBN-13: 978-0198537830
5. D.A. Brown, G.P.A. Nobre, M.W. Herman, Phys. Rev. C **98**, 024616 (2018)
6. G. Noguere et al., EPJ Web Conf. **146**, 02036 (2017)
7. M. Simonius, Phys. Lett. **52B**, 279 (1974); P.A. Moldauer, Phys. Rev. **157**, 907 (1967)
8. P.A. Moldauer, Phys. Rev. Lett. **19**, 1047 (1967)
9. S.F. Mughabghab, *Atlas of Neutron Resonances: Resonance Parameters and Neutron Cross Sections, Z = 1-100* (Elsevier, Amsterdam 2006); D.A. Brown et al., Nucl. Data Sheets **148**, 1 (2018)
10. J. Raynal, ECIS code, distributed by the NEA DATA Bank, Paris, France (2003)
11. R. Capote et al., Nucl. Data Sheets **110** (12), 3107 (2009)
12. Y. Alhassid et al, Phys. Rev. C **99**, 024621 (2019)
13. N. Auerbach, V. Zelevinsky, Rep. Prog. Phys. **74** 106301 (2011)

14. M.O. Scully, A.A. Svidzinsky, *Science* **325**(5947), 1510–1511 (2009). <https://doi.org/10.1126/science.1176695>
15. M. Herman, R. Capote, B.V. Carlson, et al., *Nucl. Data Sheets* **108**, 2655 (2007)
16. N. Otuka et al., *Nucl. Data Sheets* **120**, 272 (2014); V.V. Zerkin, B. Pritychenko, *Nucl. Inst. Meth. A* **888**, 31 (2018)

Multi-step Direct Reaction Models Including Collectivity in Nucleon Induced Reactions



E. V. Chimanski, R. Capote, B. V. Carlson, and A. J. Koning

1 Introduction

Pre-equilibrium nuclear reaction is known as a particle emission process that takes place after the first projectile–target interaction but long before the equilibrium of the compound system is reached. Griffin in 1966, pioneered the description of such events with the so-called Exciton Model [1]. Since then, many improvements and extensions as well as new models were developed to describe pre-equilibrium phenomena [2–6]. These models, although being very sophisticated, are limited by their semi-classical nature, i.e., they do not take into account the interference effects, which are quantum-based features. Quantum mechanical models were developed during the late 1970s to the late of 1980s in the framework of a multi-step formalism by Agassi [7], Tamura [8], Feshbach [9], and Nishioka [10, 11].

In the quantum mechanical approach, the pre-equilibrium space is divided into two components: events involving continuum components belong to the P space and are called Multi-Step Direct (MSD) reactions, while those dealing with bound-states Q are named Multi-Step Compound (MSC) reactions. The MSD describes a highly energetic projectile (leading particle) that stays in the continuum and creates new particle–hole pairs on its way through the target nucleus. This process usually

E. V. Chimanski (✉)

Aeronautics Institute of Technology, São José dos Campos, Brazil
NAPC-Nuclear Data Section, International Atomic Energy Agency, Vienna, Austria
e-mail: chimanski@ita.br

R. Capote · A. J. Koning

NAPC-Nuclear Data Section, International Atomic Energy Agency, Vienna, Austria

B. V. Carlson

Instituto Tecnológico da Aeronáutica, São José dos Campos, SP, Brazil

© This is a U.S. government work and not under copyright protection in the U.S.; foreign copyright protection may apply 2021

J. Escher et al. (eds.), *Compound-Nuclear Reactions*, Springer Proceedings in Physics 254, https://doi.org/10.1007/978-3-030-58082-7_8

ends after a few interactions, or steps, with the number small enough so that the incident particle will retain some memory of its initial energy and direction.

Particle–hole excitations of the target states in the MSD theory can be taken in the so-called independent particle model [12], with no interaction between the excited modes involved, or in a slightly mixing p-h energies approach [13, 14]. Under certain statistical assumptions, the excitations can be represented by a response or strength function with a well-defined distribution. At low excitation energies, the collective nature of these states imposes obstacles to the statistical approach and the distributions become non-trivial functions of the energy.

In this work we analyze the particle–hole strength function for a collective excited state of the target nucleus. Different distributions are adjusted to it and a general fit is proposed. In addition, we also present a simplified particle–hole model we intend to employ for the transition matrix element calculations in the future. This work is organized as follows: In the next section the theoretical formalism for the one-step process is given. The two subsections are devoted for the descriptions of the methods employed. Results and Conclusions are presented in the last two sections.

2 One-Step Processes

The cross-section formulas for MSD reactions can be obtained from a Born-like expansion of the transition matrix elements [11, 14]. The number of steps is directly related to the number of terms in the expansion. At sufficiently high excitation energy, the one-step excitation can be obtained by an incoherent sum of particle–hole transition matrix elements weighted by a distribution—the response function ρ :

$$\frac{d^2\sigma}{d\Omega dE_f} = \frac{m^2}{(2\pi\hbar^2)^2} \frac{k_f}{k_i} \sum_{\text{ph}} \rho(E_x) \left| \langle \psi_{\mathbf{k}_f}^{(+)} | \langle \text{ph} | V | 0 \rangle | \psi_{\mathbf{k}_i}^{(-)} \rangle \right|^2, \quad (1)$$

where m is the projectile mass and $\langle \text{ph} | V | 0 \rangle$ represent the particle–hole matrix elements assuming the target to be initially in its ground state. The incoming $\psi_{\mathbf{k}_i}^{(-)}$ and outgoing $\psi_{\mathbf{k}_f}^{(+)}$ distorted wave functions are obtained from the projectile–target optical potential.

The distribution ρ can be obtained from the strength function of the Random Phase Approximation (RPA) states

$$\rho(E_x) \rightarrow \left| a_{\text{ph}}^x \right|^2 \quad a_{\text{ph}}^x = X_{\text{ph}}^x + Y_{\text{ph}}^x,$$

where X_{ph}^x and Y_{ph}^x are the RPA eigenvector components. In general, the sum of RPA amplitudes should be performed before squaring the matrix elements, however, as

we have already shown in Ref. [15], the sum becomes incoherent at energies above those of the underlying collective states. Here, we focus the study on the amplitudes of p-h excitations for the lower energy part of the RPA spectra. The full cross-section calculation will be addressed in future works.

2.1 Strength Function

We employ the self-consistent RPA code by Colò and collaborators [16] to obtain the necessary excited states and amplitudes. Single particle states are obtained solving the Hartree–Fock equations (we have used the Skyrme interaction SLy5 [17]) and the excited states are calculated for a given angular momentum and parity J^π . The RPA equations are [18]

$$\begin{pmatrix} A & B \\ -B & -A \end{pmatrix} \begin{pmatrix} X^x \\ Y^x \end{pmatrix} = E_x \begin{pmatrix} X^x \\ Y^x \end{pmatrix}$$

with the matrix elements given by

$$\begin{aligned} A_{mi,nj} &= (E_m - E_i)\delta_{mn}\delta_{ij} + (mj|V|in) \\ B_{mi,nj} &= (mn|V|ij) \\ \sum_{nj} A_{mi,nj} X_{nj}^x + \sum_{nj} B_{mi,nj} Y_{nj}^x &= E_x X_{mi}^x, \end{aligned}$$

where the indices m, n are reserved for states above (particles) while i, j for states below (holes) the Fermi level.

The strength function ρ is defined as the contribution of each p-h mode over the entire RPA energy spectrum. In this way, we define a histogram summing up all contributions within an energy bin of size 1.5 MeV. The histogram is compared to three different distributions, a Gaussian

$$G(E) = \frac{g_0}{\sqrt{2\pi}\sigma^2} \exp\left[-\frac{(E - E_0)^2}{2\sigma^2}\right], \quad (2)$$

a Breit–Wigner,

$$BW(E) = \frac{w_0}{\pi} \frac{\gamma}{(E - E_0)^2 + \left(\frac{\gamma}{2}\right)^2}, \quad (3)$$

and an exponential

$$\text{Exp}(E) = e_0 \exp \left[\frac{(E - E_0)}{\beta} \right]. \quad (4)$$

The widths σ , γ , and β of the distributions are taken to represent the p-h mixing caused by the residual interaction. Their mean energy values E_0 are close to the energy of the mode that most contributes to the state.

2.2 Simplified Particle–Hole Basis

The calculation of the p-h transition matrix elements using the single particle states from the Hartree–Fock (HF) solutions can be very time consuming due to the slow convergence of the mean field. As a first approximation we use a simplified model based on quantum harmonic oscillator (QHO) functions. Our work is reduced to building and diagonalizing the following matrix [19]:

$$H_{v'v} = \int_0^\infty r^2 dr g_{v'l}(r) g_{vl}(r) \left[\frac{\hbar^2}{2m_n} \left(\frac{4v + 2l + 3}{b^2} - \frac{r^2}{b^4} \right) + v_{WS}(r) + v_C(r) + \frac{1}{2} \left[j(j+1) - l(l+1) - \frac{3}{4} \right] v_{LS}(r) \right] \quad (5)$$

where v' , v are the principal QHO quantum numbers, with l the orbital and j the total angular momentum, respectively. The interactions and their parameters are the following: the central Wood–Saxon

$$v_{WS}(r) = \frac{-V_0}{1 + \exp[(r - R_0)/a_0]},$$

where

$$R_0 = r_0 A^{1/3} \text{ fm}, \quad r_0 = 1.27 \text{ fm}, \quad a_0 = 0.67 \text{ fm}, \quad V_0 = 51 \pm \frac{33(N - Z)}{A} \text{ MeV},$$

with + for proton and – for neutron states; the spin–orbit interaction

$$v_{LS}(r) = v_{LS}^0 r_0^2 \frac{1}{r} \left[\frac{d}{dr} \frac{1}{1 + \exp[(r - R_0)/a]} \right], \quad v_{LS}^0 = 0.44V_0 \text{ MeV};$$

and the Coulomb repulsion

$$\frac{Ze^2}{2R_0} \left[3 - \left(\frac{r}{R_0} \right)^2 \right] \text{ for } r \leq R_0 \quad \text{and} \quad Ze^2/r \text{ for } r > R_0.$$

The Blomqvist–Molinari formula [20] is used for the harmonic oscillator parameter

$$b = \frac{197.33}{\sqrt{940} \times \hbar\omega} \text{ fm}, \quad \hbar\omega = \left(45A^{-1/3} - 25A^{-2/3}\right) \text{ MeV}.$$

3 Results

We take the 3^- excited states of the double-magic target Ni^{56} ($A=56$, and $Z=28$) for the particle–hole response function analysis. We show in Fig. 1 the contribution of a low-energy p-h component along the excitation energy spectrum. We immediately notice that this mode dominates the lower (left side) energy part and has a long tail toward more energetic states. A Gaussian function fit to it gives $g_0 = 0.67$, $\sigma = 2.5 \text{ MeV}$, and $E_0 = 12.12 \text{ MeV}$, while the Breit–Wigner provides $w_0 = 0.44$, $\gamma = 0.82 \text{ MeV}$, and $E_0 = 13.12 \text{ MeV}$. The former furnishes a better description of the large contributions but ignores the important contributions from the high energy part of the spectrum. One may notice that the peaked BW distribution has its mean value shift to the right compared to the non-interacting energy component. In addition, we also attempt to adjust the exponential function of Eq. (4) to the tail of the distribution with $e_0 = 5.0 \times 10^{-5}$, $\beta = 20.0 \text{ MeV}$, and $E_0 = 25.0 \text{ MeV}$. This part of the histogram seems to be well described by both the BW and the exponential distributions. As a more general representation for the strength function, we propose a linear combination of the Gaussian function, accounting for the lower energy part of the spectra, plus either the BW or the exponential distributions for a better approximation of the higher energy tail of the histogram. With the BW tail we have

$$F(E) = G(E) + \text{BW}(E), \quad (6)$$

where the best fit is given by $g_0 = 0.92$, $w_0 = 0.04$, $\sigma = \gamma = 2.5 \text{ MeV}$ with a mean value for both functions $E_0 = 12.12 \text{ MeV}$. If an exponential approximation is used with

$$K(E) = G(E) + \text{Exp}(E), \quad (7)$$

we obtain $g_0 = 1$ and $e_0 = 5.5 \times 10^{-5}$ with the other parameters held constant. Figure 2 presents a comparison of the two cases and the histogram data. The very final part of the tail of the distribution is better reproduced by the BW curve (K) while the exponential (F) fits nicely in the middle part of the spectra.

Before closing, we present in Fig. 3 the particle–hole spectrum of proton states obtained with the simplified model described in Sect. 2.2. The components are formed by all quasi-bound p-h pairs with particle energies lying below the sum of the Coulomb plus centrifugal barrier. This model permits a very large basis, which

Fig. 1 Strength function for a collective (low energy) excited 3^- state of ^{56}Ni . The histogram represents the contribution of a particular p-h mode, shown as the solid vertical line $E_{\text{ph}} = 12.0$ MeV, along the RPA energy states. The parameters of the curves are given in the text

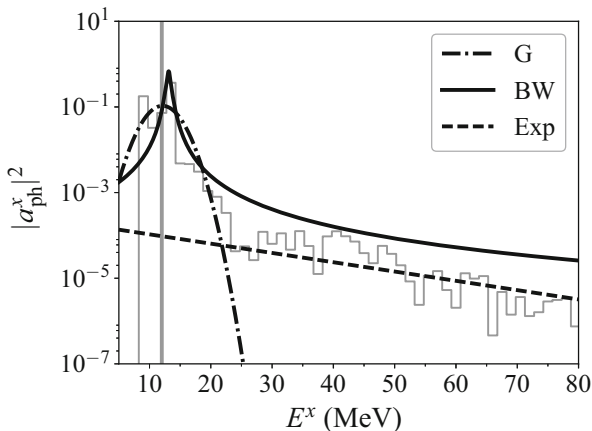
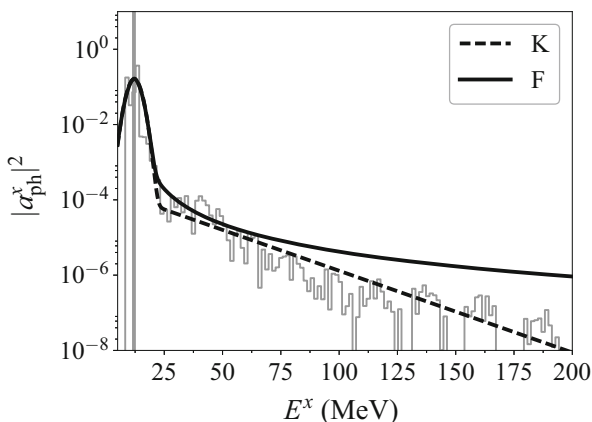


Fig. 2 Two general fits for the strength function of Fig. 1. The constants and linear coefficients are given in the text



serves to calculate the particle–hole transition matrix elements for the cross-section formula over a wide range of excitation energies and angular momenta.

4 Conclusions

The RPA strength function was studied for the 3^- collective states of ^{56}Ni . In this case, its width accounts for the particle–hole configuration mixing present in the state. The strength function for low-energy p-h components can be a complicated function of excitation energy. The presence of a very long tail toward high energetic states reflects the importance of those components in the description of decay transitions. We found that the combination of a Gaussian distribution with a Breit–Wigner or an exponential produces good agreement with the histogram data. Collective states present properties that are difficult to be taken into account statistically,

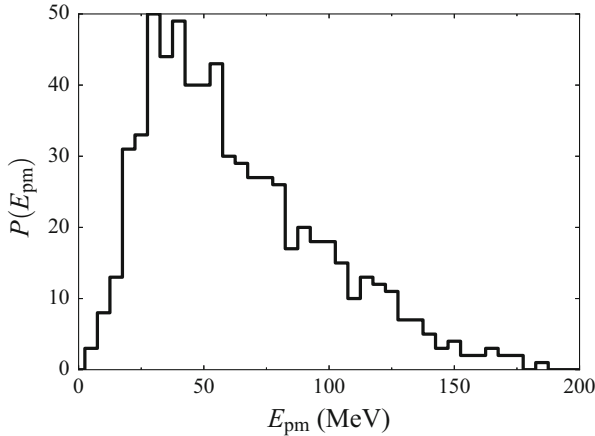


Fig. 3 Proton particle–hole state basis for ^{56}Ni target obtained with the simplified Hamiltonian (5)

the transition matrix elements are coherent in phase, making the cross-section calculation difficult to be performed. For the formulas shown here, the phases of different p-h components are hidden in the squared value of the amplitude, and the many modes present in collective states could be represented by a distribution with a large spreading energy width. The combined function seems to represent better the whole spectrum for low-energy modes that contribute to collective states. The best reproduction of such distribution was shown to be a complicated combination of different functions due to all non-trivial coupling matrix elements of the RPA model.

To avoid the use of HF single particle states, we have presented a simplified model for calculating the single particle states to generate the p-h components. The distribution of the modes obtained provide a very large basis, allowing calculation of cross sections for reactions from small to high excitation energies in a beyond mean-field approximation.

Acknowledgments EVC acknowledges financial support from grants 2016/07398-8 and 2017/13693-5 of the São Paulo Research Foundation (FAPESP). BVC acknowledges financial support from grant 2017/05660-0 of the São Paulo Research Foundation (FAPESP) and grant 306433/2017-6 of the CNPq. EVC and BVC acknowledge support from the INCT-FNA project 464898/2014-5.

References

1. Griffin, J. J., Statistical model of intermediate structure. *Phys. Rev. Lett.* **17**, 478 (1996)
2. C. K. Cline, M. Blann, The pre-equilibrium statistical model: description of the nuclear equilibration process and parameterization of the model. *Nucl. Phys. A.* **172**, 225–259 (1971)

3. M. Blann, New precompound decay model. *Phys. Rev. C.* **54**, 1341–1349 (1996)
4. M. Blann, M. Chadwick, New precompound decay model: angular distributions. *Phys. Rev. C.* **57**, 233–243 (1998)
5. C.A. Soares Pompeia, B.V. Carlson, Configuration mixing in pre-equilibrium reactions. *Phys. Rev. C.* **74**, 054609 (2006)
6. B.V. Carlson, J.E. Escher, M.S. Hussein, Theoretical descriptions of compound-nuclear reactions: open problems and challenges. *J. Phys. G Nucl. Part. Phys.* **41**, 094003 (2014)
7. D. Agassi, H.A. Weidenmüller, G. Mantzouranis, The statistical theory of nuclear reactions for strongly overlapping resonances as a theory of transport phenomena. *Phys. Rep.* **22**, 145–179 (1975)
8. T. Tamura, T. Udagawa, H. Lenske, Multistep direct reaction analysis of continuum spectra in reactions induced by light ions. *Phys. Rev. C.* **26**, 379–404 (1982)
9. H. Feshbach, A. Kerman, S. Koonin, The statistical theory of multi-step compound and direct reactions. *Ann. Phys.* **125**, 429–476 (1980)
10. H. Nishioka, J.J.M. Verbaarschot, H.A. Weidenmüller, S. Yoshida, Statistical theory of precompound reactions: the multistep compound process. *Ann. Phys.* **172**, 67–99 (1986)
11. H. Nishioka, H.A. Weidenmüller, S. Yoshida, Statistical theory of precompound reactions: The multistep direct process. *Ann. Phys.* **183**, 166–187 (1988)
12. A.J. Koning, J.M. Akkermans, Randomness in multi-step direct reactions. *Ann. Phys.* **208**, 216–250 (1991)
13. R. Bonetti, A.J. Koning, J. Akkermans, P. Hodgson, The Feshbach-Kerman-Koonin multistep direct reaction theory. *Phys. Rep.* **247**, 1–58 (1994)
14. A.J. Koning, M.B. Chadwick, Microscopic two-component multistep direct theory for continuum nuclear reactions. *Phys. Rev. C.* **56**, 970–994 (1997)
15. E.V. Chimanski, B.V. Carlson, R. Capote, A.J. Koning, Quasiparticle nature of excited states in random-phase approximation. *Phys. Rev. C.* **99**, 014305 (2019)
16. C. Gianluca et. al. Self-consistent RPA calculations with Skyrme-type interactions: the skyrmerpa program. *Comput. Phys. Commun.* **184**, 142–161 (2013)
17. E. Chabanat, P. Bonche, P. Haensel, J. Meyer, R. Schaeffer, A Skyrme parametrization from subnuclear to neutron star densities Part II. Nuclei far from stabilities. *Nucl. Phys. A.* **635**, 231–256 (1998)
18. D.J. Rowe, *Nuclear Collective Motion: Models and Theory* (World Scientific, New York, 2010)
19. J. Suhonen, *From Nucleons to Nuclei: Concepts of Microscopic Nuclear Theory* (Springer, Berlin, 2007)
20. J. Blomqvist, A. Molinari, Collective 0- vibrations in even spherical nuclei with tensor forces. *Nucl. Phys. A.* **106**, 545–569 (1968)

New Symmetry-Adapted *ab initio* Approach to Nuclear Reactions for Intermediate-mass Nuclei



Alexis Mercenne, Kristina D. Launey, Jutta E. Escher, Tomas Dytrych, and Jerry P. Draayer

1 Introduction

Ab initio descriptions of reactions of nuclei heavier than ^{16}O remain a challenge in nuclear physics. Their theoretical and experimental study is of utmost importance to identify various quantum mechanisms that can explain the complexity of nuclei. In addition, many simulations of astrophysical phenomena are very sensitive to nuclear reaction cross sections. For example, simulations of X-ray burst nucleosynthesis have been found to be sensitive to several nuclear reaction rates for intermediate- and medium-mass nuclei [1], pointing to the need for accurate cross sections. For theoretical predictions, this level of accuracy can be achieved through an *ab initio* description of nuclear reactions. Recent progresses in *ab initio* nuclear theory using QCD-inspired realistic interactions along with the continuous improvement of high performance computing have given the necessary tools to theoretical approaches such as the no-core shell model (NCSM) to provide an *ab initio* description of the structure of light nuclei [2, 3]. Its recent implementation within the RGM [4], the NCSM/RGM, has allowed a microscopic study of nuclear reactions [5–7], pursuing the long-standing goal of unifying nuclear structure and reactions. Recently, it has been demonstrated that the SA-NCSM [8, 9], which employs a physically relevant

A. Mercenne (✉) · K. D. Launey · J. P. Draayer
Department of Physics and Astronomy, Louisiana State University, Baton Rouge, LA, USA
e-mail: amercenne1@lsu.edu

J. E. Escher
Lawrence Livermore National Laboratory, Livermore, CA, USA

T. Dytrych
Department of Physics and Astronomy, Louisiana State University, Baton Rouge, LA, USA
Nuclear Physics Institute, Academy of Sciences of the Czech Republic, Řež, Czech Republic

basis, can use drastically reduced configuration spaces with practically the same accuracy of results, and has been successfully applied up to medium-mass nuclei [10, 11]. Motivated by the need for calculated nuclear cross sections in experimental research and astrophysical studies, and following the success of the NCSM/RGM for light nuclei, we combine the SA-NCSM with the RGM. As a first step, we focus on reactions of two clusters, in which the projectile is a nucleon.

2 Ab initio Symmetry-Adapted Framework for Nuclear Reactions

In the RGM framework, the nucleons are organized within different groups, or clusters, “resonating” through the inter-cluster exchange of nucleons. This antisymmetrization between the different clusters guarantees the Pauli exclusion principle, which, along with the consideration of the cluster internal structure, is one of the most important features of the approach. In the case of two clusters, the wave function is written as (in notations of Ref. [6]):

$$|\Psi^{J^\pi T}\rangle = \sum_\nu \int_r dr r^2 \frac{g_\nu^{J^\pi T}(r)}{r} \hat{A} |\Phi_{\nu r}^{J^\pi T}\rangle, \quad (1)$$

where the index ν represents all quantum numbers that define channels and partitions: $\nu = \{(A-a)\alpha_1 I_1 T_1; a\alpha_2 I_2 T_2; \ell s\}$, and the cluster states are defined as $|\Phi_{\nu r}^{J^\pi T}\rangle = [((A-a)\alpha_1 I_1 T_1) \otimes (a\alpha_2 I_2 T_2)]^{(sT)} \times Y_\ell(\hat{r}_{A-a,a})^{(J^\pi T) \frac{\delta(r-r_{A-a,a})}{r r_{A-a,a}}}$. The amplitudes $g_\nu^{J^\pi T}(r)$ describe the relative motion between the target and the projectile for all channels ν , and the cross section can be extracted from their asymptotic behavior. The $g_\nu^{J^\pi T}(r)$ functions are the solutions to the Schrödinger equation:

$$\sum_\nu \int dr r^2 \left[H_{\nu'\nu}^{J^\pi T}(r, r') - E N_{\nu'\nu}^{J^\pi T}(r', r) \right] \frac{g_\nu^{J^\pi T}(r)}{r} = 0. \quad (2)$$

Here, the Hamiltonian $H_{\nu'\nu}^{J^\pi T}(r', r)$ and norm $N_{\nu'\nu}^{J^\pi T}(r', r)$ kernels are expressed as $\langle \Phi_{\nu' r'}^{J^\pi T} | \hat{A} \hat{O} \hat{A} | \Phi_{\nu r}^{J^\pi T} \rangle$ with \hat{O} being the identity and the Hamiltonian operator, respectively, and where \hat{A} is the antisymmetrizer ensuring the Pauli exclusion principle. The kernels are computed using the wave functions of the clusters. Eq. (2) can then be solved using an R -matrix approach [12, 13].

An ab initio application of this approach is the NCSM/RGM [6], which uses NCSM wave functions and realistic interactions. However, the method becomes numerically challenging for heavier systems due to the size and complexity of the configuration space. We address the limitation of the NCSM/RGM by combining the SA-NCSM with the RGM formalism, where the former allows for the calculation of the intermediate mass wave functions required by the RGM.

In the SA-NCSM, the microscopic many-body basis is based on the spherical harmonic oscillator single-particle basis, and labeled by irreducible representations according to the group chain:

$$\text{SU}(3)_{(\lambda\mu)} \supset_{\kappa} \text{SO}(3)_L \supset \text{SO}(2)_{M_L}. \quad (3)$$

Consequently, for any given total spin J and its projection M , the wave function of a nucleus will be described within a basis $\{|\alpha_i(\lambda_i\mu_i)\kappa_i(L_i S_i)JM\rangle\}$ with each component weighted by a coefficient C_i . Here α_i represents additional quantum numbers needed to enumerate the complete shell-model space.

In the SA-RGM, the channels are defined by coupling each component of the SA-NCSM wave functions between the projectile and the target. Consequently, the channels with good SU(3) spin and isospin quantum numbers are given in the case of one nucleon projectile as

$$|\Phi_{\gamma n}^{\rho(\lambda\mu)\kappa(LS)JMTM_T}\rangle = \left\{ |\alpha_1(\lambda_1\mu_1)S_1T_1\rangle \otimes |(n0)\frac{1}{2}\frac{1}{2}\rangle \right\}^{\rho(\lambda\mu)\kappa(LS)JMTM_T}, \quad (4)$$

where the index $\gamma \equiv \{\alpha_1(\lambda_1\mu_1)S_1T_1; (n0)\frac{1}{2}\frac{1}{2}\}$ labels the channel basis, with $(n0)$ representing the SU(3) labels of the projectile with spin $\frac{1}{2}$ and isospin $\frac{1}{2}$. Note that there is no dependence on the orbital momentum of the target and the projectile.

In this basis, the exchange matrix, which ensures the antisymmetrization in the kernels, has the following form (in conventional notations [14]):

$$\begin{aligned} & \langle \Phi_{\gamma' n'}^{\rho'(\lambda'\mu')\kappa'(L'S')JMTM_T} | \hat{P}_{A,A-1} | \Phi_{\gamma n}^{\rho(\lambda\mu)\kappa(LS)JMTM_T} \rangle \\ &= \frac{1}{A-1} \delta_{\rho\rho'} \delta_{(\lambda\mu)(\lambda'\mu')} \delta_{\kappa\kappa'} \delta_{LL'} \delta_{SS'} \sum_{\substack{\tau\rho_o(\lambda_o\mu_o) \\ S_o\bar{\rho}}} \Pi_{\tau S_o S'_1 T'_1} (-1)^{n+n'-(\lambda_o+\mu_o)} \\ & \times (-1)^{T_1+\frac{1}{2}+T'} (-1)^{S_1+\frac{1}{2}+S'} \left\{ \begin{array}{cc} S_1 & S_o \\ \frac{1}{2} & S \end{array} \right\} \left\{ \begin{array}{cc} S'_1 & \\ & \frac{1}{2} \end{array} \right\} \left\{ \begin{array}{ccc} T_1 & \tau & T'_1 \\ \frac{1}{2} & T & \frac{1}{2} \end{array} \right\} \\ & \times \sqrt{\frac{\dim(\lambda_o\mu_o)}{\dim(n0)}} \text{U} [(\lambda_1\mu_1)(\lambda_o\mu_o)(\lambda'\mu')(n'0); (\lambda'_1\mu'_1)\bar{\rho}\rho'(n0)\rho_o\rho''] \\ & \times \langle \alpha'_1(\lambda'_1\mu'_1)S'_1T'_1 | | | a_{(n0)\frac{1}{2}\frac{1}{2}}^\dagger \otimes \tilde{a}_{(0\bar{n}')\frac{1}{2}\frac{1}{2}} \rangle^{\rho_o(\lambda_o\mu_o)S_o\tau} | | | \alpha_1(\lambda_1\mu_1)S_1T_1 \rangle_{\bar{\rho}}. \end{aligned} \quad (5)$$

Clearly, the presence of the delta Kronecker functions in Eq. (5) makes the exchange matrix diagonal within this SU(3) basis, allowing for several numerical simplifications [15]. Furthermore, matrix calculations avoid complications of dealing with the

orbital momentum, which is introduced at the very last step of the calculation, for input to the R -matrix approach. Namely, we can retrieve the partial-wave expansion

$$\begin{aligned}
 |\Phi_{vn}^{JM T M_T}\rangle = & \sum_i C_i \sum_{\substack{j\rho(\lambda,\mu) \\ \kappa LS}} \Pi_{I_1 L S j} \langle (\lambda_1^i \mu_1^i) \kappa_1^i L_1^i; (n0)0\ell | |(\lambda\mu) K L\rangle_\rho \\
 & \times (-1)^{I_1+J+j} \Pi_{Sj} \left\{ \begin{matrix} I_1 & \frac{1}{2} & s \\ \ell & J & j \end{matrix} \right\} \left\{ \begin{matrix} L_1^i & S_1^i & I_1 \\ \ell & \frac{1}{2} & j \\ L & S & J \end{matrix} \right\} |\Phi_{\gamma n}^{\rho(\lambda,\mu)\kappa(LS)JM T M_T}\rangle
 \end{aligned} \tag{6}$$

and calculate the norm $N_{v'v}^{J\pi T}(r', r)$ using the formula of Ref. [6]. Note that the summation over i represents the expansion of the target wave function in terms of the SU(3) basis states, where i is given by $\{\alpha_1^i(\lambda_1^i \mu_1^i) \kappa_1^i L_1^i S_1^i\}$. The Hamiltonian kernel is calculated straightforwardly using the same procedure, but the details are more complicated and are omitted for brevity here.

3 Results

To demonstrate the efficacy of the approach, we present results for norm and Hamiltonian kernels for light and intermediate-mass nuclei.

SA-NCSM and SA-RGM computations are performed in laboratory coordinates. The center-of-mass (CM) spuriousity is removed for the target wave function. To simplify the calculations the present results are reported for a projectile–target system with the CM included (the removal of the CM is work in progress and is based on an efficient group-theoretical algorithm to be reported in another publication). Nonetheless, this CM effect is expected to be negligible for reactions for one nucleon plus an $A \gtrsim 16$ target, such as ^{16}O and ^{20}Ne .

First, we have performed a benchmark calculation for p - ^4He , where we compare the exchange part of the norm in laboratory coordinates for the NCSM/RGM approach, according to Eqs. (37) and (50) of Ref. [6], and the SA-RGM approach using Eqs. (5) and (6) (Fig. 1). The SA-RGM result has been obtained using a ^4He wave function truncated to only several SU(3) basis states, and is in excellent agreement with the NCSM/RGM calculation. It is important to mention that the SA-RGM approach with the complete SU(3) wave function provides exactly the same results as in the NCSM/RGM.

The first results for the kernels for reactions of intermediate-mass nuclei using various realistic nucleon–nucleon (NN) interactions are now available. In these calculations, we use SA-selected model spaces for the target wave functions, as complete SU(3) (equivalent to NCSM) model spaces for a sufficiently large number of shells are prohibitive. As an illustrative example, we show the norm kernel for p - ^{16}O with the NNLO_{sat} [16] interaction and p - ^{20}Ne with the NNLO_{opt} [17]

Fig. 1 Exchange part of the norm kernel ($\ell = 0$) for $p\text{-}^4\text{He}$. The NCSM/RGM calculation was performed using the formalism of Ref. [6] and the complete ^4He wave function. The SA-RGM calculation was performed using Eq. (5) and a truncated ^4He wave function, where only SU(3) components with a probability greater than 1% are selected. Calculations are performed in 4 shells and for $\hbar\Omega = 15$ MeV

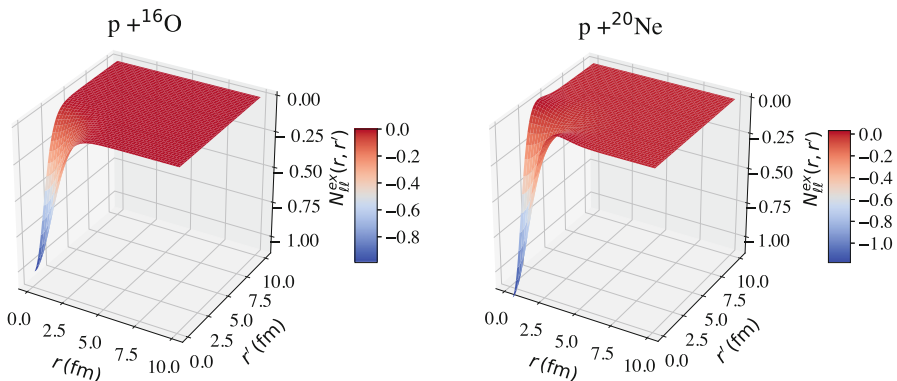
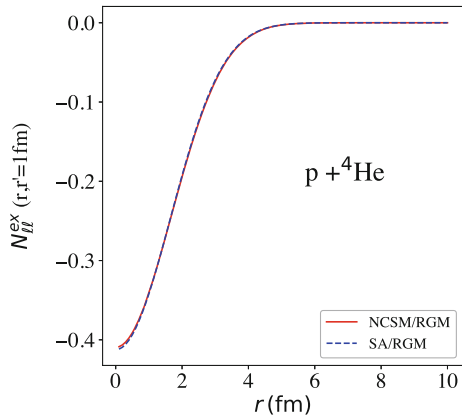


Fig. 2 Exchange part of the norm kernel ($\ell = 0$). The target wave function is calculated using the chiral NNLO_{sat} NN in 10 shells ($\hbar\Omega = 16$ MeV) for ^{16}O , and the chiral NNLO_{opt} NN in 13 shells ($\hbar\Omega = 15$ MeV) for ^{20}Ne , with selected SU(3) configurations that have a contribution greater than 2%

interaction (Fig. 2). As expected, the norm kernel vanishes at large distances, which is consistent with the Pauli principle. Results are shown for a model space for the projectile that yields convergence. Indeed, we find that the norm kernel converges comparatively quickly for the NNLO_{sat} interaction and, e.g., including up to 4 shells has already yielded a converged norm kernel for $p\text{-}^{16}\text{O}$ (Fig. 3).

The Hamiltonian kernel provides information on the non-local effective interaction between the projectile and the target for a given channel, and can be studied for intermediate-mass targets in the SA-RGM framework. For example, we find that the direct part of the Hamiltonian kernel for the $p\text{-}^{20}\text{Ne}$ shows a different behavior as compared to doubly-magic systems (Fig. 4, left panel). The positive peaks occurring around $r = 3$ fm might be related to the intricate structure of ^{20}Ne that exhibits clustering substructures and enhanced deformation, as shown in the density profile (Fig. 4, right panel). Further investigations of these effective interactions in this

Fig. 3 Convergence of the exchange part of the norm ($\ell = 0$) with the allowed number of shells n_{\max} for the projectile using SA-RGM. Calculations are described in the caption of Fig. 2

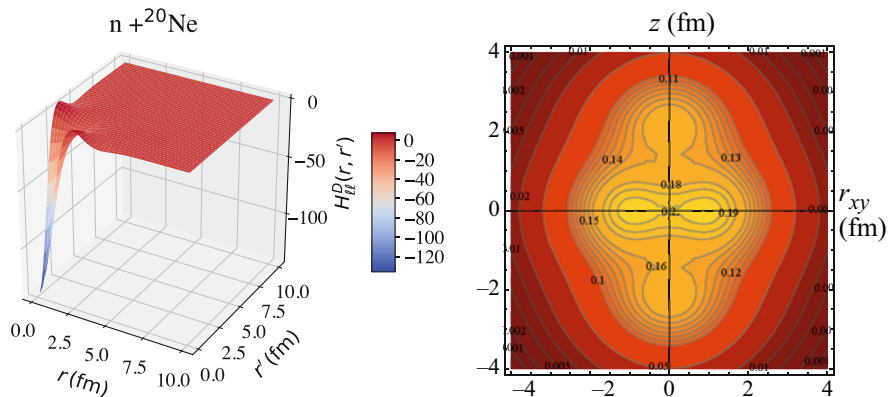
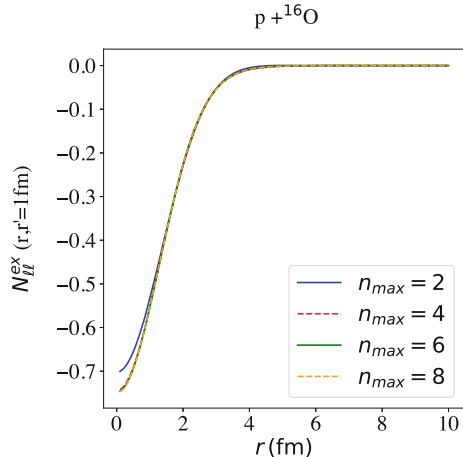


Fig. 4 Left panel: Direct part of the Hamiltonian kernel ($\ell = 0$) using the same wave function as in Fig. 2. Right panel: Corresponding one-body density profile of ${}^{20}\text{Ne}$ from the SA-NCSM calculation

region and the role of non-locality are needed, especially in relation to obtaining first-principle optical potentials.

To summarize, the use of a physically relevant basis in the SA-RGM provides a pathway to ab initio descriptions of nuclear reactions in the intermediate-mass region. The use of this basis allows several numerical procedures inherent to RGM to be simplified. The present outcome shows the applicability of the method, including benchmark calculations, convergence properties, and a discussion of non-local inter-cluster effective interactions.

We acknowledge useful discussions with P. Navrátil and S. Quaglioni. This work was supported by the U.S. National Science Foundation (OIA-1738287, ACI - 1713690), the Czech Science Foundation (16-16772S), and under the auspices of the U.S. Department of Energy by Lawrence Livermore National Laboratory under

Contract DE-AC52-07NA27344, with support from LDRD project 19-ERD-017. In addition, this work benefitted from computing resources provided by LSU (www.hpc.lsu.edu), Blue Waters, and NERSC.

References

1. R.H. Cyburt et al., *Astrophys. J.* **830**, 2 (2016)
2. P. Navrátil, J.P. Vary, B.R. Barrett, *Phys. Rev. Lett.* **84**, 5728 (2000)
3. B.R. Barrett, P. Navrátil, J.P. Vary, *Prog. Part. Nucl. Phys.* **69**, 131 (2013)
4. Y.C. Tang, M. LeMere, D.R. Thompson, *Phys. Rep.* **47**, 167 (1978)
5. S. Quaglioni, P. Navrátil, *Phys. Rev. Lett.* **101**, 092501 (2008)
6. S. Quaglioni, P. Navrátil, *Phys. Rev. C* **79**, 044606 (2009)
7. S. Baroni, P. Navrátil, S. Quaglioni, *Phys. Rev. Lett.* **110**, 022505 (2013)
8. T. Dytrych et al., *Phys. Rev. Lett.* **111**, 252501 (2013)
9. K.D. Launey, T. Dytrych, J.P. Draayer, *Prog. Part. Nucl. Phys.* **89**, 101 (2016)
10. K.D. Launey et al., *AIP Conf. Proc.* **2038**, 020004 (2018)
11. J.P. Draayer, T. Dytrych, K.D. Launey, in *Emergent Phenomena in Atomic Nuclei from Large-scale Modeling: A Symmetry-guided Perspective* (World Scientific, New York, 2017)
12. P. Descouvemont, D. Baye, *Rep. Prog. Phys.* **73**, 3 (2010)
13. P. Descouvemont, *Comput. Phys. Commun.* **200**, 199 (2016)
14. J.P. Draayer, Y. Akiyama, *J. Math. Phys.* **14**, 12 (1973)
15. K.T. Hecht, *Nucl. Phys. A* **283**, 223 (1977)
16. A. Ekström et al., *Phys. Rev. C* **91**, 051301 (2015)
17. A. Ekström et al., *Phys. Rev. Lett.* **110**, 192502 (2013)

Part III
Optical Models

Linking Nuclear Reactions and Nuclear Structure to Study Exotic Nuclei Using the Dispersive Optical Model



W. H. Dickhoff

1 Introduction

How do the properties of protons and neutrons in the nucleus change from the valley of stability to the respective drip lines? The answer can be developed by studying the propagation of a nucleon through the nucleus at positive energy, generating experimentally accessible elastic scattering cross sections, as well as the motion of nucleons in the ground state at negative energy. The latter information sheds light on the density distribution of both protons *and* neutrons relevant for clarifying properties of neutron stars. Detailed knowledge of this propagation process allows for an improved description of other hadronic reactions, including those that purport to extract structure information, like transfer or knockout reactions. Structure information associated with the removal of nucleons from the target nucleus is therefore subject of these studies and must be supplemented by the appropriate description of the hadronic reaction utilized to extract it. Consequently, establishing a much tighter link between reaction and structure studies than is common practice is an important goal of this research.

In our group we apply the Green's functions method [1, 2] to the nuclear many-body problem to address this issue with special emphasis on reaching the limits of stability. The method can be utilized to correlate huge amounts of experimental data, like elastic nucleon cross sections, analyzing powers, etc., as well as structure information like removal energies, density distributions, and other spectral properties. This is achieved by relating these data to the nucleon self-energy employing its causal properties in the form of a subtracted dispersion relation. The

W. H. Dickhoff (✉)

Department of Physics, Washington University, St. Louis, MO, USA

e-mail: wimd@physics.wustl.edu

<https://web.physics.wustl.edu/wimd/>

© This is a U.S. government work and not under copyright protection in the U.S.; foreign copyright protection may apply 2021

J. Escher et al. (eds.), *Compound-Nuclear Reactions*, Springer Proceedings in Physics 254, https://doi.org/10.1007/978-3-030-58082-7_10

current implementation and corresponding details can be found in [3]. The method is known as the dispersive optical model (DOM) and has proceeded way beyond its original form [4]. A more general review of the optical model is available in [5]. We discuss some recent developments of the DOM with applications to transfer reactions in Sect. 2, the analysis of the $(e, e'p)$ reaction solely with DOM ingredients in Sect. 3, predictions of neutron distributions in Sect. 4, and finally offer some conclusions in Sect. 5.

2 Transfer Reactions and the DOM

Transfer reactions are under intense study in order to develop a reliable method to generate accurate results given certain ingredients like overlap functions and optical potentials. A remaining source of uncertainty in the calculation of transfer reaction observables is the optical potential for the relevant nucleons and the deuteron. Our group has made several contributions to this effort documented in Refs. [6, 7] mostly involving exploratory efforts.

Deuteron-induced reactions have played an important role in elucidating properties of neutrons that are either added to or removed from the target nucleus. This role will be even more prominent when such transfer reactions are studied in inverse kinematics at radioactive beam facilities like FRIB [8, 9]. While scientifically compelling in its own right, the (d, p) reaction also yields indirect access [10] to the study of neutron capture and therefore provides essential information for the (n, γ) reaction which is critical for the study of the understanding of the r -process.

The present state of the reaction description can be summarized by noting that the distorted-wave Born approximation and coupled-channel approaches have mostly studied discrete final states. The treatment of the continuum was proposed in the late 1970s but efforts ended in the 1990s, with an unresolved controversy. Only recently, three different groups [11–13] have revived this subject and during a recent workshop at MSU/FRIB [14] have concluded that the relevant issues have now been resolved.

The main ingredients of the present state of the (d, p) reaction description allows a simultaneous treatment of transfer, elastic breakup, and the formation of the compound nucleus. Critical ingredients for the relevant calculations are provided by the deuteron optical potential, the description of the propagation of the added neutron, and the final proton optical potential. Phenomenological optical potentials suffer from being non-dispersive, local, and are not constrained by negative energy data. A proper description of the reaction therefore requires dispersive, non-local potentials that are also constrained by negative energy data. Such potentials are provided by the latest implementation of the DOM [3] for the neutron and proton propagation. An initial assessment of the DOM ingredients has been implemented by employing the local version [15] for Ca isotopes including an extrapolation to ^{60}Ca . These results together with an overview of the current theory relevant for elastic and non-elastic breakup have been published in [16]. Already at this

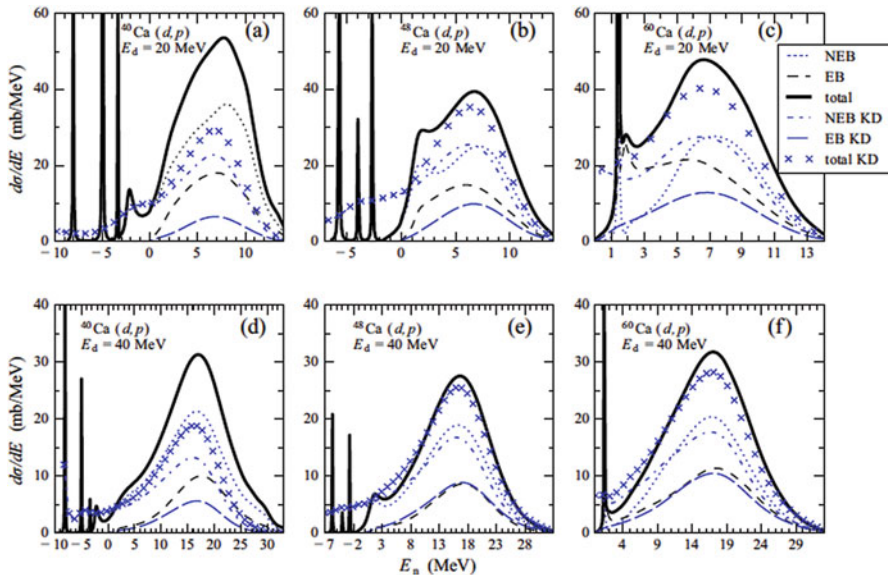


Fig. 1 Comparison of KD phenomenological optical potential and the DOM [16]: elastic breakup (EB) and non-elastic breakup (NEB) proton spectra for the reactions $^{40}\text{Ca}(d, p)$, $^{48}\text{Ca}(d, p)$, and $^{60}\text{Ca}(d, p)$ at $E_d = 20$ MeV and $E_d = 40$ MeV

early stage, a clear preference of DOM-generated potentials emerges over a more traditional global optical potential like the one of [17] labeled KD, as illustrated in Fig. 1.

As the DOM potentials are constructed to smoothly connect the positive and negative energy domain, they accurately describe the peaks that occur when a neutron is added in a bound state, whereas phenomenological potentials do not provide a suitable extrapolation to negative energy. Available data are well described with these potentials [16]. Further developments are necessary to raise the standard for the description of the deuteron and employ non-local dispersive potentials for nucleons in order to analyze data from this reaction employing rare isotopes in inverse kinematics. The main missing ingredient is an appropriate description of the deuteron for which only local, non-dispersive potentials are available [18–20]. We are presently developing tools to describe the deuteron by a non-local, dispersive potential that is constrained by corresponding elastic scattering data. The proposed approach depends on recognizing that elastic deuteron scattering can be interpreted as the propagation of an interacting proton–neutron pair in the medium provided by the target nucleus [21].

3 $^{40}\text{Ca}(e, e' p)^{39}\text{K}$ Reaction and Spectroscopic Factors

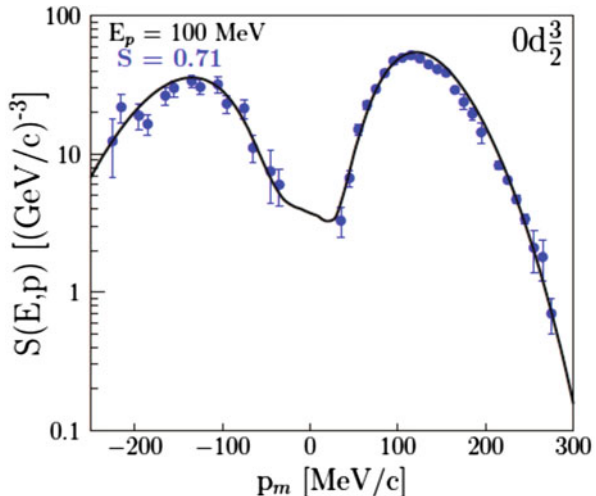
Several papers have appeared in the past questioning the relevance of spectroscopic factors [22, 23] and the possibility of measuring momentum distributions or occupation numbers [24]. It is useful to point out that Fermi liquid theory developed by Landau [25–27] relies on the notion of a quasiparticle with a corresponding strength (spectroscopic factor) near the Fermi surface that can be experimentally probed through specific heat measurements [28]. For finite systems like atoms and molecules the corresponding information is accessed by analyzing the $(e, 2e)$ reaction [2, 29, 30]. Similar efforts in nuclear physics have attempted to extract spectroscopic factors from the $(e, e' p)$ reaction [31] for valence hole states in mostly double-closed-shell nuclei (see also Refs. [2, 32]).

Experimental results of the $(e, e' p)$ reaction have been included in the local DOM in the past by employing the extracted spectroscopic factors [33, 34] in fits with local potentials to the ^{40}Ca and ^{48}Ca nuclei [35, 36] and to data in other domains of the chart of nuclides [15]. A better approach has now been implemented based on the non-local DOM developments [3, 37, 38] that also allows an assessment of the quality of the distorted-wave impulse approximation (DWIA) that is utilized to describe the reaction. We note that the conventional analysis of the reaction employed standard local non-dispersive optical potentials to describe the proton distorted waves [39]. We have thus arrived at a stage with the DOM that all ingredients for the DWIA description can be supplied from one self-energy that generates the proton distorted waves at the desired outgoing energies, as well as the overlap function with its normalization. Important to note is that these ingredients are not adjusted in any way to $(e, e' p)$ data.

The non-local DOM description of ^{40}Ca data was presented in [37]. In the mean time, additional experimental higher-energy proton reaction cross sections [40] have been incorporated which caused some adjustments of the DOM parameters compared to [37]. Adjusting the parameters from the previous values [37] to describe these additional experimental results leads to an equivalent description for all data except these reaction cross sections. The required additional absorption at higher energies leads to a loss of strength below the Fermi energy, reducing the spectroscopic factors by about 0.05 compared to the results reported in [37], thereby also documenting the importance of reaction cross section data for protons at higher energy.

Using a recent version of the code DWEEPY [41], our DOM ingredients have been utilized to describe the knockout of a proton from the $0d_{3/2}$ and $1s_{1/2}$ orbitals in ^{40}Ca with fixed normalizations of 0.71 and 0.60, respectively [42]. The DOM at present generates only one main peak for $1s_{1/2}$ orbit so the employed value of 0.60 for the spectroscopic factor takes into account the experimentally observed low-energy fragmentation. Experimental data were obtained at Nikhef in parallel kinematics for three outgoing proton energies: 100, 70, and 135 MeV. Data for the latter two energies were never published before. The resulting description of the $(e, e' p)$ cross sections is at least as good as the Nikhef analysis which yielded

Fig. 2 Comparison of the spectral distribution measured at Nikhef for outgoing proton energies of 100 MeV to DWIA calculations using the proton distorted waves, overlap function, and its normalization from a non-local DOM parameterization. Results are shown for the knockout of a $0d_{3/2}$ proton from ^{40}Ca to the ground state of ^{39}K



spectroscopic factors of 0.65 ± 0.06 and 0.51 ± 0.05 for these orbits at 100 MeV [33], as illustrated in Fig. 2. Our results demonstrate that the DWIA reaction model is still satisfactory at 70 MeV and 135 MeV outgoing proton energies. By applying the bootstrap method used for the neutron skin calculation of [38], we have generated errors for the spectroscopic factors for these orbits with values 0.71 ± 0.04 and 0.60 ± 0.03 , for the $0d_{3/2}$ and $1s_{1/2}$ orbitals in ^{40}Ca , respectively. The results further suggest that the chosen window around 100 MeV proton energy provides the best and cleanest method to employ the DWIA for the analysis of this reaction.

We therefore make a strong case that the canonical suppression of the spectroscopic factors as pioneered by the Nikhef group [31] continues to generate values of around 0.7 although there are qualitative differences in the construction of the cross sections on account of the non-local potentials that determine the distorted proton waves. Further insight into the claim that the $(e, e'p)$ reaction can yield absolute spectroscopic factors for low-lying discrete states in the final nucleus [32, 43, 44] has therefore been provided, while demonstrating that a consistent description of the reaction ingredients as provided by the non-local DOM is essential.

4 Neutron Distributions and the DOM

The efficacy of the DOM has recently been documented when its fully non-local implementation was extended to ^{48}Ca . Available ground-state properties of ^{48}Ca appropriate for a study of the properties in this system, apart from the important particle numbers of $Z = 20$ and $N = 28$, include the charge density in addition to level structure. These properties on top of the standard elastic scattering data available at positive energy have been employed to construct the $N - Z$ dependence

of the DOM potential leaving all ingredients of the fit to ^{40}Ca fixed except for radius parameters. Excellent agreement with the experimental charge density has been obtained [38] just as earlier for ^{40}Ca [37].

Recently acquired elastic neutron scattering data and total cross sections for ^{48}Ca were published earlier in our large DOM paper [15] but it was at that time not possible to generate an accurate fit to the differential cross sections at low energy employing the local implementation of the DOM. Our current non-local DOM potentials provide increased flexibility that allows for the present excellent fit to these data. Most of the properties of the first 20 neutrons in this nucleus are already well-constrained by the fit to the properties of ^{40}Ca . The additional influence of the extra 8 neutrons in this nucleus is then further constrained by these elastic scattering data and total neutron cross sections [15] as well as level structure. The neutron properties of ^{48}Ca are of extreme interest to the community since the neutron radius can be experimentally probed without ambiguity employing parity-violating elastic electron scattering experiments at Jefferson Lab [45].

To produce a theoretical error for our result for the neutron skin we have employed a method that was explored in the determination of the Chapel-Hill global optical potential [46]. These results have now been published in [38] with our neutron skin prediction of 0.249 ± 0.023 fm which is much larger than the prediction of the ab initio coupled-cluster calculation reported in [47] and most mean-field calculations [48]. We note that this work fulfills the earlier promise of the DOM, in that it can be employed to make sensible predictions of important quantities constrained by other experimental data. When envisaged earlier [35], it was thought that these predictions would involve only rare isotopes but important quantities for stable nuclei also fall under its scope. We show in Fig. 3 results for the neutron skin of ^{48}Ca plotted versus the one of ^{208}Pb as presented in [48], while adding horizontal bars for the DOM result [38] and the coupled-cluster result of [47]. Our current efforts for ^{208}Pb are also generating a large neutron skin as indicated by the large square in Fig. 3. The dashed box includes the central value of [49] but with the expected error of the PREX-II experiment. The expected error for the CREX experiment [45] is indicated by the vertical width of the box while its central value is arbitrarily chosen.

5 Conclusions

As illustrated in this paper, the DOM provides ingredients for transfer reactions, the $(e, e'p)$ reaction, and predictions for the neutron skin of ^{48}Ca and ^{208}Pb , demonstrating the relevance of this approach to simultaneously answer the questions how nucleons propagate through the nucleus at positive energy and where they are localized in the ground state. Extensions to other knockout reactions like (p, pN) and the improved description of the deuteron will likely contribute to a robust extension of the DOM to rare isotopes.

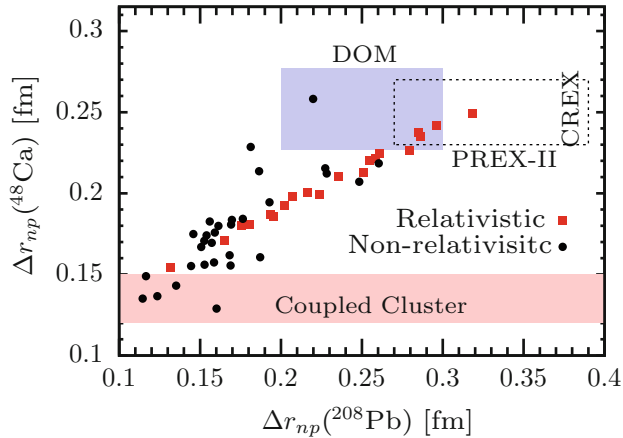


Fig. 3 Figure adapted from [48] with the results from Refs. [47] and [38] indicated by horizontal bars relevant for ^{48}Ca and the rectangle including the preliminary DOM result for ^{208}Pb . Smaller squares and circles refer to relativistic and nonrelativistic mean-field calculations cited in Ref. [48]

Acknowledgments This work was supported by the U.S. National Science Foundation under grant PHY-1613362 and contains critical contributions of Hossein Mahzoon and Mack Atkinson as part of their thesis research. Contributions of other collaborators are also gratefully acknowledged.

References

1. W.H. Dickhoff, C. Barbieri, *Prog. Part. Nucl. Phys.* **52**, 377 (2004)
2. W.H. Dickhoff, D. Van Neck, *Many-Body Theory Exposed!*, 2nd edn. (World Scientific, New Jersey, 2008)
3. W.H. Dickhoff, R.J. Charity, M.H. Mahzoon, *J. Phys. G: Nucl. Part. Phys.* **44**, 033001 (2017)
4. C. Mahaux, R. Sartor, *Adv. Nucl. Phys.* **20**, 1 (1991)
5. W.H. Dickhoff, R.J. Charity, *Prog. Part. Nucl. Phys.* **105**, 252 (2019)
6. N.B. Nguyen, S.J. Waldecker, F.M. Nunes, R.J. Charity, W.H. Dickhoff, *Phys. Rev. C* **84**, 044611 (2011)
7. A. Ross, L.J. Titus, F.M. Nunes, M.H. Mahzoon, W.H. Dickhoff, R.J. Charity, *Phys. Rev. C* **92**, 044607 (2015)
8. D.W. Bardayan, *J. Phys. G* **43**, 043001 (2016)
9. K. Wimmer, *J. Phys. G* **45**, 033002 (2018)
10. J.E. Escher, et al., *Rev. Mod. Phys.* **84**, 353 (2012)
11. G. Potel, F.M. Nunes, I.J. Thompson, *Phys. Rev. C* **92**, 034611 (2015)
12. J. Lei, A.M. Moro, *Phys. Rev. C* **92**, 061602(R) (2015)
13. B.V. Carlson, R. Capote, M. Sin. arXiv:1508.01466 (2015)
14. Deuteron-induced reactions and beyond: Inclusive breakup fragment cross sections FRIB workshop (2016). <https://indico.fnal.gov/conferenceDisplay.py?confid=11559>
15. J.M. Mueller et al., *Phys. Rev. C* **83**, 064605 (2011)
16. G. Potel, et al., *Eur. Phys. J. A* **53**(9), 178 (2017)
17. A. Koning, J. Delaroche, *Nucl. Phys. A* **713**, 231 (2003)
18. H. An, C. Cai, *Phys. Rev. C* **73**, 054605 (2006)

19. Y. Han, Y. Shi, Q. Shen, Phys. Rev. C **74**, 044615 (2006)
20. Y. Zhang, D.Y. Pang, J.L. Lou, Phys. Rev. C **94**, 014619 (2016)
21. F. Villars, *Fundamentals in Nuclear Theory* (IAEC, Vienna, 1967)
22. A.M. Mukhamedzhanov, A.S. Kadyrov, Phys. Rev. C **82**, 051601(R) (2010)
23. R.J. Furnstahl, A. Schwenk, J. Phys. G **37**, 064005 (2010)
24. R.J. Furnstahl, H.-W. Hammer, Phys. Lett. **B531**, 203 (2002)
25. L.D. Landau, Sov. Phys. JETP **3**, 920 (1957)
26. L.D. Landau, Sov. Phys. JETP **5**, 101 (1957)
27. L.D. Landau, Sov. Phys. JETP **8**, 70 (1959)
28. J.C. Wheatley, Rev. Mod. Phys. **47**, 415 (1975)
29. B. Lohmann, E. Weigold, Phys. Lett. **A86**, 139 (1981)
30. I.E. McCarthy, E. Weigold, Rep. Prog. Phys. **54**, 789 (1991)
31. L. Lapikás, Nucl. Phys. A **553**, 297 (1993)
32. W.H. Dickhoff, D. Van Neck, S.J. Waldecker, R.J. Charity, L.G. Sobotka, Phys. Rev. C **82**(5), 054306 (2010)
33. G.J. Kramer, et al., Phys. Lett. B **227**, 199 (1989)
34. G. Kramer, H. Blok, L. Lapikás, Nucl. Phys. A **679**, 267 (2001)
35. R.J. Charity, L.G. Sobotka, W.H. Dickhoff, Phys. Rev. Lett. **97**, 162503 (2006)
36. R.J. Charity, J.M. Mueller, L.G. Sobotka, W.H. Dickhoff, Phys. Rev. C **76**, 044314 (2007)
37. M.H. Mahzoon, R.J. Charity, W.H. Dickhoff, H. Dussan, S.J. Waldecker, Phys. Rev. Lett. **112**, 162503 (2014)
38. M.H. Mahzoon, M.C. Atkinson, R.J. Charity, W.H. Dickhoff, Phys. Rev. Lett. **119**, 222503 (2017)
39. J.W.A. den Herder et al., Nucl. Phys. **A490**, 507 (1988)
40. A. Auce et al., Phys. Rev. C **71**, 064606 (2005)
41. C. Giusti, F.D. Pacati, Nucl. Phys. **A485**, 461 (1988)
42. M.C. Atkinson, H.P. Blok, L. Lapikás, R.J. Charity, W.H. Dickhoff, Phys. Rev. C **98**, 044627 (2018)
43. I. Sick, P.K.A. de Witt Huberts, Commun. Nucl. Part. Phys. **20**, 177 (1991)
44. V.R. Pandharipande, I. Sick, P.K.A. de Witt Huberts, Rev. Mod. Phys. **69**, 981 (1997)
45. J. Mammei et al. CREX: parity-violating measurement of the weak charge distribution of ^{48}Ca to 0.02 fm accuracy (2013). <http://hallaweb.jlab.org/parity/prex/>
46. R.L. Varner, W.J. Thompson, T.L. McAbee, E.J. Ludwig, T.B. Clegg, Phys. Rep. **201**, 57 (1991)
47. G. Hagen et al., Nat. Phys. **12**, 186 (2016)
48. C.J. Horowitz, K.S. Kumar, R. Michaels, Eur. Phys. J. A **50**, 48 (2014)
49. S. Abrahamyan et al., Phys. Rev. Lett. **108**, 112502 (2012)

Microscopic Optical Potential from Chiral Effective Field Theory



T. R. Whitehead, Y. Lim, and J. W. Holt

1 Chiral Nuclear Optical Model Potentials

Optical model potentials are widely used to predict nucleon–nucleus scattering cross sections and reaction observables by replacing the complicated many-body system of nucleons interacting through two- and three-body forces with an average complex and energy-dependent single-particle potential. Phenomenological models [1] fitted to experimental data are very successful at describing scattering processes for nuclei near stability, but high-quality microscopic optical potentials may be more reliable for reactions involving exotic isotopes for which experimental data are scarce. Recently, microscopic optical potentials in homogeneous nuclear matter have been constructed [2, 3] based on realistic chiral two- and three-body forces. The aim of the present work is to extend this description to the case of finite nuclei, with a special focus on proton elastic scattering off calcium isotopes.

In quantum many-body theory, the nuclear optical potential is identified with the nucleon self-energy. We begin by computing the nucleon self-energy in infinite homogeneous nuclear matter at a given density and isospin asymmetry starting from a realistic chiral nuclear interaction [4] with momentum-space cutoff $\Lambda = 450$ MeV. The real and imaginary central terms of the optical potential arise naturally when the nucleon self-energy is computed to second order in many-body perturbation theory. The real spin–orbit term cannot be extracted from nuclear matter calculations and in the present work is instead calculated from the Negele–Vautherin density matrix expansion [5] using the same chiral potential. The density-dependent optical

T. R. Whitehead (✉) · Y. Lim · J. W. Holt
Cyclotron Institute, Texas A&M University, College Station, TX, USA

Department of Physics and Astronomy, Texas A&M University, College Station, TX, USA
e-mail: twhitehead@tamu.edu

potential is then folded with the relevant nuclear density distribution for the isotope under investigation, calculated using a Skyrme effective interaction fitted to the nuclear equation of state derived from the same chiral potential. The result is an energy-dependent nucleon–nucleus optical potential in position space. This local density approximation (LDA) [6] is known to give a poor description of the optical potential surface diffuseness, and therefore in the present work we employ an improved local density approximation (ILDAs) that accounts for the non-zero range of the nuclear force:

$$U(E, r)_{ILDA} = \frac{1}{(t\sqrt{\pi})^3} \int U(E, r') e^{-\frac{|r-r'|^2}{t^2}} d^3r', \quad (1)$$

where t is a distance scale associated with the average range of the nucleon–nucleon interaction. In the present study we vary t within the range $1.15 \text{ fm} < t < 1.25 \text{ fm}$.

2 Results

We have implemented the nuclear optical potentials described above in the TALYS reaction code [7]. In the top two rows of Fig. 1 we plot the proton–nucleus differential elastic scattering cross sections at the two energies $E = 25, 45 \text{ MeV}$ for the isotopes ^{40}Ca , ^{44}Ca , and ^{48}Ca . Experimental data are shown as the red points, while the results from the microscopic optical potentials are shown with the blue band. The uncertainties giving rise to the theoretical error band are obtained by varying the ILDA range parameters for both the central and spin–orbit components. In the future we plan to estimate also the uncertainties arising from the choice of chiral potential by varying the momentum-space cutoff, the order in the chiral expansion, and the regulating function. We also show in the top two rows of Fig. 1 the results (green curves) from the Koning–Delaroche phenomenological optical potential as it is implemented in the TALYS reaction code. We see that the microscopic optical potentials from chiral effective field theory give an overall reasonable description of the elastic scattering cross section within the chosen energy regime. However, at higher energies and larger scattering angles, the description starts to deteriorate.

Comparing the real and imaginary components of the microscopic optical potential to those from phenomenology, we find excellent agreement in the real part but the microscopic imaginary optical potential is too strongly absorptive. This feature is ubiquitous in nuclear matter optical potential calculations and is the reason why semi-microscopic optical potentials used today implement energy-dependent strength factors [8]. To test this, we show in the bottom two rows of Fig. 1, the results from our microscopic optical potentials for which the imaginary part has been replaced by that from the KD optical potential. We see that this replacement dramatically improves the differential elastic scattering cross sections across all energies and target isotopes. In the future we plan to investigate higher-order perturbative contributions to the self-energy and their effect on the imaginary part of the optical potential.

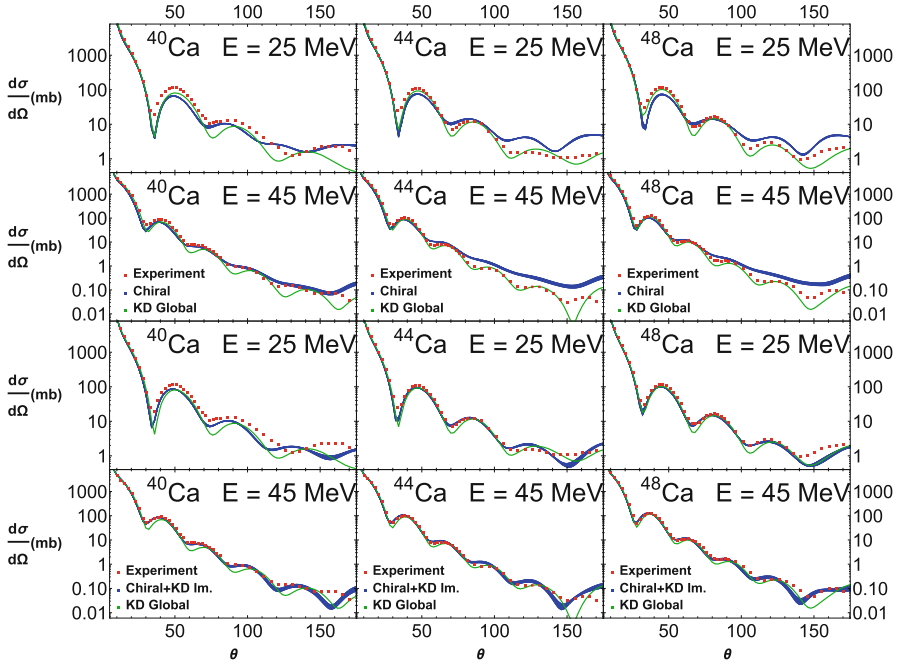


Fig. 1 Differential elastic scattering cross sections for proton–nucleus scattering at incident energies $E = 25, 45$ MeV. We show results from microscopic chiral nuclear forces (blue), the phenomenological Koning–Delaroche (KD) optical potential (green), and experimental data (red). In the bottom two rows, we have replaced the microscopic imaginary part with the phenomenological imaginary part of the KD optical potential

The work is supported by the U.S. Department of Energy National Nuclear Security Administration under Grant No. DE-NA0003841 and by the National Science Foundation under Grant No. PHY1652199.

References

1. A.J. Koning, J. P. Delaroche, Nucl. Phys. A **713**, 231 (2003)
2. J.W. Holt, N. Kaiser, G.A. Miller, W. Weise, Phys. Rev. C **88**, 024614 (2013)
3. J.W. Holt, N. Kaiser, G.A. Miller, Phys. Rev. C **93**, 064603 (2016)
4. L. Coraggio, J.W. Holt, N. Itaco, R. Machleidt, L.E. Marcucci, F. Sammarruca, Phys. Rev. C **89**, 044321 (2014)
5. J.W. Holt, N. Kaiser, W. Weise, Eur. Phys. J. A **47** (2011)
6. J.P. Jeukenne, A. Lejeune, C. Mahaux, Phys. Rev. C **16**, 80 (1977)
7. A.J. Koning, S. Hilaire, M.C. Duijvestijn, in *Proceedings of the International Conference on Nuclear Data for Science and Technology* (EDP Sciences, Les Ulis, 2008)
8. S. Goriely, J.-P. Delaroche, Phys. Lett. **B653**, 178 (2007)

Part IV
Level Densities

Nuclear Level Densities: From Empirical Models to Microscopic Methods



Y. Alhassid

1 Introduction

The nuclear level density is among the most important statistical nuclear properties. It appears in Fermi's golden rule for transition rates. Along with gamma strength functions, it is a required input to the Hauser–Feshbach theory [1] of compound nuclear reactions. The excited compound nucleus can decay into various channels, and its decay rate in any given channel is proportional to the available phase space, i.e., the corresponding level density of the residual nucleus. The level density has many applications in diverse areas such as stellar nucleosynthesis and nuclear reactor technology.

The state density at total energy E is defined as the number of states per unit energy

$$\rho(E) = \text{Tr} \delta(E - \hat{H}), \quad (1)$$

where \hat{H} is the system's Hamiltonian. For a system with discrete energy levels E_i , the state density $\rho(E) = \sum_i \delta(E - E_i)$ is singular. Usually we are interested in a smoothed version of this density, i.e., the average state density.

While qualitative features of level densities can be understood by simple models, a quantitative understanding presents a major challenge, in particular in the presence of correlations beyond the mean-field approximation.

Y. Alhassid (✉)

Center for Theoretical Physics, Sloane Physics Laboratory, Yale University, New Haven, CT, USA

e-mail: yoram.alhassid@yale.edu

<https://alhassidgroup.yale.edu>

© This is a U.S. government work and not under copyright protection in the U.S.; foreign copyright protection may apply 2021

J. Escher et al. (eds.), *Compound-Nuclear Reactions*, Springer Proceedings in Physics 254, https://doi.org/10.1007/978-3-030-58082-7_12

The outline of this brief review is as follows. In Sect. 2 we discuss the thermodynamics approach for calculating level densities, which is based on calculation of the nuclear partition function at finite temperature. In Sect. 3 we discuss the level density of non-interacting fermions, known as the Fermi gas level density, and simple models for the spin and parity distributions. In Sect. 4 we summarize experimental methods used to measure level densities. In Sect. 5 we review the main empirical models for level densities, namely, the back-shifted Fermi gas model, the constant-temperature formula and the composite (Gilbert–Cameron) formula. We then describe the major microscopic approaches for calculating level densities. In Sect. 6 we discuss the mean-field approximation and the combinatorial method. Methods based on the configuration-interaction (CI) shell model that take into account correlations beyond the mean field are discussed in Sects. 7.1 and 7.2. In Sect. 7.1 we discuss spectral averaging theory, which is based on the calculation of moments of the Hamiltonian. In Sect. 7.2 we review the auxiliary-field quantum Monte Carlo (AFMC) method for calculating level densities and its applications.

2 Thermodynamics Approach

2.1 Canonical Ensemble

We assume the nucleus to be in contact with a heat reservoir at temperature T , in which case its equilibrium configuration is described by the canonical Gibbs ensemble $e^{-\beta\hat{H}}$, where $\beta = 1/T$ is the inverse temperature and \hat{H} is the Hamiltonian.

The partition function $Z(\beta) = \text{Tr} e^{-\beta\hat{H}}$ is the Laplace transform of the state density $\rho(E)$, i.e., $Z(\beta) = \int_0^\infty dE e^{-\beta E} \rho(E)$. The level density is then the inverse Laplace transform of the partition function

$$\rho(E) = \frac{1}{2\pi i} \int_{-i\infty}^{i\infty} d\beta e^{\beta E} Z(\beta). \quad (2)$$

The inverse Laplace transform is numerically ill-defined. It can be evaluated in the saddle-point approximation and provides the average level density [2]

$$\rho(E) \approx (2\pi T^2 C)^{-1/2} e^{S(E)}, \quad (3)$$

where $S(E)$ is the canonical entropy and C is the canonical heat capacity given by

$$S = \ln Z + \beta E ; \quad C = \frac{dE}{dT}. \quad (4)$$

The value of β used in Eqs. (3) and (4) is determined as a function of E by the saddle-point condition

$$E = -\frac{\partial \ln Z}{\partial \beta} = E(\beta). \quad (5)$$

2.2 Grand-Canonical Ensemble

A similar thermodynamic approach can be followed in the grand-canonical ensemble, for which the number of particles fluctuates and only its average value is fixed. The state density at energy E and particle number A are now given by a double inverse Laplace transform of the grand-canonical partition $Z_{\text{gc}}(\beta, \alpha) = \text{Tr} e^{-\beta H + \alpha \hat{A}}$ (the parameter α is related to the chemical potential μ by $\alpha = \beta\mu$). In the saddle-point approximation we find [2, 3]

$$\rho(E, A) \approx \frac{1}{2\pi \sqrt{-\det D}} e^{S(E, A)}, \quad (6)$$

where $S = \ln Z_{\text{gc}} + \beta E - \alpha A$ is the entropy, and D is the 2×2 matrix of second partial derivatives of $\ln Z_{\text{gc}}$ with respect to β and α . The values of β and α are determined as a function of E and A from the saddle-point equations

$$-\frac{\partial \ln Z_{\text{gc}}}{\partial \beta} = E, \quad \frac{\partial \ln Z_{\text{gc}}}{\partial \alpha} = A. \quad (7)$$

3 Non-interacting (Fermi Gas) Models

For non-interacting fermions, it is easier to use the grand-canonical formalism of Sect. 2.2.

We first consider one type of nucleons. The logarithm of the many-particle grand-canonical partition function for non-interacting fermions is

$$\ln Z_{\text{gc}} = \int_0^\infty d\varepsilon g(\varepsilon) \ln \left[1 + e^{-\beta(\varepsilon - \mu)} \right], \quad (8)$$

where $g(\varepsilon)$ is the single-particle density of states.

The thermal energy can be calculated as a function of temperature using the low-temperature expansion of Sommerfeld [4] for temperature $T \ll T_F$ (where T_F is the Fermi temperature). To second order in T

$$E = E_0 + aT^2, \quad (9)$$

where E_0 is the ground-state energy and $a = \frac{\pi^2}{6}g(\epsilon_F)$ (ϵ_F is the Fermi energy, i.e., the energy of highest occupied single-particle level).

The corresponding heat capacity is $C = dE/dT = 2aT$. Using $C = TdS/dT$, we determine the entropy to be $S = 2aT = 2\sqrt{aE_x}$, where $E_x = E - E_0$ is the excitation energy. The saddle-point approximation (6) then leads to Bethe's formula for one type of nucleons [5]

$$\rho(E_x) = \frac{1}{\sqrt{48E_x}} e^{2\sqrt{aE_x}}. \quad (10)$$

A similar derivation for both protons and neutrons with $Z \approx N$ gives [2]

$$\rho(E_x) = \frac{\sqrt{\pi}}{12} a^{-1/4} E_x^{-5/4} e^{2\sqrt{aE_x}}, \quad (11)$$

where $a = \frac{\pi^2}{6}[g_p(\epsilon_F^{(p)}) + g_n(\epsilon_F^{(n)})]$. For $Z \neq N$, the state density is given by an equation similar to Eq. (11) but contains an additional factor of $g/(2\sqrt{g_p g_n})$ on its r.h.s. (which is of order unity).

In the free Fermi gas model, assuming A nucleons in a box, $a = \frac{\pi^2 A}{4\epsilon_F} \approx A/15 \text{ MeV}^{-1}$. A more realistic estimate is obtained for an isotropic harmonic oscillator potential, for which $a \approx A/10 \text{ MeV}^{-1}$. Using a Woods–Saxon potential, it was found that $a \approx A/10.7 \text{ MeV}^{-1}$ in medium-mass nuclei [6].

3.1 Spin-Cutoff Model

The spin-cutoff model assumes random coupling of single-particle spins [3, 7]. In this model, the distribution of the spin projection $M = \sum_i m_i$ is Gaussian

$$\frac{\rho_M}{\rho} = \frac{1}{\sqrt{2\pi}\sigma} e^{-M^2/2\sigma^2}, \quad (12)$$

where σ is the spin-cutoff parameter. Using the equipartition theorem at temperature T , we find

$$\sigma^2 = \frac{IT}{\hbar^2}, \quad (13)$$

with I being the thermal moment of inertia. At higher excitation energies, I approaches its rigid-body value [2], but it decreases at low excitation energies because of pairing correlations.

The spin distribution is calculated from

$$\rho_J = \rho_{M=J} - \rho_{M=J+1} \approx - \left. \frac{d\rho_M}{dM} \right|_{M=J+1/2}. \quad (14)$$

Using Eq. (12), we find for the spin-cutoff model

$$\frac{\rho_J}{\rho} = \frac{2J+1}{2\sqrt{2\pi}\sigma^3} e^{-J(J+1)/2\sigma^2}. \quad (15)$$

3.2 Parity Distribution

A simple model for the parity distribution of level densities is obtained by assuming the particles occupy the single-particle states independently and randomly [3]. We divide the single-particle levels into two groups of positive and negative parities, and denote by π the parity of the group with the smaller occupation probability p_π . The probability to have n particles in this group is then a binomial distribution

$$P(n) = \binom{A}{n} p_\pi^n (1 - p_\pi)^{A-n}, \quad (16)$$

where A is the total number of excited particles. For an even-particle system, a negative (positive) parity many-particle state corresponds to odd (even) values of n , and the total probability to have a negative (positive) parity is obtained by summing $P(n)$ over all odd (even) values of n . For small p_π and large A , we can approximate (16) by a Poisson distribution $f_\pi = \frac{f^n}{n!} e^{-f}$, which depends on a single parameter $f = Ap_\pi$, the total occupation of the π -parity orbitals. For an even-particle system, the ratio of negative- to positive-parity partition functions at a given temperature is then given by Alhassid et al. [8]

$$\frac{Z_-}{Z_+} = \sum_{n \text{ odd}} P(n) / \sum_{n \text{ even}} P(n) = \tanh f. \quad (17)$$

Equation (17) holds more generally for an even-even nucleus with $f = f_p + f_n$ being the total average occupation of the π -parity orbitals for both protons and neutrons. For an even-even nucleus, the positive-parity states dominate at low excitations, but equilibration of both parities is achieved above a certain excitation energy. In practical applications, it is often assumed that the parity distribution is already equilibrated at the neutron resonance energy.

4 Experimental Methods

The measurement of level densities is a challenging task. There are several methods but all have systematic uncertainties and are limited to certain energy regimes:

- Level counting at low excitation energies. This requires the knowledge of a complete set of measured energy levels [9].
- Neutron and proton resonance data [10] provide an estimate of the level density at the neutron or proton threshold energy. The measured resonance level spacing (usually s wave and sometimes also p wave) provides the level density at certain values of the spin/parity determined by the selection rules. The conversion to total densities requires a model for the spin distribution, and often a spin-cutoff model with rigid-body moment of inertia is used.
- Particle evaporation spectra [11], which depend on the level density through the Hauser–Feshbach formalism [1]. This method requires the knowledge of particle transmission coefficients, which can be calculated from optical potential models.
- The “Oslo method” which uses the measured particle and γ -ray coincidence matrix [12]. The extraction of level densities in this method requires the knowledge of level counting data at low energies and neutron resonance data.

Progress has often been achieved by combining several of these methods.

5 Empirical Models

Several phenomenological models have been introduced to describe level densities in the presence of correlations.

5.1 Back-Shifted Fermi Gas Formula

Pairing correlations and shell effects are empirically taken into account in Bethe’s formula by shifting the ground-state energy by a back-shift parameter Δ

$$\rho(E_x) = \frac{\sqrt{\pi}}{12} a^{-1/4} (E_x - \Delta)^{-5/4} e^{2\sqrt{a(E_x - \Delta)}}. \quad (18)$$

This back-shifted Bethe formula for the state density includes two parameters a and Δ that can be treated as adjustable parameters. They can for example be determined from level counting data at low excitation energies and neutron resonance data [13, 14].

In the state density, each level with spin J is counted $2J + 1$ times (i.e., the magnetic degeneracy is included). The level density is defined by counting only once each level with spin J . Assuming a spin-cutoff model (15), the level density $\tilde{\rho}$ is related to the state density ρ by

$$\tilde{\rho}(E_x) = \sum_J \rho(E_x, J) = \frac{\rho(E_x)}{\sqrt{2\pi\sigma}}. \quad (19)$$

Global fits using an energy-dependent parameter a that includes shell effects were carried out in Ref. [15].

5.2 Constant-Temperature Formula

At low excitation energies it is found empirically that the level density $\tilde{\rho}$ is well described by an exponential function

$$\tilde{\rho}(E_x) = \frac{1}{T_1} e^{(E_x - E_1)/T_1} \quad (20)$$

where E_1 and T_1 are parameters. T_1 can be interpreted as an effective temperature

$$T_1^{-1} = d \ln \tilde{\rho}(E_x) / dE_x. \quad (21)$$

5.3 Composite (Gilbert–Cameron) Formula

The composite formula for the level density, also known as Gilbert–Cameron formula [16], is a constant-temperature formula (20) at low energies and a back-shifted Fermi gas formula (19) and (18) at higher excitations. Both the level density and its first derivative are matched at a certain excitation energy E_M , so overall the composite formula has only two adjustable parameters.

6 Mean-Field and Combinatorial Methods

6.1 Mean-Field Methods

Hartree–Fock (HF) mean-field theory using Skyrme interactions plus finite-temperature BCS has been applied in Ref. [17] to the large number of nuclei that are involved in nucleosynthesis.

A mean-field theory provides the intrinsic level density $\rho_{\text{int}}(E_x)$. It has to be augmented by collective enhancement factors (vibrational and rotational)

$$\rho(E_x) = K_{\text{vib}}(E_x)K_{\text{rot}}(E_x)\rho_{\text{int}}(E_x), \quad (22)$$

where the factors $K_{\text{vib}}(E_x)$ and $K_{\text{rot}}(E_x)$ describe the enhancement of the density due to vibrational and rotational collective states. The energy dependence of these factors, and in particular, their decay with excitation energy E_x , is one of the least understood issues in studies of level densities, and are usually parameterized by phenomenological expressions [18].

6.2 Combinatorial Methods

The combinatorial models are based on counting the number of ways to distribute the nucleons among single-particle levels at a given total excitation energy [19–22]. They are often combined with a mean-field theory such as the Hartree–Fock–Bogoliubov (HFB) approximation. Examples of cumulative level densities calculated in the mean-field plus combinatorial approach are shown in Fig. 1.

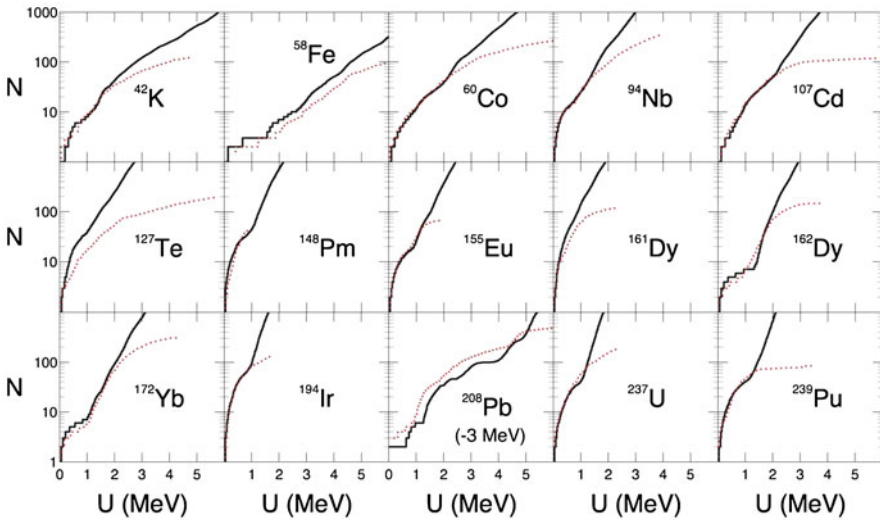


Fig. 1 Cumulative level densities calculated in the combinatorial approach (solid histograms) are compared with cumulative number of observed levels (dotted histograms) at low excitation energy U . Adapted from Ref. [19]

7 Configuration-Interaction Shell Model Methods

The CI shell model includes shell effects and correlations beyond the mean-field approximation, and thus can in principle provide the most precise microscopic calculation of level densities. However, the combinatorial growth of the dimensionality of the many-particle model space with the number of valence nucleons and/or the number of valence orbitals has hindered its application in mid-mass and heavy nuclei.

7.1 Spectral Averaging Theory (Moment Method)

The spectral averaging theory, also known as the moment method, describes the density as a superposition of Gaussian densities for various partitions of the single-particle orbitals with centroids and widths that are determined by the first two moments of the Hamiltonian [23–26].

The method requires a reliable calculation of the ground-state energy, which is required for determining the excitation energy. The calculation of second moments is time consuming in large model spaces, and so far the method has been applied to light and mid-mass nuclei, where it provides good agreement with experimental data and with exact CI shell model calculations (in *sd*-shell nuclei) [27]. For more details of the method and its applications see Refs. [28, 29].

7.2 Auxiliary-Field Quantum Monte Carlo Method

The auxiliary-field quantum Monte Carlo (AFMC) method, also known in nuclear physics as the shell model Monte Carlo (SMMC) [30–34], is based on the Hubbard–Stratonovich (HS) transformation [35], in which Gibbs ensemble $e^{-\beta\hat{H}}$ is written as a superposition of ensembles \hat{U}_σ describing non-interacting nucleons moving in external auxiliary fields $\sigma(\tau)$

$$e^{-\beta\hat{H}} = \int \mathcal{D}[\sigma] G_\sigma \hat{U}_\sigma, \quad (23)$$

where G_σ is a Gaussian weight. The calculation of the integrand for a given configuration of the auxiliary fields σ reduces to matrix algebra in the single-particle space of typical dimension ~ 50 – 100 . The integration over the large number of auxiliary fields is carried out using Monte Carlo methods.

The AFMC state density is calculated using the thermodynamic approach of Sect. 2.1 [36–38]. The canonical thermal energy $E(\beta)$ is calculated as a function

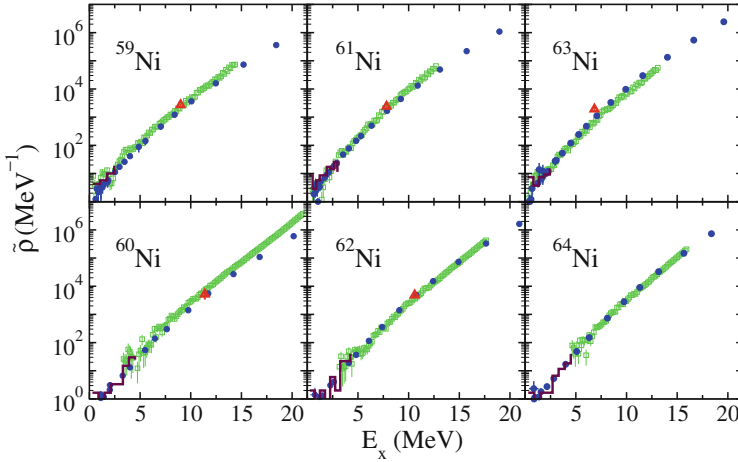


Fig. 2 Level densities of $^{59-64}\text{Ni}$ isotopes versus excitation energy E_x . The AFMC level densities (blue circles) are compared with level densities determined by proton evaporation experiments (green symbols) [45], neutron resonance data when available (red triangles), and level counting data at low excitation energies (blue histograms). Taken from Ref. [43]

of β and Eq. (5) is integrated to find the partition function $Z(\beta)$. The entropy and heat capacity are calculated from Eqs. (4), and the average state density is then given by Eq. (3).

7.2.1 Mid-mass Nuclei

AFMC methods were applied to mid-mass nuclei using the complete $fp_{g9/2}$ shell [36, 39–41]. The single-particle levels and orbitals are taken from a Woods–Saxon potential with spin–orbit interaction. The two-body interaction includes the dominating components [42] of effective nuclear interactions: monopole pairing and multipole–multipole interactions with quadrupole, octupole, and hexadecapole components.

AFMC level densities of nickel isotopes $^{59-64}\text{Ni}$ are shown by the blue circles in Fig. 2 [43]. These densities do not include the magnetic degeneracy $2J + 1$ of each level with spin J and are obtained by projection on $M = 0$ for even-mass nuclei and $M = 1/2$ for odd-mass nuclei [44]. The AFMC densities are in excellent agreement with experimental data without any adjustable parameters.

7.2.2 Heavy Nuclei: The Lanthanides

The AFMC approach was extended to the proton–neutron formalism, in which protons and neutrons can occupy different shells [46]. This formulation was used

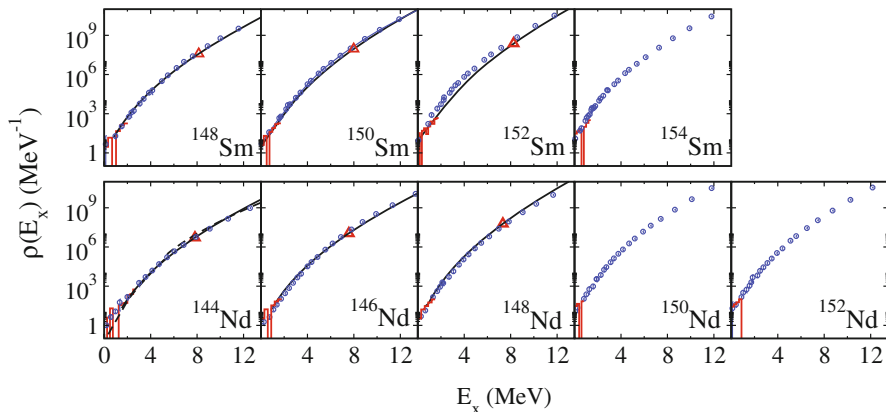


Fig. 3 State densities in even-mass samarium and neodymium isotopes vs. excitation energy E_x . The AFMC densities (blue circles) are compared with level counting data (histograms) at low excitation energies, and with neutron resonance data (triangles) when available. Adapted from Refs. [47, 48]

to study chains of samarium and neodymium isotopes which exhibit a crossover from vibrational to rotational collectivity as a function of the number of neutrons. The corresponding CI shell model space includes the complete 50–82 shell plus $1f_{7/2}$ orbital for protons, and the complete 82–126 shell plus the $0h_{11/2}$ and $1g_{9/2}$ orbitals for neutrons.

Figure 3 shows AFMC state densities (open circles) for chains of samarium and neodymium isotopes [47, 48]. Good agreement is seen with experimental data.

7.2.3 Rotational Enhancement in Deformed Nuclei

Finite-temperature mean-field approximations to level densities were benchmarked in Ref. [49] against exact AFMC results. The mean-field approximation is formulated in the grand-canonical ensemble, and it is necessary to project on fixed number of protons and neutrons to compare with the canonical AFMC results. Particle-number projection was carried out using various approximations (including the saddle-point approximation) and by exact projection after variation [50].

In Fig. 4, the mean-field HF level density of a deformed nucleus ^{162}Dy is compared with the AFMC density. The HF describes the intrinsic states, and thus the enhancement of the exact AFMC density (compared with HF density) is due to rotational bands that are built on top of the intrinsic bandheads. The corresponding rotational enhancement factor decays to 1 in the vicinity of the mean-field shape transition ($E_x \sim 30$ MeV) from a deformed to a spherical shape.

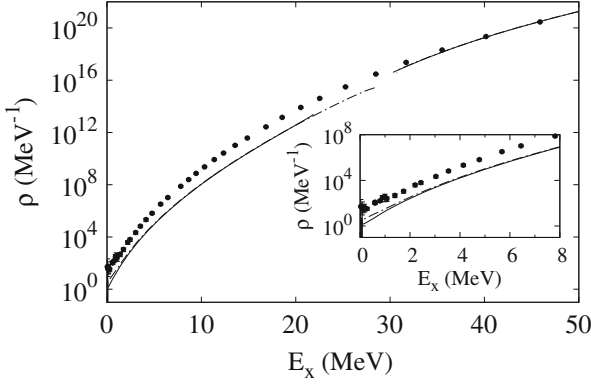


Fig. 4 State density of ^{162}Dy vs. excitation energy E_x . The AFMC state density (solid circles) is compared with the HF density (solid line). The inset shows the low excitation energy region. Taken from Ref. [49]

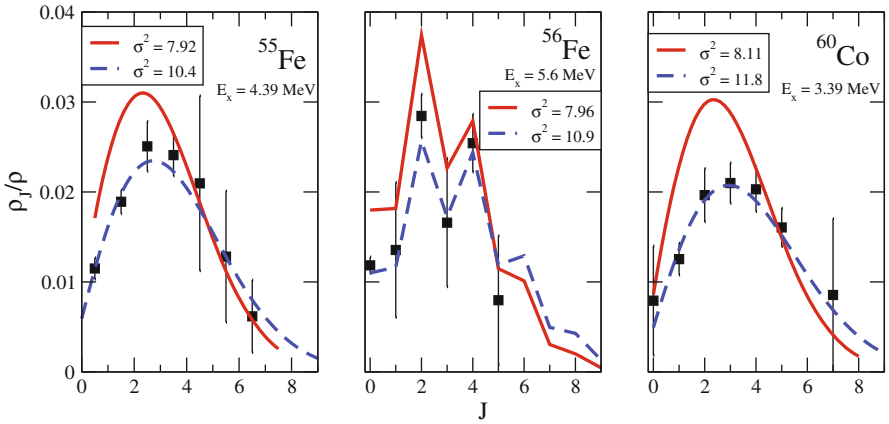


Fig. 5 Spin distributions ρ_J/ρ versus J for ^{55}Fe , ^{56}Fe , and ^{60}Co . The solid squares are the AFMC results of Ref. [40], and the solid lines are empirical distributions [51, 52]. The dashed lines are obtained from the solid lines by scaling the spin-cutoff parameter σ to larger values, taking into account the larger excitation energies used in the AFMC calculations. Taken from Ref. [51]

7.2.4 Spin and Parity Distributions

Exact spin projection was implemented in AFMC and used to calculate the spin distributions in mid-mass nuclei [40]. It was found that the spin-cutoff model works well except at low excitation energies in even–even nuclei for which a staggering effect in spin was observed.

Figure 5 shows spin distributions ρ_J/ρ as a function of spin J for the odd–even nucleus ^{55}Fe , the even–even nucleus ^{56}Fe , and the odd–odd nucleus ^{60}Co . AFMC

results are compared with empirical distributions determined from the analysis of complete sets of experimentally known nuclear energy levels [51, 52]. A staggering effect in spin can be seen in ^{56}Fe .

The spin-cutoff parameter can be related to the thermal moment of inertia through Eq. (13). For even–even nuclei, the moment of inertia is found to be suppressed below the pairing transition [40, 44].

Exact parity projection was also implemented in AFMC [8, 36]. The resulting parity distributions in mid-mass nuclei were found to be well described by Eq. (17) when, below the pairing transition temperature, f is taken to be the average occupation of the quasi-particle states with parity π .

7.2.5 The Deformation Dependence of Level Densities

Modeling of shape dynamics, e.g., fission, requires knowledge of the level density as a function of intrinsic deformation. The theory of deformation has mostly relied on mean-field approximation that breaks rotational invariance.

In Ref. [53] a model-independent method was developed to calculate distributions of intrinsic deformation within the rotationally invariant framework of the CI shell model without invoking a mean-field approximation. The method uses a projection on the axial quadrupole operator in the laboratory frame [54, 55], and is based on a Landau-like expansion of the logarithm of the quadrupole shape distribution in quadrupole invariants [56, 57] up to fourth order. We note that this expansion is similar to the Landau expansion of the free energy used to describe shape transitions in nuclei with the quadrupole deformation playing the role of the order parameter [58, 59].

The method of Ref. [53] enables the calculation of shape-dependent state densities $\rho(E_x, \beta, \gamma)$ as a function of excitation energy E_x and intrinsic quadrupole deformation parameters β, γ . To facilitate the presentation of the shape-dependent densities, the $\beta - \gamma$ plane is divided into three regions: spherical, prolate, and oblate as shown in Fig. 6, and $\rho(E_x, \beta, \gamma)$ is integrated over each one of these regions using the metric $4\pi^2\beta^4|\sin 3\gamma|d\beta d\gamma$ to obtain $\rho_{\text{shape}}(E_x)$. In Fig. 7, the fraction $\rho_{\text{shape}}(E_x)/\rho(E_x)$ of the state density in each of these three regions is shown as a function of excitation energy for spherical (^{148}Sm), transitional (^{150}Sm), and deformed ($^{152}\text{Sm}, ^{154}\text{Sm}$) nuclei.

As is seen in Fig. 7, the spherical region dominates the state density in ^{148}Sm . In the deformed ^{152}Sm and ^{154}Sm nuclei, the prolate region dominates the state density at lower excitation energies but the spherical density becomes comparable and exceeds the prolate density at higher excitations where a shape transition occurs in the mean-field approximation.

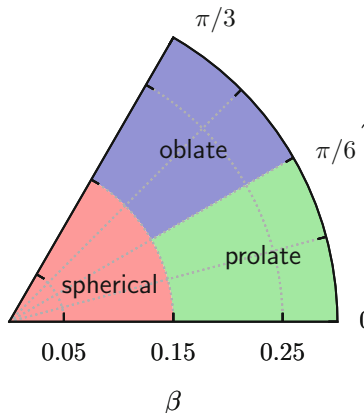


Fig. 6 Three shape regions in the $\beta - \gamma$ plane of intrinsic quadrupole deformation. Taken from Ref. [53]

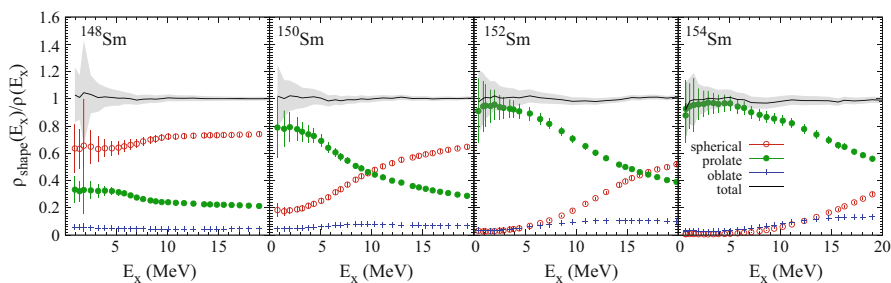


Fig. 7 Fraction $\rho_{\text{shape}}(E_x)/\rho(E_x)$ of the state density in each of the three intrinsic deformation regions of Fig. 6 for even-mass $^{148-154}\text{Sm}$ isotopes vs. excitation energy E_x . Taken from Ref. [53]

8 Conclusion

Phenomenological models of level densities are often based on empirical modifications of the Fermi gas model and on the constant-temperature formula.

Mean-field and combinatorial models are the most common microscopic approaches to level densities and have been applied across the table of nuclei. However, they must be supplemented by empirical collective enhancement factors.

The moment method and the auxiliary-field Monte Carlo (AFMC) method include correlations beyond the mean-field approximation within the framework of the CI shell model. The moment method has been applied to light and mid-mass nuclei, while AFMC has been applied to nuclei as heavy as the lanthanides.

Acknowledgments I would like to thank G.F. Bertsch, M. Bonett-Matiz, L. Fang, P. Fanto, C.N. Gilbreth, S. Liu, A. Mukherjee, M.T. Mustonen, H. Nakada, and C. Özen for their collaboration on parts of the work reviewed above. This work was supported in part by the U.S. DOE grants Nos. DE-SC0019521 and DE-FG02-91ER40608. The research presented here used resources of the National Energy Research Scientific Computing Center, which is supported by the Office of Science of the U.S. Department of Energy under Contract No. DE-AC02-05CH11231. We also thank the Yale Center for Research Computing for guidance and for use of the research computing infrastructure.

References

1. W. Hauser, H. Feshbach, Phys. Rev. **87**, 366 (1952)
2. A. Bohr, B. R. Mottelson, *Nuclear Structure*, vol. 1 (Benjamin, New York, 1969)
3. T. Ericson, Adv. Phys. **9**, 425 (1960)
4. A. Sommerfeld, Z. Phys. **47**, 1 (1928)
5. H.A. Bethe, Phys. Rev. **50**, 332 (1936)
6. Y. Alhassid, G.F. Bertsch, L. Fang, Phys. Rev. C **68**, 044322 (2003)
7. H.A. Bethe, Rev. Mod. Phys. **9**, 69 (1937)
8. Y. Alhassid, G.F. Bertsch, S. Liu, H. Nakada, Phys. Rev. Lett. **84**, 4313 (2000)
9. For discrete level scheme data, see the ENSDF database at <https://www.nndc.bnl.gov/ensdf/>
10. For neutron and proton resonance data, see the RIPL-3 database at <https://www-nds.iaea.org/RIPL-3/>
11. A.V. Voinov, Problem of level densities in compound nuclear reactions, in *Proceedings of the 6th International Workshop on Compound-Nuclear Reactions and Related Topics* (Springer International Publishing, Cham, 2021)
12. A. Schiller, L. Bergholt, M. Guttormsen, E. Melby, J. Rekstad, S. Siem, Nucl. Instrum. Meth. Phys. Res. A **447**, 498 (2000)
13. W. Dilg, W. Schantl, H. Vonach, M. Uhl, Nucl. Phys. A **217**, 269 (1973)
14. T. von Egidy, H. Schmidt, A. Bekhami, Nucl. Phys. A **481**, 189 (1988)
15. A. Koning, S. Hilaire, S. Goriely, Nucl. Phys. A **810**, 13 (2008)
16. A. Gilbert, A.G.W. Cameron, Can. J. Phys. **43**, 1446 (1965)
17. P. Demetriou, S. Goriely, Nucl. Phys. A **695**, 95 (2001)
18. R. Capote, M. Herman, P. Oblozinsky, P.G. Young, S. Goriely, T. Belgya, A.V. Ignatyuk, A.J. Koning, S. Hilaire, V.A. Plujko, M. Avrigeanu, O. Bersillon, M.B. Chadwick, T. Fukahori, Z. Ge, Y. Han, S. Kailas, J. Kopecky, V.M. Maslov, G. Reffo, M. Sin, E.S. Soukhovitskii, P. Talou, Nucl. Data Sheets **110**, 3107 (2009)
19. S. Hilaire, S. Goriely, Nucl. Phys. A **779**, 63 (2006)
20. S. Goriely, S. Hilaire, A.J. Koning, Phys. Rev. C **78**, 064307 (2008)
21. S. Hilaire, M. Girod, S. Goriely, A.J. Koning, Phys. Rev. C **86**, 064317 (2012)
22. H. Uhrenholt, S. Åberg, A. Dobrowolski, T. Døssing, T. Ichikawa, P. Møller, Nucl. Phys. A **913**, 127 (2013)
23. K. Mon, J. French, Ann. Phys. **95**, 90 (1975)
24. V.K.B. Kota, R.U. Haq (eds.), *Spectral Distributions in Nuclei and Statistical Spectroscopy* (World Scientific, Singapore, 2010)
25. M. Horoi, M. Ghita, V. Zelevinsky, Phys. Rev. C **69**, 041307 (2004)
26. R.A. Sen'kov, M. Horoi, V. Zelevinsky, Comput. Phys. Commun. **184**, 215 (2013)
27. R.A. Sen'kov, V. Zelevinsky, Phys. Rev. C **93**, 064304 (2016)
28. V. Zelevinsky, M. Horoi, Prog. Part. Nucl. Phys. **105**, 180 (2019)

29. V. Zelevinsky, S. Karampagia, Nuclear shell model and level density, in *Proceedings of the 6th International Workshop on Compound-Nuclear Reactions and Related Topics CNR*18* (Springer International Publishing, Cham, 2021)
30. G.H. Lang, C.W. Johnson, S.E. Koonin, W.E. Ormand, *Phys. Rev. C* **48**, 1518 (1993)
31. Y. Alhassid, D.J. Dean, S.E. Koonin, G. Lang, W.E. Ormand, *Phys. Rev. Lett.* **72**, 613 (1994)
32. S.E. Koonin, D.J. Dean, K. Langanke, *Phys. Rep.* **278**, 2 (1997)
33. Y. Alhassid, *Int. J. Mod. Phys. B* **15**, 1447 (2001)
34. Y. Alhassid, in *Emergent Phenomena in Atomic Nuclei from Large-Scale Modeling: A Symmetry-Guided Perspective*, ed. by K.D. Launey (World Scientific, Singapore, 2017), pp. 267–298
35. J. Hubbard, *Phys. Rev. Lett.* **3**, 77 (1959); R.L. Stratonovich, *Dokl. Akad. Nauk. S.S.S.R.* **115**, 1097 (1957)
36. H. Nakada, Y. Alhassid, *Phys. Rev. Lett.* **79**, 2939 (1997)
37. W.E. Ormand, *Phys. Rev. C* **56**, 1678 (R) (1997)
38. K. Langanke, *Phys. Lett. B* **438**, 235 (1998)
39. Y. Alhassid, S. Liu, H. Nakada, *Phys. Rev. Lett.* **83**, 4265 (1999)
40. Y. Alhassid, S. Liu, H. Nakada, *Phys. Rev. Lett.* **99**, 162504 (2007)
41. A. Mukherjee, Y. Alhassid, *Phys. Rev. Lett.* **109**, 032503 (2012)
42. M. Dufour, A.P. Zuker, *Phys. Rev. C* **54**, 1641 (1996)
43. M. Bonett-Matiz, A. Mukherjee, Y. Alhassid, *Phys. Rev. C* **88**, 011302 (R) (2013)
44. Y. Alhassid, M. Bonett-Matiz, S. Liu, H. Nakada, *Phys. Rev. C* **92**, 024307 (2015)
45. A.V. Voinov, S.M. Grimes, C.R. Brune, T. Massey, A. Schiller, *EPJ Web Conf.* **21**, 05002 (2012); A.V. Voinov (private communication)
46. Y. Alhassid, L. Fang, H. Nakada, *Phys. Rev. Lett.* **101**, 082501 (2008)
47. C. Özen, Y. Alhassid, H. Nakada, *Phys. Rev. Lett.* **110**, 042502 (2013)
48. Y. Alhassid, C. Özen, H. Nakada, *Nucl. Data Sheets* **118**, 233 (2014)
49. Y. Alhassid, G.F. Bertsch, C.N. Gilbreth, H. Nakada, *Phys. Rev. C* **93**, 044320 (2016)
50. P. Fanto, Y. Alhassid, G.F. Bertsch, *Phys. Rev. C* **96**, 014305 (2017)
51. T. von Egidy, D. Bucurescu, *Phys. Rev. C* **78**, 051301 (R) (2008)
52. T. von Egidy, D. Bucurescu, *Phys. Rev. C* **80**, 054310 (2009)
53. M.T. Mustonen, C.N. Gilbreth, Y. Alhassid, G.F. Bertsch, *Phys. Rev. C* **98**, 034317 (2018)
54. Y. Alhassid, C.N. Gilbreth, G.F. Bertsch, *Phys. Rev. Lett.* **113**, 262503 (2014)
55. C.N. Gilbreth, Y. Alhassid, G.F. Bertsch, *Phys. Rev. C* **97**, 014315 (2018)
56. K. Kumar, *Phys. Rev. Lett.* **28**, 249 (1972)
57. D. Cline, *Ann. Rev. Nucl. Part. Sci.* **36**, 683 (1986)
58. S. Levit, Y. Alhassid, *Nucl. Phys. A* **413**, 439 (1984)
59. Y. Alhassid, S. Levit, J. Zingman, *Phys. Rev. Lett.* **57**, 539 (1986)

Problem of Level Densities in Compound Nuclear Reactions



Alexander Voinov

1 The Problem Overview

The purpose of this contribution is to give a brief overview of experimental basis for level density models currently used in modern nuclear reaction codes such as Empire [1] and Talys [2]. The goal is to understand the source of uncertainties associated with those models which result in uncertainties in cross section calculations. The discussion of the possible ways of their improvements will follow.

Modern reaction codes including those mentioned above are used in variety of applications including astrophysics calculations and evaluation of reaction cross sections for the ENDF data base [3]. Therefore, the robustness of model inputs in general and level density models in particular is crucial for accuracy of calculations. Each code has an option to input different level density models. This is certainly helpful when codes are used for analysis of available experimental data but it results in ambiguities and uncertainties when they are used for predictions of unknown cross sections either in energy or nuclear chart regions where experimental data are not available. It is appropriate to mention here specific studies on uncertainties of Hauser-Feshbach (HF) calculations which reveal a factor of up to 3 uncertainty for stable nuclei and much greater for nuclei off the stability line. These uncertainties are mainly due to the difference in HF inputs and specifically due to different level density models [4].

From physics point of view, the reaction cross section is generally due to different reaction mechanisms, however, the compound mechanism [5] constitutes a substantial fraction or even dominates at low energies ($< \sim 5$ MeV/A) which are relevant to most of applications. The theory of this model was developed in Ref. [6]

A. Voinov (✉)

Department of Physics and Astronomy, Ohio University, Athens, OH, USA
e-mail: voinov@ohio.edu

© This is a U.S. government work and not under copyright protection in the U.S.; foreign copyright protection may apply 2021

J. Escher et al. (eds.), *Compound-Nuclear Reactions*, Springer Proceedings in Physics 254, https://doi.org/10.1007/978-3-030-58082-7_13

which is referred to as the Hauser-Feshbach theory of nuclear reactions. This theory is phenomenological in the sense that it uses input parameters to calculate reaction cross sections. Input parameters are based on nuclear structure quantities which determine probability of creation and decay of a compound nucleus. These are particle and γ transmission coefficients, and the nuclear level density. These quantities are largely based on models and are source of uncertainties in cross section calculations. For review of the present status of these quantities we refer to Ref. [7].

HF theory is used as a main tool to calculate reaction cross sections in different areas of basic and applied physics (examples are astrophysics and data evaluations). Therefore the problem of the uncertainties of the input parameters is considered to be important. This calls for specific studies of input parameters both experimentally and theoretically. For the present, the level density and γ -strength functions are considered to be the most uncertain inputs since particle transmission coefficients are derived from the optical model and are based on much broader experimental data sets compared to the level density and γ -strength. Here we will focus on level density problems.

2 Understanding the Source of Level Density Model Uncertainties

The reason for uncertainties in level density models is basically the same as the reason of uncertainties of any other theoretical model in nuclear physics, namely the lack of experimental data which are used to constrain these models. Majority of nuclear physics models use parameters which are adjusted to fit experimental data. Such models are usually referred to as phenomenological or semi-phenomenological models depending on fraction of the microscopic approach used in these models. Even some models which appear to be based on microscopic approach usually have adjustable parameters which require experimental data to fit.

Most of all, the following types of level density models are currently used in reaction codes for practical calculations: the first one is phenomenological models which are based on analytical formulas and the second type of models is based on microscopic calculations. Phenomenological models mainly use two types of analytical formulas: the first one is based on Fermi-gas model (FGM) of Ref.[8] and the other uses a combination of Fermi-gas at higher excitation energies, typically above the neutron separation energy, and the constant temperature formula at low excitation energies. The latter model is referred to as a Gilbert and Cameron model (GCM) [9]. FGM and GCM have different excitation energy dependence because of inclusion of the constant temperature model formula in GCM. This has a physical implication of whether a nucleus undergoes a first-order phase transition when it is excited. In macro-physics the first-order phase transition is observed in the process of melting ice when the heat is received but the temperature remains constant.

Variations arising from employing of different (FGM or GCM) level density models represent the first source of uncertainties. Both FGM and GCM model prescriptions have parameters which are traditionally determined based on comprehensive data on neutron resonances [10] (discussed in the next section). For details about specific formulas and their parameterizations recommended for practical applications one can refer to the Refs.[1, 7].

Microscopic level density calculations used as input in Talys and Empire are those from Refs.[11, 12]. Calculations are available in table form for all nuclei. These level density model calculations might be consistent, depending on a specific nucleus, with either FGM or GCM models or might exhibit completely different excitation energy dependence. So, again, the difference in an excitation energy dependence in different models is a key factor which determines level density uncertainties.

Parameters for all level density models including microscopic ones from Refs. [11, 12] (which also use renormalization parameters) are determined based on comprehensive, but a single data set only which is data set on neutron resonance spacings. Data on neutron resonances are available for all stable plus one neutron nuclei, however, they are very limited in terms of spin, parity, and excitation energy ranges. Thus, the limitation of experimental data set on which models (model parameterizations) are based is the main source of level density model uncertainties. More specific discussion on limitation of neutron resonance and other experimental data is presented in the next section.

3 Review of Available Experimental Data Sets and Their Limitations

3.1 Neutron Resonance Spacings

As already mentioned in the previous section the data on neutron resonance spacings is the only data set the current level density models use for their parameterizations. Therefore, understanding of limitations of these data and their influence on uncertainties of level density models is important. The neutron resonances represent individual nuclear levels excited in low-energy neutron induced reactions. The energy of neutrons is in eV range for heavy nuclei and in keV range for middle mass and light ones. Therefore, the excitation energy range for neutron resonances is very limited and is just above the neutron separation energy. Reactions with low-energy neutrons are dominated by reactions with zero orbital momentum, so the spins of the neutron resonances (the so called s-resonances) are in a very narrow range of $(I_t \pm 1/2)$, where I_t is the spin of a target nucleus. All s-wave resonances have one parity only equal to the parity of the ground state target nucleus. For middle mass and light nuclei, contribution of p-wave resonances (for neutrons with orbital momentum equal one) becomes apparent which creates difficulties of distinguishing

between s and p-wave resonances. P-wave resonances are in the range $(I_t \pm 3/2)$ and have opposite parity from the parity of the target nucleus. The fact that neutron resonances are known in very limited energy and spin intervals indicates that level density models are only constrained in these intervals. Both excitation energy and spin dependences at lower and higher energies require model assumptions.

Along with neutron resonance data, data from discrete level scheme are used to constrain model level density functions at the low excitation energy region. Discrete level scheme is well known up to a certain excitation energy, typically, up to 2–4 MeV depending on the mass range. However, model function in the low-energy region might not perform well causing further uncertainties in model parameterizations. The transition region from discrete states to continuum might be prone to the structure effects, such as pairing and/or shell ones resulting in deviation of model functions from smooth behavior.

The other potential issue comes from often non-trivial analysis of neutron resonances. Missing resonances due to experimental threshold as well as misidentification of resonance spins and parities (due to difficulties in distinguishing between s-wave and p-wave resonances) might lead to incorrect estimates of resonance spacings. There are two major data sources on parameters of neutron resonances, these are in Refs. [7] and [10]. The fact that for some nuclei resonance parameters are different indicates the existence of the problem of neutron resonance evaluations.

3.2 The Oslo Method

The experimental method known as the ‘‘Oslo method’’ allows studying the nuclear level density extracted from the particle- γ coincidence matrix $P(E_{\text{ex}}, E_\gamma)$, where E_{ex} and E_γ are excitation energy and γ -ray energy, respectively [13]. Reactions (${}^3\text{He}, {}^3\text{He}'\gamma$), (${}^3\text{He}, \alpha\gamma$), ($d, p\gamma$), or similar are used. As it is shown in Ref. [13], such a technique allows extracting the level density function $\rho(E^*)_{\text{oslo}}$ which is related to the ‘‘true’’ level density function $\rho(E^*)_{\text{true}}$ through the following transformation:

$$\rho(E^*)_{\text{true}} = \rho(E^*)_{\text{oslo}} A \exp(BE^*). \quad (1)$$

Coefficients A and B need to be determined from auxiliary information, usually, the density of levels in the discrete energy region (the first anchor point) and the density of neutron resonances (the second anchor point) are used. Density of discrete levels are well known up to a certain excitation energy from a level scheme [7]. The density of neutron resonances known only in a very limited spin interval (see Sect. 3.1) has to be converted to the total level density, integrated over all spins populated in Oslo type experiments. This conversion relies on models because of lack of experimental information on spin distribution in the region of neutron resonances, as was mentioned in the previous Sect. 3.1 and will be discussed in Sect. 3.4.

Although, the original $\rho(E^*)_{oslo}$ is not able to provide model independent absolute level density values, it delivers very unique information about the excitation energy dependence of the level density function. As it is seen from Eq. 1, $\rho(E^*)_{oslo}$ is able to show deviations from the exponential form of the excitation energy dependence $A \exp(BE^*)$ or from the constant temperature level density formula if we express $A = 1/(t \exp(x_0/t))$ and $B = 1/t$. Indeed, if we assume that the “true” level density has the constant temperature energy dependence, we will get $\rho(E^*)_{oslo} = 1$ when A and B are adjusted to minimize the ratio $\rho(E^*)_{true}/(A \exp(BE^*))$. Any deviations from one would show the deviations from the constant temperature energy dependence. Such an analysis has been performed in Ref. [14] which showed the preference of the constant temperature model over FGM for the range of nuclei studied with Oslo technique.

Also, the Oslo method delivers very unique information about the level density behavior between discrete and continuum excitation energy regions. This region can still be affected by nuclear structure properties resulting in the level density functions being not as smooth as phenomenological models (FGM or GCM) suggest.

3.3 *The Particle Evaporation*

The method is based on measurements of particle evaporation spectra from compound nuclear reactions [15]. Spectra are interpreted in framework of the Hauser-Feshbach theory of nuclear reactions [6] according to which the differential cross section of an outgoing particle in respect to its energy is proportional to the product of particle transmission coefficients T and the level density ρ of a residual nucleus populated by this particle. Schematically, it can be written as $\sigma \propto T \cdot \rho$, but a more complete and accurate formula is presented in Ref. [6]. Since the accuracy of transmission coefficients calculated from optical models usually exceeds the accuracy of level density models, the latter can be benchmarked using experimental differential cross sections σ (or spectra) of outgoing particles. Moreover, the level density excitation energy function can be obtained by direct unfolding of experimental cross sections [15].

The advantage of this method is that it, firstly, allows obtaining the level density in a wide spin and excitation energy intervals compared to the method based on the neutron resonance counting. Secondly, the method is capable of determining the absolute values of level densities. This feature distinguishes it from the Oslo method which requires data on neutron resonance spacings and model dependent spin distribution function.

The systematic uncertainties of the method can potentially be caused by possible contribution of pre-equilibrium processes which distort the shape of particle evaporation spectra, especially their high energy parts that might lead to incorrect determination of the level density or its parameters. This is considered to be the main drawback of the method. Also, the uncertainties arising from unknown

spin distributions of populated nuclei can also take place for some of reactions. To minimize these uncertainties, the careful selection of beam species and their energies is needed to ensure the compound mechanism is dominant and effect of the spin dependence is minimized. Spectra measured at backward angles are used for these purposes.

Existing experimental information on the level density from particle evaporation is scarce. There were few groups involved in these kinds of experiments in 60s–80s using reactions such as (α, p) , (p, α) [16, 17], (p, n) , (α, n) [18], and (n, α) [19] on nuclei from 50–70 mass range. Unfortunately, available data do not allow making some general conclusions on level density regularities. The quality of data points in some of these works is poor (small number of points, large binning interval, point-to-point fluctuations). The analysis of these data was made with different techniques and assumptions. Some experiments were analyzed with the simple Weisskopf model [20] which does not account for angular momentum values of compound and residual nuclei. Many experimental spectra have not been measured in the region of discrete known levels populated by evaporated particles or population of discrete levels was not included in statistical model calculations at that time.

Experiments conducted by our group suggested improvements and showed capability of this technique to extract level densities for individual nuclei and to benchmark existing level density models [21–24].

3.4 Spin Distribution

The spin distribution of the nuclear level density $\rho(J)$ is an important and most uncertain parameter in level density calculations. Model level densities use the Gaussian form of the spin distribution with the spin cutoff parameter σ determining the widths of this distribution:

$$\rho(J) = \frac{1}{\sqrt{2\pi}\sigma} \frac{(J + 1/2)}{\sigma^2} \exp\left(-\frac{(J + 1/2)^2}{2\sigma^2}\right). \quad (2)$$

The spin cutoff parameter is coupled with level density parameters, namely the parameter a and δ (see Ref. [7] for details). The spin distribution and its parameterization are based on FGM [8] and currently have a little support from experimental data. Different model formulas for the spin cutoff parameters can be found in Refs.[1, 7, 25, 26]. Although there is a general consensus that the spin cutoff estimates based on the rigid body model of inertia [7, 25] work at the excitation energy near the neutron binding energy range and higher, there are indications that they overestimate the spin cutoff values at low excitation energies. For example, it overestimates spin cutoff values derived from low-energy discrete levels with known spins [7]. Therefore reaction codes such as Empire and Talys, for some of their models, use linear interpolation for the spin cutoff parameter between the region

of discrete levels and the neutron binding energy. However, such an approach still needs experimental support. Theoretical studies based on Monte-Carlo Shell model calculations [27] support decreasing of the spin cutoff parameter at low energies in the region of iron isotopes.

It has been shown in Ref. [28] that the anisotropy of the angular distribution of outgoing particles in compound nuclear reactions is determined by the orbital momentums of incoming and outgoing particles and by the spin distribution of the levels populated in residual nucleus. It creates possibility of studying the spin cutoff parameter experimentally from studying particle angular distributions from compound nuclear reactions. There are few experimental studies available in literature [18, 29, 30]. In some of them there are indications of deviations of the spin cutoff parameter from the form of the Eq. 2. However, there are no established conclusions achieved so far, which suggests that more experiments are needed.

There is an experimental technique to study the level density for specific spin states and parities using high resolution (p, p') experiments [31]. Level density is extracted from fluctuations of high resolution spectra of outgoing protons. Such a technique with combination of other techniques, for example, with particle evaporation spectra would allow us to study the spin cutoff parameter as well.

Further experimental studies of the spin cutoff parameter are considered to be extremely important for constraining level density models.

4 Possible Projects on Constraining Level Density Models

It appears that widely used level density models based only on data from neutron resonances reached the limit of their accuracy. It suggests that the best strategy to constrain model uncertainties is to conduct analysis of experimental information delivered by all experimental techniques and methods including, but not limited to, neutron resonances, the Oslo and particle evaporation methods, inelastic proton scattering. This type of analysis has not been performed so far and all level density models used in modern reaction codes continue using parameterizations based on neutron resonances only. The following possible projects to address this problem appear to be important

- Study of systematics deviations of the level density excitation energy dependence from the constant temperature model using experimental data obtained with Oslo and particle evaporation techniques. It would help constraining the excitation energy dependence of model functions, including problem of distinguishing between FGM and GCM.
- Study of level densities with the analysis of particle evaporation spectra from compound nuclear reactions. It would be possible to obtain absolute values of level densities. By comparing the absolute values with data from neutron resonance spacings, the spin distribution and the spin cutoff parameter can be estimated.

- Experimental study of the spin cutoff parameter from angular distribution of particles evaporated from compound nuclear reactions and by analysis of combined data from neutron resonances, evaporation spectra and from (p, p') experiments of Ref.[31].

Acknowledgement This work has been supported by Department of Energy grant DE-NA0002905.

References

1. M. Herman, R. Capote, B. Carlson, P. Obložinský, M. Sin, A. Trkov, H. Wienke, V. Zerkin, Empire: nuclear reaction model code system for data evaluation. Nucl. Data Sheets **108**, 2655 (2007). <https://doi.org/10.1016/j.nds.2007.11.003>
2. A.J. Koning, S. Hilaire, M.C. Duijvestijn, Talys-1.2, in *Proceedings of the International Conference on Nuclear Data for Science and Technology* (April 22–27, 2007, Nice), ed. by O. Bersillon, F. Gunsing, E. Bauge, R. Jacqmin, S. Leray (EDP Sciences, Les Ulis, 2008), p. 211. <http://www.talys.eu/>
3. M.B. Chadwick, M. Herman, P. Obložinský et al., ENDF/B-VII.1 nuclear data for science and technology: cross sections, covariances, fission product yields and decay data. Nucl. Data Sheets **112**, 2887 (2011). <https://doi.org/10.1016/j.nds.2011.11.002>
4. M. Beard, E. Uberseder, R. Crowter, M. Wiescher, Comparison of statistical model calculations for stable isotope neutron capture. Phys. Rev. C **90**, 034619 (2014). <https://doi.org/10.1103/PhysRevC.90.034619>
5. N. Bohr, Neutron capture and nuclear constitution. Nature **137**, 344 (1936)
6. W. Hauser, H. Feshbach, The inelastic scattering of neutrons. Phys. Rev. **87**, 366 (1952). <https://doi.org/10.1103/PhysRev.87.366>
7. R. Capote, M. Herman, P. Obložinský, P.G. Young, S. Goriely, T. Belgya, A.V. Ignatyuk, A.J. Koning, S. Hilaire, V.A. Plujko, M. Avrigneanu, O. Bersillon, M.B. Chadwick, T. Fukahori, Z. Ge, Y. Han, S. Kailas, J. Kopecky, V.M. Maslov, G. Reffo, M. Sin, E.S. Soukhovitskii, P. Talou, Reference input parameter library (RIPL-3). Nucl. Data Sheets **110**(12), 3107 (2009). <https://www-nds.iaea.org/RIPL-3>
8. H.A. Bethe, An attempt to calculate the number of energy levels of a heavy nucleus. Phys. Rev. **50**, 332 (1936). <https://doi.org/10.1103/PhysRev.50.332>
9. A. Gilbert, A.G.W. Cameron, A composite nuclear-level density formula with shell corrections. Can. J. Phys. **43**, 1446 (1965). <https://doi.org/10.1139/p65-139>
10. S.F. Mughabghab, *Atlas of Neutron Resonances* (Elsevier, Amsterdam, 2006)
11. S. Goriely, S. Hilaire, A.J. Koning, Improved microscopic nuclear level densities within the Hartree-Fock-Bogoliubov plus combinatorial method. Phys. Rev. C **78**, 064307 (2008). <http://dx.doi.org/10.1103/PhysRevC.78.064307>
12. S. Hilaire, M. Girod, S. Goriely, A.J. Koning, Temperature-dependent combinatorial level densities with the DIM Gogny force. Phys. Rev. C **86**, 064317 (2012). <https://doi.org/10.1103/PhysRevC.86.064317>
13. A. Schiller, L. Bergholt, M. Guttormsen, E. Melby, J. Rekstad, S. Siem, Extraction of level density and γ strength function from primary γ spectra. Nucl. Instrum. Methods **A447**, 498 (2000). [http://dx.doi.org/10.1016/S0168-9002\(99\)01187-0](http://dx.doi.org/10.1016/S0168-9002(99)01187-0)
14. M. Guttormsen, M. Aiche, F.L. Bello Garrote, L.A. Bernstein, D.L. Bleuel, Y. Byun, Q. Ducasse, T.K. Eriksen, F. Giacoppo, A. Görgen, F. Gunsing, T.W. Hagen, B. Jurado, M. Klintefjord, A.C. Larsen, L. Lebois, B. Leniau, H.T. Nyhus, T. Renstrøm, S.J. Rose, E. Sahin, S. Siem, T.G. Tornøyi, G.M. Tveten, A. Voinov, M. Wiedeking, J. Wilson, Experimental level densities of atomic nuclei. Eur. Phys. J. A **51**(12), 170 (2015). <https://doi.org/10.1140/epja/i2015-15170-4>

15. H. Vonach, Extraction of level density information from non-resonance reactions, in *Proceedings of the IAEA Advisory Group Meeting on Basic and Applied Problems of Nuclear Level Densities*, ed. by M.R. Bhat, BNL Report No. BNL-NCS-51694. Upton, Long Island, 11973 (1983), p. 247
16. C.C. Lu, L.C. Vaz, J.R. Huizenga, Spin distribution of the nuclear level density near $A = 60$. *Nucl. Phys.* **197**, 321 (1972)
17. A. Alevra, M. Duma, I.R. Lukas-Koch, M.T. Magda, M.E. Nistor, A. Chevarier, N. Chevarier, A. Demeyer, G. Hollinger, Tran Minh Duc, *Nucl. Phys.* **A265**, 376 (1976). [http://dx.doi.org/10.1016/0375-9474\(76\)90550-9](http://dx.doi.org/10.1016/0375-9474(76)90550-9)
18. S.M. Grimes, J.D. Anderson, J.W. McClure, B.A. Pohl, C. Wong, Level density and spin cutoff parameters from continuum (p,n) and (α ,n) spectra. *Phys. Rev. C* **10**, 2373 (1974). <https://doi.org/10.1103/PhysRevC.10.2373>
19. R. Fischer, G. Traxler, M. Uhl, H. Vonach, $^{56}\text{Fe}(n, \alpha)^{53}\text{Cr}$ and $^{60}\text{Ni}(n, \alpha)^{57}\text{Fe}$ reactions at $E_n = 14.1$ MeV. *Phys. Rev. C* **30**, 72 (1984). <http://dx.doi.org/10.1103/PhysRevC.30.72>
20. V. Weisskopf, Statistics and nuclear reactions. *Phys. Rev.* **52**, 295 (1937). <https://doi.org/10.1103/PhysRev.52.295>
21. A.V. Voinov, S.M. Grimes, C.R. Brune, M.J. Hornish, T.N. Massey, A. Salas, Test of nuclear level density inputs for Hauser-Feshbach model calculations. *Phys. Rev. C* **76**, 044602 (2007). <https://doi.org/10.1103/PhysRevC.76.044602>
22. A.V. Voinov, S.M. Grimes, C.R. Brune, M. Guttormsen, T.N. Massey, A. Schiller, S. Siem, Experimental study of level density and γ -strength functions from compound nuclear reactions, in *Proceedings of the 2007 International Workshop in Compound Nuclear Reactions and Related Topics (CNR*2007)* (American Institute of Physics, Melville, 2007), p. 61
23. A.V. Voinov, B.M. Oginni, S.M. Grimes, C.R. Brune, M. Guttormsen, A.C. Larsen, T.N. Massey, A. Schiller, S. Siem, Nuclear excitations at constant temperature. *Phys. Rev. C* **79**, 031301(R) (2009). <http://dx.doi.org/10.1103/PhysRevC.79.031301>
24. A.V. Voinov, S.M. Grimes, C.R. Brune, A. Bürger, A. Gørgen, M. Guttormsen, A.C. Larsen, T.N. Massey, S. Siem, C. Kalbach, Equilibrium and pre-equilibrium processes in the $^{55}\text{Mn}(^6\text{Li}, \text{xp})$ and $^{57}\text{Fe}(\alpha, \text{xp})$ reactions. *Phys. Rev. C* **83**(5), 054605 (2011). <http://dx.doi.org/10.1103/PhysRevC.83.054605>
25. T. von Egidy, D. Bucurescu, Correlations between the nuclear level density parameters. *Phys. Rev. C* **72**, 044311 (2005). <https://doi.org/10.1103/PhysRevC.72.067304>
26. T. von Egidy, D. Bucurescu, *Phys. Rev. C* **80**, 054310 (2009). <https://doi.org/10.1103/PhysRevC.80.054310>
27. H. Nakada, Y. Alhassid, Total and parity-projected level densities of iron-region nuclei in the auxiliary fields Monte Carlo shell model. *Phys. Rev. Lett.* **79**, 2939–2942 (1997). <https://doi.org/10.1103/PhysRevLett.79.2939>
28. T. Ericson, V. Strutinski, Angular distribution in compound nucleus processes. *Nucl. Phys.* **8**, 284 (1958)
29. M.T. Magda, A. Alevra, I.R. Lukas, D. Plostinaru, E. Trutia, M. Molea, Statistical emission and nuclear level densities in (a, n) reactions. *Nucl. Phys. A* **140**, 23 (1970). [http://dx.doi.org/10.1016/0375-9474\(70\)90881-X](http://dx.doi.org/10.1016/0375-9474(70)90881-X)
30. P. Hille, P. Speer, M. Hille, K. Rudolph, W. Assmann, D. Evers, *Nucl. Phys. A* **232**, 157 (1974)
31. Y. Kalmykov, C. Özen, K. Langanke, G. Martínez-Pinedo, P. von Neumann-Cosel, A. Richter, Spin- and parity-resolved level densities from the fine structure of giant resonances. *Phys. Rev. Lett.* **99**, 202502 (2007). <https://doi.org/10.1103/PhysRevLett.99.202502>

Nuclear Shell Model and Level Density



Vladimir Zelevinsky and Sofia Karampagia

1 Introduction

The knowledge of the nuclear level density as a function of excitation energy and nuclear spin is necessary for many practical problems of nuclear physics and its applications. There are several approaches to this task. Frequently the empirical expressions are used based on the traditional Fermi-gas picture, with or without the backshift parameter reflecting the existence of the pairing gap, and with the adjusted main parameter. [1–3]. The combinations of the mean-field combinatorics, pairing and some collective effects were used in the most broad attempts for the general description of the level density [4, 5]. The shell-model Monte Carlo method accounts for more parts of the interparticle interactions [6–8]. The general introduction to the problem and some historical comments can be found in the recent review article [9].

It seems natural to use the full solution of the nuclear shell model without making approximations in the choice of the parts of the interaction taken into account. Certainly, there are obvious deficiencies in using the shell model for the extraction of the level density. The shell-model interactions are presented typically by the matrix elements of the two-body processes. The dozens and hundreds matrix elements should be carefully selected based on the original nucleon-nucleon interaction, theoretical arguments, and detailed fit of well-known experimental quantities. This selection has to be done before applications to the level density and checked by the

V. Zelevinsky (✉)

Department of Physics and Astronomy and NSCL/FRIB, Michigan State University, East Lansing, MI, USA

e-mail: zelevins@frib.msu.edu

S. Karampagia

Department of Physics, Grand Valley State University, Allendale, MI, USA

© This is a U.S. government work and not under copyright protection in the U.S.; foreign copyright protection may apply 2021

J. Escher et al. (eds.), *Compound-Nuclear Reactions*, Springer Proceedings in Physics 254, https://doi.org/10.1007/978-3-030-58082-7_14

spectroscopic output in the form of level energies, expectation values of observables, and transition probabilities. Currently such work that took many years of adjustment can be considered reliable for the nuclei of *sd* and *pf* shells and a little beyond. The possibility of the exact diagonalization is obviously limited by the size of the huge Hamiltonian matrix, in spite of the fast computational progress. Therefore the Hilbert space has to be truncated with the appropriate renormalization of the matrix elements. This truncation limits the trustworthy predictions because, starting from some excitation energy, the truncated parts of the Hilbert space enter the game with the new particle configurations and new levels. Finally, the standard versions of the shell model are based on the harmonic oscillator scheme and do not feel the continuum thresholds and finite life time of the levels beyond that. (This, however, is a common feature of current approaches to the level density problem).

With all deficiencies of the shell model, it still gives the most reliable description of nuclear spectroscopy. In practice, even being limited by the space truncation and increasing widths of the continuum states, the shell-model predictions of the level density, at least up to $A \approx 60 - 70$, agree with the available information below excitation energy 12–15 MeV, and probably even beyond. It turns out to be an important advantage of the shell model that it accounts for all (allowed by conservation laws) interaction matrix elements. In many theoretical approaches, only the mean field and collective interactions are accounted for. The shell model adds here all possible incoherent collision-like processes which turn out to influence the level density in an important way making it a smooth function of excitation energy. There is an obvious objection based on the deficit of information from low-lying spectroscopy about such processes that makes these matrix elements ill defined. However, one can argue that their exact values are of less importance; there are many of them and their action is statistically averaged.

Here we come to the role of what is called quantum chaos and thermalization in a small mesoscopic system of interacting constituents. The equilibration here comes without an external heat bath, just due to the interaction that becomes effectively strong along with the growing level density, simply because of combinatorics. Starting from some excitation energy above the pairing gap, the neighboring wave functions within the same symmetry class become more and more mixed and similar by their main properties as was understood long ago [10]. The excitation energy is distributed over the growing number of degrees of freedom as in the classical compound nucleus picture. Statistical characteristics of stationary states, such as the level spacing distribution, informational entropy, number of principal components, correlational measures, etc., are smoothly changing along the spectrum as functions of energy, similarly to thermodynamic equilibrium [11–13]. Those properties are analogous to the predictions of the extreme limit of the Gaussian Orthogonal Ensemble (GOE) in spite of the fact that two-body interactions are not at all random (any two-body matrix element is repeated many times in the Hamiltonian matrix for different background of spectators). In this way, the dense set of mixed stationary states creates chaotic properties which in turn self-consistently lead to the generic behavior of the level density.

This was qualitatively understood long ago, see, for example, [14–16]. In the book [17] it was suggested to describe the nuclear level density in the restricted orbital space by the sequence of statistical moments corresponding to Gaussian distributions of the observables. Later it became possible to formulate a practical “moments method,” see [9] and the references therein, which works very well reproducing exact shell-model results and avoiding the diagonalization of huge matrices. The computational aspects of the moments method are formulated in [18]. Another possible way to avoid the full diagonalization is currently under way [19] based on the Lanczos algorithm.

2 Moments Method

In the moments method we start from the shell-model Hamiltonian in a truncated space using the mean-field basis of many-body states. The basis states are divided into partitions p by distributing the particles over the mean-field levels. The first moment is just the mean-field energy for a given partition p with the dimension $D_{\alpha p}$ and a given set of exact quantum numbers α ,

$$E_{\alpha p} = \langle H_{\alpha p} \rangle \equiv \frac{1}{D_{\alpha p}} \text{Tr}^{(\alpha p)}(H). \quad (1)$$

This trace includes the matrix elements of the interactions diagonal with respect to the occupancies of the given partition. The second moment,

$$\langle H_{\alpha p}^2 \rangle \equiv \frac{1}{D_{\alpha p}} \text{Tr}^{(\alpha p)}(H^2), \quad (2)$$

includes the bilinear combinations of mean-field energies and interaction matrix elements forming the two-step processes based on the partition p with the inclusion of transitions to the configurations outside this partition and back. These moments can be read just from the Hamiltonian matrix.

The first two moments allow one to construct the effective Gaussian $G_{\alpha p}(E)$ with the centroid (1) and the width defined as its variance by the second moment (2). This determines the effective contribution of a partition p to the level density of the class of states α ,

$$\rho_{\alpha}(E) = \sum_p D_{\alpha p} G_{\alpha p}(E). \quad (3)$$

There are important technical details (renormalization of the unphysical tails of the Gaussians, the fit of the ground state energy, removal of spurious center-of-mass excitations, and so on) which can be found in [18] and other publications. As a

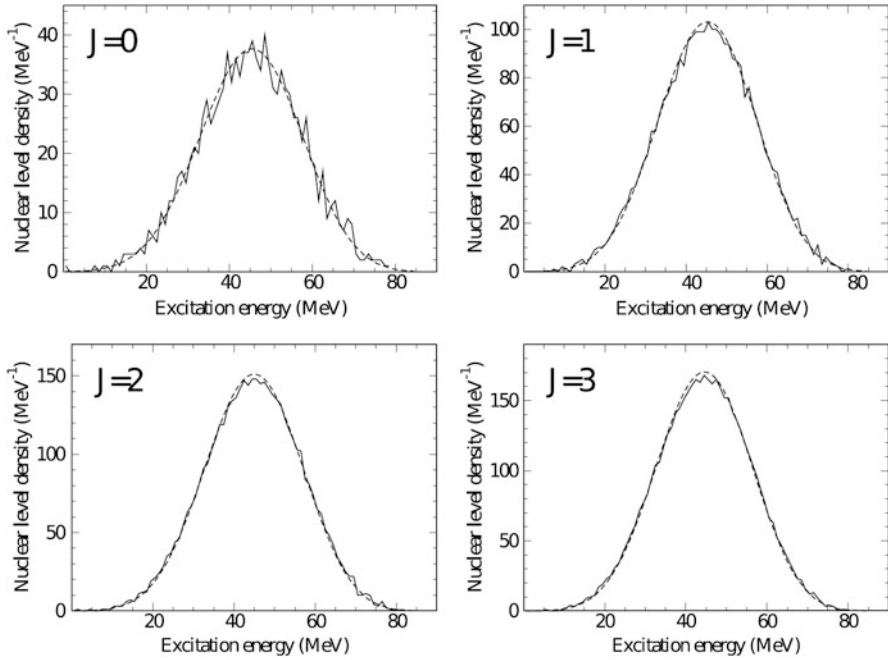


Fig. 1 Nuclear level densities for ^{24}Mg , positive pairing and various spins, for the sd -shell and USDB two-body interaction (taken from [20]); full shell-model diagonalization (solid curves) vs moments method (dashed curves)

result, there comes a reliable computational method that leads to the shell-model level density avoiding the full diagonalization. Figure 1 shows the agreement of the level density found by this method [20] with the result of the shell-model solution.

A useful feature of the method is that it is easy to study the role of individual components of the residual interaction in formation of the total level density. As stressed earlier, the level density as a function of energy is a smooth function without sharp peaks visible in calculations that account for the collective parts of the interaction Hamiltonian only. Figure 2 demonstrates the evolution of the level density in this direction as we include more incoherent interactions in the Hamiltonian [20]. Here amplitudes k_1 and k_2 refer, correspondingly, to the strengths of pairing and non-pairing matrix elements in the Hamiltonian; they are equal to 1 in the realistic Hamiltonian.

The quality of description from the main viewpoint of the experiment is illustrated by Fig. 3. Here it is just a quality check for the used shell-model Hamiltonian.

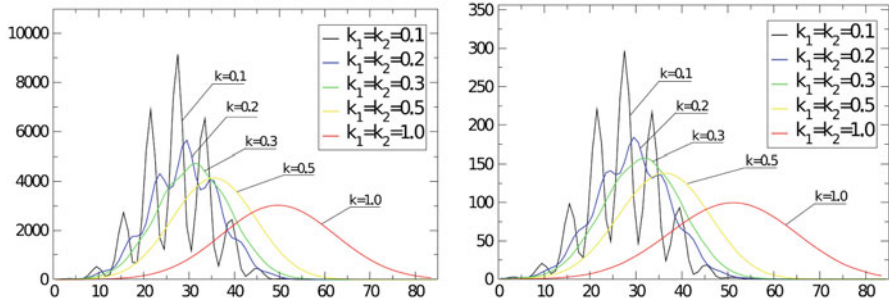
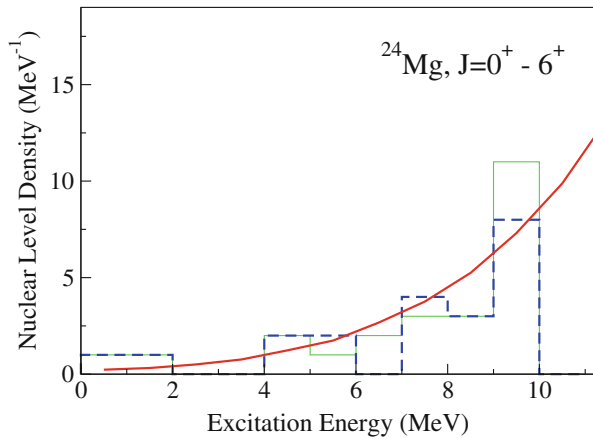


Fig. 2 Level density for ^{28}Si in *sd*-model space. Different curves correspond to different scale factors, $k = k_1 = k_2 = 0.1, 0.2, 0.3, 0.5, 1.0$ when the pairing and non-pairing parts of the interaction scale similarly. The left graph corresponds to the total density with all J included, while the right graph describes the evolution of the $J = 0$ density. Source: Taken from [20]

Fig. 3 Comparison of experimental nuclear level density for positive parity states (green stair line) with the analogous level density calculated with the USDB shell model (blue dashed stair line) and the moments method (solid red line) for ^{24}Mg



3 Exponential Model (“Constant Temperature”)

The calculations for all nuclei of the *sd*-shell were performed [21] for various sectors of the Hilbert space. Here we come to the practically important problem. It would be very useful to be able to suggest experimentalists a simple parametrization for the level density as a function of excitation energy in a given class of states with very few parameters which can be determined from the data and carry a clear physical meaning. There is a tradition to use the back-shifted Fermi-gas formula that gives a reasonable description of the data. However, the main parameter in this description that is supposed to be determined by the density of single-particle levels at the Fermi surface, in empirical fits typically has to be taken significantly larger. Such a description also has to include the evolution of the level density as a function of the occupancy of the orbitals as well as effects of deformation and collective modes. During last years the competing phenomenological description in terms of

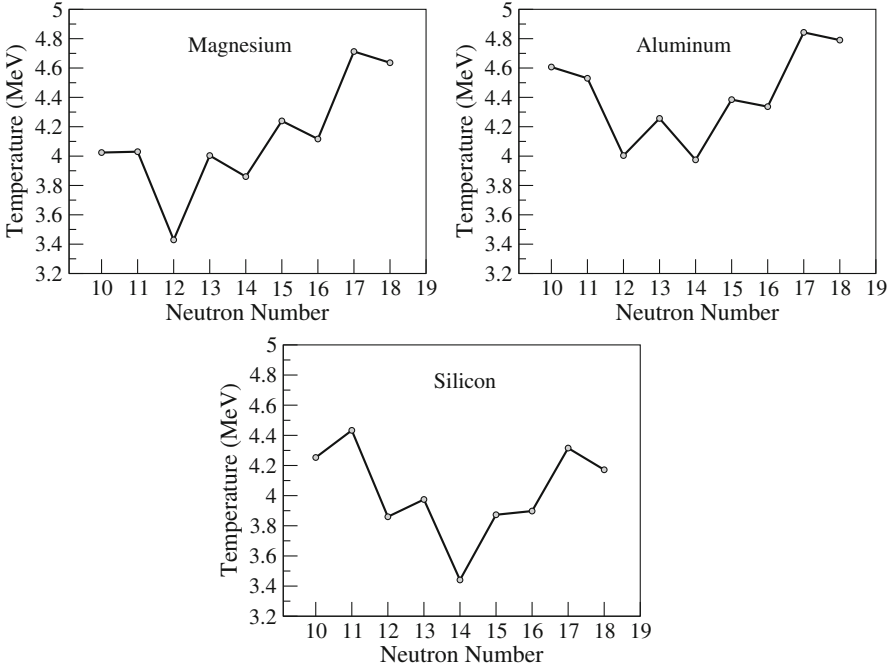


Fig. 4 Effective temperature parameter T for the isotopes of magnesium, aluminum, and silicon. The level density is calculated with the USDB version of the shell model. Source: Adapted from Ref. [9]

the so-called “constant temperature model” [1, 22] became more popular. The main feature of this model is a pure exponential growth of the level density,

$$\rho(E) = \rho_0 e^{E/T}, \quad (4)$$

with a normalization constant ρ_0 that is often parameterized as $(1/T) \exp(-E_0/T)$. Indeed, this function fits quite well the shell model results and available data. Such a fit was done in Ref. [21] for all sd -nuclei and all classes of states. The global prescription of the parameter T for some isotopes is shown in Fig. 4.

We call the parameter T in Eq. (3) the effective temperature. Probably more appropriate would be to give a special name to the inverse quantity $1/T$ which characterize the rate of the growth of $\rho(E)$. It is obvious that the exponential increase (4) cannot continue too long as the statistical quantities will diverge. But we know from the full shell-model solution that the total level density has, apart from the edges, the Gaussian form. At some excitation energy, the curve (3) will smoothly join the global Gaussian. The numerical estimate of the parameters [23] agrees with this scenario. The smooth growth of the level density (3) demonstrates the

continuous process of chaotization of dynamics (partly, indeed, due to the relaxation of pairing correlations) and establishing of properties similar to the GOE.

The parameter T changes in a regular way from nucleus to nucleus, Fig. 4. The minimum value, and therefore the fastest rate of chaotization of dynamics, belongs to the even-even isotope ${}^{28}_{14}\text{Si}_{14}$ where all interactions with various isospin values of pairs are present. Similarly, for the odd- A nuclei, the minimum T belongs to the closest nucleus, $N = Z \pm 1$ [24]. Excluding the spin-orbit coupling, one can also noticeably decrease the parameter T as all perturbative interactions become stronger for degenerate orbitals leading to faster onset of chaos.

Interesting physics is related to the collective motion. Long ago the collective enhancement of low-energy level density was predicted due to the excess of soft phonons and rotational bands [25]. Varying the shell-model Hamiltonian one can induce the onset of the deformation [26]. For the quadrupole deformation, the main microscopic role is played by the two-body collisions when one of the particles has a change $\Delta\ell = \pm 2$ of its orbital momentum. This can be easily model in the shell model. Then we see the corresponding increase of the low-lying level density [27] in agreement with the idea of the collective enhancement. In such a way, the relative easiness of calculations allows one to study the roles of individual components of interaction (Fig. 5).

Apart from specific applications, including astrophysical reactions, there are still many unsolved but practically important theoretical problems: to understand the partial values of the parameter T for the classes of states with different total spin J and its dependence on the nuclear deformation (the physics of random coupling

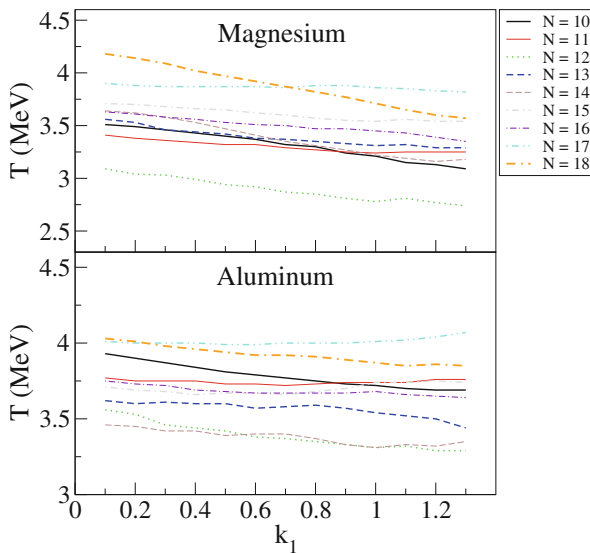


Fig. 5 Evolution of the effective temperature parameter T under variation of the pairing strength k_1 for the isotopes of magnesium and aluminum

of individual spins); to establish the limits of applicability of the shell model from the viewpoint of level density for various groups of nuclei and along the energy scale; to move to heavier nuclei, maybe with random interactions instead of exact matrix elements of incoherent two-body collisions; to study the continuum effects and corresponding reformulation of the level density problem; to compare in detail the Fermi-liquid and constant temperature phenomenology. A special interest is in comparison of microscopic calculations with phenomenological models almost always used by practitioners. Here we have a chance to establish the detailed relation between shell-model interactions and standard parameters of temperature, entropy, spin cut-off, etc. and try to predict microscopically the degree of validity of such a description and global evolution of the parameters. This is important for understanding the process of thermalization in a closed mesoscopic system without any heat bath. Here the interactions play the role of the thermalizing agent and the ideas of statistical physics can be applied to small systems of strongly interacting constituents.

Acknowledgments The whole development of the method was done in collaboration with M. Horoi and R.A. Sen'kov; discussions with N. Auerbach and B.A. Brown are acknowledged. We thank students A. Renzaglia and A. Berlaga for participation in the research. The work on level density was supported by NSF grants PHY-1068217 and PHY-1404442, and the grant from the Binational Science Foundation US-Israel.

References

1. T. Ericson, *Adv. Phys.* **9**, 425 (1960)
2. A. Gilbert, A.G.W. Cameron, *Can. J. Phys.* **43**, 1446 (1965)
3. T. von Egidy, D. Bucurescu, *J. Phys. Conf. Ser.* **338**, 012028 (2012)
4. S. Goriely, S. Hilaire, A.J. Koning, *Phys. Rev. C* **78**, 064307 (2008)
5. S. Hilaire, M. Girod, S. Goriely, A.J. Koning, *Phys. Rev. C* **86**, 064317 (2012)
6. Y. Alhassid, G.F. Bertsch, S. Liu, H. Nakada, *Phys. Rev. Lett.* **84**, 4313 (2000)
7. Y. Alhassid, S. Liu, H. Nakada, *Phys. Rev. Lett.* **99**, 162504 (2007)
8. Y. Alhassid, A. Mukherjee, H. Nakada, C. Ozen, *J. Phys. Conf. Ser.* **403**, 012012 (2012)
9. V. Zelevinsky, M. Horoi, *Prog. Part. Nucl. Phys.* **105**, 180 (2019)
10. I.C. Percival, *J. Phys. B* **6**, L229 (1973)
11. V. Zelevinsky, B.A. Brown, N. Frazier, M. Horoi, *Phys. Rep.* **276**, 85 (1996)
12. V. Zelevinsky, *Annu. Rev. Nucl. Part. Phys.* **46**, 237 (1996)
13. V.V. Flambaum, F.M. Izrailev, *Phys. Rev. E* **56**, 5144 (1997)
14. J.B. French, K.F. Ratcliff, *Phys. Rev. C* **3**, 94 (1971)
15. T.A. Brody, J. Flores, J.B. French, P.A. Mello, A. Pandey, S.S.M. Wong, *Rev. Mod. Phys.* **55**, 385 (1981)
16. V.K.B. Kota, R.U. Haq (eds.), *Spectral Distributions in Nuclei and Statistical Spectroscopy* (World Scientific, Singapore, 2010)
17. S.S.M. Wong, *Nuclear Statistical Spectroscopy* (Oxford, University Press, 1986)
18. R.A. Sen'kov, M. Horoi, V.G. Zelevinsky, *Comput. Phys. Commun.* **184**, 215 (2013)
19. B.A. Brown, W.E. Ormand, LLNL-PROC-758995 (2018)
20. R. Sen'kov, V. Zelevinsky, *Phys. Rev. C* **93**, 064304 (2016)
21. S. Karampagia, R.A. Sen'kov, V. Zelevinsky, *At. Data Nucl. Data Tables* **120**, 1 (2018)

22. L.G. Moretto, A.C. Larsen, F. Giacoppo, M. Guttormsen, S. Siem, A.V. Voinov, J. Phys. Conf. Ser. **580**, 012048 (2015). arXiv: 1406.2642
23. V. Zelevinsky, S. Karampagia, A. Berlaga, Phys. Lett. B **783**, 428 (2018)
24. S. Karampagia, A. Renzaglia, V. Zelevinsky, Nucl. Phys. A **962**, 46 (2017)
25. A.V. Ignatyuk, K.K. Istekov, G.N. Smirenkin, Sov. J. Nucl. Phys. **29**, 450 (1979)
26. M. Horoi, V. Zelevinsky, Phys. Rev. C **81**, 034306 (2010)
27. S. Karampagia, V. Zelevinsky, Phys. Rev. C **94**, 014321 (2016)

Constraining Level Densities Using Spectral Data



G. P. A. Nobre, D. A. Brown, and M. W. Herman

1 Introduction

As the nuclear excitation energy grows, due to the exponential increase of the number of levels, one must deal with the level densities (LD) rather than with individual levels. Several phenomenological models exist to describe the general behavior of (LD), such as the Gilbert-Cameron (GC) [1] and others, which assume simplified functional forms of the LD and are constrained by the often limited availability of experimental data. It is known that there are only a few ways to experimentally constrain LD, such as through the D_0 (LD at neutron separation energy of the compound nucleus) or the matching at the excitation energy region transitioning from discrete levels to LD.

More fundamental and predictive LD models like the microscopic Hartree-Fock-Bogoliubov (HFB) [2] incorporated to the RIPL-3 parameter library [3] provide more global and consistent LD, based on the intrinsic structure properties of nuclei and observed distribution of discrete levels. This brings reliability to the LD in the whole range of excitation energy, not only near the discrete-level cut-off or at D_0 . Additionally, the HFB model provides more realistic spin and parity distributions which emerge naturally from the model, while a phenomenological model such as GC simplistically assumes equal distributions for parities and a Gaussian-like distribution for spins.

G. P. A. Nobre (✉) · D. A. Brown
National Nuclear Data Center, Brookhaven National Laboratory, Upton, NY, USA
e-mail: gnobre@bnl.gov

M. W. Herman
National Nuclear Data Center, Brookhaven National Laboratory, Upton, NY, USA
Los Alamos National Laboratory, Los Alamos, NM, USA

In nuclear reaction evaluations, however, predictive models are seldom employed since the greater flexibility of parameter fitting of phenomenological models may lead to better cross-section agreements [4]. In this work we aim to circumvent this apparent deficiency of the HFB LD model by using experimental data from neutron double-differential spectra cross sections on ^{56}Fe to impose direct constraints on the HFB total LD for ^{56}Fe and ^{56}Mn . We show that we can obtain a more realistic LD and at least equally good cross sections compared to a fitted Gilbert-Cameron model, in particular for the $^{56}\text{Fe}(n,p)$ reaction which is of dosimetry interest. This way we can combine the predictive power of a microscopic model with good description of observed data, as required by a variety of applications. We also investigate the consequences of this approach in the prediction of inelastic gamma cross sections as compared to measured data.

2 Description of LD Models

LD models are crucial for Hauser-Feshbach and pre-equilibrium reaction mechanisms. Phenomenological models tend to better reproduce average behaviors while missing detailed structure components. We will discuss the phenomenological GC and the microscopic HFB models, as implemented in EMPIRE [5].

2.1 Gilbert-Cameron Model

Most phenomenological LD models are based in some form on the analytical expression derived from the Fermi Gas Model [1]. We assume that the density of intrinsic levels with spin J , parity π , and excitation energy E_x can be factored in terms of its state density and spin and parity dependence. The Gilbert-Cameron model [1] splits the excitation energy range into two parts, with different functional forms applied to each of them. Below a chosen matching energy U_x a constant-temperature state density is employed while above U_x the back-shifted Fermi Gas state density is adopted, with pairing energy given by $\Delta = n \frac{12}{\sqrt{A}}$, where A is the nucleus mass number and n is 0, 1, or 2 for odd-odd, odd-even, and even-even nuclei, respectively. Some model parameters are internally determined by imposing that the total LD and its derivative are continuous at the matching point U_x .

2.2 HFB Model

EMPIRE has implemented within its options the microscopic combinatorial approach [2] developed for RIPL-3 [3]. It consists of using single-particle level

schemes obtained from constrained axially symmetric Hartree-Fock-Bogoliubov method (HFBM) based on the BSk14 Skyrme force to construct incoherent particle-hole state densities as functions of the excitation energy E_x , the spin projection M (on the intrinsic symmetry axis of the nucleus), and the parity π . Collective effects are incorporated through a boson partition function providing vibrational state densities dependent on multiphonon energies.

3 Implementing Constraints from Neutron Differential Spectra Data

We adopted the $n + {}^{56}\text{Fe}$ reaction as our test case to identify the impact of details of LD in the cross sections, using the same parametrization employed in the fast-region evaluation of ${}^{56}\text{Fe}$ present in the ENDF/B-VIII.0 evaluation [6, 7] as part of the CIELO project [8], ensuring that all calculated cross sections are mutually consistent and in good agreement with experimental data. We performed reaction calculations using five different approaches for the LD: (a) assuming the GC model for all nuclei, as done in the ${}^{56}\text{Fe}$ evaluation [6, 7] (green curves in Figs. 1, 2, 3, and 4); (b) assuming HFB LD as available from RIPL, with no modifications to it (red curves in Figs. 1, 2, and 3); (c) same as (b) but fitting two parameters of ${}^{56}\text{Mn}$ LD to (n,p) data (blue curves in Figs. 2, 3, and 4); (d) same as (c) but with the ${}^{56}\text{Fe}$ LD structures smoothed out in order to improve agreement with experimental data of neutron double-differential spectra (magenta curves in Figs. 1, 3, and 4); (e) same as (d) but with ${}^{56}\text{Mn}$ smoothed and refitted to (n,p) cross sections (cyan curves in Figs. 2 and 3).

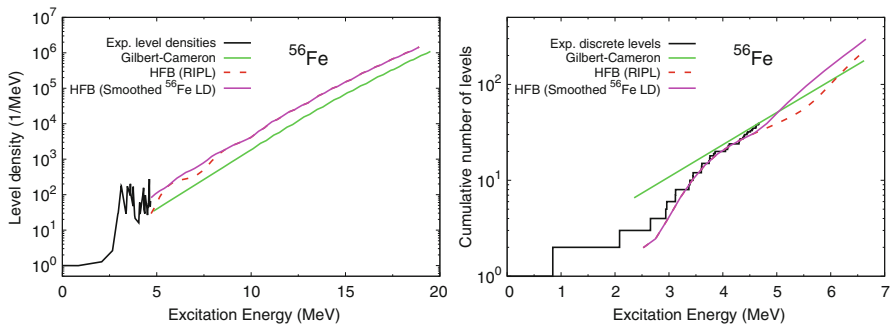


Fig. 1 Level densities and cumulative number of levels of ${}^{56}\text{Fe}$ for the different LD approaches explained in Sect. 3. Red curves made dashed to facilitate visualization

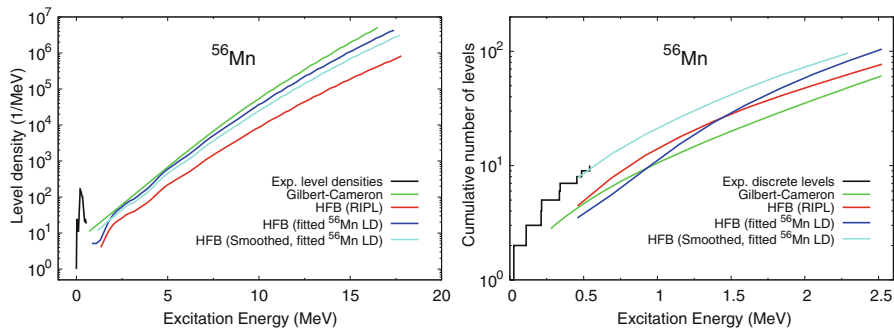
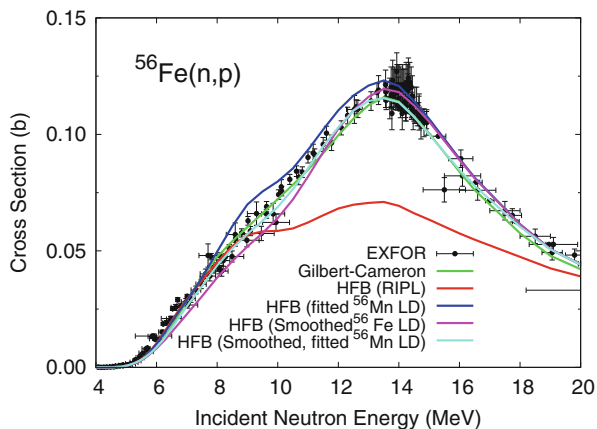


Fig. 2 Level densities and cumulative number of levels of ^{56}Mn for the different LD approaches explained in Sect. 3

Fig. 3 $^{56}\text{Fe}(n,p)^{56}\text{Mn}$ cross section obtained from the adoption of the different LD approaches explained in Sect. 3. Experimental data from EXFOR [9]



4 Discussion

By comparing the green and red curves in Fig. 1 we see that while the GC LD is smooth (as it comes from constant-temperature analytical forms), the HFB LD present fluctuations, or structures, in the range $5 \lesssim E_x \lesssim 9$ MeV. Both GC and HFB (from RIPL) models approximately reproduce reasonably well the number of levels at around 4.5 MeV which is around where one would normally impose the transition from the discrete levels to LD. This transition point, or excitation energy cut-off, can however be rather arbitrary. One can clearly see from Fig. 1 that the HFB predicted cumulative number of levels yields a much better agreement with the overall behavior of observed discrete levels, which makes it much more independent from the choice of excitation energy at which the transition to LD is made. Even though these two apparently similarly reasonable (from the perspective of discrete-level matching) LD models, they lead to dramatically different (n,p) cross sections (Fig. 3). Even after fitting ^{56}Mn LD parameters (blue curve), the

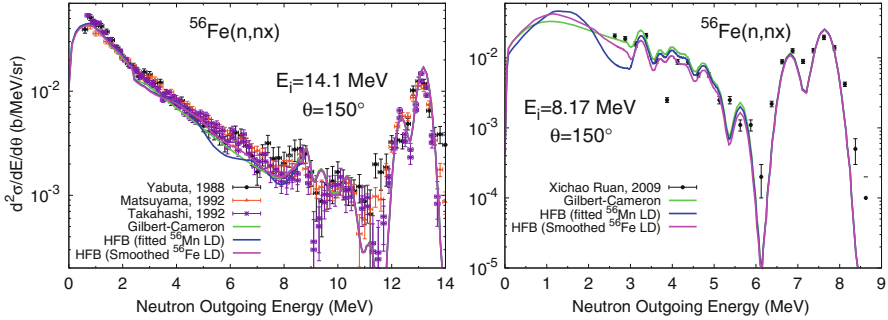


Fig. 4 Example of double-differential spectra for at 150 degrees and neutron incident energies of 14.1 MeV (left panel) and 8.17 MeV (right panel) for the different LD approaches explained in Sect. 3. Data from EXFOR [9]

agreement with (n,p) data is still not optimal. Therefore, additional constraints for the LD are needed. By noticing direct correlations between the ^{56}Fe LD for a given E_x region and the DD cross section at certain neutron-outgoing energies, we were able to use the experimental knowledge of DD spectra to impose constraints on LD. For this we smoothed the structures of the HFB LD by rescaling the tabulated values of HFB LD to the point that effects of these structures would not appear in calculated DD spectra and that the agreement with DD experimental data would be satisfactory (Fig. 4). The result of this is shown as the magenta curves. Even though this produced a considerably better agreement with (n,p) data, this is still not as good as the GC one. This can be remediated by smoothing and refitting the ^{56}Mn LD to minimize χ^2 relative to (n,p) experimental data. This resulted in the cyan curves. In addition to obtaining better (n,p) cross sections, this also leads to a more realistic ^{56}Mn LD relative to the observed discrete levels (Fig. 2).

5 Impact on Inelastic Gammas

Another application of using experimental DD spectra to constrain HFB level densities is in the description of inelastic gamma cross-section data. Recently, cross-section measurements of gamma emissions corresponding to transitions between excited levels have provided new information which is very useful to complement neutron and reaction cross sections in usual neutron evaluations. From a theoretical standpoint, predicting and consistently fitting gamma cross sections can be a challenge due to the variety of mechanisms involved. Therefore, a more predictive and fundamental LD model would provide better reliability for calculated gamma cross sections. We have done the comparison between GC and modified HFB models for all transitions measured in the work of Negret et al. [10], and also other transitions that were not measured. We have found that in some cases there are very little differences. However, for some transitions there are noticeable differences in

calculated cross sections, with the HFB one generally aligning better with observed data. Much greater discrepancy was observed in transitions involving states of opposite parity of that of the ground state, which gives more significance to a more predictive and internally consistent set of LD, especially when experimental data are not available.

6 Summary and Conclusions

Even though it is known that cross sections strongly depend on level densities (LD) there are normally very little direct experimental input in the determination of their details. In this work we explored this feature by imposing constraints in extended regions of LD by observing their impact on the agreement of neutron double-differential spectra with experimental data. This allowed us to extract experiment-based information about LD that is useful for the structure theory community which develop microscopic LD models, as well as to increase the internal self-consistency of models used reaction calculations leading to evaluation-level quality of cross sections. Additionally, this proved to be a method to obtain more reliable inelastic gamma cross sections, in particular for those transitions without measured data or those involving levels with parity opposite of that of the ground state. One might expect that these effects are more pronounced for the nuclei close to the shell closures.

Acknowledgments The work at Brookhaven National Laboratory was sponsored by the Office of Nuclear Physics, Office of Science of the U.S. Department of Energy under Contract No. DE-AC02-98CH10886 with Brookhaven Science Associates, LLC. Work at Los Alamos National Laboratory was carried out under the auspices of the National Nuclear Security Agency of the U.S. Department of Energy under Contract No. DE-AC52-06NA25396.

References

1. A. Gilbert, A.G.W. Cameron, *Can. J. Phys.* **43**, 1446 (1965)
2. S. Goriely, S. Hilaire, A.J. Koning, *Phys. Rev.* **C78**, 064307 (2008)
3. R. Capote et al., *Nucl. Data Sheets* **110**, 3107 (2009)
4. G.P.A. Nobre et al., *EPJ Web Conf.* **111**, 03001 (2016)
5. M. Herman et al., *Nucl. Data Sheets* **108**, 2655 (2007)
6. M. Herman et al., *Nucl. Data Sheets* **148**, 214 (2018)
7. D.A. Brown et al., *Nucl. Data Sheets* **148**, 1 (2018)
8. M.B. Chadwick et al., *Nucl. Data Sheets* **148**, 189 (2018)
9. V.V. Zerkin, B. Pritychenko, *Nucl. Inst. Meth. A* **888**, 31 (2018)
10. A. Negret et al., *Phys. Rev.* **C90**, 034602 (2014)

Rotational Enhancement Factor for Nuclear Level Density



S. M. Grimes

1 Introduction

Bethe was the first to examine the nuclear level density problem. He showed [1] that the density of nuclear states per MeV was given by

$$\rho_T(E) = \frac{\sqrt{\pi}}{12} \frac{\exp(2\sqrt{aE})}{a^{1/4} E^{5/4}}. \quad (1)$$

In this equation, E is the energy of excitation in MeV and a is the constant called the level density parameter which is normally found to be approximately $A/8 \text{ MeV}^{-1}$, where A is the mass number. By making the assumption that a nucleus is spherical, Bethe was able to show that

$$\rho(E, J) = \frac{\rho_T(E)(J + 1/2)}{\sqrt{2\pi}\sigma^3} \exp\left(-\frac{(J + 1/2)^2}{2\sigma^2}\right) = \rho_L(E)S(J). \quad (2)$$

In this equation, $\rho_L(E, J) (= \rho_T(E)/\sqrt{2\pi}\sigma)$ is the total number of levels per MeV and σ is the spin cutoff parameter (expectation of $\langle J_z^2 \rangle > 1/2$). $S(J)$ is the fraction of the levels which have spin J :

$$S(J) = \frac{(J + 1/2)}{\sigma^2} \exp\left(-\frac{(J + 1/2)^2}{2\sigma^2}\right). \quad (3)$$

If the nucleus is spherical,

S. M. Grimes (✉)

Department of Physics and Astronomy, Ohio University, Athens, OH, USA

e-mail: grimes@ohio.edu

© This is a U.S. government work and not under copyright protection in the U.S.; foreign copyright protection may apply 2021

J. Escher et al. (eds.), *Compound-Nuclear Reactions*, Springer Proceedings in Physics 254, https://doi.org/10.1007/978-3-030-58082-7_16

$$\sum_J (2J + 1) \rho(E, J) = \rho_T(E) S(J) \quad (4)$$

since each level consists of $(2J + 1)$ degenerate states with spin projections $(-J < J_z < J)$, where J_z is the spin projection on the z -axis.

Bohr and Mottelson [2] discussed in some details the effect of nuclear deformation. In most cases nuclear deformation results in an axially symmetric ellipsoidal form. This results in two spin cutoff factors. σ_{\parallel} is the cutoff factor for rotations about the symmetry axes (z -axis), while σ_{\perp} is the factor for rotations about an axis perpendicular to a symmetry axis. Bohr and Mottelson conclude that level density for deformed nucleus will be a factor of σ_{\perp}^2 larger than would the case for a corresponding spherical nucleus. A similar result has been obtained by Junghans [3]. More recently, an analysis of the situation for level densities in deformed nuclei [4] has concluded that the rotational enhancement factor is not only dependent on E (σ_{\perp}^2 varies approximately as $E^{1/2}$) but includes a significant change with J . It is proposed that

$$R(E, J, K) = \frac{(J + 1)^2 - K^2}{2J + 1} \exp \left[-K^2 \cdot \left(\frac{1}{2\sigma_{\parallel}^2} - \frac{1}{2\sigma_{\perp}^2} \right) \right]. \quad (5)$$

In this expression, K is the projection of the angular momentum J on a symmetry axis. K is found to be a good quantum number for $E \leq 3$ MeV, but as the level density increases at higher energies, K values become mixed. Thus, it is more reasonable to define an enhancement factor which depends only on J and E

$$R_1(E, J) = \frac{\sum_{K=0}^J R(E, J, K) \rho(E, J, K)}{\sum_{K=0, 1/2} \rho(E, J, K)}. \quad (6)$$

The lower limit on the sum will be zero for even-A and 1/2 for odd-A.

This factor varies rapidly with J . Note that for $J = 0$ or 1/2 the factor is 1 (no enhancement). An enhancement comes from two effects. First, the deformation splits a level of spin J into $(J + 1/2)$ (odd-A) or $J + 1$ (even-A) levels of spin J but differing K as a result of deformation. In addition, the adding of rotational bands increases level density for all J values larger than the J of the band head. This will not enhance the density of the lowest value of J . Thus, although this function grows approximately as J^2 , it is only one for the $J = 0$ or $J = 1/2$ levels.

2 Level Densities from Low-Energy Resonance Counting

At low energies, neutrons can only interact with nuclei in $l = 0$ states. Thus, for even-even targets, neutrons excite only compound nuclear levels of spin 1/2 and positive parity. An odd-A target or an even-A target with spin $J_0 \neq 0$ will allow

the excitation of levels with spin $J = J_0 \pm 1/2$. To obtain the total level density, one must correct the inferred level density for levels of other J values. It is usually assumed that the spin distribution proposed by Bethe is valid, in which a correction factor would be

$$\rho_T(E) = \frac{\rho(E, 1/2)}{S(1/2)} \sum_J S(J) \quad (7)$$

for even- A targets or

$$\rho_T(E) = \frac{\rho(E, J_0 - 1/2) + \rho(E, J_0 + 1/2)}{S(J_0 - 1/2) + S(J_0 + 1/2)} \sum_J S(J) \quad (8)$$

for non-zero spin targets. An additional factor of two is applied to the right hand side of Eqs. 7 and 8 to correct for levels of the other parity. It is obvious from Ref. [4] that the correction formula will be different for deformed nuclei. The corresponding formulas based on Eq. 6 will be

$$\rho_T(E) = \frac{\rho(E, 1/2) \sum_J S(J) R_1(E, J)}{S(1/2) R_1(E, 1/2)} \quad (9)$$

and

$$\begin{aligned} \rho_T(E) = & \frac{\rho(E, J_0 - 1/2) + \rho(E, J_0 + 1/2)}{S(J_0 - 1/2) R_1(E, J_0 - 1/2) + S(J_0 + 1/2) R_1(E, J_0 + 1/2)} \\ & \times \sum_J S(J) R_1(E, J) \end{aligned} \quad (10)$$

for $J_0 = 0$ and $J_0 \neq 0$, respectively. In each case, the right hand side also must be multiplied by a factor of two to correct for levels of the missing parity.

Two compilations of level density parameters from low-energy resonances have been published in Refs. [5, 6]. In the compilation by Rohr [5], there is a specific statement that the results did not show an enhanced level density for deformed nuclei. The conclusion of Ref.[6] is more confusing. The authors derived level density parameters using the conventional Bethe formulas. They find that the a values for deformed nuclei are close to those for nearby spherical nuclei. They then divide the level density by the factor predicted in Ref. [2, 3]. They then calculated the revised a which they refer to as intrinsic. Despite this second step, it is still true that the authors of Ref. [6] do not find higher level densities for deformed nuclei. An important point is that both Refs. [5, 6] used the Bethe spin distribution for both deformed and spherical nuclei. Bethe [1] specifically states that he assumes spherical symmetry in deriving his spin formula.

In table 1 the results of Iljinov et al. [6] are summarized for some deformed nuclei. For each of the nuclei listed, the neutron binding energy, the observed spins,

and the measured level spacing (eV) are provided. The values indicated by a_1 show the level density parameters inferred by the authors by calculating the level density correction using Eqs. 7 and 8. This level density is then divided by the rotational enhancement factor proposed in Refs. [2] and [3]. A new a (labeled a_2) is deduced from the reduced level density. a_1 values are similar to the a values proposed by the authors for neighboring spherical nuclei.

The same input data were then re-analyzed using Eq. 9 or 10 as appropriate. A very substantial increase in level density was observed. This yielded the level density parameters a_3 . Finally, the rotational enhancement factor was inferred by calculating the level density by utilizing the Bethe spin distribution. This then results in parameters a_4 . a_4 values are intrinsic level density parameters (those which would be observed if a nucleus was not deformed) and are consistent with neighboring spherical nuclei. To use Eqs. 9 and 10 values for σ_{\perp} are needed. Values for σ_{\parallel} were obtained from the results of calculations in Ref. [7]. It may be shown that the relationship between σ_{\perp} and σ_{\parallel} is

$$\frac{\sigma_{\perp}^2}{\sigma_{\parallel}^2} = \frac{1 + \frac{1}{2}\beta + \frac{16}{7}\beta^2 + \beta^3}{1 - \beta + \frac{10}{7}\beta^2 - \frac{2}{7}\beta^3}. \quad (11)$$

In this expression the β is the nuclear deformation and $\beta > 0$ is the prolate shape, $\beta = 0$ is a spherical shape, and $\beta < 0$ is an oblate shape. Terms in β^4 and β^5 are also present in the exact form of Eq. 11, but they have less than 1% effect.

Note that the values for the rotational enhancement factor in Table 1 range from a value of about 8 for $A \approx 25$ to a of about 60 for $A \approx 240$. These are reasonably consistent with theoretical predictions in Refs. [2] and [3].

Table 1 Level densities for deformed nuclei inferred with spherical and deformed spin distributions

Nucleus	Spin	S_n	D	a_1	a_2	a_3	a_4	R
^{24}Na	1,2	6.96	$9.5 \cdot 10^4$	3.49	1.75	4.35	2.76	8.3
^{25}Mg	1/2	7.33	$4.7 \cdot 10^5$	3.67	1.92	6.33	4.14	7.6
^{26}Mg	2,3	11.073	$5.5 \cdot 10^4$	4.16	2.37	4.48	2.85	8.75
^{159}Dy	1/2	6.83	30	20.81	13.05	30.0	22.1	47.8
^{161}Dy	1/2	6.45	27.3	22.12	14.06	32.3	23.7	42.9
^{162}Dy	2,3	8.197	2	21.34	13.58	26.8	18.4	45.3
^{163}Dy	1/2	6.27	69	21.08	13.01	31	22.4	42.5
^{164}Dy	2,3	7.63	5	21.2	13.24	26.9	19.2	46.1
^{165}Dy	1/2	5.71	170	21.05	12.67	31.7	22.8	44
^{235}U	1/2	5.298	10.6	30.26	19.23	44.8	32.8	63
^{238}U	0,1	6.15	3.5	30.55	19.58	45.1	32.8	67

3 Summary

There has been a long-standing inconsistency between theoretical predictions for the rotational enhancement factor and values obtained from resonance measurements. A resolution of these inconsistencies comes from realization that this factor does not only depend on energy but also has a rapid dependence on J as well. When this dependence is introduced, the experimental results brought into agreement with theory.

Acknowledgement This work has been supported by Department of Energy grant DE-NA0002905.

References

1. H.A. Bethe, An attempt to calculate the number of energy levels of a heavy nucleus. *Phys. Rev.* **50**, 332 (1936)
2. A. Bohr, B.R. Mottelson, *Nuclear Structure* (W. A. Benjamin, New York, 1969)
3. A.R. Junghans, M. de Jong, H.G. Clerc, A.V. Ignatyuk, G.A. Kudyayev, K.H. Schmidt, Projectile-fragment yields as a probe for the collective enhancement in the nuclear level density. *Nucl. Phys. A* **629**(3), 635–655 (1998). [https://doi.org/10.1016/S0375-9474\(98\)00658-7](https://doi.org/10.1016/S0375-9474(98)00658-7)
4. S.M. Grimes, A Hauser-Feshbach code for deformed nuclei. *Phys. Rev. C* **88**, 024613 (2013)
5. G. Rohr, New perspectives on the level density of compound resonances. *Z. Phys. A: At. Nucl.* **318**(3), 299–308 (1984). <https://doi.org/10.1007/BF01418087>
6. A. Iljinov, M. Mebel, N. Bianchi, E.D. Sanctis, C. Guaraldo, V. Lucherini, V. Muccifora, E. Polli, A. Reolon, P. Rossi, Phenomenological statistical analysis of level densities, decay widths and lifetimes of excited nuclei. *Nucl. Phys. A* **543**(3), 517–557 (1992). [https://doi.org/10.1016/0375-9474\(92\)90278-R](https://doi.org/10.1016/0375-9474(92)90278-R)
7. S.M. Grimes, A.V. Voinov, T.N. Massey, Mass-number and excitation-energy dependence of the spin cutoff parameter. *Phys. Rev. C* **94**, 014308 (2016). <https://doi.org/10.1103/PhysRevC.94.014308>

Role of Fluctuations on the Pairing Properties of Nuclei in the Random Spacing Model



M. A. A. Mamun, C. Constantinou, and M. Prakash

1 Pairing in Systems of Large and Small Numbers of Particles

The Bardeen-Cooper-Schrieffer (BCS) theory of superconductivity [1, 2] predicts a sharp discontinuity in the constant-volume specific heat C_V at a certain critical temperature T_c for which the pairing gap Δ of fermions determined from the gap and number equations [3, 4]

$$\mathcal{G} \equiv \sum_k \frac{1}{E_k} \tanh\left(\frac{E_k}{2T}\right) - \frac{2}{G} \quad (1)$$

$$N = \sum_k \left[1 - \frac{\epsilon_k - \lambda}{E_k} \tanh\left(\frac{E_k}{2T}\right) \right] + \frac{\Delta}{T} \frac{\partial \Delta}{\partial \alpha} \mathcal{G} \quad (2)$$

vanishes. Above, G is the strength of the pairing interaction, T is the temperature, λ is the chemical potential, $\alpha = \lambda/T$, $E_k = \sqrt{(\epsilon_k - \lambda)^2 + \Delta^2}$ is the quasiparticle energy, and ϵ_k are the single particle (sp) energies. The corresponding energy E and entropy S are obtained from

M. A. A. Mamun (✉) · M. Prakash
Department of Physics and Astronomy, Ohio University, Athens, OH, USA
e-mail: ma676013@ohio.edu; prakash@ohio.edu

C. Constantinou
Department of Physics, Kent State University, Kent, OH, USA
e-mail: cconsta5@kent.edu

$$E = \sum_k \epsilon_k \left[1 - \frac{\epsilon_k - \lambda}{E_k} \tanh\left(\frac{E_k}{2T}\right) \right] - \frac{\Delta^2}{G} - \left(\Delta^2 - \Delta T \frac{\partial \Delta}{\partial T} \right) \mathcal{G} \quad (3)$$

$$S = 2 \sum_k \left\{ \ln \left[1 + \exp\left(-\frac{E_k}{T}\right) \right] + \frac{E_k/T}{1 + \exp(E_k/T)} \right\} - \frac{\Delta}{T} \left(\frac{\lambda}{T} \frac{\partial \Delta}{\partial \alpha} - T \frac{\partial \Delta}{\partial T} \right) \mathcal{G}. \quad (4)$$

These relations enable the evaluation of $C_V = dE/dT|_{V,N} = T(\partial S/\partial T)|_{V,N}$.

The grand potential Ω of the system is

$$\Omega(T, \Delta) = \sum_k (\epsilon_k - \lambda - E_k) - 2T \sum_k \ln \left[1 + \exp\left(-\frac{E_k}{T}\right) \right] + \frac{\Delta^2}{G}. \quad (5)$$

In a mean field description of the BCS theory, $(\partial \Omega/\partial \Delta)|_T = 0 = \mathcal{G}$ which leads to the most probable gap Δ_{mp} . For systems with large numbers of particles, fluctuations in the order parameter Δ are very small as the probability distribution

$$P(\Delta) \propto \exp[-\Omega(T, \Delta)/T] \quad (6)$$

where the grand potential Ω is very sharply peaked at Δ_{mp} . In this case, Eqs. (2)–(4) revert back to the standard mean field BCS equations. For $\Delta \neq \Delta_{\text{mp}}$, $\mathcal{G} \neq 0$, and Eqs. (2)–(4) and hence C_V receive additional contributions.

In systems with small numbers of particles, fluctuations in Δ are not small. As first noted by Anderson in his paper “Theory of Dirty Superconductors” [5], the pairing phenomenon is suppressed due to large fluctuations in Δ which in turn leads to a “shoulder-like” or “S-shaped” smooth curve for C_V vs T . That a similar suppression would occur in nuclei also was first noted by Moretto in Ref. [3]. The absence of a sharp second order phase transition due to pairing in nanoparticles and nuclei is shown in Fig. 1, which contains results of Auxiliary Field Monte Carlo (AFMC) calculations for C_V vs T including fluctuations by Alhassid et al. [6]. Such “S-shaped” heat capacities in nuclei have been observed in experiments by the Oslo group [7].

2 Fluctuations in the Order Parameter Δ

Fluctuations can arise from many sources. When T is too low or Δ varies too rapidly with time, a thermodynamic treatment becomes inadequate and a fully quantum approach that accounts for correlations beyond mean field theory, pairing vibrations and suppression of pairing due to rotational motion, etc., becomes necessary [8–18]. A semiclassical treatment of thermal fluctuations based on Eq. (6) and $\mathcal{G} \neq 0$ in

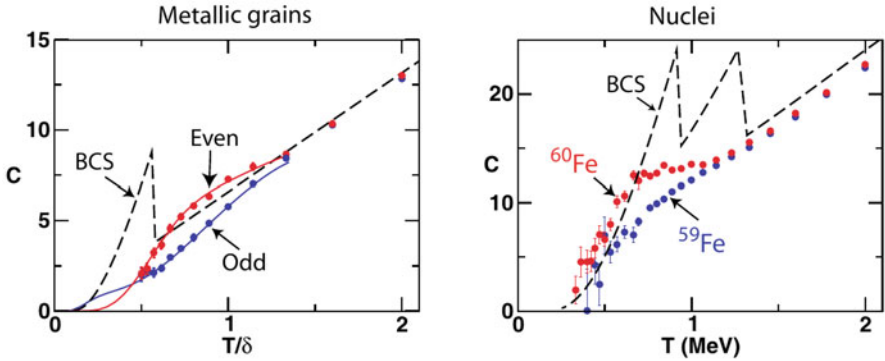


Fig. 1 Specific heat in nanoparticles (left) and iron isotopes (right) demonstrating the disappearance of a second order phase transition present in the mean field BCS formalism. Figure adapted from Alhassid [6]

Eqs. (1)–(4) is afforded when Δ is strongly coupled to all other intrinsic degrees of freedom, that is when $\Delta \gg \delta$, where $\delta = 1/g$ is the mean level spacing of the sp energy levels near the Fermi sea [3, 8]. For infinite systems (e.g., bulk nuclear matter) $P(\Delta)$ approaches a delta function, $\delta \ll \Delta$, whence fluctuations are negligible and mean field BCS with $\mathcal{G} = 0$ is a reasonable description. In contrast, for small systems such as nanoparticles or light-to-medium heavy nuclei, $\delta \sim \Delta$ or $\delta \geq \Delta$ particularly at $T \neq 0$, fluctuations in Δ are large and suppress superconductivity and superfluidity. In this case, the mean field BCS approach is no longer applicable as it neglects the influence of fluctuations.

Figure 2 illustrates the role of fluctuations in the constant spacing (CS) model with $g = 5 \text{ MeV}^{-1}$ for doubly degenerate sp energy levels for $N = 144$ and $\Delta(0) = 1 \text{ MeV}$ at $T = 0$. For this choice, $G = 0.0581 \text{ MeV}$, $\hbar\omega \simeq 41N^{-1/3} = 7.78 \text{ MeV}$, with levels uniformly distributed between $\pm 2\hbar\omega$ around $\lambda_{\text{mp}}(0) = -1.3471 \text{ MeV}$ at $T = 0$. The probability $P(\Delta)$ is normalized such that $P(\Delta_{\text{mp}}) = 1$ for all T . For all curves shown, $\lambda(T)$ vs T is calculated for each $\Delta \neq \Delta_{\text{mp}}$ using Eq. (2) thus ensuring number conservation. The results in this figure are similar to those of Ref. [3] where $g = 7 \text{ MeV}^{-1}$ was used.

The salient features in the left panel of Fig. 2 are (1) for low T such that $T/\Delta(0) \ll 1$, $P(\Delta)$ is symmetrical around Δ_{mp} , (2) with increasing T , $P(\Delta)$ becomes increasingly asymmetrical, and (3) for $T \geq T_c \simeq 0.57 \text{ MeV}$, $P(\Delta)$ is peaked at $\Delta = 0$. For all $T \neq 0$, the term involving the nonzero \mathcal{G} in Eq. (2) gives significant contributions. As $P(\Delta)$ is very broad for $T \rightarrow T_c$ and beyond, use of average thermodynamic quantities $\langle \tilde{O} \rangle = \sum \tilde{O} P(\Delta) / \sum P(\Delta)$ is more appropriate than those with Δ_{mp} . The right panel of Fig. 2 provides contrasts between Δ_{mp} and Δ_{av} as well as for gaps differing by $\pm 1\sigma$ from Δ_{av} . The latter gaps are nonzero for $T > T_c$, unlike Δ_{mp} , indicating that pairing correlations persist beyond T_c . The excitation energies $E_x = E(T) - E(0)$ and C_V with the gaps shown in Fig. 2 are shown in Fig. 3. As noted in Refs. [3], and confirmed

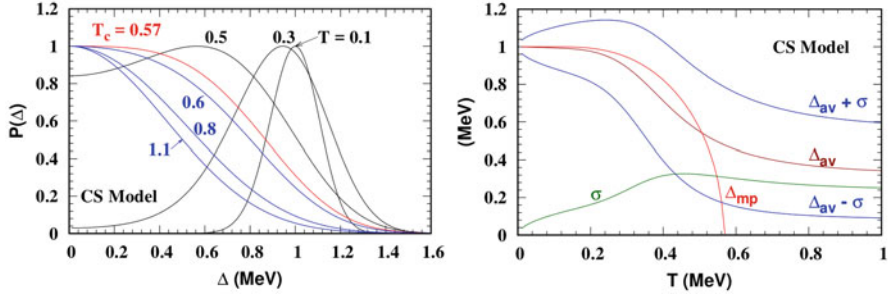


Fig. 2 Probability distribution of the pairing gap (left) and the gap as a function of temperature (right) in the constant spacing (CS) model. Figure adapted from [19]

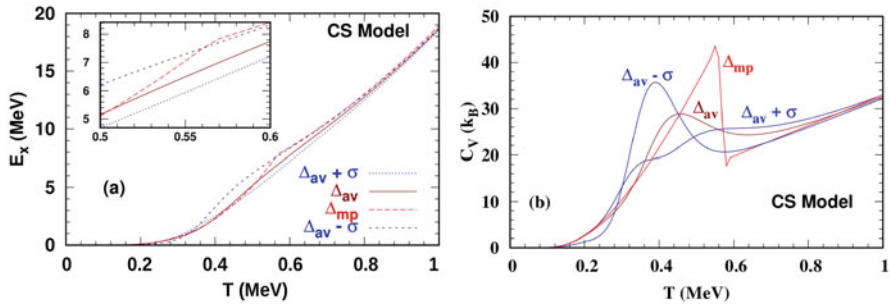


Fig. 3 Excitation energies (a) and specific heats at constant volume (b) with the gaps shown in Fig. 2. Figure adapted from [19]

here, the second order phase transition present for Δ_{mp} is considerably altered by fluctuations. Notably, the C_V vs T curve is devoid of a discontinuity at T_c with smoothly varying gaps.

3 The Random Spacing Model

Recently, the random spacing (RS) model in which the sp energy levels are randomly distributed around the Fermi energy to mimic those of nuclei obtained via the use of different energy density functionals (EDF's) was introduced [19]. In a set consisting of a very large number of randomly generated sp levels for a given nucleus, some are likely to represent the true situation especially considering the variation that exists when different EDF's and pairing schemes are used.

Figure 4 presents an illustration of the similarity between the sp energy levels of nuclei from Hartree-Fock-Bogoliubov calculations using a Skyrme EDF (SkO') [20–22] and those of the RS model. One advantage of this model is that using



Fig. 4 (Left) Single particle energy levels of nuclei from HFB calculations using a Skyrme EDF (SkO') [20–22]. (Right) Results of HFB calculations for $N = 76$ and three realizations from the RS model. Dotted lines represent the Fermi surface. Figure adapted from [19]

easily generated sp levels, statistically based bounds can be placed on the pairing properties of each nucleus.

Including fluctuations using Δ_{av} as outlined in Sect. 2, the specific heat C_V as a function of temperature is shown in Fig. 5 using a large number of the RS model sp energy levels. The levels were randomly distributed within a window of $2\hbar\omega$ around the Fermi level for $N = 144$. Each level was endowed with the degeneracy $d = 2j + 1$ characteristic of shell model sp energy levels with angular momentum j . Increasing the number of random realizations in the ensemble makes the band denser, but the borders remain more or less the same. This feature indicates that results obtained using realistic EDF's would lie within the band shown. This feature is particularly useful for performing sensitivity tests in astrophysical settings that harbor exotic nuclei. Note also the absence of a second order phase transition as evidenced by the shoulder-like or S-shaped structure of C_V around T_c of the mean field BCS model.

Results of C_V using Δ_{mp} , Δ_{av} , and $\Delta_{av} \pm \sigma$ for two realizations among hundreds of individual random realizations of sp energy levels are shown in the right panel of Fig. 5. Although the overall features in this figure are similar to those of the CS Model, quantitative differences exist owing to the different bunching and degeneracy of the individual sp energy levels of the RS model.

4 Outlook

Calculations of level densities and the spin distributions of nuclei including fluctuations in the RS model are in progress and will be reported elsewhere. A semiclassical treatment of fluctuations is strictly valid only when the mean sp level spacing around the Fermi surface is smaller or nearly equal to the zero temperature pairing gap and a fully quantum treatment of fluctuations becomes necessary otherwise to overcome the limitations of the mean field BCS formalism [8–18]. Contrasting the semiclassical and quantum treatments of fluctuations in the canonical and grand

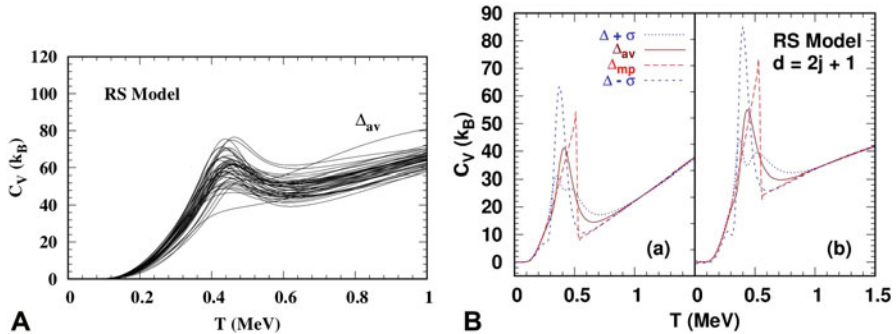


Fig. 5 Specific heat obtained using the RS model with the inclusion of fluctuations (A). Two independent realizations of the RS model with use of the most probable and average gaps including $1\text{-}\sigma$ deviations (B). Figure adapted from [19]

canonical approaches [12, 18] as well as investigations of fluctuations in highly neutron-rich isotopes with more advanced techniques in the context of the RS model are other investigations under study.

Acknowledgments Beneficial communications with P.-G. Reinhardt, Steve Grimes, Alexander Voinov and Tom Massey are gratefully acknowledged. This work was performed with research support from the U.S. DOE grant No. DE-FG02-93ER-40756.

References

1. J. Bardeen, L.N. Cooper, J. R. Schrieffer, Phys. Rev. **106**, 162 (1957)
2. J. Bardeen, L.N. Cooper, J.R. Schrieffer, Phys. Rev. **108**, 1175 (1957)
3. L.G. Moretto, Phys. Lett. B **40**, 1 (1972)
4. L.G. Moretto, Nucl. Phys. A **185**, 145 (1972)
5. P.W. Anderson, J. Phys. Chem. Solids **11**, 26 (1959)
6. Y. Alhassid, Thermal signatures of pairing correlations in nuclei and metal nanoparticles, in *50 Years of Nuclear BCS: Pairing in Finite Systems*, ed. by R.A. Broglia, V. Zelevinsky (World Scientific, Singapore, 2013), p. 608
7. R. Chankova et al., Phys. Rev. C **73**, 034311 (2006)
8. L.D. Landau, E.M. Lifshitz, *Statistical Physics Part 1* (Pergamon Press, Oxford, 1980)
9. G. Falci, R. Fazio, F.W.J. Hekking, A. Mastellone, J. Low Temp. Phys. **118**, 355 (2000)
10. Y.R. Shimizu, P. Donati, R.A. Broglia, Phys. Rev. Lett. **85**, 2260 (2000)
11. A. Schiller et al., Phys. Rev. C **63**, 021306 (2001)
12. Y. Alhassid, G.F. Bertsch, L. Fang, S. Liu, Phys. Rev. C **72**, 064326 (2005)
13. K. Kaneko, A. Schiller, Phys. Rev. C **76**, 064306 (2007)
14. U. Agvaanluvsan et al., Phys. Rev. C **79**, 014320 (2009)
15. H.K. Toft et al., Phys. Rev. C **81**, 064311 (2010)
16. H.K. Toft et al., Phys. Rev. C **83**, 044320 (2011)
17. Z. Kargar, V. Dehghani, J. Phys. G. Nucl. Part. Phys. **40**, 045108 (2013)
18. Y. Alhassid, G.F. Bertsch, C.N. Gilbreth, H. Nakada, Phys. Rev. C **93**, 044320 (2016)
19. M.A.A. Mamun, C. Constantinou, M. Prakash, Phys. Rev. C **97**, 064324 (2018)

20. J. Friedrich, P.-G. Reinhard, *Phys. Rev. C* **33**, 335 (1986)
21. K. Langanke, J.A. Maruhn, S.E. Koonin (eds.), *Computational Nuclear Physics I*, Chap. 2 (Springer, London, 1991)
22. P.-G. Reinhard et al., *Phys. Rev. C* **60**, 014316 (1999)

Part V
Gamma-Ray Strength Functions

Gamma Strength Functions and the Brink-Axel Hypothesis



Peter von Neumann-Cosel

1 Gamma Strength Function

The GSF describes the average γ decay behavior of a nucleus. It depends on the level densities at the initial and final energies. In general all multipoles allowed for electromagnetic processes contribute but in practice E1 dominates. Thus, the isovector giant dipole resonance (IVGDR) dominates the GSF at higher excitation energies as indicated on the r.h.s. of Fig. 1. At lower energies M1 contributes to the total GSF (although a few % only under most conditions).

As indicated in the scheme of decay and absorption in Fig. 1, for the special case of γ decay to the g.s. the GSF can be related to the photoabsorption cross section by the principle of detailed balance

$$f^{E1}(E_\gamma, J) = \frac{2J_0 + 1}{2J + 1} \frac{1}{(\pi \hbar c)^2 E_\gamma^3} \langle \sigma_{abs} \rangle \quad (1)$$

where J , J_0 are the spins of excited and ground state, respectively, and for simplicity the relation is written for the $E1$ component only. The brackets $\langle \rangle$ indicate averaging over an energy interval.

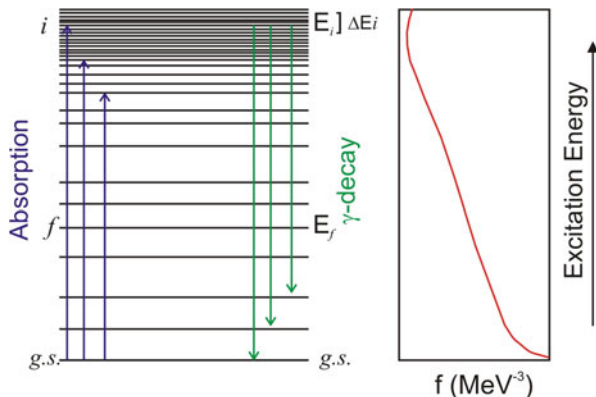
P. von Neumann-Cosel (✉)

Institut für Kernphysik, Technische Universität Darmstadt, Darmstadt, Germany
e-mail: vnc@ikp.tu-darmstadt.de

© This is a U.S. government work and not under copyright protection in the U.S.; foreign copyright protection may apply 2021

J. Escher et al. (eds.), *Compound-Nuclear Reactions*, Springer Proceedings in Physics 254, https://doi.org/10.1007/978-3-030-58082-7_18

Fig. 1 Relation between γ decay and absorption (l.h.s.) and expected energy dependence of the GSF (r.h.s.)



2 Experimental Tests of the Brink-Axel Hypothesis

Knowledge of the GSF is required for calculations of statistical nuclear reaction in astrophysics [1], reactor design [2], and waste transmutation [3]. Most applications imply an environment of finite temperature, notably in stellar scenarios [4], and thus reactions on excited states (e.g. in a (n,γ) reaction) become relevant. Their contributions to the reaction rates are usually estimated applying the generalized Brink-Axel (BA) hypothesis [5, 6], which states that the GSF is independent of the properties of the initial and final states (and thus should be the same in γ emission and absorption experiments). Although historically formulated for the IVGDR, where it seems to hold approximately for not too high temperatures [7], this is nowadays a commonly used assumption to calculate the low-energy E1 and M1 strength functions. Recent theoretical studies [8, 9] put that into question demonstrating that the strength functions of collective modes built on excited states do show an energy dependence. However, numerical results for E1 strength functions showed an approximate constancy consistent with the BA hypothesis [8].

The so-called Oslo method, where primary spectra of γ decay following compound nuclear reactions are extracted, is a major source of data on the GSF below the particle thresholds. Since the γ transmission probability is proportional to the product of the GSF and the final-state LD, assumption of the generalized BA hypothesis is a prerequisite of the analysis [10]. Recent Oslo-type experiments have indeed demonstrated independence of the GSF from excitation energies and spins of initial and final states in a given nucleus in accordance with the BA hypothesis [11, 12]. However, there are a number of results which clearly indicate violations in the low-energy region when comparing γ emission and absorption experiments. For example, the GSF in heavy deformed nuclei at excitation energies of 2–3 MeV is dominated by the orbital M1 scissors mode [13] and potentially large differences in $B(M1)$ strengths are observed between γ between upward [14] and downward [15, 16] GSFs. Furthermore, at very low energies (<2 MeV) an increase of GSFs is observed in Oslo-type experiments [12, 17], which for even–even nuclei cannot have

a counterpart in ground-state absorption experiments on even–even nuclei because of the pairing gap.

For the low-energy E1 strength in the region of the PDR, the validity of the BA hypothesis is far from clear when comparing results from the Oslo method with photoabsorption data. Below particle thresholds most information on the GSF stems from nuclear resonance fluorescence (NRF) experiments, which suffers from the problem of unobserved branching ratios to excited states. These can be corrected in principle by Hauser–Feshbach calculations assuming statistical decay [18]. The resulting correction factors are sizable and show a strong dependence on the neutron threshold energy and the g.s. deformation. On the other hand, there are clear indications of non-statistical decay behavior of the PDR from recent measurements [19–21]. Violation of the BA hypothesis was also claimed in a simultaneous study of the (γ, γ') reaction and average ground-state branching ratios [22] in ^{142}Nd (see, however, Ref. [23]). Clearly, information on the GSF in the PDR energy region from independent experiments is called for.

3 Gamma Strength Function and Level Density from (p,p') Scattering

A new method for the measurement of complete E1 strength distributions in nuclei from about 5 to 25 MeV has been developed using relativistic Coulomb excitation in inelastic proton scattering at beam energies of a few hundred MeV and scattering angles close to 0° [24–29]. The experiments also permit extraction of the M1 part of the GSF due to spinflip excitations [30], which energetically overlaps with the PDR strength. Furthermore, when performed with good energy resolution, the level density (LD) can be extracted independently of the GSF in the excitation region of the IVGDR from the giant resonance fine structure [31]. This allows an important test of the model-dependent decomposition of LD and GSF in the Oslo method [10].

The case of ^{208}Pb is used as an example to illustrate the methods [24, 25] and the comparison to the Oslo data [32]. Details on the experimental techniques can be found in Ref. [33]. The top part of Fig. 2 shows a spectrum of the $^{208}\text{Pb}(p,p')$ reaction in the excitation region $E_x = 4 - 25$ MeV measured with the magnetic spectrometer placed at 0° . One observes prominent transitions at low excitation energies, which can be shown to have E1 character, and a resonance-like structure around 7 MeV, which contains E1 and M1 parts due to the energetic overlap of the PDR and the spinflip-M1 resonance. The prominent structure peaking at 13 MeV represents the IVGDR.

A separation of E1/M1 cross sections and contributions from other multipoles is possible with a multipole decomposition analysis (MDA) of the angular distributions [25, 26, 29]. The measurement of spin transfer observables with a polarized beam provides a separation of spinflip and non-spinflip cross sections [24, 27, 29], which can be related to E1 and M1 components by the different reaction

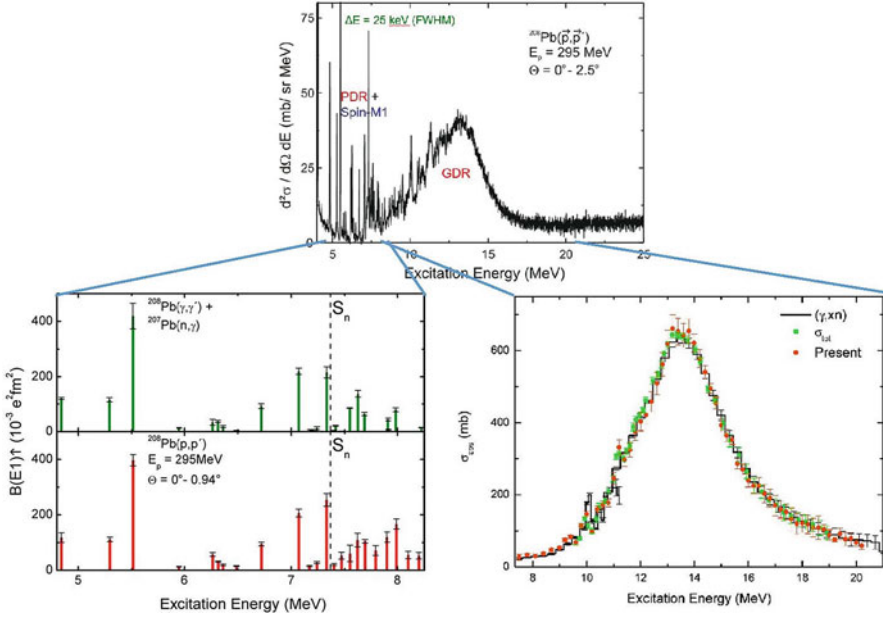


Fig. 2 Top: Experimental spectrum of the $^{208}\text{Pb}(p,p')$ reaction at $E_p = 295\text{ MeV}$ and $\Theta_{\text{lab}} = 0^\circ$. Bottom: Comparison of the $B(E1)$ strength distribution deduced from the (p,p') experiment below S_n and the photoabsorption cross section above S_n with results from other experiments. Data from Ref. [24]

mechanisms. Good agreement is found between these completely independent methods.

The E1 cross sections can be converted to $B(E1)$ strengths, respectively photoabsorption cross sections, with the virtual photon method [34]. The bottom part of Fig. 2 shows a comparison of the deduced $B(E1)$ strength distribution in ^{208}Pb with data from (γ, γ') and (n, γ) reactions [35–37] (l.h.s.) and photoabsorption experiments [38, 39] in the giant resonance region (r.h.s.). Excellent agreement is obtained [24].

The M1 cross sections can be converted to spin-M1 matrix elements with the “unit cross section method” originally developed to extract the analog GT strength from charge-exchange reactions [40]. Assuming that orbital contributions to the total M1 strength are negligible [14] one can extract electromagnetic $B(M1)$ strength distributions from the proton scattering data [30, 41]. In the case of ^{208}Pb the M1 contribution to the GSF is small, not exceeding 10% at the maximum of the resonance.

Figure 3 presents the GSF deduced from the $^{208}\text{Pb}(p,p')$ data [32] in comparison to results from an Oslo experiment [42]. The inset shows an extension of the low-energy region, where both experiments overlap. The comparison of the present GSF derived from ground-state absorption with the Oslo results shows larger values in

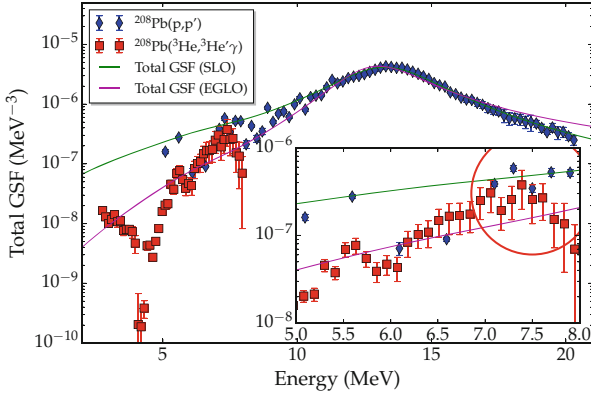


Fig. 3 GSF deduced from the $^{208}\text{Pb}(p,p')$ data (blue diamonds) [24, 25] in comparison with results from an Oslo-type experiment (red squares) [42]. From Ref. [32]

the PDR energy region, where both data sets overlap. However, the fluctuations of the GSF are very strong due to the anomalously small level densities in the closed-shell nucleus ^{208}Pb , which prevents conclusions on a possible violation of the BA hypothesis in the PDR energy region.

Fluctuations of the cross sections in the energy region of the IVGDR are observed in the high-resolution (p,p') experiments (cf. Fig. 2). They can be related to the density of $J^\pi = 1^-$ states. The LD is extracted with a fluctuation analysis described e.g. in Refs. [31, 43–45]. A prerequisite of the method is a separation of the cross sections populating the IVGDR from other contributions. In the present case this is achieved by using the MDA results.

A quantitative description of the fluctuations is given by the autocorrelation function

$$C(\epsilon) = \frac{\langle d(E_x) \cdot d(E_x + \epsilon) \rangle}{\langle d(E_x) \rangle \cdot \langle d(E_x + \epsilon) \rangle}. \quad (2)$$

The quantity $d(E_x)$ is called stationary spectrum and quantifies the fluctuations around the mean at a given energy E_x . The value $C(\epsilon = 0) - 1$ is nothing but the variance of $d(E_x)$

$$C(\epsilon = 0) - 1 = \frac{\langle d^2(E_x) \rangle - \langle d(E_x) \rangle^2}{\langle d(E_x) \rangle^2}. \quad (3)$$

According to Ref. [46], this experimental autocorrelation function can be approximated by the expression

$$C(\epsilon) - 1 = \frac{\alpha \cdot \langle D \rangle}{2\Delta E \sqrt{\pi}} \times f(\sigma, \sigma_>), \quad (4)$$

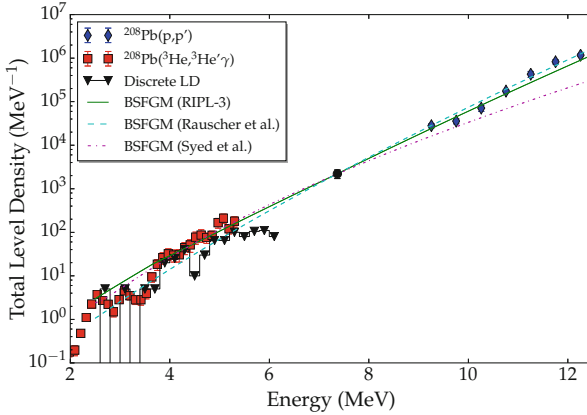


Fig. 4 Total LD in ^{208}Pb from the (p, p') data [24, 25] in comparison with results from an Oslo-type experiment [42]. From Ref. [32]

where the function f depends on the chosen parameters (folding widths σ, σ_{\geq}) only. α is the sum of the normalized variances of the assumed spacing and transition width distributions. If only transitions with the same quantum numbers ($J^{\pi} = 1^{-}$ in the present case) contribute to the spectrum, it can be directly determined as the sum of the variances of the Wigner and Porter–Thomas distribution, respectively, and the mean level spacing $\langle D \rangle$ and LD $\rho(E) = 1/\langle D \rangle$ can be extracted from Eq. (3).

In order to compare with the results from the Oslo experiment, the 1^{-} LD needs to be converted to a total LD. The spin distribution is calculated with the aid of systematic backshifted Fermi-gas model (BSFGM) parameterizations and their variation is taken as a measure of the systematic uncertainty of the procedure (for details see Ref. [32]). Figure 4 displays the resulting LD in the region 9.5–12.5 MeV (blue diamonds) together with results of the Oslo experiment at lower energies (red squares) [42] and the data point at neutron threshold from neutron capture [47]. Several BSFGM results are shown as solid, dashed, and dotted lines, respectively. The RIPL-3 parameterization [47] provides a very satisfactory description of all experimental data indicating that the decomposition into GSF and LD in the Oslo method is essentially correct.

Another study of this type was performed for ^{96}Mo [29], a considerably deformed nucleus with LDs high enough to permit a comparison with the GSF from a decay experiment averaging over appropriate energy intervals. The choice of ^{96}Mo was motivated by the large discrepancies of GSFs derived from Oslo [48, 49] and NRF [18] experiments. The l.h.s. of Fig. 5 summarizes the available GSF data. The energy region below neutron threshold is expanded on the r.h.s. showing the results from the Oslo (open circles), the NRF (black circles), and the (p, p') experiment (red circles). For γ energies between 6 and 8 MeV covered by all experiments, the GSF deduced from Coulomb excitation lies between the two other results but overall agrees better with the Oslo result (for details see Ref. [29]).

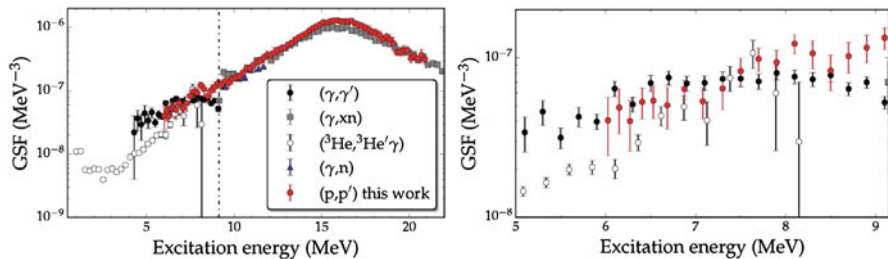
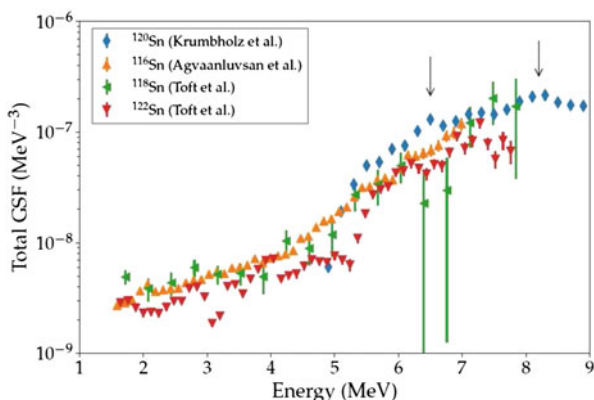


Fig. 5 GSF of ^{96}Mo from the (p,p') data (red circles) compared with $(^3\text{He}, ^3\text{He}'\gamma)$ [48, 49] (open circles) and (γ, γ') data including a statistical model correction for unobserved branching ratios [18] (black circles). From Ref. [29]

Fig. 6 GSF of ^{120}Sn in the energy region from 5 to 9 MeV from the (p,p') data (blue diamonds) [26, 27] in comparison with Oslo-type results for ^{116}Sn (orange upward triangles) [50], ^{118}Sn (sideward green triangles) [51], and ^{122}Sn (downward red triangles) [51]. The arrows indicate resonance-like structures in the (p,p') results



Finally, we have extracted the GSF of ^{120}Sn from the data described in Refs. [26, 27], again including the M1 part due to the spinflip resonance. In the GDR region fair agreement with previous experiments is obtained [27]. The energy region below neutron threshold is displayed in Fig. 6 and exhibits two pronounced resonance-like structures around 6.5 and 8 MeV indicated by arrows. Data from an Oslo-type experiment are not available for ^{120}Sn ; however, the neighboring even-even Sn isotopes 116 [50] and 118,122 [51] have been studied. Since the low-energy structure is known to change little across the stable even-even Sn isotopes one can also expect that changes of the GSF are limited (although the PDR is expected to have some dependence on neutron excess [52]).

For γ energies from 5 to about 7.5 MeV covered by both types of experiments one finds reasonable agreement at the lower and upper end of the interval. In contrast, the Oslo data show a smooth energy dependence and no resonance-like structure around 6.5 MeV pointing to a violation of the BA hypothesis. It should be noted that this bump is systematically seen in 0° (p,p') cross sections for all stable even-even Sn isotopes [53] and has also been observed in ^{124}Sn with isoscalar probes [54, 55].

4 Concluding Remarks

The generalized BA hypothesis is a crucial assumption for the application of statistical nuclear reaction theory with photons in the entrance or exit channel. Of particular importance is the question whether data from g.s. absorption experiments represent the GSF in the (quasi)continuum region. While its validity is fairly well established above neutron threshold in medium-mass and heavy nuclei, the situation is less clear at lower γ energies when comparing decay and absorption experiments. There are clear violations like the low-energy enhancement [17] and the larger scissors mode strength [15] in the decay. For the (PDR + spinflip M1) energy region there are conflicting results.

The present contribution discusses a new approach to extract the GSF (including the spin-M1 part) from (p,p') scattering at energies of a few hundred MeV and at very forward angles. This method directly measures the g.s. decay width and avoids the problems of NRF data, where one needs to correct for unknown branching ratios to excited states. When performed with high energy resolution, such data not only provide the GSF but also the LD, thus permitting an important test of the assumptions made in Oslo-type experiments for their decomposition. So far, three cases have been analyzed. The study of ^{208}Pb remains inconclusive because the anomalously low LD leads to large intensity fluctuations [32]. For ^{96}Mo consistency within the experimental uncertainties is found [29]. The results in ^{120}Sn point to a violation of the BA hypothesis [53]. Clearly, a more systematic study is needed—e.g. on the role of deformation—and emphasis should be put to establish more cases, where GSF and LD from Oslo-type and (p,p') experiments (as well as the LD from neutron capture) can be compared.

Acknowledgments I thank S. Bassauer for his contribution to the analysis of the present results and A. Tamii and the collaborators at RCNP for the excellent experiments. This work was funded by the Deutsche Forschungsgemeinschaft (DFG, German Research Foundation)—Project number 279384907–SFB 1245.

References

1. M. Arnould, S. Goriely, K. Takahashi, *Phys. Rep.* **450**, 97 (2007)
2. M.B. Chadwick et al., *Nucl. Data Sheets* **112**, 2887 (2011)
3. M. Salvatore, G. Palmiotti, *Prog. Part. Nucl. Phys.* **66**, 144 (2011)
4. M. Wiescher, F. Käppeler, K. Langanke, *Annu. Rev. Astron. Astrophys.* **50**, 165 (2012)
5. D.M. Brink, Ph.D. Thesis, Oxford University (1955)
6. P. Axel, *Phys. Rev.* **126**, 671 (1962)
7. P.F. Bortignon, A. Bracco, R.A. Broglia, *Giant Resonances: Nuclear Structure at Finite Temperature* (Harwood Academic, Amsterdam, 1998)
8. C.W. Johnson, *Phys. Lett. B* **750**, 72 (2015)
9. N. Quang Hung, N. Dinh Dang, L.T. Quynh Huong, *Phys. Rev. Lett.* **118**, 022502 (2017)
10. A. Schiller et al., *Nucl. Instrum. Methods A* **447**, 498 (2000)
11. M. Guttormsen et al., *Phys. Rev. Lett.* **116**, 012502 (2016)

12. A.C. Larsen et al., *J. Phys. G* **44**, 064005 (2017)
13. D. Bohle et al., *Phys. Lett. B* **137**, 27 (1984)
14. K. Heyde, P. von Neumann-Cosel, A. Richter, *Rev. Mod. Phys.* **82**, 2365 (2010)
15. M. Guttormsen et al., *Phys. Rev. Lett.* **109**, 162503 (2012)
16. C.T. Angell et al., *Phys. Rev. Lett.* **117**, 142501 (2016)
17. A. Voinov et al., *Phys. Rev. Lett.* **93**, 142504 (2004)
18. G. Rusev et al., *Phys. Rev. C* **79**, 061302 (2009)
19. C. Romig et al., *Phys. Lett. B* **744**, 369 (2015)
20. B. Löher et al., *Phys. Lett. B* **756**, 72 (2016)
21. J. Isaak et al., *Phys. Lett. B* **788**, 225 (2019)
22. C.T. Angell et al., *Phys. Rev. C* **86**, 051302(R) (2012)
23. Erratum to Ref. [22], *Phys. Rev. C* **91**, 039901(E) (2015)
24. A. Tamii et al., *Phys. Rev. Lett.* **107**, 062502 (2011)
25. I. Poltoratska et al., *Phys. Rev. C* **85**, 041304(R) (2012)
26. A.M. Krumbholz et al., *Phys. Lett. B* **744**, 7 (2015)
27. T. Hashimoto et al., *Phys. Rev. C* **92**, 031305(R) (2015)
28. J. Birkhan et al., *Phys. Rev. Lett.* **118**, 252501 (2017)
29. D. Martin et al., *Phys. Rev. Lett.* **119**, 182503 (2017)
30. J. Birkhan et al., *Phys. Rev. C* **93**, 041302(R) (2016)
31. I. Poltoratska et al., *Phys. Rev. C* **89**, 054322 (2014)
32. S. Bassauer, P. von Neumann-Cosel, A. Tamii, *Phys. Rev. C* **94**, 054313 (2016)
33. A. Tamii et al., *Nucl. Instrum. Method. A* **605**, 3 (2009)
34. C.A. Bertulani, G. Baur, *Phys. Rep.* **163**, 299 (1988)
35. N. Ryezayeva et al., *Phys. Rev. Lett.* **89**, 272502 (2002)
36. R. Schwengner et al., *Phys. Rev. C* **81**, 054315 (2010)
37. R. Köhler et al., *Phys. Rev. C* **35**, 1646 (1987)
38. A. Veyssiere et al., *Nucl. Phys.* **A159**, 561 (1970)
39. K.P. Schelhaas et al., *Nucl. Phys.* **A489**, 189 (1988)
40. M. Ichimura, H. Sakai, T. Wakasa, *Prog. Part. Nucl. Phys.* **56**, 446 (2006)
41. M. Mathy et al., *Phys. Rev. C* **95**, 054316 (2017)
42. N.U.H. Syed et al., *Phys. Rev. C* **79**, 024316 (2009)
43. Y. Kalmykov et al., *Phys. Rev. Lett.* **96**, 012502 (2006)
44. Y. Kalmykov et al., *Phys. Rev. Lett.* **99**, 202502 (2007)
45. I. Usman et al., *Phys. Rev. C* **84**, 054322 (2011)
46. B. Jonson et al., *CERN report* **76-13**, 277 (1976)
47. R. Capote et al., *Nucl. Data Sheets* **110**, 3107 (2009)
48. M. Guttormsen et al., *Phys. Rev. C* **71**, 044307 (2005)
49. A.C. Larsen, S. Goriely, *Phys. Rev. C* **82**, 014318 (2010)
50. U. Agvaanluvsan et al., *Phys. Rev. C* **79**, 014320 (2009)
51. H.K. Toft et al., *Phys. Rev. C* **83**, 044320 (2011)
52. D. Savran, T. Aumann, A. Zilges, *Prog. Part. Nucl. Phys.* **70**, 210 (2013)
53. S. Bassauer et al., *Phys. Lett. B* **810**, 135804 (2020); *Phys. Rev. C* **102**, 034327 (2020)
54. J. Endres et al., *Phys. Rev. Lett.* **105**, 212503 (2010)
55. L. Pellegri et al., *Phys. Lett. B* **738**, 519 (2014)

γ -Ray Strength Functions and GDR Cross Sections in the IAEA Photonuclear Data Project



H. Utsunomiya, I. Gheorghe, D. M. Filipescu, K. Stopani, S. Belyshev, T. Renstrøm, G. M. Tveten, G. Fan, H. Wang, S. Goriely, Y.-W. Lui, T. Ari-izumi, S. Miyamoto, V. Varlamov, B. Ishkhanov, A. C. Larsen, and S. Siem

1 IAEA-CRP F41032

The Coordinated Research Project (CRP) with the code F41032 was launched by the International Atomic Energy Agency (IAEA) in 2016 [1]. The goal of the CRP is to update the photonuclear data library (IAEA-TECDOC-1178) and generate a reference database for photon strength functions. We have been running the PHOENIX Collaboration to acquire new photonuclear data for the IAEA-CRP at the NewSUBARU synchrotron radiation facility in Japan. The collaboration was carried out with the University of Oslo, Extreme Light Infrastructure—Nuclear

H. Utsunomiya (✉) · T. Ari-izumi
Konan University, Kobe, Japan
e-mail: hiro@konan-u.ac.jp

I. Gheorghe · D. M. Filipescu
IFIN-HH, Bucharest-Magurele, Romania

K. Stopani · S. Belyshev · V. Varlamov · B. Ishkhanov
Lomonosov Moscow State University, Moscow, Russia

T. Renstrøm · G. M. Tveten · A. C. Larsen · S. Siem
University of Oslo, Oslo, Norway

G. Fan · H. Wang
Shanghai Advanced Research Institute, Shanghai, China

S. Goriely
Institut d'Astronomie et d'Astrophysique, Université Libre de Bruxelles, Brussels, Belgium

Y.-W. Lui
Texas A&M University, College Station, TX, USA

S. Miyamoto
University of Hyogo, Kobe, Hyogo, Japan

Physics (ELI-NP), “Horia Hulubei” National Institute for Physics and Nuclear Engineering (IFIN-HH), Skobeltsyn Institute of Nuclear Physics of Lomonosov Moscow State University (SINP-MSU), and Shanghai Institute of Applied Physics (SINAP). The new data acquired are classified into two groups, (γ, xn) cross section data with $x = 1-4$ for 11 nuclei with 100% natural abundances at γ -ray energies from $1n$ threshold up to 40 MeV and (γ, n) cross section data for 21 enriched isotopes at energies below $2n$ thresholds. The construction of γ SFs was carried out in collaboration with the Université Libre de Bruxelles (ULB).

2 Key Technical Factors

2.1 Laser Compton-Scattering γ -Ray Beam

Quasi-monochromatic pencil-like γ -ray beams are produced in the head-on collision of laser photons from relativistic electrons circulating in the NewSUBARU storage ring. Both INAZUMA (1064 nm) and Talon (532 nm) Q-switch lasers are used to produce quasi-monochromatic pulsed γ -ray beams that are energy-tunable from 4.5 to 76 MeV in collision with electrons from 0.5 to 1.5 GeV. The electron beam is energy-calibrated with the accuracy on the order of 10^{-5} [2]. The electron beam energy is precisely reproduced by the automated control of the beam optics parameters. The γ -ray energy is determined by the calibrated electron beam energy.

The energy profile of the γ -ray beam is determined by reproducing the response function of a 3.5” x 4.0” LaBr₃(Ce) detector to the laser Compton-scattering (LCS) γ -rays with the GEANT4 code which incorporates the kinematics of the LCS process and interactions between the γ -rays and the LaBr₃(Ce) detector. The LCS γ -ray beam is accompanied by a low-energy tail unique to the electron beam emittance and the collimator size. The energy spread for the standard emittance and a collimator of 2 mm aperture located at 18.5 m from the most efficient collision point is typically a few % in the full width at half maximum. The beam size on target approximately follows the geometrical aperture of the collimator with respect to the collision point.

The γ -ray flux is accurately determined from the pile-up/multi-photon spectrum with the Poisson-fitting method [3, 4] based on the fact that the number of photons involved in a γ -pulse follows the Poisson distribution.

2.2 Direct Neutron-Multiplicity Sorting

The Talon laser is operated at 1 kHz to produce a pulsed γ -ray beam that offers 1 ms pulse intervals during which one can identify multi-neutron coincidence events with a moderator-based slow neutron detector. We have developed a neutron detector

consisting of three concentric rings of 4, 9, and 18 ^3He counters embedded in a polyethylene moderator at 5.5, 13.0, and 16.0 cm from the γ -ray beam axis [5]. The detector is designed to be of flat response to neutron kinetic energies by tuning the distance and the number of ^3He counters for individual rings by GEANT4 simulation. The total detection efficiency is 36.5% with 1.6% uncertainty in one standard deviation over an energy range from 10 keV to 5.0 MeV.

The partial photoneutron cross section with the neutron multiplicity x is determined from the number of reactions (γ, xn) that took place, N_x ($x = 1, 2, 3, \dots$), in an experiment. However, the number of reactions is not a direct experimental observable. Instead, the number of neutron coincidence events is the experimental observable. In general, a moderator-based neutron detector has a strong dependence of the detection efficiency on neutron kinetic energy. In this case, the ring-ratio technique which was originally developed by the Lawrence Livermore National Laboratory [6] cannot determine the average neutron kinetic energy for the individual (γ, xn) reactions. In view of the fact that the neutron kinetic energy is different in (γ, xn) reactions with a different x and in the emission order of neutrons in the same (γ, xn) reactions, one encounters a difficulty in neutron-multiplicity sorting with the ring-ratio technique.

The best way for overcoming the difficulty is to utilize a flat-efficiency detector to determine the number of reactions N_x by solving a set of equations for the experimental observables, the number of neutron coincidence events. One can refer to Ref. [5] for details of the direct neutron-multiplicity sorting with a flat-efficiency detector.

3 Data Acquisition, Evaluation, and Compilation

We have successfully acquired all the data as originally time-scheduled as follows. The institute which is responsible for the data reduction of (γ, xn) cross sections is shown in the parentheses. The data reduction of (γ, n) cross sections is undertaken by the University of Oslo.

I. (γ, xn) data on 11 nuclei

2015: ^9Be (Konan), ^{208}Bi (ELI-NP/IFIN-HH)

2016: ^{89}Y (SINP-MSU), ^{169}Tm (ELI-NP/IFIN-HH), ^{197}Au (Konan)

2017: ^{59}Co (SINP-MSU), ^{165}Ho (ELI-NP/IFIN-HH), ^{181}Ta (Konan)

2018: ^{103}Rh (SINP-MSU), ^{139}La (Konan), ^{159}Tb (ELI-NP/IFIN-HH)

II. (γ, n) data on 21 nuclei

2015: ^{89}Y , ^{203}Tl , ^{205}Tl

2016: ^{13}C , ^{58}Ni , ^{60}Ni , ^{61}Ni , ^{64}Ni , ^{137}Ba , ^{138}Ba , ^{185}Re , ^{192}Os

2017: ^{64}Zn , ^{66}Zn , ^{68}Zn , ^{182}W , ^{183}W , ^{184}W

2018: ^{156}Gd , ^{157}Gd , ^{158}Gd , ^{160}Gd

The data newly acquired in the PHOENIX Collaboration are evaluated by the Japan Atomic Energy Agency (JAEA), the Chinese Nuclear Data Center (CNDC), and Korean Atomic Energy Research Institute (KAERI) and compiled in the IAEA updated photonuclear data library. The data are also used to supplement the (γ, γ') and the Oslo method data to construct the photon strength function and compiled in the IAEA reference database for photon strength functions.

4 γ -Ray Strength Function

Figure 1 shows the γ -ray strength function (γ SF) for Ni isotopes constructed with the γ SF method [7] which has been devised to investigate systematically (γ, n) and (n, γ) cross sections over an isotopic chain. The present (γ, n) data are used as experimental constraints on the model E1 and M1 γ SFs from the Hartree–Fock–Bogolyubov plus quasi-particle random phase approximation based on the Gogny DIM interaction. The recent systematics of the γ SF [8] has been taken into account; the γ SF in de-excitation mode differs from that in excitation mode in the zero-limit behavior of both E1 and M1 strengths, the latter of which is referred to as M1 upbend. In the figure, the M1 γ SF is shown for two different zero-limit values, 3×10^{-8} and 10^{-7} MeV^{-3} .

The mean field plus QRPA calculations need some phenomenological corrections, which include a broadening of the QRPA strength to take the neglected damping of collective motions into account as well as a shift of the strength to lower energies due to the contribution beyond the one-particle–one-hole excitations and the interaction between the single particle and low-lying collective phonon degrees of freedom. As such phenomenological corrections [8], we have introduced an E1 damping width of 4.5 MeV which is smaller than the systematics of $\Gamma_{E1} = 7 - A/45 \text{ MeV}$ [8] due to the closed proton shell in Ni isotope and M1 damping width of 2 MeV. As a consequence, a factor of 2/3 on the overall E1 strength is required to reproduce the present peak photoneutron cross section in the GDR region. More details can be found in Ref. [7].

5 GDR Cross Section

5.1 ^{209}Bi

Previously we published GDR cross sections for ^{209}Bi [12]. We found it necessary to take into account the effect of the electromagnetic interaction (pair production, Compton scattering, and photoelectric absorption) of high-energy γ -ray beams in the thick (7 mm or 10 mm) ^{209}Bi target material on the (γ, xn) cross sections [13]. The interaction produces the secondary gamma rays which can induce the giant

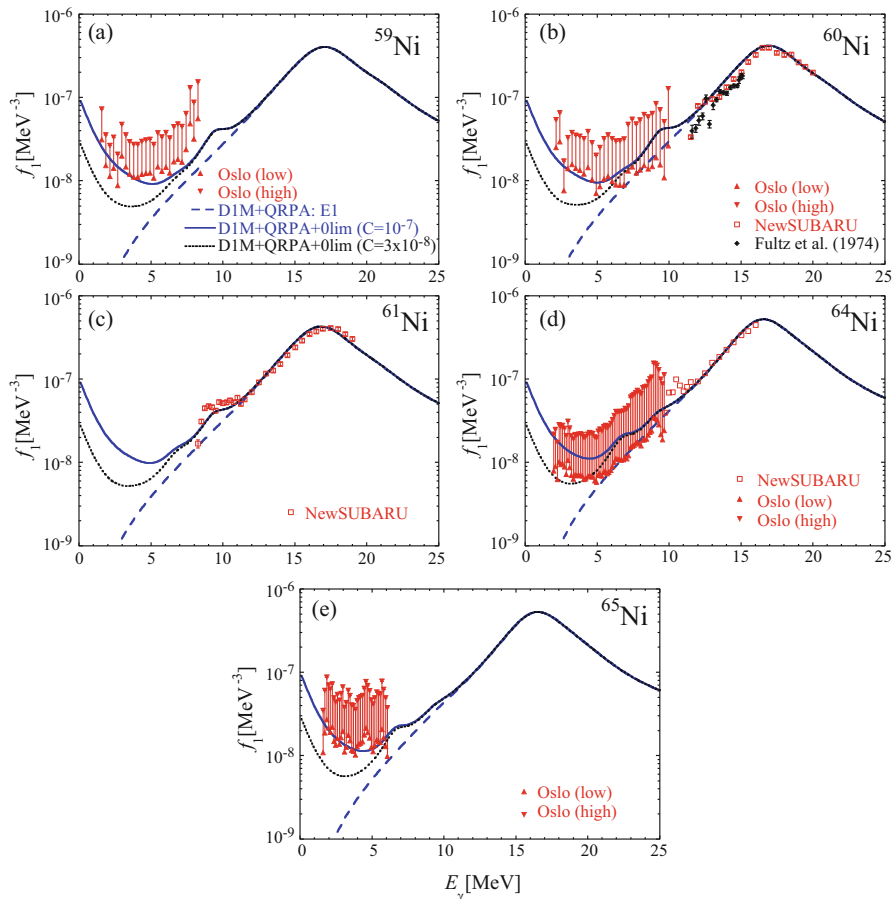
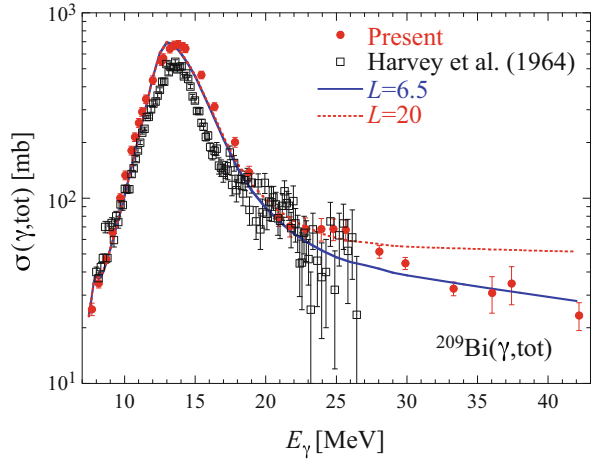


Fig. 1 (a)–(e) γ SF for the $^{59,60,61,64,65}\text{Ni}$ isotopes. The red triangles correspond to the upper and lower limits of the γ SF extracted from the Oslo data and the red open squares to the NewSUBARU photoneutron data. The dashed blue curve represents the DIM + QRPA E1 strength and the black dotted (blue full) line the DIM + QRPA +0lim E1 + M1 dipole strength obtained with $C = 3 \times 10^{-8} \text{ MeV}^{-3}$ ($C = 10^{-7} \text{ MeV}^{-3}$). The γ SF of $^{64,65}\text{Ni}$ is taken from Refs. [9, 10] (red triangles). The γ SF extracted from the $^{60}\text{Ni}(\gamma, n)$ data of Fultz et al. [11] (black diamonds) is also shown in panel (b)

dipole resonance most effectively in the peak region around 13 MeV governed by the (γ, n) channel. Thus, the secondary gamma rays produce extra neutrons which we previously assigned to reaction neutrons of the (γ, n) channel associated with the primary gamma rays. We have corrected the (γ, xn) cross section for the effect. As a result, the (γ, n) cross section is significantly reduced above 30 MeV, while the (γ, xn) cross section with $x = 2-4$ remains the same.

Fig. 2 (Color online)
Comparison of the revised total experimental cross section with the TALYS predictions for two values of the Levinger parameter $L = 6.5$ (solid line) and $L = 20$ (dashed line)



Here, we show the total photoneutron cross section in Fig. 2, leaving details on partial photoneutron cross sections in Ref. [13]. The asymptotic value of the total cross section is reproduced by the default pre-equilibrium calculation with an ordinary value ($L = 6.5$) of the Levinger parameter for the quasi-deuteron contribution. Previously we discussed the large cross section at the high energies in terms of an increase of the L value and the surface effect. With the corrected cross sections, however, there is no need to require a large value $L = 20$ nor to invoke the surface effect anymore.

5.2 ^{159}Tb

Figure 3 shows partial photoneutron cross sections (γ, xn) with $x = 1$ and 2 for ^{159}Tb . The ^{159}Tb is one of 19 nuclei for which the Livermore and Saclay data of partial photoneutron cross sections show serious discrepancies [14]. One can see that the present (γ, n) cross section is rather consistent with the Saclay data, while the ($\gamma, 2n$) cross section agrees with the Livermore data.

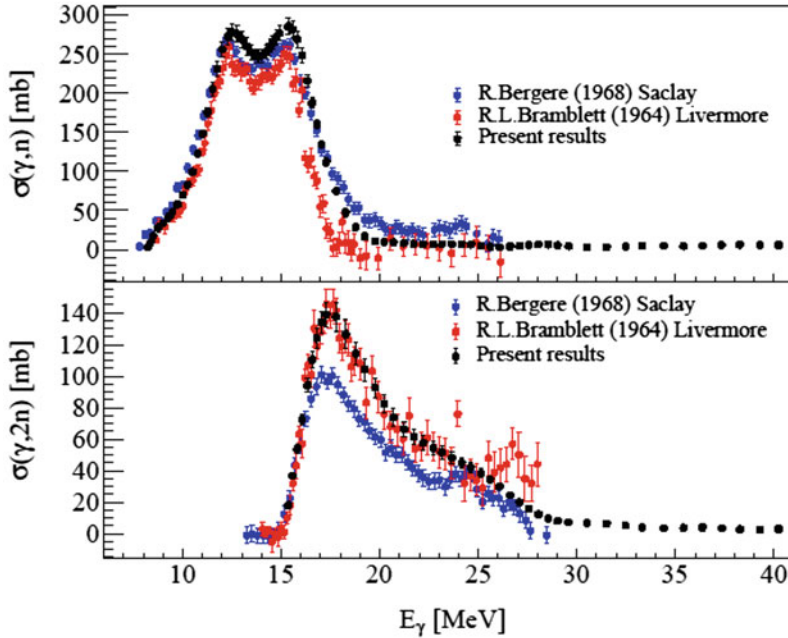


Fig. 3 Partial cross sections (γ, xn) with $x = 1$ and 2 for ^{159}Tb in comparison with the Livermore [15] and Saclay [16] data

6 Summary

We have made an intensive effort of measuring (γ, n) and GDR cross sections within the framework of the international PHOENIX Collaboration for the IAEA-CRP F41032 on creating compilations of photonuclear reactions and photon strength functions. The two compilations have been published in 2019 [17] and 2020 [18], respectively, followed by publications of the individual photonuclear data in the context of nuclear reaction and structure in nuclear physics and nucleosynthesis of heavy elements in nuclear astrophysics.

References

1. P. Dimitriou et al., EPJ Web of Conf. **93**, 06004 (2015)
2. H. Utsunomiya et al., IEEE Trans. Nucl. Sci. **61**, 1252 (2014)
3. T. Kondo et al., Nucl. Instrum. Methods A **659**, 462 (2011)
4. H. Utsunomiya et al., Nucl. Instrum. Methods A **896**, 103 (2018)
5. H. Utsunomiya et al., Nucl. Instrum. Methods A **871**, 135 (2017)
6. S.C. Fultz et al., Phys. Rev. **162**, 1098 (1967)
7. H. Utsunomiya et al., Phys. Rev. C **98**, 054619 (2018)
8. S. Goriely, S. Hilaire, S. Péru, K. Sieja, Phys. Rev. C **98**, 014327 (2018)
9. L. Crespo Campo et al., Phys. Rev. C **94**, 044321 (2016)

10. L. Crespo Campo et al., Phys. Rev. C **96**, 014312 (2017)
11. S.C. Fultz, R.A. Alvarez, B.L. Berman, P. Meyer, Phys. Rev. C **10**, 608 (1974)
12. I. Gheorghe et al., Phys. Rev. C **96**, 044604 (2017)
13. I. Gheorghe et al., Phys. Rev. C **059901**(E), 99 (2019)
14. V.V. Varlamov et al., Eur. Phys. J. A **50**, 114 (2014)
15. R.L. Bramblett et al., Phys. Rev. **133**, B869 (1964)
16. R. Bergere, H. Beil, A. Veyssiere, Nucl. Phys. A **121**, 463 (1968)
17. S. Goriely *et al.*, Eur. Phys. J. A **55**, 172 (2019)
18. T. Kawano *et al.*, Nuclear Data Sheets **163**, 109 (2020)

Neutron Capture on Actinides Studied with DANCE



J. L. Ullmann, B. Baramsai, T. A. Bredeweg, A. J. Couture, R. C. Haight, M. Jandel, T. Kawano, A. L. Keksis, S. Mosby, J. M. O'Donnell, C. Prokop, R. S. Rundberg, G. Rusev, D. J. Vieira, C. Walker, J. B. Wilhelmy, C.-Y. Wu, J. A. Becker, A. Chyzch, R. A. Henderson, G. E. Mitchell, and M. Krticka

1 Introduction

Neutron capture cross sections in the continuum region have been difficult to calculate accurately [1], and measured cross sections are favored when accurate results are needed. Calculations usually use the Hauser–Feshbach approach (Eq. 1), where k_n is the neutron wave number, g_c is a statistical spin factor, T_n is the neutron transmission coefficient, T_γ is the γ -ray transmission coefficient, and $W_{n\gamma}$ is the width fluctuation factor. Good agreement with measurements is often obtained if T_γ is normalized to the measured s-wave resonance spacing D_0 and average s-wave radiation width $\langle\Gamma_\gamma\rangle$, $T_\gamma = 2\pi\langle\Gamma_\gamma\rangle/D_0$.

J. L. Ullmann (✉) · B. Baramsai · T. A. Bredeweg · A. J. Couture · R. C. Haight · T. Kawano
A. L. Keksis · S. Mosby · J. M. O'Donnell · C. Prokop · R. S. Rundberg · G. Rusev · D. J. Vieira
C. Walker · J. B. Wilhelmy
Los Alamos National Laboratory, Los Alamos, NM, USA
e-mail: ullmann@lanl.gov

M. Jandel
Los Alamos National Laboratory, Los Alamos, NM, USA

University of Massachusetts, Lowell, MA, USA

C.-Y. Wu · J. A. Becker · A. Chyzch · R. A. Henderson
Lawrence Livermore National Laboratory, Livermore, CA, USA

G. E. Mitchell
North Carolina State University, Raleigh, NC, USA

M. Krticka
Charles University, Prague, Czech Republic

$$\sigma_{capt}(E_n) = \frac{\pi}{k_n^2} \sum_{J\Pi} g_c \frac{T_n T_\gamma}{T_n + T_\gamma} W_{n\gamma}. \quad (1)$$

The gamma-ray transmission coefficient is defined as

$$T_\gamma = \sum_{j^\pi_{XL}} \int_0^{E'} 2\pi E_\gamma^{(2L+1)} f_{XL}(E_\gamma) \rho(E_x, j^\pi) dE_x, \quad (2)$$

where $f_{XL}(E_\gamma)$ is the photon strength function and $\rho(E_x, j^\pi)$ is the nuclear level density.

There has been a great deal of recent progress in understanding capture calculations, including the study of low-energy behavior of the E1 strength function, the Oslo method for determining strength functions and level densities, the recognition of the need for additional components in the strength function in addition to the E1 GDR, and extensive QRPA calculations by Goriely, Hilaire, and co-workers [2].

In addition to the capture cross section, the shape of the gamma-ray cascade spectrum can be measured and compared to calculations, providing an additional constraint on the strength function and level density. Our plan is to measure the γ -ray spectra from discrete neutron capture resonances using DANCE and compare to calculations made using the DICEBOX code [3] propagated through a GEANT-4 model of DANCE [4]. We will then vary the strength-function models and parameters to achieve a “good” description of the measured spectra. The “best” parameters will then be used to calculate the capture cross section at $E_n \geq 2$ keV using the CoH₃ Hauser–Feshbach code [5].

2 DANCE

The Detector for Advanced Neutron Capture Experiments (DANCE) is a nearly 4π BaF₂ array consisting of 160 crystals of 4 different shapes, each with a volume of 734 cm³. It is highly efficient so that resonance-region measurements can be made with less than 1 mg/cm² of material, but good results for neutron energies greater than 1 keV require somewhat thicker samples. The detector is located on FP-14 at the Los Alamos Neutron Science Center, 20.25 m from the upper-tier water moderator. DANCE is a calorimetric detector capable of detecting and summing the complete gamma cascade following capture. If all of the cascade gammas are detected, the summed energy is the Q value of the capture reaction, and can be used to identify capture events.

3 Results for Even Uranium Isotopes

The gamma-ray spectra from neutron capture on $^{234,236,238}\text{U}$ were studied using targets from 1 to 3 mg/cm² thick. For these isotopes, the continuum fission cross section is negligible below about 0.5 MeV. DICEBOX calculations of the spectra were made using the prescription of Kopecky and Uhl [6] for the photon strength function: a generalized Lorentzian form (GLO) for the E1 giant dipole, and standard Lorentzians (SLO) for the M1 “spin-flip” resonance and E2 contribution. The parameters for the giant dipole were taken from the Empire compilation [7], and for the spin-flip and E2 contributions from RIPL-3. In addition, a low-lying (about 2–3 MeV) M1 component, consistent with the scissors-mode resonance, was also included. The scissors mode was represented by 2 standard Lorentzians, at 2.15 and 2.90 MeV. The energy and width of the Lorentzians were taken from an Oslo-method analysis [8], while the strengths were varied to provide the best representation of the spectra. The same parameters were used for all three isotopes. It was shown in ref. [9] that the gamma-ray spectra could not be reproduced by the Kopecky and Uhl prescription, but additional strength at low energies, most likely M1, was required. That analysis was updated and extended to $^{234,236}\text{U}$ in ref. [10], with results shown below in Fig. 1. Figure 1 shows gamma-ray spectra for several $1/2^+$ resonances in each isotope and for several gamma-ray multiplicities. The calculations labeled CoH₃ were made using the generalized Lorentzian (GLO) form for the giant dipole with parameters from ref [7]. The calculations labeled MGLO were made using the modified generalized Lorentzian form [11] for the

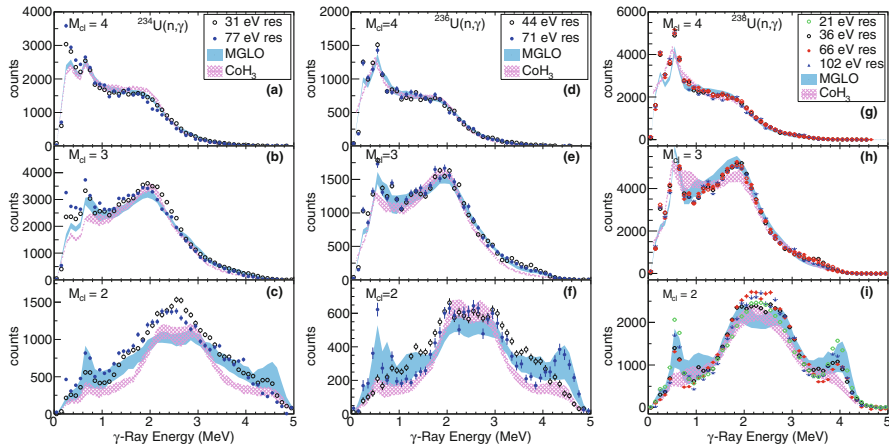


Fig. 1 Measured γ -ray spectra for several $1/2^+$ resonances in $^{234,236,238}\text{U}(n,\gamma)$ compared to calculations made with photon strength-function and nuclear level-density parameters obtained from systematics used in the CoH₃ code and using the MGLO and GLO models for the E1 strength. The GLO calculations are labeled “CoH₃” in the figure, see text for more details. The resonance energies are indicated in each panel. The y-axis counts are arbitrarily normalized

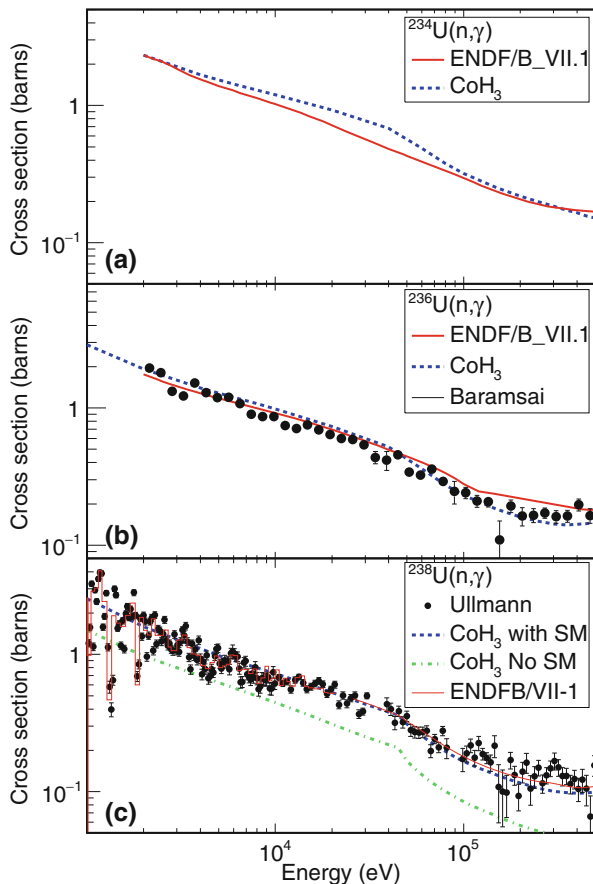


Fig. 2 Uranium capture cross sections compared to calculations

giant dipole with parameters from ref. [12]. The level densities were the Gilbert–Cameron form with updated parameters [13].

Figure 2 shows the cross sections calculated with CoH₃ compared to measurements. The calculations used the GLO form of the E1 photon strength function with parameters described above. The MGLO form was not available in CoH₃. M1 scissors mode, M1 “spin-flip,” and E2 contributions were included, with parameters as described above. The data for ²³⁸U is from ref. [9], and was normalized to low-lying resonances. The data for ²³⁶U is from ref. [14] and was normalized with experimentally determined efficiencies. There is no data for ²³⁴U in the EXFOR database, and the ²³⁴U calculation is compared to the ENDF/B-VII.1 evaluation. A recent measurement of ²³⁴U(*n*, γ) made at DANCE is being analyzed. Note the calculations are absolute and not renormalized to the data; very good agreement in magnitude and shape was obtained.

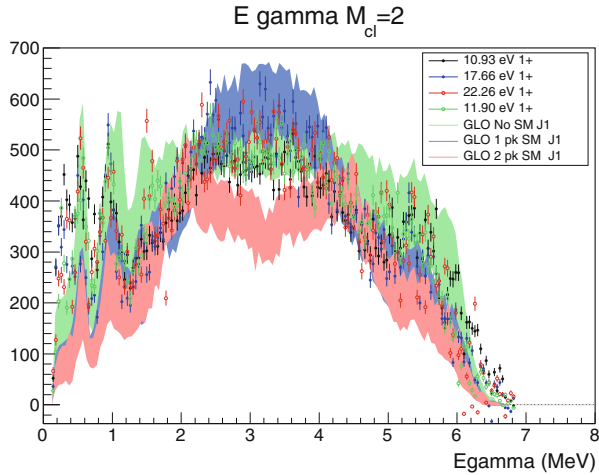


Fig. 3 Measured γ -ray spectra for several 1^+ resonances in $^{239}\text{Pu}(n,\gamma)$ compared to calculations made with photon strength-function and nuclear level-density parameters described in the text, and using the GLO models for the E1 GDR strength. The y-axis counts are arbitrarily normalized

4 Results for ^{239}Pu

Measurements of neutron capture on ^{239}Pu are complicated by the large fission cross section for ^{239}Pu , and fission tagging is crucial. The gamma-ray spectrum following capture was measured with a 2.43 mg/cm^2 ^{239}Pu target mounted in a parallel-plate avalanche counter inserted at the target location of DANCE [15]. A preliminary analysis of the multiplicity-two spectrum from several resonances is shown in Fig. 3. DICEBOX calculations of the cascade were made using the GLO form for the giant dipole, with parameters taken as for the U isotopes. However, a two-Lorentzian scissors mode did not provide satisfactory results, and a one-Lorentzian scissors mode with parameters from the global systematics of Ref. [1] was used.

Cross-section calculations for $^{239}\text{Pu}(n,\gamma)$ were made using the CoH₃ code with parameters similar to those used in the gamma spectrum calculation. Very good agreement with the data from an accurate measurement of $^{239}\text{Pu}(n,\gamma)$ recently reported by Mosby et al.[16] was obtained, without renormalization.

5 Summary

We have shown that gamma-cascade spectra provide another test and constraint on the strength function and level densities used in capture cross-section calculations. The standard Kopecky–Uhl prescription, consisting of a GLO giant-dipole form plus a standard Lorentzian “M1 spin-flip” and E2 contribution is not sufficient

to calculate the shape of gamma-ray spectra observed in $^{234,236,238}\text{U}(n, \gamma)$ and $^{239}\text{Pu}(n, \gamma)$ reactions, and that additional strength at low energies (2 to 3 MeV), most likely an M1 scissors-mode resonance, is required. Accurate calculations of the capture cross section can be made by including the scissors mode in the photon strength function, with proper choice of models for the level density and E1 portion of the strength function. We note that the calculations are sensitive to the input parameters, and precise data and theory are needed to fix the models and their parameters.

References

1. M.R. Mumpower et al., Estimation of M1 scissors mode strength for deformed nuclei in the medium to heavy mass region by statistical Hauser-Feshbach model calculations. *Phys. Rev. C* **96**, 024612 (2017)
2. S. Hilaire, S. Goriely, Towards more predictive nuclear reaction modelling, in *Proceedings of the 6th International Workshop on Compound-Nuclear Reactions and Related Topics* (Springer International Publishing, Cham, 2021)
3. F. Bečvář, Simulation of γ cascades in complex nuclei with emphasis on assessment of uncertainties of cascade-related quantities. *Nucl. Instr. Meth. A* **417**, 434 (1998)
4. M. Jandel et al., GEANT4 simulations of the DANCE array. *Nucl. Instrum. Meth. B* **261**, 1117 (2007)
5. T. Kawano, P. Talou, M.B. Chadwick, T. Watanabe, Monte Carlo simulation for particle and γ -ray emissions in statistical Hauser-Feshbach model. *J. Nucl. Sci. Technol.* **47**, 462 (2010)
6. J. Kopecky, M. Uhl, Test of gamma-ray strength functions in nuclear reaction model calculations. *Phys. Rev. C* **41**, 1941 (1990)
7. M. Herman et al., EMPIRE-3.2 Malta (rev.1) Modular system for nuclear data calculations and nuclear data evaluation User's Manual, INDC(NDS)-0603, 2015. *Nucl. Data Sheets* **108**, 2655 (2007). www-nds.iaea.org/empire/resources/empire.pdf
8. M. Guttormsen et al., Scissors resonance in the quasicontinuum of Th, Pa, and U isotopes. *Phys. Rev. C* **89**, 014302 (2014)
9. J.L. Ullmann et al., Cross section and γ -ray spectra for $^{238}\text{U}(n, \gamma)$ measured with the DANCE detector array at the Los Alamos Neutron Science Center. *Phys. Rev. C* **89**, 034603 (2014)
10. J.L. Ullmann et al., Constraining the calculation of $^{234,236,238}\text{U}(n, \gamma)$ cross sections with measurements of the gamma-ray spectra at DANCE. *Phys. Rev. C* **96**, 024627 (2017)
11. J. Kroll et al., Strength of the scissors mode in odd-mass Gd isotopes from the radiative capture of resonance neutrons. *Phys. Rev. C* **88**, 034317 (2013)
12. S.S. Dietrich, B.L. Berman, Atlas of photoneutron cross sections obtained with monoenergetic photons. *At. Data Nucl. Data Tables* **38**, 199 (1988)
13. T. Kawano, S. Chiba, H. Koura, Phenomenological nuclear level densities using the KTUY05 nuclear mass formula for applications off-stability. *J. Nucl. Sci. Technol.* **43**, 1 (2006)
14. B. Baramsai et al., Radiative neutron Capture cross section from ^{236}U . *Phys. Rev. C* **96**, 024619 (2017)
15. C.-Y. Wu et al., A compact gas-filled avalanche counter for DANCE. *Nucl. Instrum. Meth. A* **78**, 694 (2012)
16. S. Mosby et al., Unifying measurement of $^{239}\text{Pu}(n, \gamma)$ in the keV to MeV energy regime. *Phys. Rev. C* **97**, 04160R (2018)

Deconvolution of the Photon Strength Function



Richard B. Firestone

There is ongoing interest in comparing photonuclear PSF data with reaction PSF data measured at the Oslo cyclotron and elsewhere. Significant differences in these measurements occur due to large variations in the spin distributions and level densities populated by each reaction. It is important to recognize that the PSF is different from the nuclear structure GSF which is based on reduced matrix elements defined as $B(\sigma L)$ values. This is because the PSF is defined as the product of LDF and GSF functions. In addition, photonuclear reactions excite higher levels from the ground state while reactions populate γ -rays that deexcite these higher levels. The GSF depends on the γ -ray direction due to differences in the population of magnetic substates in the initial and final states. Thus a γ -ray populating an excited state may have a different strength than the same energy γ -ray deexciting that state.

Photonuclear reactions measure the cross section for predominantly E1 excitation of levels above the neutron separation energy, S_n . These transitions populate only a narrow range of excited state spins, J_{XS} , with respect to the ground state spin, J_{GS} , where $J_{XS} = J_{GS}, J_{GS} \pm 1$, and a single parity, $\pi_{XS} = -\pi_{GS}$. For even–even nuclei only $J_{XS}^{\pi} = 1^{-}$ states are populated. In order to extract the photonuclear GSF a J^{π} dependent LDF is required. Conversely, Oslo charged particle reactions populate levels below the neutron separation energy, S_n , that deexcite by γ -rays of all multipolarities. These data are analyzed by the Oslo method [1] which determines both an absolute LDF and a relative PSF. Attempts to renormalize the Oslo PSF data for comparison with the photonuclear PSF and other PSF data is problematic because the level densities and spin distributions populated in these experiments vary widely.

R. B. Firestone (✉)

Nuclear Engineering Department, University of California, Berkeley, CA, USA
e-mail: rbfirestone@lbl.gov

© This is a U.S. government work and not under copyright protection in the U.S.; foreign copyright protection may apply 2021

J. Escher et al. (eds.), *Compound-Nuclear Reactions*, Springer Proceedings in Physics 254, https://doi.org/10.1007/978-3-030-58082-7_21

Blatt and Weisskopf [2] derived the standard GSF analysis which consists of single particle reduced matrix elements, $B(\sigma L)$, for γ -ray transitions with multipolarity σL that is given by

$$\begin{aligned} B(EL) \downarrow &= \frac{\Gamma_\gamma(EL) \cdot L[(2L+1)!!]^2}{8\pi(L+1)e^2 b^L} \left(\frac{\hbar c}{E_\gamma}\right)^{2L+1} \\ B(ML) \downarrow &= \frac{\Gamma_\gamma(ML) \cdot L[(2L+1)!!]^2}{8\pi(L+1)\mu_N^2 b^L} \left(\frac{\hbar c}{E_\gamma}\right)^{2L+1} \end{aligned} \quad (1)$$

where $\Gamma_\gamma(\sigma L)$ is the transition width, $\hbar c = 1.9733 \times 10^{-11}$ MeV·cm, $e^2 = 1.43998 \times 10^{-13}$ MeV·cm, and $\mu_N^2 = 1.59234 \times 10^{-41}$ MeV·cm³. The photoexcitation, $B(\sigma L) \uparrow$, and deexcitation, $B(\sigma L) \downarrow$, matrix elements are related by the spin dependent term

$$B(\sigma L) \uparrow = \frac{2J_f + 1}{2J_i + 1} B(\sigma L) \downarrow, \quad (2)$$

where J_i is the spin of the initial state and J_f is the spin of the final state for photoexcitation.

Photonuclear experiments measure the photoexcitation cross section, σ_γ (mb/MeV), populating states above S_n . The predominantly $E1$ average PSF, $\overline{F_{E1}^{(\gamma,n) \uparrow}}$, is related to the cross section by detailed balance and was defined by Uhl and Kopecky [3] as

$$\begin{aligned} \overline{F_{E1}^{(\gamma,n) \uparrow}} &= \frac{\sigma_\gamma(E_x, E1)}{3\pi^2 \hbar^2 c^2 E_\gamma} = \frac{\overline{\Gamma_{E1}^{(\gamma,n)}}}{D \cdot E_\gamma^{2L+1}} \\ &= \rho(E_x, J^\pi) \cdot \frac{2J_f + 1}{2J_i + 1} \frac{\overline{B(E1) \downarrow}}{C(E1)} \\ &= \rho(E_x, J^\pi) \cdot \overline{f_{E1}^{(\gamma,n) \uparrow}}, \end{aligned} \quad (3)$$

where $D = 1/\rho(E_x, J^\pi)$ is the average level spacing or inverse of the level density and the dimensionless constant $C(E1) = 9560$ from Eq. 1. Notably the PSF is the product of the GSF and the level density. The average photonuclear GSF, $\overline{f_{E1}^{(\gamma,n) \uparrow}}$, is uniquely associated with the GDR and distinct from other possible $E1$ GSF modes. The average photonuclear reduced matrix element is simply $\overline{B(E1) \uparrow} = 9560 \times \overline{f_{E1}^{(n,\gamma) \uparrow}}$.

The photonuclear cross section for photon absorption is described by a Lorentzian shape whose strength is determined by the dipole sum rule. The PSF was elegantly described by the Brink-Axel (BA) formulation [4, 5] as

$$\overline{F_{E1}^{(\gamma,n) \uparrow}} = \overline{F_{E1}^{BA \uparrow}} = \frac{1}{3(\pi \hbar c)^2} \sum_{i=1}^{i=2} \frac{\sigma_{G_i} E_\gamma \Gamma_{G_i}^2}{(E_\gamma^2 - E_{G_i}^2)^2 + E_\gamma^2 \Gamma_{G_i}^2}, \quad (4)$$

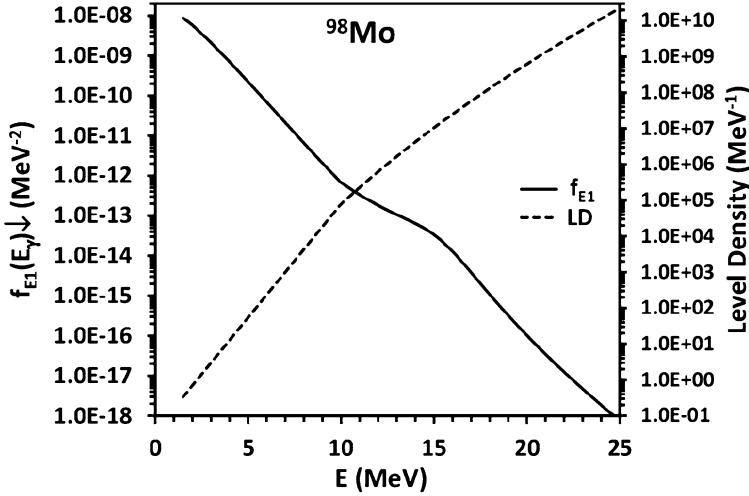


Fig. 1 Deconvolution of ^{98}Mo PSF into GSF and LDF components assuming the HFB LDF formulation of Goriely et al. [7]

where E_{G_i} , Γ_{G_i} , and σ_{G_i} are the energy, width, and cross section for the GDR, respectively. Although the BA formulation is experimentally verified by photonuclear reactions down to $E_x \approx S_n$, it is valid down to the GS although at low excitations, where the level density is low, experimental agreement may be worse due to Porter–Thomas [6] fluctuations. From Eq. 3 average photonuclear GSF can be written as

$$\overline{f_{E1}^{BA}} \downarrow = \frac{2J_i + 1}{2J_f + 1} \frac{\overline{F_{E1}^{BA}} \uparrow (E_\gamma)}{\rho(E_x, J^\pi)} \quad (5)$$

where for even–even nuclei $J_f^\pi = 1^-$ and $\frac{2J_i+1}{2J_f+1} = \frac{1}{3}$. The photonuclear GSF can be deconvoluted from the PSF using the Hartree–Fock–Bogoliubov (HFB) LDF calculated by Goriely et al. [7]. The separated LDF and GSF functions are shown for ^{98}Mo photonuclear data in Fig. 1. Remarkably the GSF is a nearly continuous function showing little trace of the GDR. The slight variation in the GSF near the GDR is an artifact of the assumption that the LDF is continuous, so the origin of the GDR peak remains a mystery.

Considerable charged particle- $\gamma\gamma$ coincidence data has been measured at the Oslo University cyclotron with the CACTUS NaI detector array [8]. Through a sophisticated unfolding process [1] they have accurately determined absolute experimental LDFs and the relative PSFs. Normalization of the photon strength data to an absolute scale remains problematic. Often this is done by normalizing the Oslo PSF to the photonuclear PSF near S_n . However, as is shown by Eq. 3, this method is insufficient. Normalization at a single energy fails to account for large differences

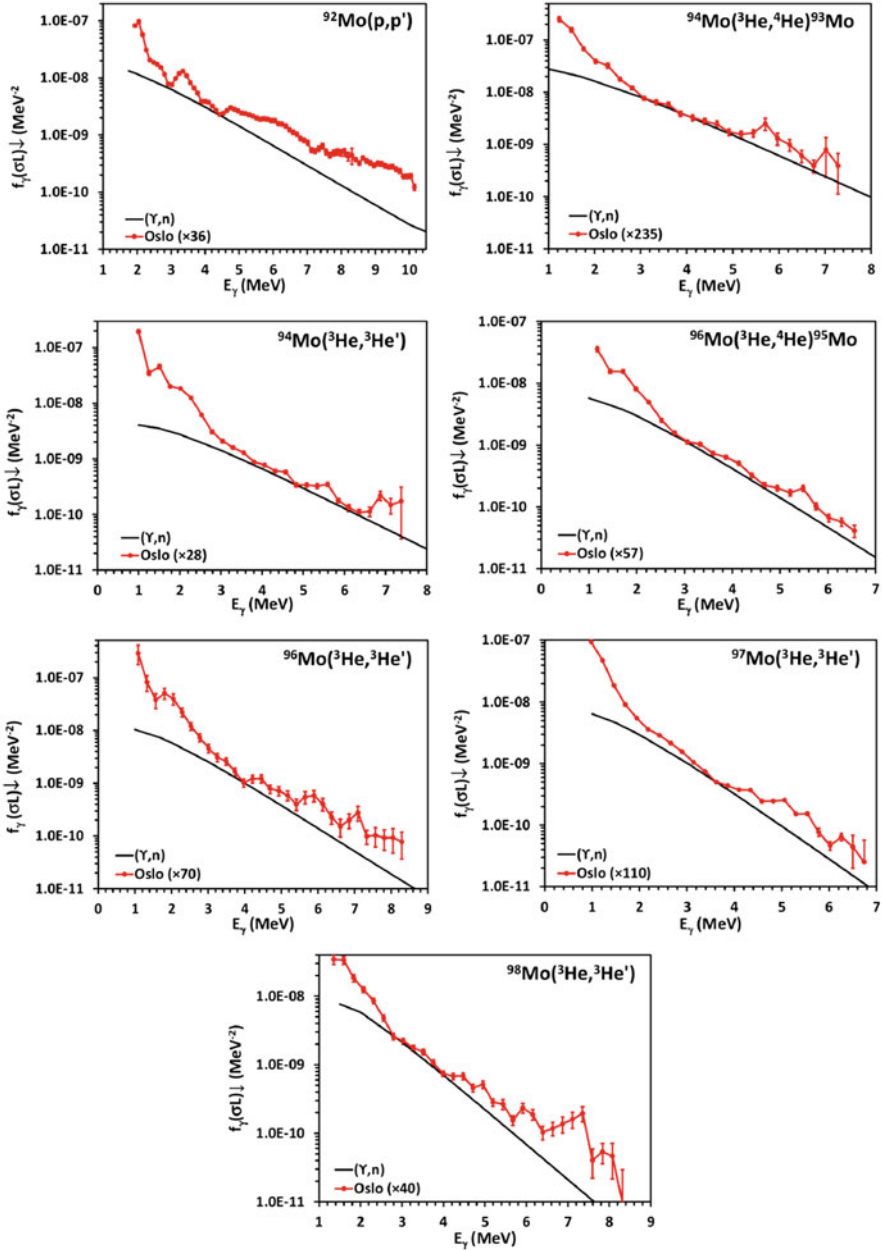


Fig. 2 Comparison of renormalized Oslo GSFs for $^{92-98}\text{Mo}$ [9, 10] (red curves) with photonuclear GSFs (black curves). The Oslo GSFs are normalized so that no points fall below the photonuclear GSFs

in the photonuclear and Oslo LDFs at all energies. Oslo experiments also populate a much larger range of level spins and parities that may deexcite by M1, E2, and nuclear structure related E1 transitions.

The Oslo GSF, $\overline{f^{Oslo}} \downarrow (E_\gamma)$ can be deconvoluted from the Oslo PSF by dividing out their experimental level densities, $\rho_{Oslo}(E_x, J^\pi)$ as shown in Eq. 6

$$\overline{f^{Oslo}} \downarrow (E_\gamma) \propto \frac{\overline{F^{Oslo}} \downarrow (E_\gamma)}{\rho_{Oslo}(E_x, J^\pi)}. \quad (6)$$

No exact normalization is possible for these data; however, the relative GSF trends can be inferred. Also, no $B(\sigma L)$ matrix elements can be inferred because $\overline{f^{Oslo}} \downarrow (E_\gamma)$ represents a composite strength for all multipolarities. Indeed there is no evidence that a constant, energy dependent, GSF is even appropriate for M1, E2, and some E1 transitions.

Renormalized Oslo reaction GSFs for $^{92-98}\text{Mo}$ [9, 10] are compared with the corresponding photonuclear GSFs in Fig. 2. The photonuclear GSFs are calculated with the BA formulation using RIPL-3 [11] GDR parameters. Here the Oslo GSF data are normalized so that no values fall below the BA values. In all cases the Oslo GSFs show significant enhancement at both low and high γ -ray energies. The low-energy enhancement is consistent with earlier shell model calculations [12] for $^{56,57}\text{Fe}$ and can be ascribed to M1 transitions between levels of the same seniority. The high-energy enhancement is consistent with bremsstrahlung measurements on the same isotopes and has been ascribed [13] to pygmy resonances.

I have demonstrated that PSFs can be deconvoluted into the product of a LDF and a GSF. The photonuclear GSF is a nearly continuous function that decreases rapidly with increasing transition energy, as would be expected if the nuclear structures of widely separated levels are very different. A new method is described for extracting the Oslo GSF from their PSF data. The Oslo GSF for the isotopes $^{92-98}\text{Mo}$ has been analyzed and reveals both low- and high-energy upbends in all cases.

Acknowledgments This work was performed under the auspices of the U.S. Department of Energy by the University of California, supported by the Director, Office of Science, Office of Basic Energy Sciences, of the U.S. Department of Energy at Lawrence Berkeley National Laboratory under Contract No. DE-AC02-05CH11231. I especially wish to thank my colleagues at the University of Oslo for our many scientific discussions and their hospitality during my many visits there that inspired my interest in this subject.

References

1. A. Schiller, L. Bergholt, M. Guttormsen, E. Melby, J. Rekstad, S. Siem, Extraction of level density and γ strength function from primary γ spectra. *Nucl. Instrum. Methods* **447**, 498 (2000)
2. J. Blatt, V. Weisskopf, *Theoretical Nuclear Physics* (John Wiley and Sons, New York, 1952)

3. M. Uhl, J. Kopecky, Gamma-ray strength function models and their parameterization. Tech. Rep. ECN-RX-94-099 (1995)
4. P. Axel, Electric dipole ground-state transition width strength function and 7-Mev photon interactions. *Phys. Rev.* **126**, 671 (1962)
5. D. Brink, Some aspects of the interaction of fields with matter. Ph.D. Thesis, Oxford University (1956). Unpublished
6. C. Porter, R. Thomas, Fluctuations of nuclear reaction widths. *Phys. Rev.* **104**, 483 (1956)
7. S. Goriely, S. Hilaire, A. Koning, *Phys. Rev. C* **78**, 064312 (2008)
8. M. Guttormsen, A. Atac, G. Lvhiden, S. Messelt, T. Ramsy, J. Rekestad, T.F. Thorsteinsen, T.S. Tvetter, Z. Zelazny, Statistical gamma-decay at low angular momentum. *Phys. Scr. T* **32**, 54 (1990)
9. R. Chankova, A. Schiller, U. Agvaanluvsan, E. Algin, L. Bernstein, M. Guttormsen, F. Ingebretsen, T. Lnnroth, S. Messelt, G. Mitchell, J. Rekestad, S. Siem, A. Larsen, A. Voinov, S. Ødegård, Level densities and thermodynamical quantities of heated $^{93-98}\text{Mo}$ isotopes. *Phys. Rev. C* **73**, 034311 (2006)
10. G.M. Tveten, A. Spyrou, R. Schwengner, F. Naqvi, A. Larsen, T. Eriksen, F.B. Garrote, L. Bernstein, D. Bleuel, L.C. Campo, M. Guttormsen, F. Giacoppo, A. Grgen, T.W. Hagen, K. Hadynska-Klek, M. Klintefjord, B. Meyer, H. Nyhus, T. Renstrm, S. Rose, E. Sahin, S. Siem, T.G. Tornyi, Completing the nuclear reaction puzzle of the nucleosynthesis of ^{92}Mo . *Phys. Rev. C* **94**, 025804 (2016)
11. T. Belgya, O. Bersillon, R. Capote, T. Fukahori, G. Zhigang, S. Goriely, M. Herman, A. Ignatyuk, S. Kailas, A. Koning, P. Obložinský, V. Plujko, P. Young, Handbook for calculation of nuclear reaction data. Reference Input Parameter Library-2, Technical Report. IAEA-TECDOC 1506. International Atomic Energy Agency, Vienna (2006)
12. B. Brown, A. Larson, Large low-energy $m1$ strength for $^{56,57}\text{Fe}$ within the nuclear shell model. *Phys. Rev. Lett.* **113**, 252502 (2014)
13. M. Erhard, A.R. Junghans, C. Nair, R. Schwengner, R. Beyer, J. Klug, K. Kosev, A. Wagner, E. Grosse, Experimental study of the electric dipole strength in the even Mo nuclei and its deformation dependence. *Phys. Rev. C* **81**, 034319 (2010)

Part VI
Oslo Method

Attempting to Close the Loop on the Oslo Technique at ^{198}Au : Constraining the Nuclear Spin Distribution



Paul Koehler , John Ullmann , Aaron Couture , and Shea Mosby 

1 Introduction

Average s -wave neutron resonance spacings D_0 and total radiation widths $\langle\Gamma_{\gamma 0}\rangle$ are routinely used to calibrate nuclear level densities (NLDs) and photon strength functions (PSFs) obtained with the Oslo technique [1]. However, there is more information beyond D_0 and $\langle\Gamma_{\gamma 0}\rangle$, so it is possible to use additional pieces of the neutron resonance data to test other calibrations as well as assumptions inherent in the extraction of NLDs and PSFs from the Oslo data. For example [2], the distribution of total radiation widths can be calculated, in the framework of the nuclear statistical model (NSM), using the same NLD and PSF which were calibrated using D_0 and $\langle\Gamma_{\gamma 0}\rangle$ from the same neutron resonance data set. Recently published NLDs [3] and PSFs [4] for ^{198}Au , together with new Γ_{γ} data from our new R -matrix analysis of new neutron total cross section data and previous neutron total [5] and capture [6] data make possible such a test for ^{198}Au as described herein.

2 New $^{197}\text{Au} + n$ Total Cross Section Data and R -Matrix Analysis

At the Los Alamos Neutron Science Center (LANSCE), we have been developing [7] the Device for Indirect Neutron Capture Experiments on Radionuclides (DICER) to tightly constrain (n, γ) cross sections on short-lived radionuclides by measurement and analysis of resonance neutron total cross sections on the same nuclides.

P. Koehler (✉) · J. Ullmann · A. Couture · S. Mosby
Group P-27, Los Alamos National Laboratory, Los Alamos, NM, USA
e-mail: koehler@lanl.gov

© This is a U.S. government work and not under copyright protection in the U.S.; foreign copyright protection may apply 2021
J. Escher et al. (eds.), *Compound-Nuclear Reactions*, Springer Proceedings in Physics 254, https://doi.org/10.1007/978-3-030-58082-7_22

As DICER is being developed, we are making test measurements with smaller and smaller samples. One of the first tests used a ^{197}Au sample which was 0.00169 at/b thick. A collimator 6 mm in diameter defined the neutron beam at the sample, 30 m from the neutron-production target. Neutrons were detected with a ^6Li -glass scintillator 64.4 m from the neutron-production target. Separate measurements with no sample and with thick Bi, Cu, and Tm samples were made with the same apparatus to be able to calculate the total cross section and to measure and subtract small backgrounds.

Initial comparison of our new DICER data to the latest ENDF evaluation [8] revealed several differences. Therefore, a new R -matrix analysis of our data as well as the most recent neutron total [5] and capture [6] data was undertaken.

The R -matrix program SAMMY [9] was used to perform a simultaneous analysis of the three data sets. Resonance spins (1^+ or 2^+) were taken from Ref. [10]. In total, 281 resonances were fitted between 4.9 eV and 5 keV. Good fits were obtained to all three data sets. In contrast, the ENDF parameters provide a poor description of the data in many instances. Example data and fits are shown in Fig. 1.

Reliable Γ_γ values for testing the Oslo data could be obtained only for the subset of resonances for which the spins were known and for which the neutron widths were large enough for Γ_γ to be determined with sufficient accuracy. In the present

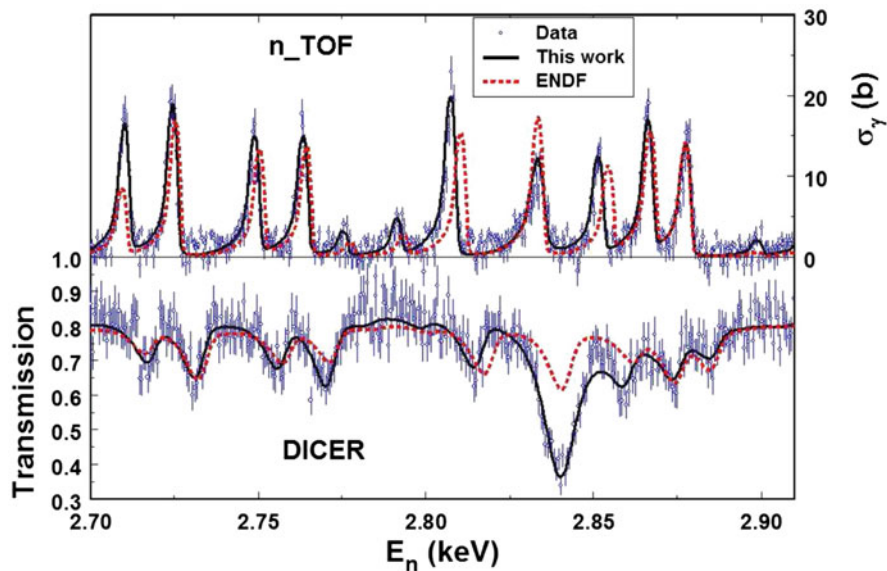


Fig. 1 Example $^{197}\text{Au}(n, \gamma)$ data from n_TOF [6] (upper panel with scale on the right), new $^{197}\text{Au} + n$ total cross section data (shown as transmission in lower panel with scale on the left) from DICER, and SAMMY R -matrix descriptions of the data using the latest ENDF parameters (dashed red curves) and from this work (solid black curves). There are no GELINA transmission data in this energy range

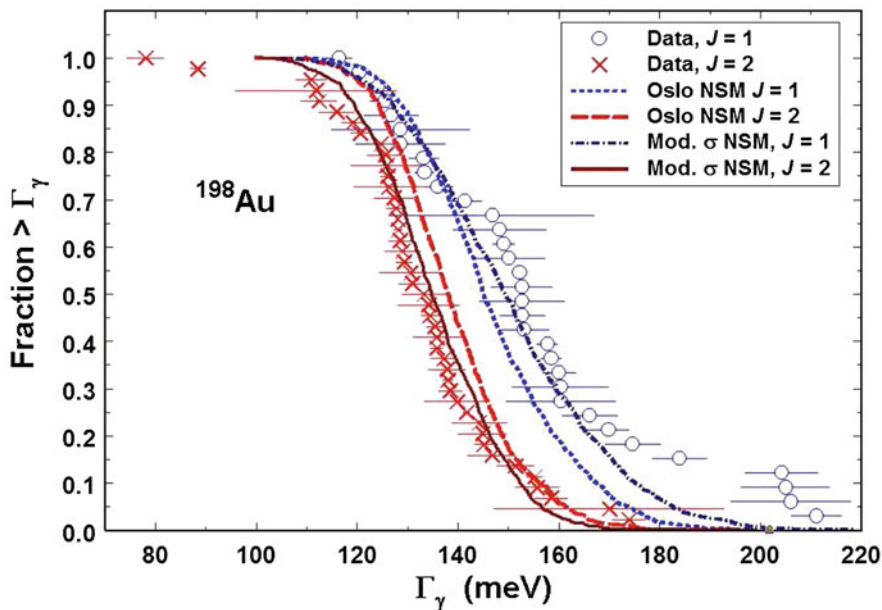


Fig. 2 Measured (blue circles and red X's) and NSM-calculated cumulative total radiation-width distributions for ^{197}Au $J = 1$ and 2 neutron resonances. The calculations were performed using the published Oslo NLD and PSF (short-dashed light blue and long-dashed light red curves) and modified NLD and PSF calibrated using alternative spin distribution A4 shown in Fig. 3 (dot-dashed dark blue and solid dark red curves)

case, there were 33 $J^\pi = 1^+$ and 44 $J^\pi = 2^+$ resonances satisfying these conditions. Cumulative Γ_γ distributions for these two subsets of resonances are shown in Fig. 2.

3 Statistical Model Calculation and Results

Given a PSF and NLD, it is straightforward [2] to calculate Γ_γ distributions in the framework of the NSM. The total radiation width Γ_γ is the sum of all partial radiation widths $\Gamma_{\lambda\gamma f}(XL)$ between resonance λ and final level f which can be reached by a transition of type X (electric or magnetic) and multipolarity L , $\Gamma_\gamma = \sum_f \sum_{XL} \Gamma_{\lambda\gamma f}(XL)$. The NSM assumes the partial radiation widths follow a Porter–Thomas distribution (PTD) [11] around their expectation value, $\langle \Gamma_{\lambda\gamma f}(XL) \rangle = \frac{f_{XL}(E_\gamma)E_\gamma^3}{\rho(E_\lambda, J_\lambda, \pi_\lambda)}$, where $E_\gamma = B_n - E_f$ is the γ -ray energy, $\rho(E_\lambda, J_\lambda, \pi_\lambda)$ is the NLD of resonances with spin J_λ and parity π_λ at energy E_λ , and $f_{XL}(E_\gamma)$ is the PSF for XL transitions.

Calculating a Γ_γ distribution then involves the following steps. A complete level scheme above a critical excitation energy E_c is generated according to

the NLD. Below $E_c = 0.626$ MeV, values of E_f , J_f , and π_f determined from experiments are used. Spin and parity selection rules are properly taken into account for individual transitions. Partial radiation widths are then calculated by random sampling from PTDs characterized by the corresponding expectation values. To obtain a distribution of Γ_γ values, this process is repeated numerous times using the same level scheme but new PTD sampling each time.

Results of calculating Γ_γ distributions for 1^+ and 2^+ resonances in ^{198}Au using published NLDs [3] and PSFs [4] measured with the Oslo technique are compared to our new data in Fig. 2. From this figure, it can be seen that the calculated distributions are significantly narrower and closer together than the data. Below, we describe how the Oslo NLD and PSF can be adjusted, within the confines of the technique, to obtain agreement between calculation and data.

The width of the Γ_γ distribution is a consequence of sampling from the PTD but the magnitude of the width depends on details of the NLD and PSF. Transitions to levels near the ground state tend to have the greatest influence on the width of the distribution because they have the largest partial widths. The spin distribution of the NLD can affect the width of the Γ_γ distributions in several ways. For example, increasing the number of levels of a given spin (to which resonance transitions can occur) near the ground state can make the distribution narrower because the fluctuations will be damped by averaging over more contributions. The spin distribution also affects the slope of the PSF, which affects the widths of the Γ_γ distributions. For example, a PSF with steeper energy dependence (due to a broader spin distribution at higher excitations) can lead to a wider Γ_γ distribution, by increasing the relative sizes of the largest partial widths.

The spin distribution of the NLD also affects the separation between the Γ_γ distributions for the two s -wave-resonance spins in at least two ways. First, the expectation value is inversely proportional to the average level density, $\rho(E_\lambda, J_\lambda, \pi_\lambda)$, for resonances of a given spin. Because there are more $J = 2$ than $J = 1$ resonances, the expectation value is smaller for the larger spin and hence the cumulative distribution for $J = 2$ is, on average, to the left of the $J = 1$ distribution in Fig. 2. In the present work, this component is fixed because the relative number of resonances of the two spins is obtained from our R -matrix analysis.

The second way the spin distribution affects the separation between the Γ_γ distributions for the two spins is through the relative number of $J = 0$ to $J = 3$ final states. This is because, assuming dipole transition dominate, only $J = 1$ ($J = 2$) resonances can decay to $J = 0$ ($J = 3$) levels. Therefore, increasing the number of $J = 0$ relative to $J = 3$ levels, especially near the ground state where the corresponding partial widths are larger, will increase the separation between the two Γ_γ distributions. On the other hand, too many low-spin levels near the ground state can lead to a narrowing of the distributions as explained above. So, the spin distribution is constrained in opposite directions by the widths and relative spacing between the Γ_γ distributions for the two s -wave-resonance spins.

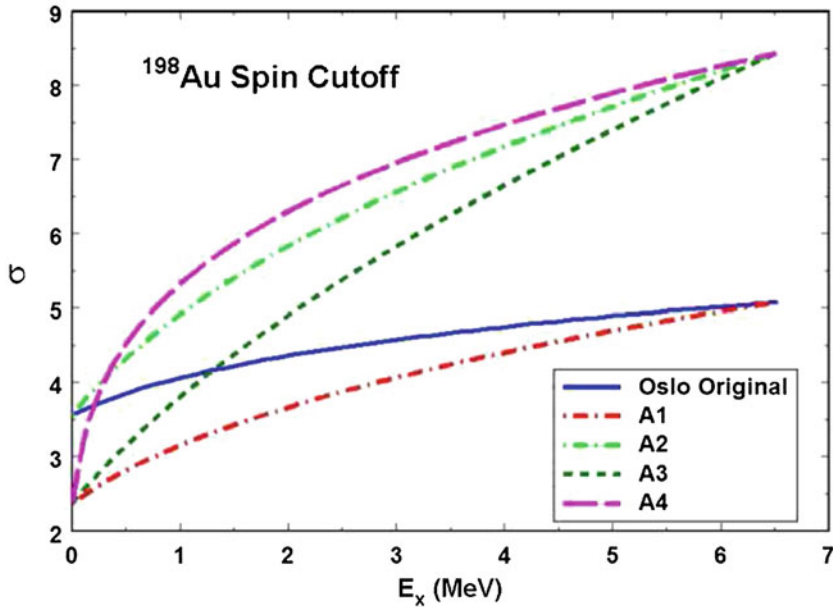


Fig. 3 Various values of the spin-cutoff parameter, as a function of excitation energy, used in the NSM calculations of the Γ_γ distributions. See text for details

The spin distribution typically is parameterized in terms of the spin-cutoff parameter σ , $\rho_J = \frac{2J+1}{2\sigma^2} e^{-\frac{J(J+1)}{2\sigma^2}} \rho$, where σ is a function of excitation energy. In this framework, we found that decreasing spin cutoff at low excitation $\sigma(0)$ (from the Oslo value of 3.56 to 2.37) together with increasing the spin cutoff near the neutron separation energy $\sigma(\text{Sn})$ (from 5.08 to 8.43), and using the steeper energy dependence of σ suggested in Ref. [12] rather than that of Ref. [13] (which was used in the Oslo analysis) results in much better agreement with the Γ_γ -distribution data, as shown in Fig. 2. As far as we know, these changes are all within what is allowed by the available data. In fact, we arrived at $\sigma(0) = 2.37$ by fitting the known levels below E_c .

Various choices of σ we have explored are illustrated in Fig. 3. Only the A2 and A4 versions yielded quantitative agreement (within two standard deviations for all parameters) with a maximum-likelihood (ML) analysis of the data (assuming a Gaussian distribution as in Ref. [14], see Table 1), but $\sigma(0)$ for A2 seems to be larger than allowed by the known levels below E_c . Only A4 assumes the energy dependence of Ref. [12]. The others follow Ref. [13].

Table 1 Gaussian Γ_γ distribution parameters from ML analysis of the data (row 3) and NSM calculations (rows 4–8). σ_G is the standard deviation of the assumed Gaussian distribution

Case	$\langle \Gamma_\gamma \rangle_{J=1} - \langle \Gamma_\gamma \rangle_{J=2}$ (meV)	σ_G (meV)	
		$J = 1$	$J = 2$
Data	21.8 ± 4.9	24.1 ± 3.1	16.3 ± 1.8
Oslo	7.7	14.8	12.5
A1	11.4	13.3	10.4
A2	13.4	22.2	14.7
A3	14.8	18.8	12.8
A4	13.5	23.7	16.6

4 Conclusions

Distributions of total radiation widths for ^{197}Au neutron resonances were obtained from simultaneous R -matrix analysis of new data from DICER as well as previous data from n _TOF and GELINA. These data were compared to calculated distributions in the framework of the NSM using published NLDs and PSFs measured using the Oslo technique. There were significant differences between the measured and calculated distributions. We obtained agreement with the data by adjusting the spin distribution of the NLD. As far as we know, the spin distribution is otherwise poorly constrained, except at very low excitation in ^{198}Au . The technique we used is applicable to other nuclides for which there are high-quality neutron resonance data and could be used to obtain much better constraints on the nuclear spin distribution as a function of excitation energy. As the spin distribution affects the shapes of the NLD and PSF extracted using the Oslo technique, this work could have broad implications.

References

1. A.C. Larsen et al., Analysis of possible systematic errors in the Oslo method. *Phys. Rev. C* **83**, 034315 (2011)
2. P.E. Koehler et al., Extreme nonstatistical effects in γ decay of ^{95}Mo neutron resonances, *Phys. Rev. C* **88**, 041305(R) (2013)
3. F. Giacoppo et al., Level densities and thermodynamical properties of Pt and Au isotopes. *Phys. Rev. C* **90**, 054330 (2014)
4. F. Giacoppo et al., γ decay from the quasicontinuum of $^{197,198}\text{Au}$. *Phys. Rev. C* **91**, 054327 (2015)
5. I. Sirakov et al., Results of total cross section measurements for ^{197}Au in the neutron energy region from 4 to 108 keV at GELINA. *Eur. Phys. J. A* **49**, 144 (2013)
6. C. Massimi et al., $^{197}\text{Au}(n,\gamma)$ cross section in the resonance region. *Phys. Rev. C* **81**, 044616 (2010)
7. Koehler, P. E.: Total Cross Sections as a Surrogate for Neutron Capture, Los Alamos National Laboratory Report LA-UR-14-21466 (2014)
8. D.A. Brown et al., ENDF/B-VIII.0. Nuclear Data Sheets **148**, 1 (2018)

9. Larson, N. M.: Updated Users' Guide for SAMMY, Oak Ridge National Laboratory Technical Report No. ORNL/TM-9179/R8 (2008)
10. R.N. Alves et al., Determination du spin et des parametres des resonances pour $^{197}\text{Au}+n$ de 1000 eV a 2100 eV. Nucl. Phys. **A131**, 450 (1960)
11. C.E. Porter, R.G. Thomas, Fluctuation of nuclear reaction widths. Phys. Rev. **104**, 483 (1956)
12. S.M. Grimes et al., Level density and spin cutoff parameters from continuum (p,n) and (α ,n) spectra. Phys. Rev. C **10**, 2373 (1974)
13. T. von Egidy, D. Bucurescu, Experimental energy-dependent nuclear spin distributions. Phys. Rev. C **80**, 054310 (2009)
14. M. Asghar et al., The neutron cross sections of thorium and the analysis of the resonances up to 1 keV. Nucl. Phys. **76**, 196 (1966)

Impact of Restricted Spin-Ranges in the Oslo Method: The Example of $(d,p)^{240}\text{Pu}$



F. Zeiser, G. Potel, G. M. Tveten, A. C. Larsen, M. Guttormsen, T. A. Laplace, S. Siem, D. L. Bleuel, B. L. Goldblum, L. A. Bernstein, F. L. Bello Garrote, L. Crespo Campo, T. K. Eriksen, A. Gorgen, K. Hadynska-Klek, J. E. Midthb, T. Renstrm, E. Sahin, T. Torny, A. Voinov, and M. Wiedeking

1 Introduction

Proper knowledge of neutron-induced cross sections from thermal energies to several MeV is important for many physical applications. However, the lack of a mono-energetic neutron source in the full energy range hampers direct cross-section measurements. The short half-lives of many isotopes of astrophysical interest make it impossible to create targets for direct measurements using neutron

F. Zeiser (✉) · G. M. Tveten · A. C. Larsen · M. Guttormsen · S. Siem · F. L. Bello Garrote · L. Crespo Campo · T. K. Eriksen · A. Gorgen · K. Hadynska-Klek · J. E. Midthb · T. Renstrm · E. Sahin · T. Torny
Department of Physics, University of Oslo, Oslo, Norway
e-mail: fabio.zeiser@fys.uio.no

G. Potel
Facility for Rare Isotope Beams, Michigan State University, East Lansing, MI, USA

T. A. Laplace · B. L. Goldblum
Department of Nuclear Engineering, University of California, Berkeley, CA, USA

D. L. Bleuel
Lawrence Livermore National Laboratory, Livermore, CA, USA

L. A. Bernstein
Department of Nuclear Engineering, University of California, Berkeley, CA, USA
Lawrence Berkeley National Laboratory, Berkeley, CA, USA

A. Voinov
Department of Physics and Astronomy, Ohio University, Athens, OH, USA

M. Wiedeking
iThemba LABS, Somerset West, South Africa

beams. In these cases, calculations within the statistical framework can provide an alternative approach to obtain (n,x) cross-sections. These rely essentially on precise measurements of nuclear level densities (NLD) and γ -ray strength functions (γ SF) [1].

The Oslo Method [2, 3] can be used to analyze particle- γ coincidence spectra from transfer reactions to simultaneously extract NLDs and γ SFs. In a campaign to study actinides the method has been applied to the compound nuclei $^{231-233}\text{Th}$, $^{232,233}\text{Pa}$, $^{237-239}\text{U}$, ^{238}Np [4–7], and ^{243}Pu [8] using different light-ion reactions. The extracted γ SFs show a significant enhancement between about 2 and 4 MeV, which is consistent with the location [9] of a low energy orbital M1 scissors resonance (SR).

Larsen et al. [3] have shown that the population of a limited spin range may lead to distortions of the γ SF. This has been observed in some of the previous studies on actinides [4–8] due to the low-spin transfer using the (d,p) reaction mechanism, where an ad hoc procedure for the correction was adopted. In this proceeding, we focus on the first systematic analysis of the impact on the Oslo Method results for a realistic spin-parity population for the $(d,p)^{240}\text{Pu}$ reaction.

2 Experimental Setup and Data Analysis

The $(d,p)^{240}\text{Pu}$ experiment was conducted using a 12 MeV deuteron beam at the Oslo Cyclotron Laboratory (OCL). The 0.4 mg/cm^2 thick ^{239}Pu target was purified using an anion-exchange resin column procedure [10] prior to electroplating on a 1.9 mg/cm^2 beryllium backing.

The outgoing charged particles were detected with the SiRi particle telescope [11]. SiRi consists of 64 silicon particle telescopes with a thickness of $130\text{ }\mu\text{m}$ for the front (ΔE) and $1550\text{ }\mu\text{m}$ for the back (E) detectors, and was placed at backwards angles (126° to 140°). The CACTUS array [12] measured coincident γ rays and was composed of 26 lead collimated $5'' \times 5''$ NaI(Tl) crystals with a total efficiency of 14.1(2)% at $E_\gamma = 1.33\text{ MeV}$. Additionally, four Parallel Plate Avalanche Counters (PPAC) [13] were used to detect fission events.

The reaction kinematics allowed for selection of (d,p) events and conversion of the detected proton energy to the excitation energy E_x of the compound nucleus ^{240}Pu . Prompt γ rays were selected from a $\pm 14\text{ ns}$ wide time-window with background correction applied. The γ -ray spectra were unfolded following the procedure of [14], using response functions [15] that were updated in 2012.

Next, an iterative subtraction technique [16] was applied to obtain the primary γ rays $P(E_x, E_\gamma)$ (also called first-generation γ rays) for each E_x bin from the initial spectra, which include all γ rays of the decay cascades. Here we relied on the assumption that the (d,p) -reaction will populate a similar spin-parity distribution for the levels in an E_x bin i as would be populated from γ -decay from a higher

excitation energy bin j . Consequently, by subtracting the γ -ray spectra from bins with lower excitation energy, only the primary γ rays remain.

3 Extraction of NLD and γ SF

For γ rays emitted in the statistical regime (i.e., high level density) we can determine the NLD at the excitation energy of the final state, $\rho(E_{x,f})$, and the γ -ray transmission coefficient, $\mathcal{T}(E_\gamma)$ [2]:

$$P(E_{x,i}, E_\gamma) \propto \rho(E_{x,f}) \mathcal{T}(E_\gamma), \quad (1)$$

up to a transformation with the parameters A , B , and α ,

$$\tilde{\rho}(E_i - E_\gamma) = A \exp[\alpha (E_i - E_\gamma)] \rho(E_i - E_\gamma), \quad (2)$$

$$\tilde{\mathcal{T}}(E_\gamma) = B \exp[\alpha E_\gamma] \mathcal{T}(E_\gamma). \quad (3)$$

To select the γ decay channel, only excitation energies E_x below the neutron separation energy ($S_n = 6.534$ MeV [17]) must be considered. In this experiment, we applied more stringent constraints due to the onset of sub-barrier fission events at about 4.5 MeV [18, 19]. A more detailed analysis of the prompt fission γ rays can be found in [20]. The final extraction regions were $E_\gamma^{\min} = 1.2$ MeV, $E_x^{\min} = 2.4$ MeV, $E_x^{\max} = 4.0$ MeV. It remained then to find the transformation parameters corresponding to the correct physical solution.

The level density at low E_x was normalized to the discrete level scheme [21] was normalized to the discrete level scheme [21] up to an excitation energy $E_c \approx 1$ MeV. Above this energy we expect that the low-lying level scheme is now known completely anymore. At the neutron separation energy S_n , we obtain $\rho(S_n)$ from the average neutron resonance spacing for s-waves, $D_0 = 2.20(9)$ eV, taken from RIPL-3 [22] following [2]. The latter conversion depends on the spin-parity distribution; we assumed equal parities and used the spin distribution $g(E_x, I)$ proposed by Ericson [23, Eq. (3.29)] together with the rigid-body moment of inertia approach for the spin cut-off parameter σ by von Egidy and Bucurescu [24]. Additionally, we extrapolated from the highest E_x data points up to S_n . In accordance with findings for other actinides [5], this was performed assuming a constant temperature level density formula [25]. The resulting level density ρ is displayed in Fig. 1a.

The remaining parameter B for the normalization of the transmission coefficient \mathcal{T} can be determined [29, 30] from the average total radiative width $\langle \Gamma_\gamma \rangle(S_n) = 43(4)$ meV [22]. The γ -ray strength function $f(E_\gamma)$ was obtained from the transmission coefficient \mathcal{T} assuming dominance of dipole strength, $f(E_\gamma) = \mathcal{T}(E_\gamma)/(2\pi E_\gamma^3)$, and is shown in Fig. 1b.

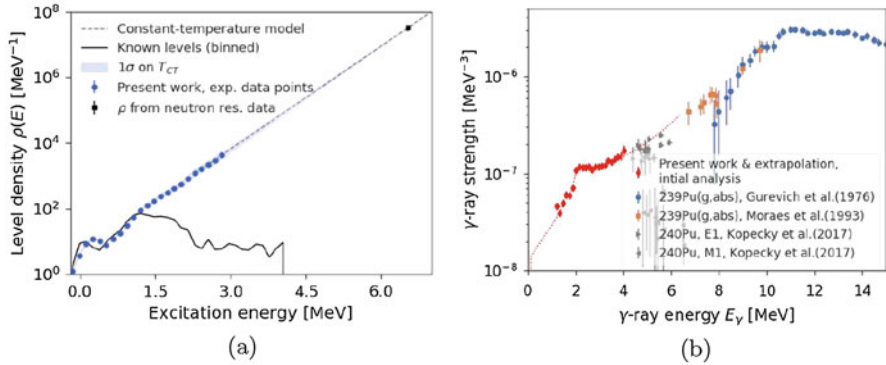


Fig. 1 Initially extracted total level density (a) and γ SF (b) for ^{240}Pu (a). We used a constant temperature interpolation with $T_{CT} = 0.415(10)$. The γ SF is displayed together with data from [26–28] (b). The presented error bars include contributions from both statistical and systematic errors of the unfolding and first generation method [2]

4 Impact of the Spin Distribution

In order to analyze the possible impact of a mismatch between the NLD populated in the (d,p) reaction, ρ_{pop} , and the intrinsic NLD, ρ_{int} , we will follow a 4-step procedure: (1) identify the *correct* spin distributions g_{pop} and g_{int} , (2) generate synthetic decay data with known NLD and γ SF, and the identified spin distributions, (3) analyze the results with the Oslo Method, and (4) compare the extracted NLD and γ SF to the input function to infer any systematic deviation.

The (d,p) reaction with the beam energy used in this experiment can be modeled as breakup of a deuteron with emission of a proton, followed by the formation of a compound nucleus with the remaining neutron and the target. The spin-parity distribution, $g_{\text{pop}}(E_x, J, \pi)$, has been calculated in this framework, using the distorted-wave Born approximation (DWBA) in prior form [31, 32]. Here we have taken into account detection angles for the protons and modeled the neutron–nucleus interactions by the dispersive optical model potential of [33] implemented through potential nr. 2408 listed in [22].

To study the effect on the Oslo Method, we first generated a synthetic coincidence dataset with the statistical nuclear decay code RAINIER [34] resembling the (d,p) ^{240}Pu experiment. Following the experimental analysis above, we combined the spin cut-off parameter, σ , of von Egidy and Bucurescu (labeled EB05) [24] with the distribution of Ericson [23] to obtain the intrinsic spin-distribution, g_{int} . As shown in Fig. 2, the distribution calculated with DWBA of populated levels (further labeled as $g_{\text{pop}} \neq g_{\text{int}}$) are centered at much lower spins compared to the assumed intrinsic distribution.

The generated spectra were analyzed with the Oslo Method including folding, unfolding, and the first generation method. The upper panel of Fig. 3a shows the extracted and normalized NLD together with the NLD used as input to RAINIER.

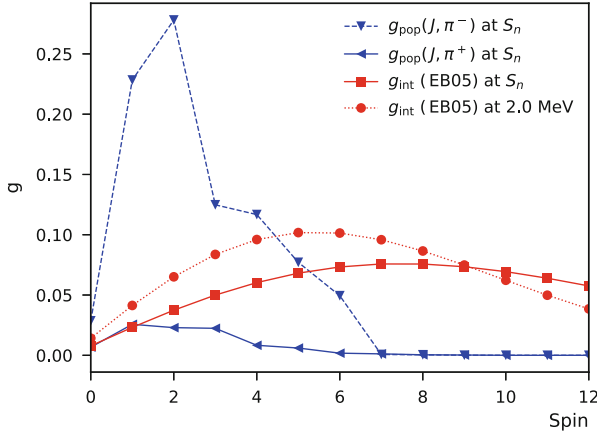


Fig. 2 Calculated spin-parity distribution at $E_x = S_n$ of the populated levels g_{pop} compared to the estimated intrinsic spin distribution g_{int} at S_n with the (Ref. [24]) spin-cut parameter. For the latter equiparity is assumed and we also display the distribution at 2 MeV. More information in the text

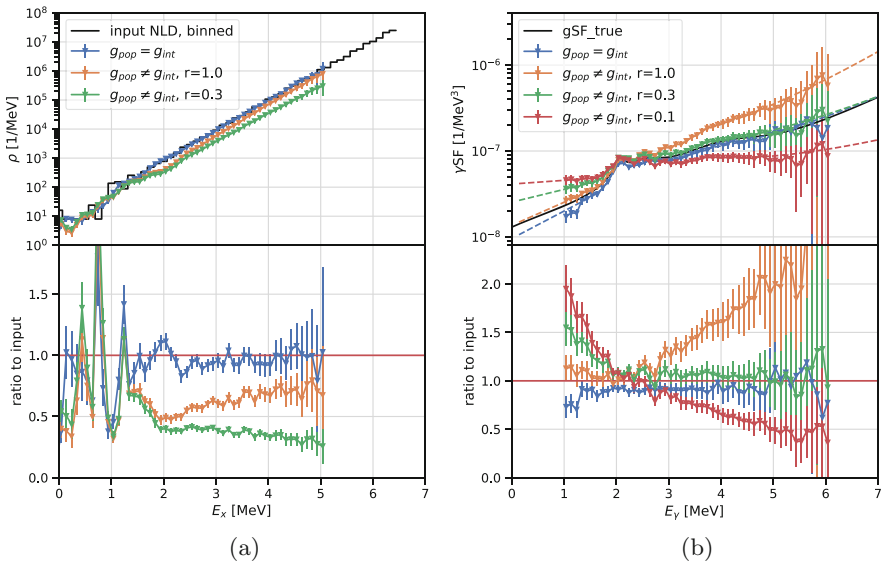


Fig. 3 Upper panels: NLD **(a)** and γ SF **(b)** extracted with the Oslo Method (with an optional correction r) from synthetic dataset. The populated spin distribution g_{pop} was either chosen equal to the intrinsic distribution g_{int} , or narrower, according to the calculations for the (d,p) reaction. The dashed lines for the γ SF denote the extrapolations assumed for the Oslo method. Lower panels: Ratio to the known input

The lower panel displays the derived ratio to the input NLD. As expected, it was observed that the NLD in the quasi-continuum (i.e., above the discrete levels) was well reproduced when $g_{\text{pop}} = g_{\text{int}}$; the assumptions of the first-generation method are fulfilled. However, when populating the nucleus by the more realistic, but *narrower* distribution $g_{\text{pop}} \neq g_{\text{int}}$, we underestimated the derived NLD in the quasi-continuum by up to approximately 40% at 2 MeV.

This deviation may be qualitatively explained by the smaller fraction of levels populated when decaying with a distribution g_{pop} much *narrower* than g_{int} (see also Fig. 2). At higher excitation energies, the ratio is forced to converge to unity due to the normalization at S_n . Note that for the normalization of the γ SF specified in the next paragraphs, we also display the NLD with $g_{\text{pop}} \neq g_{\text{int}}$ where the upper normalization point $\rho_{\text{tot}}(S_n)$ obtained from Eq. (28) in [2] was reduced by

$$\rho_{\text{red}}(S_n) = r \rho_{\text{tot}}(S_n), \quad r \leq 1. \quad (4)$$

We now turn to the extraction of the γ SF. For $g_{\text{pop}} = g_{\text{int}}$, we observed about $\lesssim 10\%$ difference between the absolute values of the extracted strength and the input function. This difference is mainly attributed to a small mismatch of the true and best-fit temperature for the NLD, which propagates to the γ SF absolute values through the normalization.

For the more realistic spin distribution $g_{\text{pop}} \neq g_{\text{int}}$, we first naively extracted the γ SF assuming that we had populated all intrinsic levels. Here the shape of the NLD curve is off since it is forced to match the calibration point at S_n . Figure 3b compares the results to the input γ SF and although the general shape is preserved, both the slope and absolute value are considerably off as compared to the input.

Next, we applied a correction inspired by [4], which is based on the assumption that the transmission coefficient \mathcal{T} is spin independent. The first generation matrix, P , should then be fit by $P \propto \rho_{\text{red}} \mathcal{T}$ to extract the correct \mathcal{T} , where ρ_{red} is obtained from Eq. (4) and indicates that we can decay only to a fraction of all intrinsic levels. This will affect the common transformation parameter α , see Eq. ((2), (3)), which determines the slope of the γ SF: The smaller r , the smaller α , which translates to a flatter slope.

The determination of the remaining scaling parameter B depends on \mathcal{T} as extracted with ρ_{red} . However, the level density available for γ decay following neutron capture is not affected by this reduction, thus we used ρ_{tot} in the $\langle \Gamma_\gamma \rangle$ normalization integral.

We varied the correction factor r of Eq. (4) and found that for $r = 0.3$ we obtained the best match between the (slope of) input and analyzed γ SF. There remained a constant off-set of about 5–10%, which could be attributed to deviations in the NLD, which propagated to the γ SF via the normalization procedure. Besides, the larger deviation towards lower γ -ray energies was traced back to a failure of the first-generation method.

5 Summary and Conclusions

We have presented the first systematic analysis of the effect of a realistic, very narrow spin distribution on the Oslo Method for the (d,p) reaction using the example of the heavy nucleus ^{240}Pu . We have shown that if the assumptions of the Oslo Method were fulfilled, i.e., if the reaction populated all levels proportionally to the intrinsic spin(-parity) distribution, we regain the correct level density and γ -ray strength. However, for such a heavy nucleus and a beam energy below the Coulomb barrier, the calculations show a rather small overlap between the populated spins and the intrinsic distribution. This leads to significant distortions in the extracted nuclear level density and γ -ray strength. We now investigate how the presented approach can be used to correct for the deviations. Finally, the impact on lower mass nuclei needs to be studied, although a significantly greater overlap of the populated and intrinsic distribution and therefore smaller impact is expected.

Acknowledgments We would like to thank J. C. Müller, E. A. Olsen, A. Semchenkov, and J. C. Wikne at the Oslo Cyclotron Laboratory for providing the stable and high-quality deuterium beam during the experiment. This work was supported by the Research Council of Norway under project Grants No. 263030 (F.Z, A.G, S.S) and 262952 (G.M.T), and by the National Research Foundation of South Africa (M.W.). A.C.L. gratefully acknowledges funding from the European Research Council, ERC-STG-2014 Grant Agreement No. 637686. This work was performed under the auspices of U.S. Department of Energy by Lawrence Livermore National Laboratory under Contract No. DE-AC52-07NA27344 (D.L.B) and the Lawrence Berkeley National Laboratory under Contract No. DE-AC02-05CH11231 (L.A.B.). The work of B.L.G., J.A.B., and T.A.L. was supported by the U.S. Department of Energy, National Nuclear Security Administration, Office of Defense Nuclear Nonproliferation Research and Development (DNN R&D) through the Nuclear Science and Security Consortium under Award DE-NA0003180. A.V. was supported under Department of Energy Contract No. DE-NA0002905.

References

1. J.L. Ullmann et al., Phys. Rev. C **96**(2), 024627 (2017)
2. A. Schiller et al., Nucl. Instrum. Methods Phys. Res. A **447**(3), 498–511 (2000)
3. A.C. Larsen et al., Phys. Rev. C **83**(3), 034315 (2011)
4. M. Guttormsen et al., Phys. Rev. Lett. **109**(16) (2012)
5. M. Guttormsen et al., Phys. Rev. C **88**(2), 024307 (2013)
6. M. Guttormsen et al., Phys. Rev. C **89**(1), 014302 (2014)
7. T.G. Tornyi et al., Phys. Rev. C **89**(4), 044323 (2014)
8. T.A. Laplace et al., Phys. Rev. C **93**(1), 014323 (2016)
9. K. Heyde et al., Rev. Mod. Phys. **82**(3), 2365–2419 (2010)
10. R. Henderson et al., Nucl. Instrum. Methods Phys. Res., Sect. A **655**(1), 66–71 (2011)
11. M. Guttormsen et al., Nucl. Instrum. Methods Phys. Res. A **648**(1), 168–173 (2011)
12. M. Guttormsen et al., Phys. Scr. **T32**, 54–60 (1990)
13. T.G. Tornyi et al., Nucl. Instrum. Methods Phys. Res. A **738**, 6–12 (2014)
14. M. Guttormsen et al., Nucl. Instrum. Methods Phys. Res. A **374**(3), 371–376 (1996)
15. L.C. Campo et al., Phys. Rev. C **94**(4) (2016)

16. M. Guttormsen et al., Nucl. Instrum. Methods Phys. Res. A **255**(3), 518–523 (1987)
17. B. Singh et al., Nucl. Data Sheets **109**(10), 2439–2499 (2008). Data extracted from the ENSDF database, version November 2010
18. B.B. Back et al., Phys. Rev. C **9**(5), 1924 (1974)
19. M. Hunyadi et al., Phys. Lett. B **505**(1–4), 27–35 (2001)
20. S.J. Rose et al., Phys. Rev. C **96**, 014601 (2017)
21. Data extracted from the ENSDF database using NNDC’s chart of nuclides. <http://www.nndc.bnl.gov/chart/>. Accessed 10 May 2015
22. R. Capote et al., Nucl. Data Sheets **110**(12), 3107–3214 (2009). Data extracted from RIPL-3 online database. <https://www-nds.iaea.org/RIPL-3/>. Accessed 10 May 2015
23. T. Ericson, Adv. Phys. **9**(36), 425 (1960)
24. T. von Egidy et al., Phys. Rev. C **72**(4), 044311 (2005)
25. A. Gilbert et al., Can. J. Phys. **43**(8), 1446 (1965)
26. J. Kopecky et al., Phys. Rev. C **95**, 054317 (2017)
27. M.A.P.V. De Moraes et al., Phys. Scr. **47**(4), 519 (1993)
28. G. Gurevich et al., Nucl. Phys. A **273**(2), 326 (1976)
29. A. Voinov et al., Phys. Rev. C **63**(4) (2001)
30. J. Kopecky et al., Phys. Rev. C **41**(5), 1941–1955 (1990)
31. G. Potel et al., Phys. Rev. C **92**(3) (2015)
32. G. Potel et al., The European Physical Journal A **53**(9) (2017)
33. R. Capote et al., J. Nucl. Sci. Technol. **45**(4), 333 (2008)
34. L. Kirsch et al., Nucl. Instrum. Methods Phys. Res., Sect. A **892**, 30 (2018)

Systematics of γ -Ray Strength Functions Within the Shell Model



J. E. Midtbø, A. C. Larsen, T. Renstrøm, F. L. Bello Garrote, and E. Lima

The γ -ray strength function $f(E_\gamma)$ plays an important role in many areas of nuclear physics. Notably, it finds widespread use in reaction rate calculations for nucleosynthesis networks [1]. In recent years, a topic of much debate has been the behavior of the γ -ray strength function at the very lowest E_γ energies, below ~ 2 MeV. It has been observed experimentally for a large number of nuclei that the strength function increases as E_γ approaches zero (a complete list is given in Ref. [2]). The presence of such a low-energy enhancement (LEE) can have a large impact on neutron-capture rates [3].

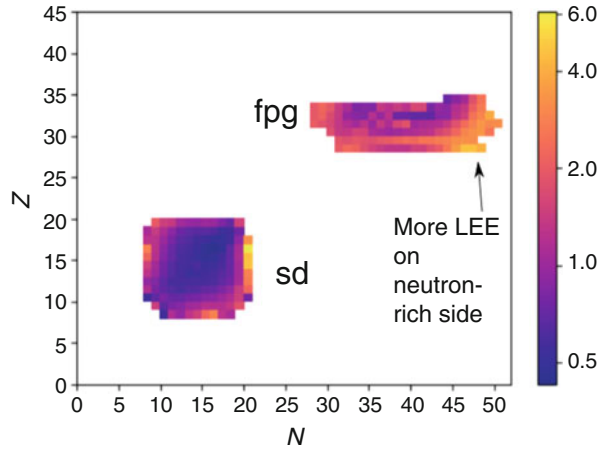
In this contribution, we present our findings from a large-scale survey on the LEE within the framework of the full-configuration shell model [2]. We have calculated $M1$ strength functions for nuclei in two mass regions, comprising all nuclei in the sd shell and isotopes of Ni, Cu, Ga, Ge, As, and Se atop a ^{56}Ni core. We use the massively parallel shell-model code KSHELL [4] and calculate hundreds of energy levels of many spins and (when available) both parities for each nucleus, as well as all allowed $M1$ transitions between the levels. We then compile a level density and extract the $M1$ γ -ray strength function.

A plot of the calculated relative steepness for each nuclide is shown in Fig. 1. The calculations reveal systematic trends:

1. The LEE is steeper near shell closures.
2. It is generally steeper in the fp shell than the sd shell, and seems to steepen with mass number. This can also be interpreted as an increase as a function of the availability of high- ℓ orbitals, as suggested in Ref. [5].
3. For both calculated regions, the low-energy enhancement is steeper on the neutron-rich side than on the proton-rich side. We interpret this as a preference

J. E. Midtbø (✉) · A. C. Larsen · T. Renstrøm · F. L. Bello Garrote · E. Lima
Department of Physics, University of Oslo, Oslo, Norway
e-mail: j.e.midtbo@fys.uio.no

Fig. 1 Steepness of the calculated LEE for each nuclide. The steepness is measured by the relative amount of integrated strength below 2 MeV



of the LEE to the so-called *shears-band regions*, where proton particles couple to neutron holes to generate a large, transverse magnetic moment [6, 7].

4. Across our 283 calculations, the low-energy $M1$ strength never disappears completely, but merely turns flat. A disappearance is what would be expected from standard models of strength functions [8].

In Fig. 2, we have marked off all nuclei that have been studied with the Oslo method, and indicate whether or not the experiment revealed an LEE. Green stars are cases where there is an LEE; orange circles are cases where no LEE was seen; and pink diamonds are cases that are unclear. This figure reveals another systematic trend: The LEE has, with few exceptions, only been seen in nuclei of relatively low mass. This seems at odds with our prediction that the low-energy enhancement increases as function of mass number. However, there is a caveat. The Oslo method has trouble resolving the γ -ray strength function below a certain energy threshold, usually about 1.5 MeV, mainly due to uncertainties in the detector response unfolding. In the few cases where the LEE has been seen in higher-mass nuclei, in $^{151,153}\text{Sm}$, a different detector with a lower energy threshold was used [9]. If the LEE steepens with mass number, it could be out of reach of present experiments above a certain mass threshold. The idea is sketched in Fig. 3.

It therefore seems likely that the LEE is present throughout the nuclear chart, but that it is “hiding” below the experimental threshold in measurements of high-mass nuclei. Hopefully, new experiments with improved low-energy sensitivity can reveal new insight into this phenomenon.

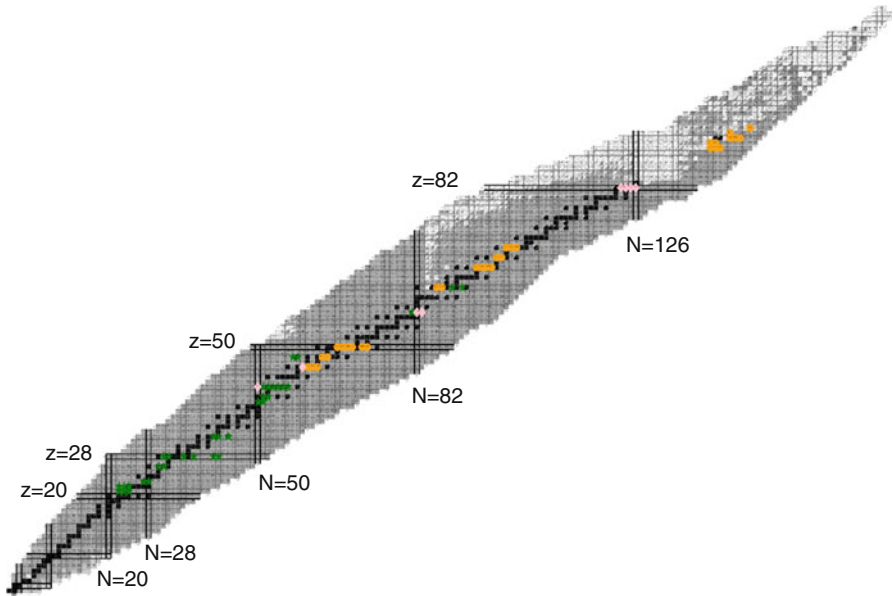
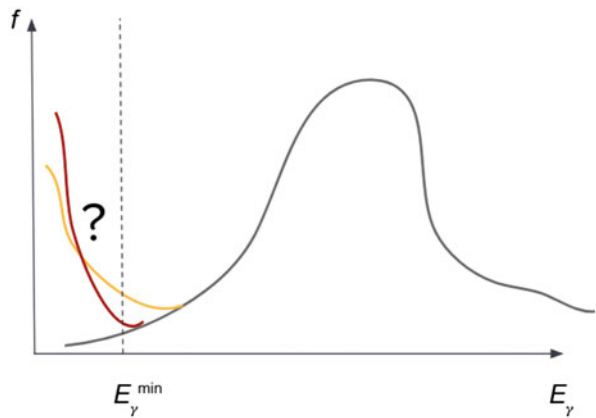


Fig. 2 Chart showing where an LEE has been seen in experiments with the Oslo method. Green stars indicate that an LEE was observed, orange circles indicate that no LEE was observed. Pink diamonds indicate cases that are unclear with respect to the LEE

Fig. 3 A sketch of how we picture the LEE's evolution as a function of mass. The yellow curve is an LEE at low mass, the red curve at high mass. $E_{\gamma, \min}$ indicates the experimental threshold for extracting the LEE



References

1. M. Arnould, S. Goriely, K. Takahashi, Phys. Rep. **450**(4), 97 (2007). <https://doi.org/10.1016/j.physrep.2007.06.002>. <http://www.sciencedirect.com/science/article/pii/S0370157307002438>
2. J.E. Midtbø, A.C. Larsen, T. Renstrøm, F.L. Bello Garrote, E. Lima, Phys. Rev. C **98**(6) (2018). <https://doi.org/10.1103/PhysRevC.98.064321>. <https://link.aps.org/doi/10.1103/PhysRevC.98.064321>

3. A.C. Larsen, S. Goriely, *Phys. Rev. C* **82**(1), 014318 (2010). <https://doi.org/10.1103/PhysRevC.82.014318>. <https://link.aps.org/doi/10.1103/PhysRevC.82.014318>
4. N. Shimizu, arXiv:1310.5431 [nucl-th] (2013). ArXiv: 1310.5431. <http://arxiv.org/abs/1310.5431>
5. B.A. Brown, A.C. Larsen, *Phys. Rev. Lett.* **113**(25), 252502 (2014). <https://doi.org/10.1003/PhysRevLett.113.252502>. <https://link.aps.org/doi/10.1103/PhysRevLett.113.252502>
6. S. Frauendorf, *Rev. Mod. Phys.* **73**(2), 463 (2001). <https://doi.org/10.1103/RevModPhys.73.463>. <https://link.aps.org/doi/10.1103/RevModPhys.73.463>
7. R. Schwengner, S. Frauendorf, A.C. Larsen, *Phys. Rev. Lett.* **111**(23), 232504 (2013). <https://doi.org/10.1103/PhysRevLett.111.232504>. <https://link.aps.org/doi/10.1103/PhysRevLett.111.232504>
8. R. Capote, M. Herman, P. Obložinský, P.G. Young, S. Goriely, T. Belgia, A.V. Ignatyuk, A.J. Koning, S. Hilaire, V.A. Plujko, M. Avrigeanu, O. Bersillon, M.B. Chadwick, T. Fukahori, Z. Ge, Y. Han, S. Kailas, J. Kopecky, V.M. Maslov, G. Reffo, M. Sin, E.S. Soukhovitskii, P. Talou, *Nucl. Data Sheets* **110**(12), 3107 (2009). <https://doi.org/10.1016/j.nds.2009.10.004>. <http://www.sciencedirect.com/science/article/pii/S0090375209000994>
9. A. Simon, M. Guttormsen, A.C. Larsen, C.W. Beausang, P. Humby, J.T. Burke, R.J. Casper, R.O. Hughes, T.J. Ross, J.M. Allmond, R. Chyzh, M. Dag, J. Koglin, E. McCleskey, M. McCleskey, S. Ota, A. Saastamoinen, *Phys. Rev. C* **93**(3), 034303 (2016). <https://doi.org/10.1103/PhysRevC.93.034303>. <https://link.aps.org/doi/10.1103/PhysRevC.93.034303>

Part VII
Surrogate Nuclear Reactions

Future Perspectives for Surrogate-Reaction Studies at Storage Rings



A. Henriques, B. Jurado, D. Denis-Petit, T. Chiron, L. Gaudefroy, J. Glorius, M. Grieser, C. Langer, Y. A. Litvinov, L. Mathieu, V. Méot, R. Pérez-Sánchez, J. Pibernat, R. Reifarh, O. Roig, B. Thomas, B. A. Thomas, J. C. Thomas, and I. Tsekhanovich

1 Introduction

Neutron cross sections of radioactive nuclei are important to understand the synthesis of elements from iron to uranium, for industrial purposes, e.g. for more sustainable and efficient energy production and in the search for new therapeutic radionuclides for medical diagnostic and treatment.

A. Henriques · B. Jurado (✉) · T. Chiron · L. Mathieu · R. Pérez-Sánchez · J. Pibernat · O. Roig
B. Thomas · B. A. Thomas · I. Tsekhanovich
CENBG, Centre d'Etudes Nucléaires de Bordeaux Gradignan, CNRS/IN2P3-Université de
Bordeaux, Bordeaux, France
e-mail: jurado@cenbg.in2p3.fr

D. Denis-Petit
CENBG, Centre d'Etudes Nucléaires de Bordeaux Gradignan, CNRS/IN2P3-Université de
Bordeaux, Bordeaux, France

CEA-DAM DIF, Arpajon, France

L. Gaudefroy · V. Méot
CEA-DAM DIF, Arpajon, France

J. Glorius · Y. A. Litvinov
GSI Helmholtzzentrum fuer Schwerionenforschung, Darmstadt, Germany

M. Grieser
Max-Planck Institut für Kernphysik, Heidelberg, Germany

C. Langer · R. Reifarh
University of Frankfurt, Frankfurt, Germany

J. C. Thomas
GANIL, Caen, France

Direct measurements of neutron capture or neutron-induced fission on unstable isotopes are very difficult and often impossible. One of the main reasons is the production and manipulation of radioactive targets. This can be overcome by inverting the reaction kinematics with radioactive beams. However, the unavailability of free-neutron targets makes the direct measurement in inverse kinematics impossible.

The most promising approach to overcome the difficulties associated with the measurement of neutron cross sections of radioactive nuclei is to use surrogate reactions [1, 2].

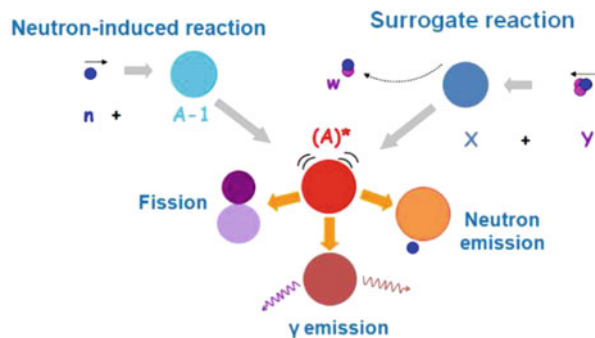
2 Surrogate Reactions

The surrogate reaction produces the compound nucleus of interest by a different reaction than the neutron capture reaction (Fig. 1) and the decay probabilities (e.g. for γ -emission and fission) are measured. The measured decay probabilities of the compound nucleus are used to precisely tune model parameters that will lead to much more accurate predictions of the desired neutron cross sections. Surrogate reactions of interest are inelastic scattering or transfer reactions with light projectile nuclei. Indeed, the power of surrogate reactions has been proven very successfully at high excitation energies for neutron-induced fission in direct kinematics with p, d, ^3He and ^4He beams [1, 3], and recently also for neutron radiative capture [2].

Since 2000, the CENBG together with other laboratories has been performing experiments to study the surrogate-reaction method [3–7]. In the past years, the experimental set-up was improved to simultaneously measure fission and γ -emission probabilities [8].

Our studies on even–odd and odd–odd fissioning nuclei, e.g. [3, 5] show evidence of a good agreement in the fission probabilities measured by surrogate and neutron-induced reactions. Thus, in many cases, fission probabilities induced by surrogate reactions can be used to provide neutron-induced fission cross sections of short-lived nuclei rather directly through the surrogate method. However, our recent results on ^{240}Pu show that the surrogate method is not directly applicable to this even–even

Fig. 1 The surrogate reaction aims to produce the same compound nucleus as the neutron-induced reaction. The study of the different decay channels (fission, γ - and particle-emission) of the compound nucleus can be used to constrain model parameters used to predict neutron cross sections



nucleus [9]. The situation is very different for γ -emission probabilities. For all the cases we have investigated the γ -probabilities induced by surrogate reactions are much higher than neutron-induced ones. This discrepancy has been attributed to the spin-parity mismatch, i.e. the difference between the angular momentum and parity of the compound nucleus populated by the neutron induced and by the surrogate reaction. Nevertheless, the γ -emission and fission probabilities are very useful to fix the parameters of some of the key ingredients of the statistical model like level densities, γ -ray strength functions and fission barriers. To establish how surrogate reactions can be used to infer neutron cross sections in regions where no neutron-induced data exist, it is necessary to build the systematics of decay probabilities involving nuclei with different structural properties located in various mass regions and different surrogate reactions.

From a technical point of view, the measurement of surrogate reactions in direct kinematics faces the following limitations: (1) Unavailability of targets from short-lived nuclei. (2) High background from competing reactions with the target contaminants and backing. (3) The heavy products of the decay of the compound nucleus are stopped in the sample and cannot be detected with particle detectors. The limitations (1) and (3) can be addressed using radioactive beams in inverse kinematics. Nevertheless, radioactive beams have rather low energy and position resolution which translates into a low excitation energy resolution. In addition, for surrogate reactions the most promising isotopes are gases (H and He), but high areal densities of such molecules are difficult to reach and the target container may introduce some background and loss of energy resolution due to angular and energy straggling in the target window and the thick target. Such difficulties can be overcome if the surrogate experiments are performed at storage rings.

Storage rings present unique opportunities for surrogate-reaction experiments. A heavy-ion storage ring is an ensemble of beam pipes and electro-magnetic devices arranged in a closed geometry where the heavy ions turn with high frequencies, about 1 MHz at 10 MeV/u. The storage of heavy ions requires to minimize the number of atomic reactions between the stored beam and the residual gas inside the ring. Therefore, heavy-ion storage rings are operated at ultra-high vacuum (UHV) conditions (10^{-11} to 10^{-12} mbar), which poses severe constraints to in-ring detection. For this reason, nuclear reactions have started to be measured only very recently at the Experimental Storage Ring (ESR) of the GSI/FAIR facility in Darmstadt, Germany [10, 11].

The most important capability of storage rings is beam cooling, which allows the reduction of the energy and position spread of the stored radioactive ions. Beam cooling takes typically a few seconds, which sets the lower limit on the half-live of the radioactive ions available. The combination of the electron cooler and the dipole magnets ensures the quality of the stored beam in terms of emittance and purity. The electron cooler can compensate the angular and energy straggling, and energy loss of the beam in the gas target. Hence, the beam passes the target always with a very low energy and position spread at the same energy. Moreover, the frequent passing of the reaction zone allows ultra-thin gas targets (10^{13} atoms/cm²) to be used and therefore no windows are necessary. This is of great advantage for surrogate

reactions since the beam will only interact with the desired material and in a well-defined interaction zone with a very well-defined energy, allowing a very precise measurement of the excitation energy of the decaying nucleus.

3 A Future Set-up for Surrogate Reactions at Ion Storage Rings

The promising advantages of performing surrogate-reaction experiments in inverse kinematics using storage rings led to the start of a project [3], which aims to carry out such studies in particular at the ESR and the CRYRING [12] storage rings of GSI/FAIR.

The set-up required for surrogate-reaction measurements is presented in Fig. 2, where the CRYRING is shown as an example of a storage ring. This unique set-up aims at simultaneous measurements of fission, γ - and particle-emission probabilities and consists of three main detection systems.

Close to the target, particle detectors are foreseen to identify and measure the kinetic energies and angles of the light nuclei (“target-like”) ejected during the surrogate reaction. Downstream the target, a fission detection system made of solar cells will cover angles in forward direction to detect fission fragments in coincidence with the target-like detectors. The heavy ions that proceed further down the ring will be deflected according to their magnetic rigidity by dipole systems

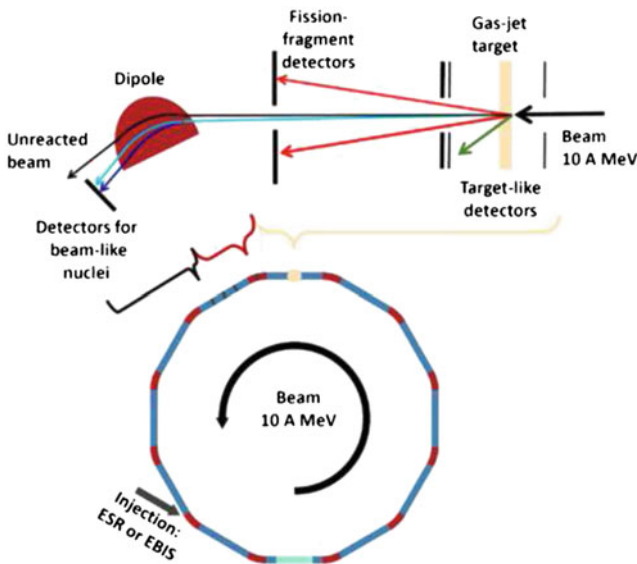


Fig. 2 Schematic view of a set-up example to be used in inverse kinematics

allowing to separate the different heavy “beam-like” products formed after γ -ray or particle-emission by the compound nucleus and detect them in coincidence with the target-like residues. Thanks to inverse kinematics, fission fragments and beam-like products are emitted in forward direction, which results in detection efficiencies that are close to 100%, much larger than in the traditional direct kinematics measurements.

4 Developments Towards a New Set-up

The vast experience of CENBG with solar cells [5, 13] as fission and/or heavy-ion detectors has triggered the investigation of solar cells as heavy-ion detectors at high energies. Indeed, the common solar cells found at the rooftops have been used to detect heavy ions at low energies about 1 MeV/u for several decades [14–16]. They are considered a good and cost-efficient alternative to Si detectors, due to their radiation resistance properties [16], making solar cells an attractive detection system. However, solar cells response to heavy ions of about 10 MeV/u and their compatibility to UHV must be investigated.

The energy, time and radiation resistance response of solar cells to more energetic heavy-ion beams were studied in three experiments carried out at the GANIL facility in Caen, France. The beam isotopes of choice (^{84}Kr and ^{129}Xe) represented examples of fission fragments and the energy of the beams ranged from 2 to 15 MeV/u, as expected in inverse kinematics. The studies considered several types (common rooftop and for space applications) of cells of different sizes (from $5 \times 5 \text{ mm}^2$ to $30 \times 30 \text{ mm}^2$). The size of the cell has implications in the cell capacitance influencing the electrical circuit that will follow, i.e. the impedance matching with the pre-amplifier. The solar cells were placed in a rotating stainless-steel support that could hold up to nine cells. The set-up containing the cells was placed just after the GANIL cyclotron CIME. A gas profiler allowed us to evaluate the beam spot size, typically of 5 mm and 7 mm in x and y directions, respectively. Each cell at its turn was placed perpendicular to the beam.

The characterization of the solar cells included investigating energy and time resolution and radiation resistance. The time resolution was measured by recording the time difference between the frequency of CIME and the cell signal with a Time to Digital Converter (TDC). Our preliminary results indicate that smaller cells exhibit a better time and energy resolution. For example, a $5 \times 5 \text{ mm}^2$ cell exposed to ^{129}Xe beam of 10 MeV/u revealed an energy resolution $\Delta E/E$ of 1.4% (RMS) and a time resolution of 4.0 ns (FWHM) (Fig. 3). While the energy resolution is lower when compared to a Si detector, the time resolution is indeed comparable.

One of the most interesting features of solar cells is their radiation hardness. Several cells were irradiated at different rates from 1.5 kHz to 1.4 MHz and their response with the number of events, as shown in Fig. 4. This figure shows the effect of irradiating a $10 \times 10 \text{ mm}^2$ cell with 703 k particles per second during 1 h with an ^{84}Kr beam at 15 MeV/u. In the energy response, there is a decrease in amplitude

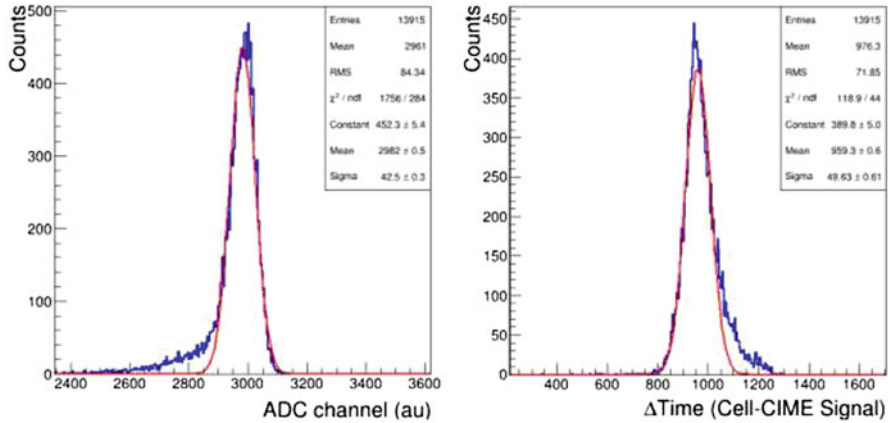


Fig. 3 Energy (left) and time (right) spectra of a $5 \times 5 \text{ mm}^2$ cell irradiated with a ^{129}Xe beam at 10 MeV/u. On both spectra the x -axis is given in channels. The time spectrum was obtained from the time difference between the cell signal (START) and the cyclotron frequency signal (STOP). The Gaussian fits drawn provided the FWHM for the energy and time resolution

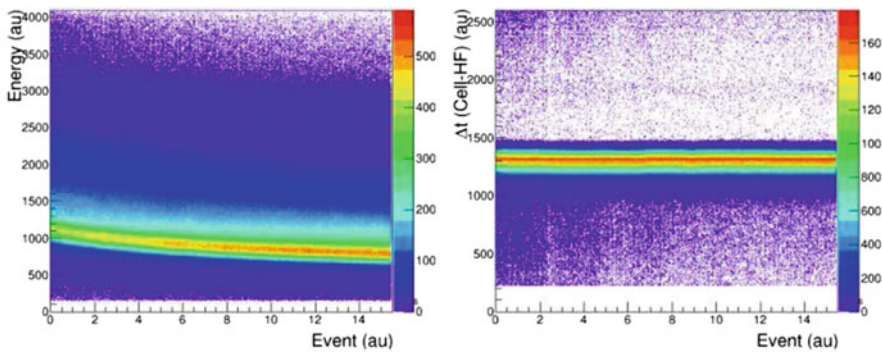


Fig. 4 Variation of the signal amplitude (left) and time difference between the cell and time signal from CIME (right) as a function of the number of recorded events during irradiation of a $10 \times 10 \text{ mm}^2$ solar cell with a ^{84}Kr beam at 15 MeV/u at a 703 k pps intensity for 1 h

affecting the energy resolution by 4%, while the time spectra remains essentially unchanged during the irradiation time. In total, after such irradiation more than 2500 M ions had impinged on the cell. Its radiation damage resistance can only be appreciated considering that a Si detector is reported to only withstand 250 M ions of 1 A MeV at a rate of 1000 pps.

5 Conclusions

Surrogate reactions are one of the most promising indirect methods to determine neutron-induced cross sections. These reactions aim to produce the same compound nucleus as the neutron-induced reaction of interest and study its decay (fission, particle- or γ -emission) probabilities. The previous fission and γ -emission probability measurements have opened many questions on how the surrogate method can be used; therefore, systematic studies are required to establish how the method can be used.

Looking forward to improve the quality of surrogate-reaction data, we aim to perform future measurements in inverse kinematics at storage rings, simultaneously measuring all the decay probabilities with good excitation energy resolution. The future set-up considers using solar cells as heavy-ion detectors. Given their cost and radiation hardness, these detection systems are not only advantageous for storage rings but possibly in beam diagnostics. We have studied the response of solar cells to heavy ions at energies up to 15 MeV/u. These studies show promising preliminary results regarding energy and time resolution, as well as radiation damage. Other exposures are foreseen in the near future to further explore the potential of solar cells as heavy-ion detectors.

Acknowledgements This work has been supported by the French “defi NEEDS”, by the European Commission within the EURATOM FP7 Framework through CHANDA (project no. 605203) and in part by the ExtreMe Matter Institute EMMI at the GSI Helmholtzzentrum fuer Schwerionenforschung, Darmstadt, Germany.

References

1. J.E. Escher et al., *Rev. Mod. Phys.* **84**, 353–397 (2012)
2. J.E. Escher et al., *Phys. Rev. Lett.* **121**, 5 (2018)
3. B. Jurado et al., *Eur. Phys. J. Web Conf.* **146**, 11006 (2017)
4. M. Petit et al., *Nucl. Phys. A* **735**, 345 (2004)
5. G. Kessedjian et al., *Phys. Lett. B* **692**, 297 (2010)
6. G. Boutoux et al., *Phys. Lett. B* **712**, 319 (2012)
7. Q. Ducasse et al., *Phys. Rev.* **94**, 024614 (2016)
8. R.P. Sanchez et al., *Nucl. Instrum. Meth. A* **933**, 63–70 (2018)
9. R. Perez Sanchez, PhD thesis. University of Bordeaux
10. Y.A. Litvinov et al., *Nucl. Instrum. Meth. B* **317**, 537–543 (2013)
11. B. Mei et al., *Phys. Rev.* **92**, 054302 (2015)
12. M. Lestinsky et al., *Eur. Phys. J. Special Topics* **225**, 797 (2016)
13. G. Kessedjian et al., *Phys. Rev.* **91**, 041601 (2015)
14. S. Siegert et al., *Nucl. Instr. Meth. A* **164**, 435 (1979)
15. M. Hsieh et al., *IEEE Electron Device Lett.* **4**, 7 (1981)
16. N.N. Ajitanand et al., *Nucl. Instr. Meth. A* **300**, 354 (1991)

Prospects for Surrogate Neutron Capture Measurements with Radioactive Ion Beams and GODDESS



Jolie A. Cizewski, Andrew Ratkiewicz, Alexandre Lepailleur, Steven D. Pain, Heather Garland, Harrison Sims, and David Walter

1 Introduction

The neutron capture (n,γ) reaction is responsible for the synthesis of almost all of the elements heavier than iron. The slow s -process proceeds close to the line of nuclear stability. In contrast, waiting points for the rapid neutron capture r -process are very neutron-rich isotopes far from stability. Reproducing the observed r -process abundance pattern is a sensitive measure of the astrophysical r -process site(s) and requires knowledge of the properties of and (n,γ) reaction rates on isotopes near the waiting points, nuclei far from stability and with very short half-lives [1].

Understanding (n,γ) rates near the r -process path is especially challenging because this reaction cannot be measured directly, because short-lived ($t_{1/2} < < 100$ days) targets cannot be manufactured and the lack of a pure neutron target for studies with radioactive ion beams. Near the $N = 82$ shell closure at ^{132}Sn , neutron capture is dominated by direct-semi-direct (DSD) capture that depends sensitively on the excitation energies and spectroscopic factors of the $3p_{1/2}$ and $3p_{3/2}$ neutron configurations. These properties have been measured [2–4] in (d,p) reactions with radioactive ion beams of $^{132,130,128,126}\text{Sn}$ and the DSD capture cross sections as a function of neutron energy have been deduced [3, 4]. While the

J. A. Cizewski (✉) · A. Lepailleur · H. Garland · H. Sims · D. Walter
Rutgers University, New Brunswick, NJ, USA
e-mail: cizewski@physics.rutgers.edu

A. Ratkiewicz
Rutgers University, New Brunswick, NJ, USA

Lawrence Livermore National Laboratory, Livermore, CA, USA

S. D. Pain
Oak Ridge National Laboratory, Oak Ridge, TN, USA

© This is a U.S. government work and not under copyright protection in the U.S.; foreign copyright protection may apply 2021

J. Escher et al. (eds.), *Compound-Nuclear Reactions*, Springer Proceedings in Physics 254, https://doi.org/10.1007/978-3-030-58082-7_26

$^{132}\text{Sn}(n,\gamma)$ cross section is expected to be dominated by DSD capture, for $N < 82$ isotopes the contribution from statistical capture, modeled in a Hauser–Feshbach formalism, is expected to dominate over DSD processes [5]. Therefore a validated surrogate for neutron capture is required to deduce the (n,γ) rate.

The neutron-transfer $(d,p\gamma)$ reaction has recently been demonstrated to be a valid surrogate for neutron capture [6]. The (d,p) reaction can also inform DSD capture. To deduce the (n,γ) cross section, the γ -decay probabilities as a function of excitation energy of several discrete gamma-ray transitions are measured. The measured decay probabilities are fit with level density and gamma-ray strength function models [7] with (d,p) -induced compound nucleus formation and spin-parity weights calculated from non-elastic breakup of the deuteron [8]. Surrogate $(d,p\gamma)$ measurements require a radioactive ion beam of intensity $>10^4$ pps, a large solid angle, segmented array of charged particle detectors, and a high-efficiency gamma-ray detector array.

2 GODDESS and ^{135}Xe

Gammasphere ORRUBA: Dual Detectors for Experimental Structure Studies (GODDESS) [9] was commissioned in 2015 at Argonne National Laboratory. Gamma radiation was measured with the 110-detector Gammasphere array of Compton-suppressed HPGe detectors coupled to the Oak Ridge Rutgers University Barrel Array (ORRUBA) of position-sensitive silicon-strip detectors [10]. Accelerated beams of ^{134}Xe and ^{95}Mo from the ATLAS accelerator interacted with CD_2 targets. Both charged particle singles and particle-gamma coincidence events were recorded. The rectangular position-sensitive silicon-strip SX3 detectors of the ORRUBA barrel were supplemented with pie-shaped, highly-segmented QQQ5 detectors that formed annular arrays mounted at angles upstream and downstream of the ORRUBA barrel. At forward angles both the QQQ5 and many of the SX3 detectors were mounted in a ΔE -E telescope to enable particle identification.

Preliminary particle energy as a function of laboratory angle data with the ^{134}Xe beam is displayed in Fig. 1. At the largest laboratory angles (that correspond to the most forward center of mass (c.m.) angles for the (d,p) reaction), only (d,p) -reaction protons are expected to be observed. Forward of 90° in the laboratory, the spectrum is dominated by elastic scattering on the CD_2 target. Angular distributions of reaction protons at smaller lab (larger c.m.) angles can be deduced from proton particle identification with ΔE -E telescopes. The red dotted lines are kinematic curves expected for ground and new $E_x > 2.0$ MeV states. The gap in counts between the ground and $E_x > 2.0$ MeV states in ^{135}Xe corresponds to the gap in excitations below and above the $N = 82$ shell closure.

A preliminary, partial level scheme of ^{135}Xe is displayed in Fig. 1. The states at 2.04 and 2.40 MeV are likely $7/2^-$ and $3/2^-$ states with significant $2f_{7/2}$ and $3p_{3/2}$

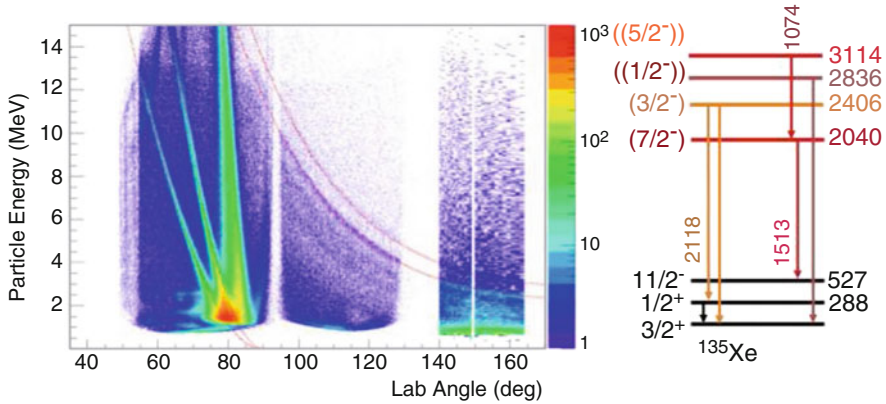


Fig. 1 (Left) Histogram of particle energy vs lab angle for the $^{134}\text{Xe} + \text{CD}_2$ measurement. Kinematic curves (red dotted) for the ground and ≈ 2 MeV states in ^{135}Xe (angles $>80^\circ$) and deuteron and proton elastic scattering (angles $<90^\circ$) are indicated. (Right) Preliminary partial level scheme for ^{135}Xe with transitions measured with Gammasphere and deduced from particle-gamma coincidences. Only the $3/2^+$ ground and $1/2^+$ 288-keV states and $t_{1/2}$ 15-min $11/2^-$ 527-keV isomer were known. The states at 2040 and 2406 keV are likely $(7/2^-)$ and $(3/2^-)$ states, respectively, based on the preliminary analysis. The states at 2836 and 3114 keV are assigned highly tentative $(1/2^-)$ and $(5/2^-)$ J^π values, respectively, based on systematics and the decay pattern. Additional analysis is required before more definite spin-parity values can be assigned

strength, respectively. These assignments are consistent with their decay patterns, preliminary angular distributions of the proton data, and systematics of the $N = 81$ isotope ^{131}Sn . The states at 2.83 and 3.11 MeV have highly tentative $1/2^-$ and $5/2^-$ assignments based on systematics and the decay pattern. Gamma rays in ^{134}Xe , the surrogate $(n, n'\gamma)$ nucleus, are observed for proton gates above the neutron separation energy.

Analysis of the $^{134}\text{Xe}(d, p\gamma)$ reaction is ongoing and will include proton angular distribution analysis to support the tentative J^π assignments. It is unlikely that there will be sufficient statistics in this commissioning experiment to deduce a surrogate (n, γ) cross section. We anticipate that there will be sufficient statistics in the subsequent measurement with ^{95}Mo beams for a surrogate (n, γ) analysis, as well as an extension of the ^{96}Mo level scheme.

3 Summary and Future Prospects

Techniques to measure the $(d, p\gamma)$ reaction with radioactive ion beams have been developed with GODDESS: the coupling of ORRUBA to a high-efficiency gamma-ray detector array. Preliminary results from the commissioning experiment with ^{134}Xe beams identify for the first time excitations in ^{135}Xe above the $N = 82$ shell gap. The analysis of the $^{95}\text{Mo}(d, p\gamma)$ reaction is proceeding. We are approved

to measure the $(d,p\gamma)$ reaction as a surrogate for (n,γ) with ORRUBA coupled to the GRETINA [11] gamma-ray detector array. Fission fragment ^{143}Ba and ^{80}Ge beams would be deployed, the latter to inform neutron capture for (weak) r-process nucleosynthesis.

Acknowledgements We thank all of the collaborators on the GODDESS project for their contributions. This work was supported in part by the U.S. Department of Energy National Nuclear Security Administration Grant No. DE-NA0000979 (Stewardship Science Academic Alliances, Rutgers), Contract No. DE-AC52-07NA27344 and LDRD 16-ERD-022 (LLNL), Office of Science, Office of Nuclear Physics Contract No. DE-AC05-00OR22725 (ORNL), and the National Science Foundation.

References

1. M.R. Mumpower, R. Surman, G.C. McLaughlin, A. Aprahamian, The impact of individual nuclear properties on r-process nucleosynthesis. *Prog. Part. Nucl. Phys.* **86**, 86 (2016)
2. K.L. Jones et al., The magic nature of ^{132}Sn explored through the single-particle states of ^{133}Sn . *Nature* **465**, 454 (2010)
3. R.L. Kozub et al., Neutron single particle structure in ^{131}Sn and direct neutron capture cross sections. *Phys. Rev. Lett.* **109**, 172501 (2012)
4. B. Manning et al., Informing direct neutron capture on tin isotopes near the $N = 82$ shell closure. *Phys. Rev. C* **99**, 041302 (2019)
5. S. Chiba et al., Direct and semi-direct capture in low-energy (n,γ) reactions of neutron-rich tin isotopes and its implications for r-process nucleosynthesis. *Phys. Rev. C* **77**, 015809 (2008)
6. A. Ratkiewicz et al., Towards neutron capture on exotic nuclei: Demonstrating $(d,p\gamma)$ as a surrogate reaction for (n,γ) . *Phys. Rev. Lett.* **122**, 052502 (2019)
7. J.E. Escher et al., Constraining neutron capture cross sections for unstable nuclei with surrogate reaction data and theory. *Phys. Rev. Lett.* **121**, 052501 (2018)
8. G. Potel, F.M. Nunes, I.J. Thompson, Establishing a theory for deuteron-induced surrogate reactions. *Phys. Rev. C* **92**, 034611 (2015)
9. S.D. Pain et al., Direct reaction measurements using GODDESS. *Phys. Procedia* **90**, 455–462 (2017)
10. S.D. Pain et al., Development of a high solid-angle silicon detector array for measurement of transfer reactions in inverse kinematics. *Nucl. Instrum. Meth. B* **261**, 110 (2007)
11. P. Fallon, A. Gade, I.Y. Lee, GRETINA and its early science. *Annu. Rev. Nucl. Part. Sci.* **66**, 321–339 (2016)

Surrogate Reaction Method for Neutron Capture and Other Reactions on Unstable Isotopes



J. E. Escher, J. T. Burke, R. O. Hughes, N. D. Scielzo, and R. J. Casperson

1 Introduction

Cross sections for compound-nuclear reactions ($a + A \rightarrow B^* \rightarrow c + C$) are important for many applications, but are often not known. Statistical cross section calculations can be quite uncertain due to the nuclear structure models describing the decay of the compound nucleus (CN), $B^* \rightarrow c + C$. Reaction measurements are difficult to impossible when the target nucleus is too short-lived or radioactive to be made into a stationary target. While inverse-kinematics experiments are a promising development for measuring charged-particle induced reactions directly, the lack of a neutron target renders this approach out of reach for neutron-induced reactions, at least for the foreseeable future.

The surrogate method [1] overcomes the challenge of an unstable target by producing the CN of interest indirectly via a light-ion (inelastic scattering or transfer) reaction δ ($d + D \rightarrow B^* + b$) involving a projectile-target combination more amenable to a measurement. The decay of the CN into the channel of interest, $\chi = c + C$, is observed in coincidence with the outgoing particle (b) from the light-ion reaction and the resulting coincidence probability $P_{\delta\chi}(E_{ex})$ is measured as a function of the excitation energy E_{ex} of the CN. This decay probability is then used, in conjunction with a calculation of the desired fusion process ($a + A \rightarrow B^*$) to determine the cross section of interest.

In principle, the surrogate method can employ a variety of light-ion reactions δ to determine reactions with various decay channels ($\chi = \gamma, n, p, \alpha, 2n, \dots$). The primary focus of past applications has been on (n,f) and (n, γ) reactions. Here,

J. E. Escher (✉) · J. T. Burke · R. O. Hughes · N. D. Scielzo · R. J. Casperson
Lawrence Livermore National Laboratory, Livermore, CA, USA
e-mail: escher1@llnl.gov

© This is a U.S. government work and not under copyright protection in the U.S.; foreign copyright protection may apply 2021

J. Escher et al. (eds.), *Compound-Nuclear Reactions*, Springer Proceedings in Physics 254, https://doi.org/10.1007/978-3-030-58082-7_27

we summarize recent progress in determining capture cross sections and discuss potential applications to other reaction mechanisms.

2 Applications to Neutron Capture

Early applications of the surrogate approach simply used the measured coincidence probability $P_{\delta\chi}(E_{ex})$ to describe the decay of the CN in the desired (neutron-induced) reaction, without regard to the fact that the manner in which the CN is produced affects the spins and parities of the CN and hence its decay. While this (Weisskopf-Ewing) approximation worked reasonably well for (n,f) reactions [1, 2], it did not produce the correct neutron capture cross sections, due to the dependence of the decay on the CN spin distribution [3]. Typically, the surrogate reaction populates spins in the CN that are much higher than those relevant to low-energy neutron capture. When the first few states of the target nucleus have low spins, this results in neutron emission being suppressed and gamma emission being enhanced, and therefore the estimated capture cross section is too high. This was explained in a number of theoretical studies of the method [4–6] and also observed experimentally [7, 8]. Employing ratio approaches did not resolve the problem [5, 9].

The key to overcoming this challenge is to treat the surrogate reaction data as a constraint for the nuclear structure models that enter the CN reaction calculation. Concretely, we write the surrogate coincidence probability as

$$P_{\delta\chi}(E_{ex}) = \sum_{J,\pi} F_{\delta}(E_{ex}, J, \pi) \cdot G_{\chi}^{CN}(E_{ex}, J, \pi), \quad (1)$$

where $F_{\delta}(E_{ex}, J, \pi)$ is the (excitation energy-dependent) spin-parity population produced in the surrogate reaction δ , and $G_{\chi}(E_{ex}, J, \pi)$ contains nuclear structure models needed to describe the decay of the CN. The decay models that enter $G_{\chi}(E_{ex}, J, \pi)$, in particular level densities and γ -ray strength functions, are expressed as phenomenological functions, with parameters that can be constrained by fitting the calculated $P_{\delta\chi}(E_{ex})$ to the measured coincidence probabilities. The $G_{\chi}(E_{ex}, J, \pi)$ obtained in this procedure can then be used to calculate the desired cross section: $\sigma_{a+A,\chi}(E_n) = \sum_{J,\pi} \sigma_{a+A}^{CN}(E_{ex}, J, \pi) \cdot G_{\chi}^{CN}(E_{ex}, J, \pi) \cdot W_{a+A,\chi}(E_{ex}, J, \pi)$, where σ_{a+A}^{CN} is the cross section for forming the CN in the desired reaction, which can be calculated using a suitable projectile-target optical potential. The width fluctuation correction factor $W_{a+A,\chi}(E_{ex}, J, \pi)$ accounts for correlations between the incident and exit channels in the desired reaction and is well approximated using Moldauer's approach [10]. Its primary effect on neutron-induced reactions is to increase the elastic scattering cross section and to reduce the cross sections for other channels, e.g., for the capture channel. Correlations between the incident charged-particle transfer or inelastic scattering channel and the decay

channel of interest in current surrogate experiments are expected to be negligible, so no correction factor is included in Eq. 1.

This idea was discussed in Refs. [1, 11] and recently used to determine the neutron capture cross sections for ^{87}Y and ^{90}Zr from surrogate (p,d γ) data [12] and ^{95}Mo from surrogate (d,p γ) data [13]. The $^{87}\text{Y}(n,\gamma)$ result represents the first application of this method to an unstable isotope (^{87}Y has a half-life of 79.8 h and prior cross section calculations had to rely on regional systematics). The $^{90}\text{Zr}(n,\gamma)$ and $^{95}\text{Mo}(n,\gamma)$ results, on the other hand, serve as benchmarks of the approach.

This approach presupposes that the spin-parity distributions $F_\delta(E_{ex}, J, \pi)$ can be calculated for the surrogate reaction selected. This is non-trivial, as the CN excitation energies relevant to capture are typically on the order of 5–10 MeV, where standard direct-reaction descriptions, such as DWBA, are no longer valid. Here, we discuss the theory developments required to determine the capture cross sections.

2.1 Capture Cross Sections from (p,d) Pickup Reactions

In Ref. [12], the (p,d) reaction was used to produce the compound nuclei $^{88}\text{Y}^*$ and $^{91}\text{Zr}^*$, which are relevant to determining the $^{87}\text{Y}(n,\gamma)$ and $^{90}\text{Zr}(n,\gamma)$ cross sections, respectively. Natural ^{89}Y and enriched ^{92}Zr targets were bombarded by a 28.5-MeV proton beam, produced by the K150 Cyclotron at Texas A&M University. The energy and angular distributions of the outgoing deuterons were measured using the Silicon Telescope Array for Reaction Studies (STARS) [14]. The coincident γ rays were detected with five HPGe clover detectors in the Livermore-Texas-Richmond (LiTeR) array [7, 14]. The Surrogate coincidence probability $P_{\delta\gamma}(E_{ex})$ was obtained by measuring N_δ , the total number of detected deuterons, and $N_{\delta\gamma}$, the number of coincidences between a deuteron and the γ -ray that identifies the relevant exit channel: $P_{\delta\gamma}^{exp}(E_{ex}, \theta_d) = N_{\delta\gamma}(E_{ex}, \theta_d)/N_\delta(E_{ex}, \theta_d)\epsilon(E_\gamma)$, where $\epsilon(E_\gamma)$ denotes the efficiency for detecting the exit channel γ -ray [15–17] (Fig. 1).

To calculate the surrogate spin-parity distribution $F_\delta^{CN}(E_{ex}, J, \pi)$ for the compound nucleus, the one-neutron removal reaction (p,d) has to be described. This requires a reaction formulation as well as nuclear structure information. In the $^{90}\text{Zr}(n,\gamma)$ example considered here, the surrogate reaction produces $^{91}\text{Zr}^*$ by removing neutrons from inner shells of the ^{92}Zr nucleus: deep hole states are involved in the production of $^{91}\text{Zr}^*$ near S_n . Their location and fragmentation as a function of E_{ex} was obtained using the dispersive optical model approach of Mahaux and Sartor [18]. At the high excitation energies involved, one-step (p,d) pickup processes have to be complemented by contributions from two-step processes such as (p,p')(p',d) and (p,d')(d',d), in which the initial ^{92}Zr or the final ^{91}Zr are inelastically excited. Due to the large number of states in the energy band populated, the different contributions can be assumed to add incoherently. Angle-integrated (p,d) cross sections can be calculated and compared to measured (p,d) cross sections as a cross-check for the calculations. While (p,d) reactions that populate low-energy states with dominant single-particle character result in cross

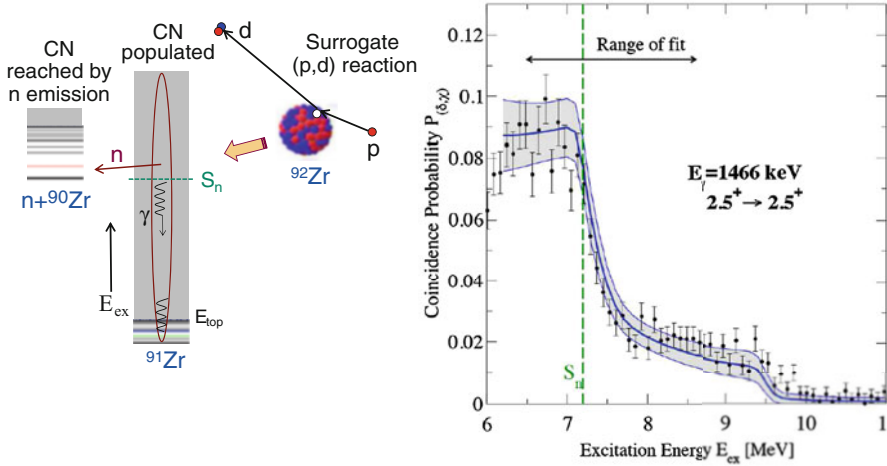


Fig. 1 Left panel: Schematic representation of the surrogate reaction approach for the benchmark reaction $^{90}\text{Zr}(n,\gamma)^{91}\text{Zr}$. The basic idea of the method is to replace the first step of the desired reaction, $n+^{90}\text{Zr}$, by an alternative reaction, $p+^{92}\text{Zr} \rightarrow d+^{91}\text{Zr}^*$, that populates the same compound nucleus, $^{91}\text{Zr}^*$. The subsequent decay of the compound nucleus into the relevant channel, $^{91}\text{Zr}+\gamma$, can then be measured and used to extract the desired cross section. Specifically, characteristic γ -ray transitions in ^{91}Zr are measured in coincidence with the outgoing deuteron. Right panel: Coincidence probability for the decay of ^{91}Zr . The measured probability of observing the 1466 keV transition in coincidence with the outgoing deuteron (black data points with error bars) is given as function of E_{ex} . The shaded region shows the result from fitting the decay model parameters. The fit produces a posterior parameter distribution which can be sampled to calculate the desired $^{90}\text{Zr}(n,\gamma)$ cross section [12]

sections with characteristic angular distributions, the measured angular behavior in the surrogate measurement exhibits little structure. This was discussed in Ref. [19].

With $F_{\delta}^{CN}(E_{ex}, J, \pi)$ obtained in this manner, one can derive constraints for the decay models, using the measured coincidence probabilities $P_{\delta\gamma}^{exp}(E_{ex})$ and Eq. 1. To do this, the $G_{\gamma}^{CN}(E_{ex}, J, \pi)$ are expressed in terms of well-established functional forms for level densities and transmission coefficients [20, 21], with parameters that are to be determined. The neutron transmission coefficients are known quite accurately for the nuclei considered [22] and are not varied. For isotopes far from stability, where transmission coefficients are less well known, such variations should be carried out. Each parameter set leads to *predicted* coincidence probabilities according to Eq. 1. A comparison with the *measured* probabilities then leads to the sought-after parameter constraints. In practice, this comparison is carried out using a Bayesian Monte-Carlo approach [23], which allows us to simultaneously account for uncertainties in the data, the structure information utilized, and shortcomings in the theoretical description. The procedure yields the desired (n,γ) cross section, along with its uncertainty, and is found to be in agreement with directly measured results [12].

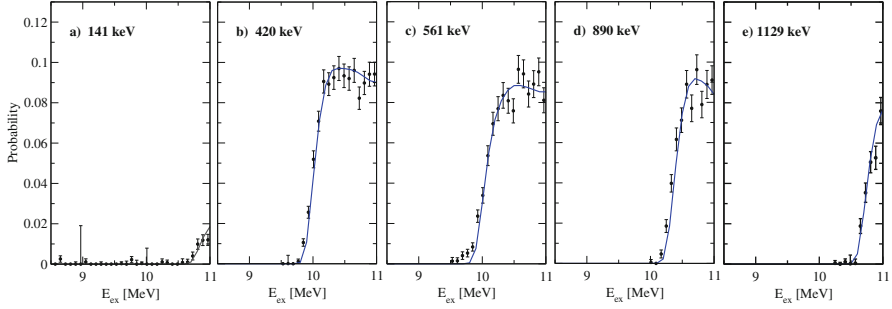


Fig. 2 Surrogate coincidence probabilities relevant to the neutron emission channel $^{91}\text{Zr} \rightarrow ^{90}\text{Zr} + n$. Shown are measurement (black data points) for five transitions in ^{90}Zr , observed in coincidence with the outgoing deuteron, as function of the ^{91}Zr excitation energy. The blue curves represent the transitions calculated with the parameters determined from the earlier fit to the γ -decay channel. The excellent agreement between the calculated and measured coincidence probabilities provides increased confidence in the approach

In addition to yielding the capture reaction, the surrogate experiment contains information on the competing neutron emission channel. Neutron emission leads to the population of excited states in ^{90}Zr which subsequently de-excite via γ emission. Selected γ -ray transitions between discrete states of ^{90}Zr were also measured in the experiment [12]. In principle, the associated coincidence probabilities $P_{\delta\chi}(E_{ex})$, where χ now refers to a particular γ transition in ^{90}Zr , can be used to constrain the calculation of the $^{90}\text{Zr}(n,n')$ cross section. Here, however, we will use the observed coincidence probabilities as a cross-check for the procedure. In Fig. 2, we compare the calculated average probabilities, obtained from the parameter fitting procedure outlined above, to the measured coincidence probabilities. The five transitions involve initial states with excitation energies between 3.6 and 4.5 MeV, but various angular momenta, between $3\hbar$ and $8\hbar$. The onset of each transition, which depends on the angular momenta of the states involved, is correctly reproduced. Overall, we observe excellent agreement for the shapes of all five transitions (the normalization was adjusted), which provides increased confidence in the calculated $F_{\delta}^{CN}(E_{ex}, J, \pi)$ and therefore the overall method.

2.2 Capture Cross Sections from (d,p) Stripping Reactions

The (d,p) reaction is expected to play a central role in inverse-kinematics experiments that aim to measure structural properties of unstable nuclei at radioactive-beam facilities. The reaction can also be used to produce a compound nucleus near and above the neutron separation energy, thus making it a candidate for surrogate applications. The reaction mechanism is complex, with multiple processes contributing to the measured surrogate coincidence probabilities: elastic

and inelastic breakup, breakup followed by partial fusion (of either the neutron or proton), and complete fusion followed by evaporation are known contribute to inclusive (d,p) measurements. Inclusive (d,p) reactions were already discussed in the 1970s, but disagreements about the proper theoretical formalism persisted [24–26]. Recently, several groups revisited the problem [27–29] and developed a consistent formalism [30]. The numerical implementation of Ref. [27] was subsequently used to calculate the spin-parity distribution relevant to a recent $^{95}\text{Mo}(d,p\gamma)$ surrogate measurement. Modeling the decay of $^{96}\text{Mo}^*$ made it then possible to indirectly determine the $^{95}\text{Mo}(n,\gamma)$ cross section, which was found to be in excellent agreement with the known capture cross section, thus providing a valuable benchmark for future (d,p) surrogate reaction applications [13].

2.3 Capture Cross Sections from Inelastic Scattering Reactions

Inelastic scattering is potentially a very valuable surrogate reaction mechanism [7, 16] that can also be used in inverse-kinematics experiments at radioactive-beam facilities. In the past, inelastic scattering with charged particles has been used extensively to study giant resonances. These studies demonstrate that inelastic scattering produces compound nuclei up to very high excitation energy (10s of MeV). Thus, it becomes possible to observe γ emission, neutron emission, and two consecutive neutron emission events in one experiment. This makes it, in principle, possible to determine (n,γ) , (n,n') , and $(n,2n)$ cross sections from surrogate inelastic scattering experiments. A proper theoretical description of such experiments requires the integration of nuclear structure and reaction descriptions, along the lines of the developments carried out in Refs. [31–35].

3 Outlook

Indirect methods are critical for determining cross sections for reactions on unstable isotopes. The approach outlined here is, in principle, applicable to other decay channels (and to other entrance channels). When considering other entrance channels, the projectile-target fusion calculation has to be modified accordingly. For example, to determine a (p,γ) cross section, a proton-nucleus optical model potential has to be employed to calculate the compound nucleus formation in the desired reaction. The decay models can be constrained analogously to the (n,γ) case. When other exit channels are of interest, different coincidence probabilities have to be measured. For fission, one can detect fission fragments in coincidence with the outgoing particle from the surrogate reaction [1]. For neutron or charged-particle channels, it is possible to detect the emitted particle of interest or—in analogy to the case discussed in Sect. 2—a γ transition that is characteristic of the channel of interest.

In summary, the framework discussed here establishes a general procedure for obtaining cross sections for short-lived nuclei from light-ion surrogate reactions. Combined with the ability to carry out experiments at radioactive-beam facilities, it becomes a powerful tool for addressing important questions for a variety of applications.

Acknowledgments This work was performed under the auspices of the U.S. Department of Energy (DOE) by Lawrence Livermore National Laboratory under contract DE-AC52-07NA27344, with partial support from LLNL's LDRD project 19-ERD-017.

References

1. J.E. Escher, J.T. Burke, F.S. Dietrich, N.D. Scielzo, I.J. Thompson, W. Younes, *Rev. Mod. Phys.* **84**, 353 (2012)
2. J.E. Escher, F.S. Dietrich, *Phys. Rev. C* **74**(5), 054601 (2006)
3. J.E. Escher, F.S. Dietrich, *Phys. Rev. C* **81**(2), 024612 (2010)
4. C. Forssén, F. Dietrich, J. Escher, R. Hoffman, K. Kelley, *Phys. Rev. C* **75**, 055807 (2007)
5. J.E. Escher, F.S. Dietrich, *Phys. Rev. C* **81**(2), 024612 (2010)
6. S. Chiba, O. Iwamoto, *Phys. Rev. C* **81**(4), 044604 (2010)
7. N.D. Scielzo, J.E. Escher, J.M. Allmond, M.S. Basunia, C.W. Beausang, L.A. Bernstein, D.L. Bleuel, J.T. Burke, R.M. Clark, F.S. Dietrich, P. Fallon, J. Gibelin, B.L. Goldblum, S.R. Leshner, M.A. McMahan, E.B. Norman, L. Phair, E. Rodriguez-Vieitez, S.A. Sheets, I.J. Thompson, M. Wiedeking, *Phys. Rev. C* **81**(3), 034608 (2010)
8. G. Boutoux, B. Jurado, V. Méot, O. Roig, L. Mathieu, M. Aïche, G. Barreau, N. Capellan, I. Comanis, S. Czajkowski, K.H. Schmidt, J. Burke, A. Bail, J. Daugas, T. Faul, P. Morel, N. Pillet, C. Théroine, X. Derkx, O. Sérot, I. Matéa, L. Tassan-Got, *Phys. Lett. B* **712**(4–5), 319 (2012)
9. R. Hatarik, L.A. Bernstein, J.A. Cizewski, D.L. Bleuel, J.T. Burke, J.E. Escher, J. Gibelin, B.L. Goldblum, A.M. Hatarik, S.R. Leshner, P.D. O'Malley, L. Phair, E. Rodriguez-Vieitez, T. Swan, M. Wiedeking, *Phys. Rev. C* **81**(1), 011602 (2010)
10. S. Hilaire, C. Lagrange, A.J. Koning, *Ann. Phys.* **306**(2), 209 (2003)
11. J.E. Escher, A.P. Tonchev, J.T. Burke, P. Bedrossian, R.J. Casperson, N. Cooper, R.O. Hughes, P. Humby, R.S. Ilieva, S. Ota, N. Pietralla, N.D. Scielzo, V. Werner, *EPJ Web Conf.* **122**, 12001 (2016)
12. J.E. Escher, J.T. Burke, R.O. Hughes, N.D. Scielzo, R.J. Casperson, S. Ota, H.I. Park, A. Saastamoinen, T.J. Ross, *Phys. Rev. Lett.* **121**, 052501 (2018)
13. A. Ratkiewicz, J.A. Cizewski, J.E. Escher, G. Potel, J.T. Burke, R.J. Casperson, M. McCleskey, R.A.E. Austin, S. Burcher, R.O. Hughes, B. Manning, S.D. Pain, W.A. Peters, S. Rice, T.J. Ross, N.D. Scielzo, C. Shand, K. Smith, *Phys. Rev. Lett.* **122**, 052502 (2019)
14. S.R. Leshner, L. Phair, L.A. Bernstein, D.L. Bleuel, J.T. Burke, J.A. Church, P. Fallon, J. Gibelin, N.D. Scielzo, M. Wiedeking, *Nucl. Instrum. Methods Phys. Res. A* **621**, 286 (2010)
15. R.J. Casperson, J.T. Burke, N.D. Scielzo, J.E. Escher, E. McCleskey, M. McCleskey, A. Saastamoinen, A. Spiridon, A. Ratkiewicz, A. Blanc, M. Kurokawa, R.G. Pizzone, *Phys. Rev. C* **90**, 034601 (2014)
16. S. Ota, J.T. Burke, R.J. Casperson, J.E. Escher, R.O. Hughes, J.J. Ressler, N.D. Scielzo, I.J. Thompson, R.A.E. Austin, B. Abromeit, N.J. Foley, E. McCleskey, M. McCleskey, H.I. Park, A. Saastamoinen, T.J. Ross, *Phys. Rev. C* **92**, 054603 (2015)

17. R.O. Hughes, J.T. Burke, R.J. Casperson, J.E. Escher, S. Ota, J.J. Ressler, N.D. Scielzo, R.A.E. Austin, B. Abromeit, N.J. Foley, E. McCleskey, M. McCleskey, H.I. Park, T.J. Ross, A. Saastamoinen, *Phys. Rev. C* **93**, 024315 (2016)
18. C. Mahaux, R. Sartor, *Advances in Nuclear Physics*, vol. 20 (Springer US, New York, 1991)
19. J.E. Escher, J.T. Burke, R.J. Casperson, R.O. Hughes, N.D. Scielzo, EPJ Web Conf. **178**, 03002 (2018)
20. P. Fröbrich, R. Lipperheide, *Theory of Nuclear Reactions* (Clarendon Press, Oxford, 1996)
21. R. Capote, M. Herman, P. Obložinský, P. Young, S. Goriely, T. Belgya, A. Ignatyuk, A. Koning, S. Hilaire, V. Plujko, M. Avrigeanu, O. Bersillon, M. Chadwick, T. Fukahori, Z. Ge, Y. Han, S. Kailas, J. Kopecky, V. Maslov, G. Reffo, M. Sin, E. Soukhovitskii, P. Talou, *Nucl. Data Sheets* **110**(12), 3107 (2009)
22. A.J. Koning, J.P. Delaroche, *Nucl. Phys.* **A713**, 231 (2003)
23. A.J. Koning, *Eur. Phys. J. A* **51**(12), 184 (2015)
24. T. Udagawa, T. Tamura, *Phys. Rev. C* **24**(3), 1348 (1981)
25. M. Ichimura, N. Austern, C.M. Vincent, *Phys. Rev. C* **34**, 2326 (1986)
26. M. Ichimura, *Phys. Rev. C* **41**, 834 (1990)
27. G. Potel, F.M. Nunes, I.J. Thompson, *Phys. Rev. C* **92**, 034611 (2015)
28. J. Lei, A.M. Moro, *Phys. Rev. C* **92**, 044616 (2015)
29. B.V. Carlson, R. Capote, M. Sin, *Few-Body Syst.* **57**(5), 307 (2016)
30. G. Potel, G. Perdikakis, B.V. Carlson, M.C. Atkinson, W. Dickhoff, J.E. Escher, M.S. Hussein, J. Lei, W. Li, A.O. Macchiavelli, A.M. Moro, F. Nunes, S.D. Pain, J. Rotureau, *Eur. Phys. J. A* **53**, 178 (2017)
31. G.P.A. Nobre, F.S. Dietrich, J.E. Escher, I.J. Thompson, M. Dupuis, J. Terasaki, J. Engel, *Phys. Rev. Lett.* **105**(20), 202502 (2010)
32. G.P.A. Nobre, F.S. Dietrich, J.E. Escher, I.J. Thompson, M. Dupuis, J. Terasaki, J. Engel, *Phys. Rev. C* **84**, 064609 (2011)
33. M. Dupuis, T. Kawano, J.P. Delaroche, E. Bauge, *Phys. Rev. C* **83**, 014602 (2011)
34. M. Dupuis, E. Bauge, S. Hilaire, F. Lechaftois, S. Péru, N. Pillet, C. Robin, *Eur. Phys. J. A* **51**(12), 168 (2015)
35. M. Dupuis, *Eur. Phys. J. A* **53**(5), 111 (2017)

Neutron Capture Cross Sections from Surrogate Reaction Data and Theory: Connecting the Pieces with a Markov-Chain Monte Carlo Approach



Oliver Gorton and Jutta E. Escher

Neutron capture cross sections can be measured by bombarding a sample of target nuclei with neutrons and detecting decay products. Such measurements cannot be completed in the laboratory when the target isotopes have half-lives that are short compared to timescales relevant to the experiment. This leaves critical gaps in nuclear data libraries. To predict the missing data, nuclear cross section calculations can, in principle, be carried out using statistical Hauser-Feshbach (HF) models [1]. In compound nuclear reactions, a compound nucleus (CN) is formed, which then decays through the available decay channels. These channels and the probability of each being taken depend on the nuclear level densities and γ -ray strength function of the CN. The general lack of nuclear structure information for medium to heavy mass nuclei leads to the need for indirect constraints on the corresponding HF parameters. The surrogate method [2] obtains these constraints using measurements of the same CN decay observed in alternative reactions.

Specifically, in Ref. [3] the decay of the CN ^{91}Zr was modeled using parametrized (phenomenological) forms for the level density and γ -ray strength function. The parameters were fitted to measured $^{92}\text{Zr}(p, d\gamma)$ data from a surrogate experiment and subsequently used to calculate the desired $^{90}\text{Zr}(n, \gamma)$ cross section. A Bayesian Monte Carlo approach was employed, which provided an average (n, γ) cross section, along with a variance, yielding an uncertainty band that is symmetric around the mean. Here, we improve the parameter estimation by introducing a Markov-Chain Monte Carlo (MCMC) approach for sampling the HF parameter

O. Gorton (✉)
San Diego State University, San Diego, CA, USA
e-mail: ogorton@sdsu.edu

J. E. Escher
Lawrence Livermore National Laboratory, Livermore, CA, USA
e-mail: escher1@llnl.gov

space, generating a joint probability distribution for the parameters without visiting every combination of parameters.

The nuclear level density model we employ is the composite Gilbert-Cameron level density [4] with the Ignatyuk treatment of the energy dependence of the level density parameter [5]. We varied five parameters within this prescription, which are, following the notation of reference [1]: the asymptotic level density parameter \tilde{a} , the shell correction energy δW , the level density damping parameter γ , the pairing energy shift Δ , and the effective moment of inertia that enters the expression for the spin-cutoff factor. The γ -ray strength function description employed was the enhanced generalized Lorentzian (EGLO) model for the E1 transitions, and the standard Lorentzian (SLO) for the M1 transitions. These models are parameterized by their peak energy, width, and strength [1]. We varied nine strength function parameters, three for each peak, with the EGLO function having two peaks, and the SLO having a single peak. A total of 14 parameters were varied simultaneously.

We employ a Metropolis-Hastings MCMC algorithm [6, 7], and explore convergence of the sampling process. The prior distributions for each parameter were finite and flat, and centered around recommended parameter values from RIPL-3 [1]. The posterior parameter distribution we obtain is sampled, yielding the $^{90}\text{Zr}(n, \gamma)$ cross section shown in Fig. 1. This method propagates all constraints encoded in

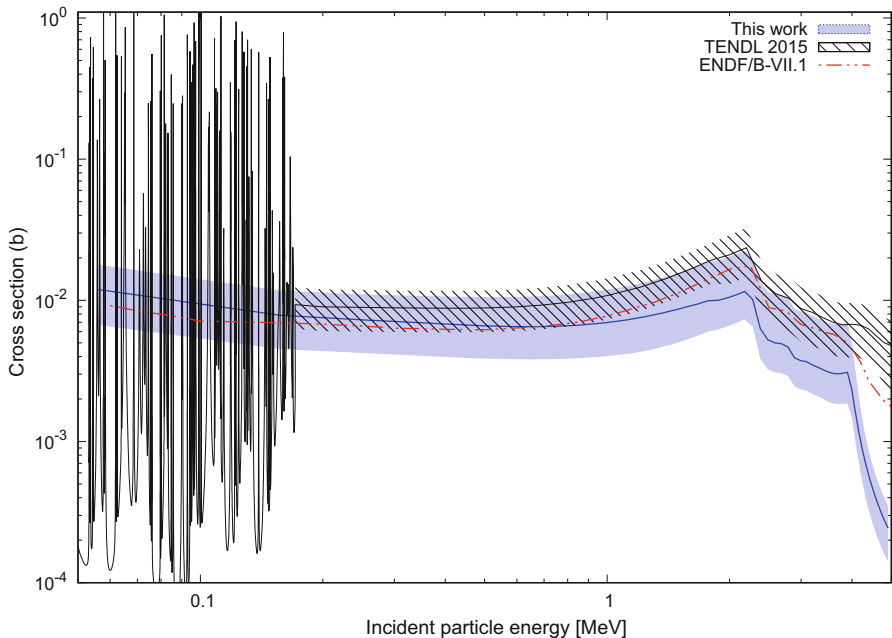


Fig. 1 Preliminary $^{90}\text{Zr}(n, \gamma)$ cross section obtained indirectly from $^{92}\text{Zr}(p, d\gamma)$ data using the newly developed MCMC approach. The solid (blue) curve is the median value and the solid (blue) band indicates the 68% confidence interval. For comparison, the Talys Evaluated Nuclear Data Library (TENDL) [8] and the Evaluated Nuclear Data File (ENDF) library results are shown as well [9]

the joint probability distribution of parameters, including correlations between the parameters. The result is seen to be in agreement with the TENDL 2015 and ENDF/B-VII.1 evaluations, both of which are based on directly measured data. In future work we will investigate correlations between the model parameters and between the cross sections at different energies.

Acknowledgments This work was performed under the auspices of the U.S. Department of Energy by Lawrence Livermore National Laboratory under contract DE-AC52-07NA27344, with support from LLNL's HEDP summer student program and LDRD project 19-ERD-017.

References

1. R. Capote et al., RIPL - reference input parameter library for calculation of nuclear reactions and nuclear data evaluations. Nucl. Data Sheets **110**, 3107 (2009)
2. J.E. Escher et al., Compound-nuclear reaction cross sections from surrogate measurements. Rev. Mod. Phys. **84**, 353 (2012)
3. J.E. Escher et al., Constraining neutron capture cross sections for unstable nuclei with surrogate reaction data and theory. Phys. Rev. Lett. **121**, 052501 (2018)
4. A. Gilbert, A. Cameron, A composite nuclear-level density formula with shell corrections. Can. J. Phys. **43**(8), 1446–1496 (1965)
5. A. Ignatyuk, et al., Sov. J. Nucl. Phys. **21**, 255 (1975)
6. W.K. Hastings, Monte Carlo sampling methods using Markov chains and their applications. Biometrika **57**, 97 (1970)
7. D.P. Kroese, T. Taimre, Z.I. Botev, *Handbook of Monte Carlo Methods*. Wiley Series in Probability and Statistics (Wiley, New York, 2011)
8. R. Koning, Modern nuclear data evaluation with the TALYS code system. Nucl. Data Sheets **113**, 2841 (2012)
9. M.B. Chadwick et al., ENDF/B-VII.0: Next generation evaluated nuclear data library for nuclear science and technology. Nucl. Data Sheets **107**, 2931 (2006)

Describing Neutron Transfer Reactions for Deformed Nuclei with a Sturmian Basis



V. G. Gueorguiev, J. E. Escher, F. S. Dietrich, and P. D. Kunz

We investigate the spin–parity distribution $P(J^\pi, E)$ of those ^{156}Gd states above the neutron separation energy $S_n = 8.536\text{ MeV}$ [1] that are expected to be populated via the neutron pickup reaction $^{157}\text{Gd}(^3\text{He}, ^4\text{He})^{156}\text{Gd}$. Investigating such one-nucleon transfer reactions is important for applications of the surrogate reaction method, an indirect approach for determining hard-to-measure compound cross sections [2]. In a surrogate reaction experiment, a charged-particle transfer or inelastic scattering reaction is employed to produce a compound nucleus, observe its decay, and use the decay observations to constrain Hauser-Feshbach calculations of a reaction that proceeds through the same compound nucleus but cannot be measured directly, e.g., neutron capture on a short-lived isotope [3, 4]. Unlike the compound-nuclear reaction of interest, the surrogate reaction is a direct reaction that produces a doorway state, which subsequently damps into the relevant compound nucleus. To fully utilize the surrogate approach, it is necessary to calculate the probabilities $P(J^\pi, E)$ for producing states with specific spin and parity, J^π , at high excitation energies E , typically around the neutron separation energy [5]. Here, we investigate the spin–parity distribution $P(J^\pi, E)$ of ^{156}Gd produced via the neutron pickup reaction $^{157}\text{Gd}(^3\text{He}, ^4\text{He})^{156}\text{Gd}$. In our initial treatment, we restrict our considerations to a one-step reaction mechanism and focus on the effect of

V. G. Gueorguiev (✉)

Institute for Advanced Physical Studies, Sofia, Bulgaria

Ronin Institute for Independent Scholarship, Montclair, NJ, USA

e-mail: Vesselin@MailAPS.org

J. E. Escher · F. S. Dietrich

Lawrence Livermore National Laboratory, Livermore, CA, USA

P. D. Kunz

Department of Physics and Astrophysics, University of Colorado, Boulder, CO, USA

© This is a U.S. government work and not under copyright protection in the U.S.; foreign copyright protection may apply 2021

J. Escher et al. (eds.), *Compound-Nuclear Reactions*, Springer Proceedings in Physics 254, https://doi.org/10.1007/978-3-030-58082-7_29

deformation. Contributions from higher-order reaction mechanisms may need to be considered [6] in the future.

In analogy with the rotor-plus-particle model [7], we view excited states in ^{156}Gd as rotational states built on intrinsic states consisting of a neutron hole in the ^{157}Gd core; that is, a neutron removal from a deformed Woods–Saxon-type single-particle state [8] in ^{157}Gd . To understand the impact of the deformation and what should be considered as a small deformation, calculations of Woods–Saxon-type single-particle states were performed using several codes [9–15]. For small non-zero deformation, we used the codes from Ref. [10–13], while for large deformation we selected only the code by Cwiok et al. [10]. The pairing effects within the core are accounted for through the BCS pairing model [16, 17], while the particle–core interaction usually dominated by a Coriolis coupling is accounted for via first-order perturbation theory to the particle–core Coriolis coupling [17]. The spectroscopic factor associated with each state is the expansion coefficient of the deformed neutron state in a spherical Sturmian basis along with the spherical form factors [17]. The cross section for one-neutron transfers to each excited state in ^{156}Gd is calculated as coherent contribution using a standard reaction code [15] based on spherical basis states. The Sturmian basis is a collection of states that are solutions to an equation that is almost the same as the Schrödinger equation under consideration, for fixed eigenenergy, but for a potential depth that is varied until the boundary conditions are satisfied [18, 19]. Using such basis states comes at the expense of a more complicated expansion but guarantees completeness and the correct asymptotic tail of the wave function and often results in fast convergence and small model spaces.

The resulting model calculations result in discrete energy states (see, e.g., Fig. 5 in Ref. [17]), and cross sections with sharp peaks (Fig. 9 in Ref. [17]), which cannot be directly compared to experiments. The current description does not include an explicit treatment of the couplings between the doorway states and more complicated configurations, which result in the damping of these states into the compound nucleus. We account for this damping by introducing a Lorentzian distribution function, which smoothes out the cross section in energy [17].

Our calculations predict that, within the assumptions discussed here, the reaction $^3\text{He}+^{157}\text{Gd} \rightarrow ^4\text{He}+^{156}\text{Gd}^*$ produces a well-behaved formation probability $P(J^\pi, E)$ within the energy range relevant to the desired reaction $^{155}\text{Gd}+n \rightarrow ^{156}\text{Gd}^*$. It is observed that the centroid and shape of the Gaussian distributions of the positive and negative parity states of the compound system can be significantly different from each other (see Fig. 1). Thus, one has to carefully verify whether it is appropriate to use the same Gaussian distribution for positive and negative parity states as has been done in some surrogate reaction models [20].

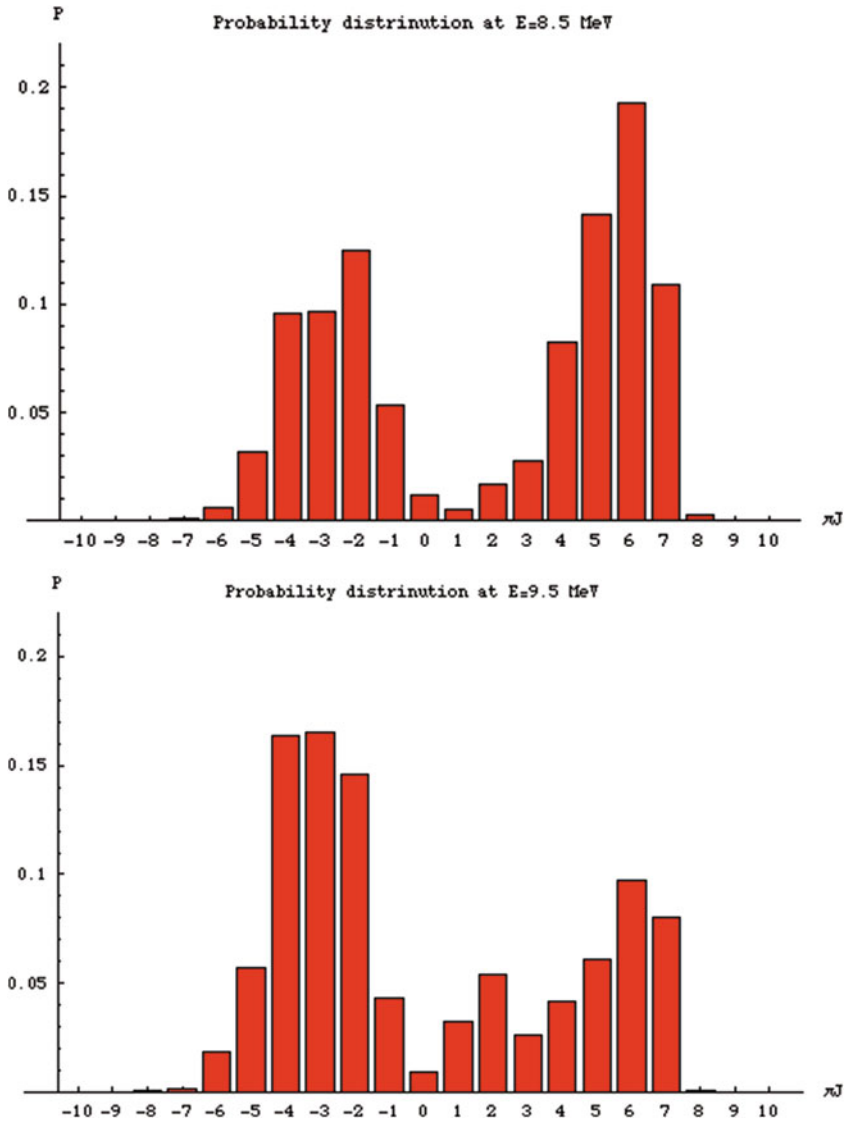


Fig. 1 $P(J^\pi; E)$ distributions for energies near the neutron separation energy in ^{156}Gd . Left graph for $E = 8.5$ MeV and right $E = 9.5$ MeV (using $\Gamma = 0.01 + 0.01E$ for the smearing function). The sign of the horizontal coordinate corresponds to the parity π , and its magnitude gives J

Acknowledgment This work was performed in part under the auspices of the US Department of Energy by Lawrence Livermore National Laboratory under contract DE-AC52-07NA27344, with support from the LDRD project 19-ERD-017.

References

1. C.W. Reich, Nuclear Data Sheets **99**, 753 (2003)
2. J.E. Escher et al., Rev. Mod. Phys. **84**, 353 (2012)
3. J.E. Escher, F.S. Dietrich, Phys. Rev. C **81**, 024612 (2010)
4. J.E. Escher et al., EPJ Web Conf. **122**, 12001 (2016)
5. V.G. Gueorguiev, J.E. Escher, Bulg. J. Phys. **44**, 489 (2017)
6. J.E. Escher et al., Phys. Rev. Lett. **121**, 052501 (2018)
7. A. Bohr, B.R. Mottelson, *Nuclear Structure II* (W.A. Benjamin, Ontario, 1975)
8. R.D. Woods, D.S. Saxon, Phys. Rev. **95**, 577 (1954)
9. B. Hird, Comput. Phys. Commun. **6**, 30 (1973)
10. S. Cwiok, J. Dudek, W. Nazarewicz et al., Comput. Phys. Commun. **46**, 379 (1987)
11. B. Hird, K.H. Huang, Can. J. Phy. **53**, 559 (1975)
12. B. Mohammed-Azizi, D.E. Medjadi, Comput. Phys. Commun. **156**, 241 (2004)
13. E. Rost, Phys. Rev. **154**, 994 (1967)
14. P.D. Kunz, Computer code dwuck4 (1990). <https://www.oecd-nea.org/tools/abstract/detail/nesc9872>
15. P.D. Kunz, Computer code chuck3 (1992). <https://people.nslc.msu.edu/~brown/reaction-codes/home.html>
16. T. Papenbrock, A. Bhattacharyya, Phys. Rev. C **75**, 014304 (2007)
17. V.G. Gueorguiev, P.D. Kunz, J.E. Escher, F.S. Dietrich, arXiv:nucl-th/0706.2002
18. M. Rothenberg, Ann. Phys. **19**, 262 (1962)
19. B.L. Andersen, B.B. Back, J.M. Bang, Nucl. Phys. A **147**, 33 (1974)
20. G. Boutoux, B. Jurado, V. Méot et al., Phys. Lett. B **712**, 319 (2012)

Part VIII
Fusion, Isotope Production, and
Superheavy Nuclei

P_{CN} Calculations for $Z = 111$ to $Z = 118$



W. Loveland and Liangyu Yao

1 Introduction

The cross section for producing a heavy evaporation residue in a complete fusion reaction can be written as a non-separable product of three factors, which express the capture cross section, the fusion probability and the survival probability.

$$\sigma_{EVR} = \frac{\pi h^2}{2\mu E} \sum_{\ell=0} (2\ell + 1) T(E, \ell) P_{CN} W_{sur}(E, \ell) \quad (1)$$

Each of these factors is dependent on the spin, but the survival probability, W_{sur} , is zero or very small for higher spin values, effectively limiting the capture and fusion terms. Many partial waves contribute to the capture cross sections, but the higher partial waves result in non-surviving events. In this work, we examine the impact of restrictions on spin placed by the survival probabilities for compound nuclear reactions resulting in the synthesis of superheavy nuclei with $Z_{CN} = 111$ –118. In doing so, we extend the previous work [1, 2] to treat the synthesis of the heaviest nuclei with $Z_{CN} = 111$ –118.

W. Loveland (✉) · L. Yao
Oregon State University, Corvallis, OR, USA
e-mail: lovelanw@onid.orst.edu

© This is a U.S. government work and not under copyright protection in the U.S.; foreign copyright protection may apply 2021
J. Escher et al. (eds.), *Compound-Nuclear Reactions*, Springer Proceedings in Physics 254, https://doi.org/10.1007/978-3-030-58082-7_30

2 Methodology

As explained in [1], the formalism for calculating the survival, against fission, of a highly excited nucleus is relatively well-understood [3]. One starts with a single particle model [4] of the level density in which one allows the level density parameter to be a function of the excitation energy. Masses and shell corrections are taken from [5]. The deformation dependent collective enhancement of the level density is taken from [6]. The decay widths for decay by neutron, charged particle and γ -emission are calculated with standard formulas. Corrections for Kramers effects [7] are made to the fission widths. The fission barrier heights are calculated using liquid drop barriers and excitation energy dependent shell corrections.

We begin with the compilation of Duellmann of evaluated evaporation residue cross sections for reactions that produce nuclei with $Z_{CN} = 111-118$ [8]. For each reaction (projectile, target and beam energy), we calculated the spin dependent evaporation residue cross section assuming $P_{CN} = 1$ using the ‘‘Empirical Model’’ of [3]. In [1], we presented evidence that this procedure results in a reasonable agreement between the calculated and measured spin dependence of the evaporation residue formation cross sections for the test case of $^{176}\text{Yb}(^{48}\text{Ca},4n)^{220}\text{Th}$ reaction and for the $^{48}\text{Ca} + ^{208}\text{Pb}$ reaction. Loveland [9] has made a detailed examination of the strengths and weaknesses of models such as [3] and placed limits on how well these models work.

3 Results

There are 28 cases we have examined. A summary of the measured and calculated evaporation residue cross sections is given in Table 1. The fusion probability, P_{CN} , is taken as the ratios of the calculated to the measured evaporation residue cross sections since we have assumed $P_{CN} = 1$ in our calculations. As expected, the P_{CN} values for the ‘‘cold fusion’’ reactions (1n out) are orders of magnitude smaller than those for the hot fusion (2n–4n out) reactions. The deduced values of P_{CN} generally get smaller as the product of the atomic numbers of the colliding nuclei, Z_1Z_2 , increases.

In Fig. 1, we show the P_{CN} values, sorted by exit channel for the hot fusion reactions, as a function of the simple scaling variable, Z_1Z_2 , the product of the atomic numbers of the reacting nuclei.

The use of other scaling variables such as x_{CN} , x_{eff} and x_m does not significantly improve the description of the data. x_{CN} is defined as

$$x_{CN} = \frac{Z_{CN}^2/A_{CN}}{50.883 \left(1 - 1.7826 \left(\frac{A_{CN} - 2Z_{CN}}{A_{CN}} \right)^2 \right)} \quad (2)$$

Table 1 Measured and calculated evaporation residue cross sections for $Z_{CN} = 111-118$

Beam	Target	Channel	σ_{meas} (pb)	σ_{calc} (pb)	PCN	Reference
^{64}Ni	^{209}Bi	1n	$3.5^{+1.9}_{-1.3}$	6910	0.000507	[10]
^{65}Cu	^{208}Pb	1n	$1.7^{+3.9}_{-1.4}$	20,500	$8.3e^{-05}$	[11]
^{48}Ca	^{238}U	3n	$2.5^{+1.8}_{-1.1}$	60	0.0417	[12]
^{48}Ca	^{238}U	4n	$0.7^{+0.6}_{-0.3}$	425	0.00165	[13]
^{48}Ca	^{238}U	4n	$0.6^{+1.6}_{-0.5}$	7	0.0857	[12]
^{70}Zn	^{208}Pb	1n	$0.5^{+1.1}_{-0.4}$	$5e+06$	$1e^{-07}$	[14]
^{48}Ca	^{237}Np	3n	0.9	5	0.18	[15]
^{70}Zn	^{209}Bi	1n	0.022	940,000	$2.34e^{-08}$	[16]
^{48}Ca	^{239}Pu	3n	0.23	16	0.0144	[17]
^{48}Ca	^{240}Pu	3n	$2.5^{+2.9}_{-1.4}$	62	0.0403	[17]
^{48}Ca	^{242}Pu	2n	0.5	244	0.00205	
^{48}Ca	^{242}Pu	3n	$3.6^{+3.4}_{-1.7}$	78	0.0463	[12]
^{48}Ca	^{242}Pu	4n	$4.5^{+3.6}_{-1.9}$	129	0.0349	[12]
^{48}Ca	^{242}Pu	5n	$0.6^{+0.9}_{-0.5}$	11.6	0.0517	[18]
^{48}Ca	^{244}Pu	3n	$8^{+7.4}_{-4.5}$	180	0.0444	[19]
^{48}Ca	^{244}Pu	4n	$9.8^{+3.9}_{-3.1}$	220	0.0445	[19]
^{48}Ca	^{244}Pu	5n	$1.1^{+2.6}_{-0.9}$	9.2	0.120	[20]
^{48}Ca	^{243}Am	2n	$2.5^{+2.7}_{-1.5}$	15.4	0.162	[21]
^{48}Ca	^{243}Am	3n	$8.5^{+6.4}_{-3.7}$	660	0.0129	[22]
^{48}Ca	^{243}Am	4n	$0.9^{+3.2}_{-0.8}$	169	0.00533	[23]
^{48}Ca	^{245}Cm	2n	0.9	6.89	0.131	[20]
^{48}Ca	^{245}Cm	3n	$3.7^{+3.6}_{-1.8}$	229	0.0162	[24]
^{48}Ca	^{245}Cm	4n	0.8	95	0.00842	[24]
^{48}Ca	^{248}Cm	3n	1.2	166	0.00723	[12]
^{48}Ca	^{248}Cm	4n	3.4	652	0.00522	[25]
^{48}Ca	^{249}Bk	3n	$1.1^{+1.2}_{-0.6}$	1660	0.000663	[26]
^{48}Ca	^{249}Bk	4n	$2.4^{+3.3}_{-1.4}$	333	0.00721	[26]
^{48}Ca	^{249}Cf	2n	0.9	50.9	0.0177	[24]

x_{eff} is defined as

$$x_{eff} = \frac{\frac{4Z_P Z_T}{A_P^{\frac{1}{3}} A_T^{\frac{1}{3}} \left(A_P^{\frac{1}{3}} + A_T^{\frac{1}{3}} \right)}}{50.883 \left(1 - 1.7826 \left(\left(\frac{A_{CN} - 2Z_{CN}}{A_{CN}} \right)^2 \right) \right)}$$

x_m is defined as

$$x_m = 0.25x_{CN} + 0.75x_{eff}$$

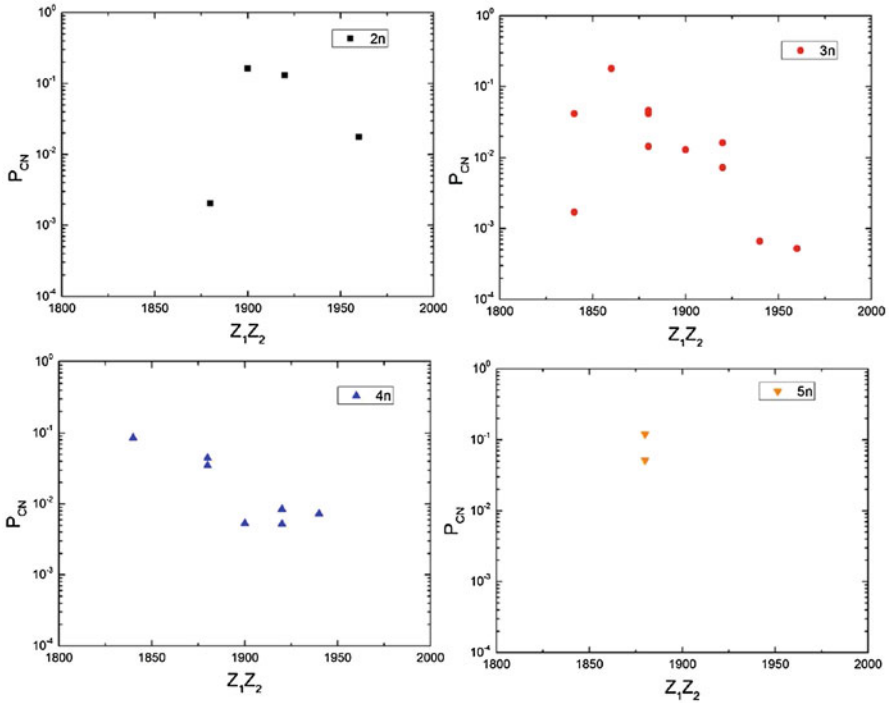


Fig. 1 The calculated values of P_{CN} for various exit channels as a function of the scaling variable $Z_1 Z_2$

All of these scaling variables seek to relate P_{CN} to the balance of attractive and repulsive forces in the reaction entrance channel. Clearly there is a certain amount of “spatter” in the plots of P_{CN} vs. $Z_1 Z_2$. In part, this “spatter” is due to the uncertainties in the measured evaporation residue cross sections which are typically uncertain to the measured value (Loveland [9] has shown that these uncertainties in P_{CN} can lead to order of magnitude uncertainties in estimations of the production cross sections for elements 119 and 120, challenging experimentalists dealing with fb production cross sections).

If we use the simple $Z_1 Z_2$ scaling factor for the 3n and 4n reactions, then we can write a simple formula for the 3n channel as

$$\log_{10}(P_{CN}(3n)) = -0.019Z_1 Z_2 + 35.0$$

and for the 4n channel

$$\log_{10}(P_{CN}(4n)) = -0.013Z_1 Z_2 + 23.2$$

Fig. 2 Comparison of the measurements of P_{CN} in this work with that of [27]

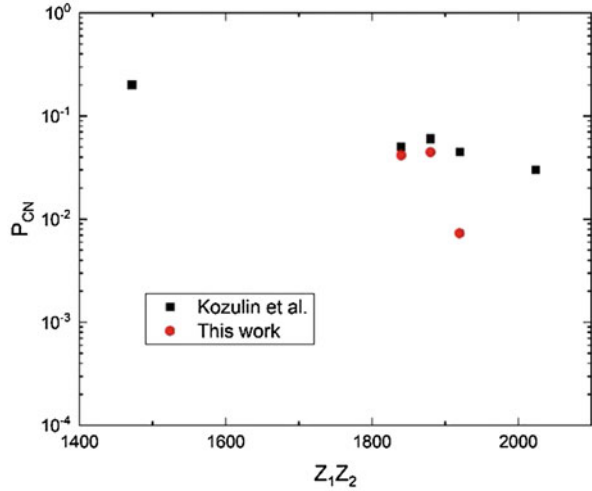
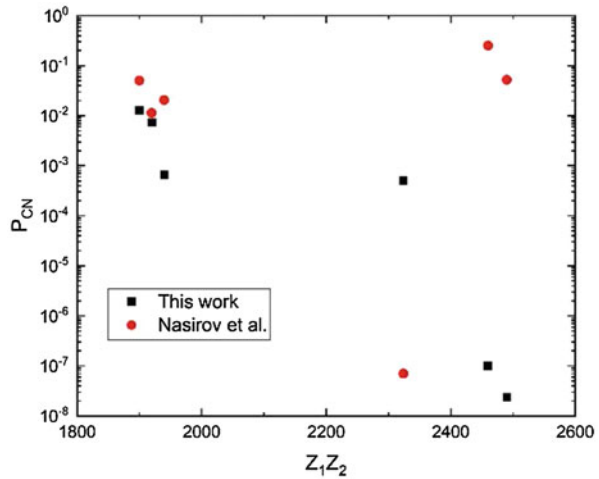


Fig. 3 Comparison of our measured values of P_{CN} with the predictions of [28]



We can ask how well these new values of P_{CN} agree with previous measurements and theoretical predictions. Kozulin et al. [27] have reported measurements of P_{CN} based upon mass–energy distributions of fission-like fragments from a variety of reactions. In Fig. 2, we compare our values of P_{CN} with the Kozulin et al. measurements. Given the intrinsic large uncertainties in our deduced P_{CN} values, the agreement between the measurements seems satisfactory.

How do our measured values of P_{CN} compare with various theoretical predictions of P_{CN} ? Given our methodology, there is no surprise that our deduced values of P_{CN} agree well with the predictions of Zagrebaev [29]. How about other predictions? In Fig. 3, we compare our deduced values of P_{CN} with predictions of Nasirov et al. [28]. For the hot fusion reactions ($Z_1Z_2 = 1800$ – 2000), the agreement seems reasonable but there is a stark disagreement for the cold fusion cases.

4 Conclusions

What have we learned from this study? We have extended the systematics of P_{CN} to cases involving the synthesis of elements 111–118. We have parameterized the new values of P_{CN} with a simple linear fit that might be useful in predictions of cross sections for the synthesis of elements 119 and 120. We have compared our measurements with previous measurements and theoretical predictions.

Acknowledgments This work was supported in part by the U.S. Department of Energy, Office of Science, Office of Nuclear Physics under Grant No. DE-SC0014380.

References

1. L. Yao, W. Loveland, Survival-mediated capture and fusion cross sections for heavy element synthesis. *Phys. Rev. C* **97**, 014608 (2018)
2. W. Loveland, L. Yao, Survival mediated heavy element capture cross sections. *EPJA Web Conf.* **163**, 00033 (2017)
3. Nuclear reactions video project, statistical model of the decay of excited nuclei, nrv.jinr.ru
4. A.V. Ignatyuk, IAEA Report No. INDC(CCP)-233/L, (1985), Unpublished
5. P. Moller, A.J. Sierk, T. Ichikawa, H. Sagawa, Nuclear ground state masses and deformations-FRDN-2012. *At. Data Nucl. Data Tables* **109–110**, 1 (2016)
6. V.I. Zagrebaev, Y. Aritomo, M.G. Itkis, Y.T. Oganessian, M. Ohta, Synthesis of superheavy nuclei: how accurately can we describe it and calculate the cross sections? *Phys. Rev. C* **65**, 014607 (2007)
7. H.A. Kramers, Brownian motion in a field of force and the diffusion model of chemical reactions. *Physica (Amsterdam)* **7**, 284 (1940)
8. Ch.E. Duellmann, (private communication)
9. W. Loveland, An experimentalist's view of the uncertainties in understanding heavy element synthesis. *Eur. J. Phys. A* **51**, 120 (2015)
10. S. Hofmann et al., New results on elements 111 and 112. *Eur. Phys. J. A* **14**, 147 (2002)
11. C.M. Folden et al., Development of an odd-Z-projectile reaction for heavy element synthesis: $^{208}\text{Pb}(^{64}\text{Ni},n)^{271}\text{Ds}$ and $^{208}\text{Pb}(^{65}\text{Cu},n)^{272}\text{111}$. *Phys. Rev. Lett.* **93**, 212702 (2004)
12. Y.T. Oganessian et al., Measurement of cross sections and decay properties of the isotopes of elements 112, 114, and 116 produced in the fusion reactions $^{233,238}\text{U}$, ^{242}Pu and $^{248}\text{Cm} + ^{48}\text{Ca}$. *Phys. Rev. C* **70**, 064609 (2004)
13. S. Hofmann et al., The reaction $^{48}\text{Ca} + ^{238}\text{U} \rightarrow ^{286}\text{112}^*$ studied at the GSI-SHIP. *Eur. Phys. J. A* **32**, 251 (2007)
14. S. Hofmann et al., New results on element 111 and 112. *Eur. Phys. J. A* **14**, 147 (2002)
15. Y.T. Oganessian et al., Synthesis of the isotope $^{282}\text{113}$ in the $^{237}\text{Np} + ^{48}\text{Ca}$ fusion reaction. *Phys. Rev. C* **76**, 011601 (2007)
16. K. Morita et al., New result in the production and decay of an isotope, $^{278}\text{113}$, of the 113th element. *J. Phys. Soc. Jpn* **81**, 103201 (2012)
17. V.K. Utyonkov et al., Experiments on the synthesis of superheavy nuclei ^{284}Fl and ^{285}Fl in the $^{239,240}\text{Pu} + ^{48}\text{Ca}$ reactions. *Phys. Rev. C* **92**, 034609 (2015)
18. P.A. Ellison et al., New superheavy element isotopes: $^{242}\text{Pu}(^{48}\text{Ca}, 5n)^{285}\text{114}$. *Phys. Rev. Lett.* **105**, 182701 (2010)
19. C.E. Duellmann et al., Production and decay of element 114: high cross sections and the new nucleus ^{277}Hs . *Phys. Rev. Lett.* **104**, 252701 (2010)

20. Y.T. Oganessian et al., Measurements of cross sections for the fusion-evaporation reactions: $^{244}\text{Pu}(^{48}\text{Ca},\text{xn})^{292-x}\text{114}$ and $^{245}\text{Cm}(^{48}\text{Ca},\text{xn})^{293-x}\text{116}$. Phys. Rev. C **69**, 054607 (2004)
21. Y.T. Oganessian et al., Investigation of the $^{243}\text{Am} + ^{48}\text{Ca}$ reaction products previously observed in the experiments on elements 113, 115, and 117. Phys. Rev. C **87**, 014302 (2013)
22. Y.T. Oganessian et al., New insights into the $^{243}\text{Am} + ^{48}\text{Ca}$ reaction products previously observed in the experiments on elements 113,115, and 117. Phys. Rev. Lett. **108**, 022502 (2012)
23. Y.T. Oganessian et al., Experiments on the synthesis of element 115 in the reaction $^{243}\text{Am}(^{48}\text{Ca},\text{xn})^{291-x}\text{115}$. Phys. Rev. C **69**, 021601 (2004)
24. Y.T. Oganessian et al., Synthesis of the isotopes of elements 118 and 116 in the ^{249}Cf and $^{245}\text{Cm} + ^{48}\text{Ca}$ fusion reactions. Phys. Rev. C **74**, 044602 (2006)
25. S. Hofmann et al., The reaction $^{48}\text{Ca} + ^{248}\text{Cm} \rightarrow ^{296}\text{116}^*$ studied at the GSI-SHIP. Eur. Phys. J. A **48**, 62 (2012)
26. Y.T. Oganessian et al., Experimental studies of the $^{249}\text{Bk} + ^{48}\text{Ca}$ reaction including decay properties and excitation function for isotopes of element 117 and discovery of the new isotope ^{277}Mt . Phys. Rev. C **87**, 054621 (2013)
27. E.M. Kozulin et al., Fission and quasifission of composite systems with Z=108-120: Transition from heavy-ion reactions involving S and Ca to Ti and Ni ions. Phys. Rev. C **94**, 054613 (2016)
28. A.K. Nasirov, G. Mandaglio, G. Giardina, A. Sobiczewski, A.I. Muminov, Effects of the entrance channel and fission barrier in the synthesis of superheavy element Z=120. Phys. Rev. C **84**, 044612 (2011)
29. V.I. Zagrebaev, Synthesis of superheavy nuclei: nucleon collectivization as a mechanism for compound nucleus formation. Phys. Rev. C **64**, 034606 (2001)

On the Role of the Curvature Corrections in the Surface Tension Coefficient upon the Orientation Effects in the Fusion Reactions



K. Cherevko, L. Bulavin, L. Jenkovszky, and V. Sysoev

Nowadays the orientation effects in fusion reactions are intensively studied. Among the possible mechanisms responsible for the changes of the barrier height and reaction cross section are the Coulomb interaction [1] and changes in the nuclear interaction potential due to curvature of the interfaces [2]. It can be seen from the literature that Coulomb effects are well understood and can explain the qualitative picture observed in the experiment. At the same time, the role of the nuclear potential is not that well determined.

The present study addresses the possible influence of the difference in between the surface tension coefficient of the semi-infinite nuclear matter σ_∞ and that for the curved interface $\sigma_{curv} = \sigma_\infty \left(1 - \frac{2\delta}{R}\right)$ [3] on the fusion of the deformed nuclei. The equation of state of nuclear matter is calculated with a Skyrme interaction.

To solve the task the earlier developed theoretical model allowing to link the surface and bulk properties of the nuclear matter [4] is used. Within that approach the Tolman δ -correction [3] for the nuclear matter on the coexistence curve can be found from the equation of state:

K. Cherevko (✉) · L. Bulavin · V. Sysoev
Physics Faculty, Taras Shevchenko National University of Kyiv, Kyiv, Ukraine
e-mail: k.cherevko@knu.ua; sysoev@univ.kiev.ua

L. Jenkovszky
Bogolyubov Institute for Theoretical Physics (BITP), Kyiv, Ukraine
e-mail: jenk@bitp.kiev.ua

$$\delta = \frac{2}{3} \frac{1}{\rho_0^2} \times \frac{-33t_0 - 160W\rho_0^{-1/3} + t_3(1+\alpha)\rho_0^\alpha \frac{1}{12} (7(3\alpha+6) - 3(3\alpha+6)^2)}{\left(15t_0 + \frac{1}{12}t_3(1+\alpha) ((3\alpha+6) - (3\alpha+6)^2)\right)^2} \sigma_\infty \quad (1)$$

where W is the parameter related to the effective masses, see Eq. (9) in Ref.[4], ρ_0 is the saturation density and α the power of the density dependence of the Skyrme interaction. To evaluate the barrier heights and positions different nuclear potentials based on the proximity concept [2] are used. Within that approach the nuclear part V_N of the total interaction potential $V_T = V_N + V_C$ is defined as:

$$V_N(r) = 4\pi\sigma b \bar{R} \Phi\left(\frac{r - C_1 - C_2}{b}\right) \quad (2)$$

with $\Phi(\zeta)$ being the universal function. In the current work we attempt to account for the curvature correction in the surface tension coefficient by changing σ in Eq. (2) for σ_{curv} with δ defined from Eq. (1). In calculating the shape of the nuclei and the shortest distance we follow the approach of [5] and for the Coulomb part V_C in case of the deformed nuclei the formalism from [1] is used. SV-min Skyrme force is used [6].

Within the suggested approach the nuclear interaction potential is calculated for the case of two deformed ^{40}Ca nuclei (Fig. 1) The barrier heights and positions for that case are given in Table 1. It can be easily seen that inclusion of curvature correction changes the barrier height and position. The observed effect increases with the increased deformation of the nuclei.

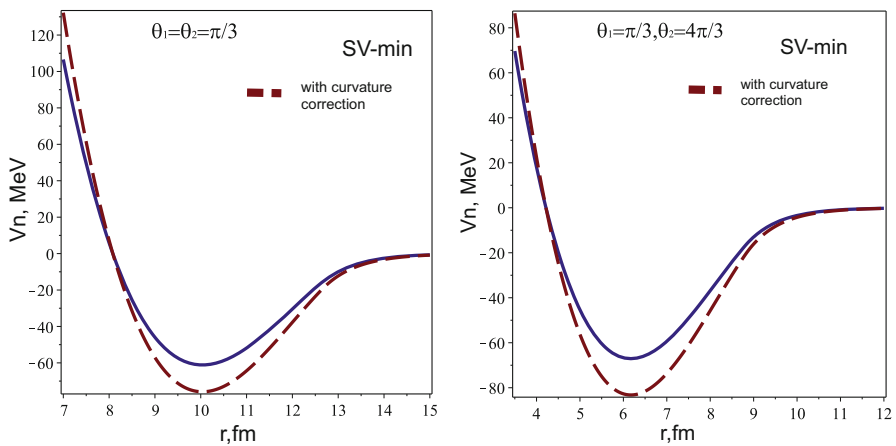


Fig. 1 Nuclear interaction potential V_N dependence on distance. $^{40}\text{Ca} + ^{40}\text{Ca}$ system

Table 1 Fusion barriers heights and positions for the deformed $^{40}\text{Ca} + ^{40}\text{Ca}$ System

$\frac{a}{b}$	θ_1 , deg	θ_2 , deg	No correction		Correction included		Experiment [7]	
			V_B , MeV	R_B , fm	V_B , MeV	R_B , fm	V_B , MeV	R_B , fm
1	–	–	54.78	9.70	54.74	9.69	50.60 ± 2.8	9.50 ± 0.5
1.2	60	60	41.72	13.01	41.24	13.05		
1.5	60	60	39.20	13.9	39.07	13.94		

From our studies it can be seen that in case of the deformed nuclei suggested correction gives a non-negligible contribution to the fusion barriers heights and positions depending on the mutual orientation of the nuclei. The obtained results suggest that accounting for the curvature correction to the surface energy is essential when studying the interaction of the deformed nuclei.

References

1. C.Y. Wong, Phys. Rev. Lett. **31**(12), 766 (1973)
2. J. Blocki, J. Randrup, W. Swiatecki, C. Tsang, Ann. Phys. **105**, 427 (1977)
3. R.C. Tolman, J. Chem. Phys. **17**(3), 333 (1949)
4. K.V. Cherevko, L.A. Bulavin, L.L. Jenkovszky, V.M. Syssoev, F.S. Zhang, Phys. Rev. C **90**, 017303 (2014)
5. R.K. Gupta, N. Singh, M. Manhas, Phys. Rev. C **70**, 034608 (2004)
6. P. Klupfel, P.G. Reinhard, T.J. Burvenich, J.A. Maruhn, Phys. Rev. C **79**, 034310 (2009)
7. R.K. Puri, R.K. Gupta, Phys. Rev. C **45**, 1837 (1992)

Excitation Function Measurements of Alpha-Induced Reaction on Natural Copper and Titanium Up To 46 MeV



Hiroshi Yashima, Masayuki Hagiwara, Toshiya Sanami, and Shunsuke Yonai

1 Introduction

The activation cross section data are required for isotope production, activation detector, residual activity assessment and so on, although experimental data are very scarce for heavy ions. We, therefore, irradiated 46.4 MeV alpha beam onto a target to obtain experimental data of residual radioactivities for low energy heavy ions.

2 Experiment and Analysis

The Irradiation experiment was performed at cyclotron facility (NIRS-930), National Institutes for Quantum and Radiological Science and Technology. A schematic view of the experimental set-up is shown in Fig. 1. The target was composed of a stack of 15 mm × 15 mm × 0.01 mm natural Cu and Ti foils, and total thickness of target was thicker than the range of projectile alpha beams. The beam current on the target was recorded with a current integrator, connected to a multichannel scaler to monitor the fluctuations of the alpha beam. The two target irradiations were performed for a shorter irradiation time and a longer

H. Yashima (✉)

Institute for Integrated Radiation and Nuclear Science, Kyoto University, Osaka, Japan
e-mail: yashima@rri.kyoto-u.ac.jp

M. Hagiwara · T. Sanami

High Energy Accelerator Research Organization, Tsukuba, Ibaraki, Japan

S. Yonai

National Institutes for Quantum and Radiological Science and Technology, Chiba, Japan

© This is a U.S. government work and not under copyright protection in the U.S.; foreign copyright protection may apply 2021

J. Escher et al. (eds.), *Compound-Nuclear Reactions*, Springer Proceedings in Physics 254, https://doi.org/10.1007/978-3-030-58082-7_32

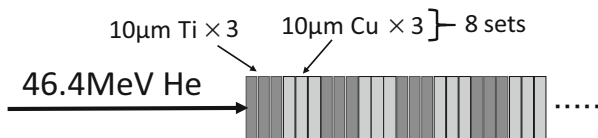


Fig. 1 A Schematic view of the experimental set-up

irradiation time, considering the half-lives of produced nuclei. The average alpha beam intensity and irradiation time were 300 nA and 10 min for short irradiation, 250 nA and 4 h for long irradiation, respectively. After irradiation, we measured the gamma-ray spectra from Cu and Ti samples with a HPGe detector. The activation cross sections σ were deduced by the following equation:

$$\sigma = \frac{\lambda C I_f}{\varepsilon \gamma N_d t I e^{-\lambda t_c} (1 - e^{-\lambda t_m}) (1 - e^{-\lambda t_i})}, \quad (1)$$

where λ is the decay constant (s^{-1}), C is the total counts of gamma-ray peak area, ε is the peak efficiency, γ is the branching ratio of gamma-rays, N_d is the atomic density of sample (atom/cm^3), t is the thickness of sample (cm), t_c is the cooling time (s), t_m is the measurement time (s), t_i is the irradiation time (s), I is the average beam intensity (alpha per second) and I_f is the correction factor for beam current fluctuation. The corresponding energy for the cross section was determined by taking into account the projectile energy degradation in the target by using the SRIM-2013 code [1].

3 Results

As an example, the excitation functions obtained for ${}^{\text{nat}}\text{Ti}(\alpha, X){}^{51}\text{Cr}$ and ${}^{\text{nat}}\text{Cu}(\alpha, X){}^{66}\text{Ga}$ reactions are shown in Fig. 2 with other experimental data [2–9], IAEA recommended data [10] and TENDL-2017 data [11].

The present data are consistent with other experimental data and IAEA recommended data. There were some differences between experimental data and TENDL-2017 data. In Fig. 2, the peak value and peak energy of the excitation function of TENDL-2017 data showed lower than these of experimental data.

4 Conclusion

The excitation function of alpha-induced reaction in Cu and Ti were measured up to 46 MeV. The present results agree well with other experimental results and IAEA

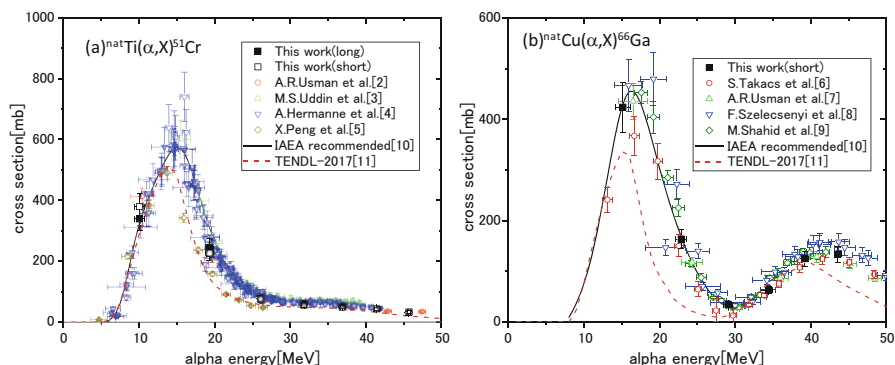


Fig. 2 Measured excitation function with other experimental data, IAEA recommended data and TENDL-2017 data

recommended data. The present results will be useful as benchmark data to evaluate nuclear data and investigate the accuracy of calculation codes.

Acknowledgement The authors express their gratitude to the accelerator staff of NIRS-930 for generous support during this experiment. This work was supported by JSPS KAKENHI Grant Number JP17K07010.

References

1. J.F. Ziegler, The stopping and range of ions in matter (SRIM). <http://www.srim.org>. Last accessed 5 July 2016
2. A.R. Usman et al., Excitation functions of alpha particles induced nuclear reactions on natural titanium in the energy range of 10.4–50.2 MeV. Nucl. Instrum. Methods B **399**, 34–47 (2017)
3. M.S. Uddin et al., Excitation functions of alpha particle induced reactions on ${}^{\text{nat}}\text{Ti}$ up to 40 MeV. Nucl. Instrum. Methods B **380**, 15–19 (2016)
4. A. Hermanne et al., Excitation functions of nuclear reactions induced by alpha particles up to 42 MeV on ${}^{\text{nat}}\text{Ti}$ for monitoring purposes and TLA. Nucl. Instrum. Methods B **152**, 187–201 (1999)
5. X. Peng et al., Excitation functions for the reactions induced by alpha-particle impact of natural titanium. Nucl. Instrum. Methods B **140**, 9–12 (1998)
6. S. Takacs et al., Crosschecking of alpha particle monitor reactions up to 50 MeV. Nucl. Instrum. Methods B **397**, 33–38 (2017)
7. A.R. Usman et al., Production cross-sections of radionuclides from α -induced reactions on natural copper up to 50 MeV. Appl. Radiat. Isotopes **114**, 104–113 (2016)
8. F. Szelecsenyi et al., Alpha beam monitoring via ${}^{\text{nat}}\text{Cu} + \alpha$ processes in the energy range from 40 to 60 MeV. Nucl. Instrum. Methods B **184**, 589–596 (2001)
9. M. Shahid et al., Measurement of excitation functions in alpha induced reactions on ${}^{\text{nat}}\text{Cu}$. Nucl. Instrum. Methods B **358**, 160–167 (2015)
10. F. Tarkanyi et al., in *Charged particle cross-section database for medical radioisotope production: diagnostic radioisotopes and monitor reactions*, IAEA-TECDOC-1211 (2001)
11. A.J. Koning et al., Modern nuclear data evaluation with the TALYS code system. Nucl. Data Sheets **113**, 2841–2934 (2012)

Measurement of the Excitation Function of $^{96}\text{Zr}(\alpha, x)^{99}\text{Mo}$ Reaction up to 32 MeV



Masayuki Hagiwara, Hiroshi Yashima, Toshiya Sanami, and Shunsuke Yonai

1 Introduction

Technetium 99m and its parent isotope: molybdenum 99 is one of the most important radioisotopes used in nuclear medicine for common diagnostic imaging technologies such as single photon emission computed tomography (SPECT). After the well-recognized worldwide shortage of $^{99\text{m}}\text{Tc}/^{99}\text{Mo}$ due to the long shutdowns of major nuclear research reactors in 2009–2010, some alternate sources of $^{99\text{m}}\text{Tc}/^{99}\text{Mo}$ using accelerators have been investigated for their stable supply [1]. We have focused on the production route of ^{99}Mo via the $^{96}\text{Zr}(\alpha, n)^{99}\text{Mo}$ reaction using a low energy accelerator. In order to estimate the production yield of ^{99}Mo and its byproducts, we irradiated 46.4 MeV alpha particles onto stacked $^{\text{nat}}\text{Zr}$ targets at a cyclotron facility (NIRS-930), National Institutes for Quantum and Radiological Science and Technology, Japan.

M. Hagiwara (✉) · T. Sanami
High Energy Accelerator Research Organization, Tsukuba, Ibaraki, Japan
e-mail: hagi@post.kek.jp

H. Yashima
Institute for Integrated Radiation and Nuclear Science, Kyoto University, Sennan-gun, Osaka, Japan

S. Yonai
National Institutes for Quantum and Radiological Science and Technology, Chiba-shi, Chiba, Japan

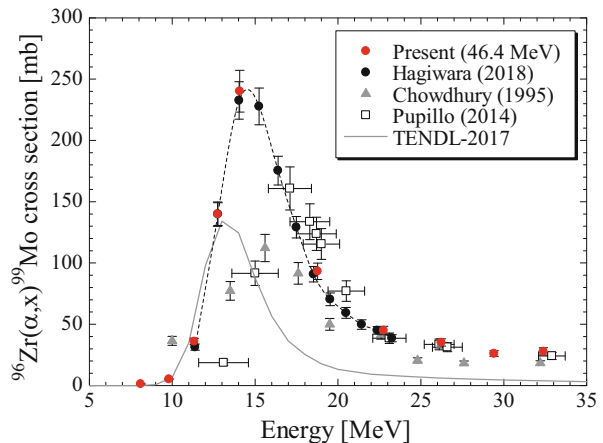
2 Experimental

The stack target was composed of natural zirconium foils, natural copper foils, and natural titanium foils with their thickness of 5 μm . The zirconium foils were sandwiched between copper and titanium foils that were acted as beam monitors, energy degraders, and recoil catcher foils. The total target thickness was thicker than the range of 46.4 MeV α particles to measure the beam current on the targets. After 1-hour irradiation with beam current of 300 nA, γ -rays from each foil were measured with a HPGe detector. The excitation function was deduced from the activity measured and the projectile energies on each foil, which were calculated by using the SRIM-2013 code [2]. The projectile energies and beam fluxes were confirmed by comparing the measured excitation function and the IAEA recommendation data for the $^{\text{nat}}\text{Ti}(\alpha, X)^{51}\text{Cr}$ reaction [3]. The uncertainties of the target thicknesses (5%), number of incident particles (3%), and efficiency determination (4%) were considered in addition to the statistical error.

3 Results

The measured excitation functions of $^{96}\text{Zr}(\alpha, x)^{99}\text{Mo}$ reaction are shown in Fig. 1 with the other experimental data [4–6] and TENDL-2017 data [7]. The present data well-traced a fitting line of our previous experimental data measured using 24 MeV α particles in HIMAC [4]. However, there were some differences between the other experimental data and TENDL-2017 data, especially for the peak values and peak energies in their excitation function. According to the present data, the production rate of ^{99}Mo using α particles could be enhanced 50% higher than ones estimated from the other data [6].

Fig. 1 Measured excitation function of the $^{96}\text{Zr}(\alpha, x)^{99}\text{Mo}$ reaction compared with TENDL-2017 and other experimental data. A dash line indicates a fitting curve of the previous experimental data reported in [4]



References

1. R. Van Noorden, *Nature* **504**(7479), 202–204 (2013)
2. J.F. Ziegler, The stopping and range of ions in matter (SRIM). <http://www.srim.org>. Accessed 5 July 2016
3. IAEA, Nuclear database homepage. <http://www-nds.iaea.org/medical/>. Accessed 5 July 2016
4. M. Hagiwara, H. Yashima, T. Sanami, S.J. Yonai, Measurement of the excitation function of $^{96}\text{Zr}(\alpha,n)^{99}\text{Mo}$ for an alternative production source of medical radioisotopes. *Radioanal. Nucl. Chem.* **318**(1), 569–573 (2018)
5. D.P. Chowdhury, S. Pal, S.K. Saha, S. Gangadharan, Determination of cross section of α -induced nuclear reaction on natural Cr and Zr by stacked foil activation for thin layer activation analysis. *Nucl. Instrum. Meth. B.* **103**(3), 261–266 (1995)
6. G. Pupillo, J. Esposito, M. Gambaccini, F. Haddad, N. Michel, Experimental cross section evaluation for innovative ^{99}Mo production via the (α,n) reaction on ^{96}Zr target. *J. Radioanal. Nucl. Chem.* **302**(2), 911–917 (2014)
7. A.J. Koning, D. Rochman, Modern nuclear data evaluation with the TALYS code system. *Nucl. Data Sheets* **113**, 2841–2934 (2012)

Part IX
Fission

A Grand Tour of Nuclear Fission Physics



W. Younes

1 Introduction

In a practical sense, modern nuclear physics began in 1932 with the discovery of the neutron by James Chadwick [1]. Shortly thereafter, Enrico Fermi working in Rome set out to form elements beyond uranium, the heaviest known element at the time, by bombarding a uranium target with neutrons. Fermi surmised that the composite system produced by the neutron-induced reaction would form higher-Z elements through a series of beta decays. These experiments lasted from 1934 to 1935, and although they observed beta activity, Fermi and his collaborators were never able to account for the large number of separate activities they measured [2, 3]. Despite this setback, other groups led by Irène Joliot-Curie in Paris and Lise Meitner in Berlin took up the search for transuranic elements from 1935 to 1938, using Fermi's approach [4]. All these attempts were doomed from the start because low-energy neutron-induced reactions on uranium targets paradoxically lead to fission products much lighter than the target, rather than to transuranic elements. The concept of nuclear fission, and the possibility that it might account for Fermi's results, was first formulated by Ida Noddack in 1934 [5]. Unfortunately, her prescient critique of Fermi's work was largely ignored. The uranium irradiation puzzle was finally solved in 1938 by the Berlin group with the identification of barium as one of the products formed in the reaction [2, 6]. In 1939, three seminal papers on fission were published. The first, by Hahn and Strassmann [7], marked the official discovery of fission. The second, by Meitner and Frisch [8], gave a model of fission using an analogy with a drop of liquid. The third paper, by Bohr and Wheeler [9], applied the liquid-drop model to interpret and predict an impressive number of fission

W. Younes (✉)

Lawrence Livermore National Laboratory, Livermore, CA, USA

© This is a U.S. government work and not under copyright protection in the U.S.; foreign copyright protection may apply 2021

J. Escher et al. (eds.), *Compound-Nuclear Reactions*, Springer Proceedings in Physics 254, https://doi.org/10.1007/978-3-030-58082-7_34

observables. The Bohr and Wheeler paper directly addressed the questions: how much energy is released in fission? How much energy has to be supplied, and is spontaneous fission possible? What is the cross section for induced fission? Which isotope in natural uranium is primarily responsible for the observed fission cross section? What is the origin of delayed neutrons? What is the mass distribution of the fragments? These and other questions will be further explored in the remainder of this lecture.

2 General Features of Fission

Various characteristic features of fission have emerged from over 80 years of study. These features are important in formulating a coherent understanding of the fission process. That being said, it is important to keep in mind that, despite overall systematic trends, observed fission properties can differ significantly between neighboring nuclei.

Nuclear fission is an extreme example of large-amplitude collective motion [10] that results in the division of a parent nucleus into two or more fragment nuclei. Binary fission (fission into two fragments) is far more common than ternary fission, which typically occurs in fewer than about one in a thousand events in thermal fission [11]. The third fragment in ternary fission is most often an α particle that tends to be emitted in a direction roughly perpendicular to the axis connecting the other two fragments [11]. The collective character of the fission process distinguishes it from other processes that break up the nucleus, such as spallation [12]. In a spallation reaction, a high-energy incident nucleon (e.g., an 800-MeV proton [13]) interacts with individual protons and neutrons in the nucleus causing the emission of secondary particles via an intranuclear cascade mechanism [12]. Once the nucleus loses enough energy through this process, particle (mostly neutron) emission continues via statistical evaporation. The different mechanisms underlying fission and spallation lead to differences in their observable properties: spallation tends to produce fragments that are close to the target in mass, whereas (low-energy) fission more often results in a pair of fragments significantly lighter than the target nucleus. In another example, the quasi-fission process where the reacting system re-separates before fission can begin differs from fission and in fact can compete with it in the formation of superheavy nuclei [14, 15].

The fission process can occur spontaneously, or it can be induced by an incident particle. Historically, induced fission was discovered first and spontaneous fission (SF) was observed in uranium nuclei sometime later [16, 17]. The SF process in actinides typically competes with α decay and is often dwarfed by the α branch but not always, as in the case of ^{250}Cm where SF dominates α decay. When viewed as a barrier penetration mechanism, the SF half-life can be calculated using the semi-classical Wentzel-Kramers-Brillouin (WKB) approximation [18] in terms of the action integral for the system [11, 19, 20]. The SF half-lives, when plotted as a function of the Z^2/A ratio of the parent nucleus, display two important features:

the SF half-life tends to decrease with increasing Z^2/A , and nuclei with an odd number of either protons or neutrons have systematically larger half-lives than the neighboring even-even nuclei [11].

In induced fission, an incident particle fuses with a target to form a compound system.¹ If the excitation energy of the compound system is sufficiently large, the parent nucleus will likely emit neutrons, and may undergo multiple-chance fission (fission without prior neutron emission is called “first-chance” fission, if one neutron is emitted the process is referred to as “second-chance” fission, etc.). Once there is no longer enough excitation energy left to emit additional neutrons, the parent nucleus can continue to de-excite through gamma emission or proceed toward scission (the breaking point of the nucleus). Various models predict a transition time to scission (also known as the saddle-to-scission time) of $10^{-20} - 10^{-19}$ s for low-energy fission [22–24]. This is a relatively long transition time compared to the orbital time of 10^{-22} s of a nucleon in the nucleus, as expected for a collective process involving the coherent motion of many or all nucleons. There are various experimental techniques that attempt to measure the time scale of the fission process. Some of these techniques probe the time scale of the entire fission process from compound-nucleus formation to scission. For example, one such approach takes advantage of the rearrangement of the electronic structure that occurs when the fragments formed, and the corresponding change in the x-rays produced [25]. Another approach, the crystal blocking technique, relies on the ordered structure of a crystal to gauge how far the parent nucleus has recoiled before the fragments are produced and fly apart, and to deduce the time delay since compound-nucleus formation [26]. Other experimental methods, looking at the properties of neutrons and gammas emitted before scission, can give a better sense of the saddle-to-scission time scale [27, 28].

The fragments produced at scission are called “primary fragments” until they emit prompt neutrons and become “secondary fragments.” These secondary fragments can then beta decay into stable nuclei, which are then referred to as “fission products” [29]. The gamma rays emitted by the fragments can be prompt, or “late prompt” [30] if they are issued from an isomeric state, and can help identify the fragments thanks to their precisely known energies. The total number of fragments with a given mass (A), charge (Z), and isomeric state (I), produced in each fission event after prompt neutron emission but before any delayed decays, is called the “independent yield” $Y(A, Z, I)$ and is normalized to 2 (or 200%) when summed over all values of A , Z , and I [29]. The total number of nuclei produced by each fission over all time is called the “cumulative yield” $Y_{\text{cu}}(A, Z, I)$, and is also normalized to 2 (or 200%) [29]. The sum yield $Y(A)$ is the sum of independent yields over all Z and I for a given mass A . The chain yield $Y_{\text{ch}}(A)$ is the cumulative yield of the last (i.e., stable) member of a decay chain of given mass A .

¹Direct reaction mechanisms can also lead to fission, but without initially going through compound-nucleus formation [21].

The mass and charge distributions of fission products have been measured for many actinides and for both SF and induced fission at various energies. Some characteristic features can be gleaned from these studies. For thermal fission, the distributions as a function of A tend to be bimodal, with one peak near the doubly magic ^{132}Sn due to quantum shell effects, and another corresponding to the lighter complementary nuclei. The two peaks are fairly broad and are separated by a dip near symmetric fission for thermal and low-energy fission [31, 32]. As the energy of the incident neutron is increased, the central dip at symmetric fission tends to fill in, and the mass peaks broaden somewhat [33]. Another feature of the fission products is that the ratio Z/A of a product tends to have a value close to the Z/A ratio of the parent. This is known as the unchanged charge distribution (UCD) rule [34]. The distribution of products as a function of Z sometimes displays an even-odd staggering pattern for low-energy fission that has been used to estimate the energy dissipated by the parent nucleus into non-collective modes of excitation before scission (see, e.g., chapter 8 in [35]).

The total energy released in a fission event is defined as the difference in rest-mass energy between the parent nucleus and the final products. This energy can also be written as the sum of the total kinetic energy (TKE) and the total excitation energy (TXE) of the primary fragments, minus any energy contributed by the incident particle in the case of induced fission (i.e., its kinetic energy plus any excitation energy gained in the formation of the compound nucleus). The TKE of the fragments can be estimated as the Coulomb repulsion energy between centers of charge of the fragments at their separation distance at scission, however, this estimate ignores any pre-scission energy acquired during the transition from saddle to scission. Precisely how the initial energy of the parent nucleus is partitioned between TKE and TXE of the fragments, and how the TXE is divided among the fragments remain open questions [36, 37].

In addition to the information that can be gathered from the fragments and products (e.g., mass distributions and TKE), the neutrons and gammas that they emit can also provide useful data that shed light on the fission process. In principle, the excitation energy and initial angular momentum imparted to the fragments could be reconstructed by measuring the neutrons and gammas they emit. The average number of prompt neutrons (multiplicity, $\bar{\nu}$) emitted as a function of primary fragment mass (A), typically follows a characteristic “sawtooth” shape and can be used to estimate the average fragment excitation energy, removed by neutron emission [38]. The energy spectrum of the neutrons emitted by the fragments is expected to have a Maxwellian shape in the center of mass frame of the fragment which, when transformed to the laboratory frame, takes on a Watt functional form [39]. In addition to the prompt neutrons emitted by the fragments, and multi-chance neutrons emitted by the parent nucleus, there are two additional sources of neutrons produced by fission: scission neutrons and delayed neutrons. Scission neutrons are thought to be emitted by the parent nucleus as it breaks apart, and the frequency with which they occur remains a source of debate [40, 41]. Their angular distribution is expected to be isotropic in the laboratory frame because they are emitted by the slowly recoiling parent nucleus, in contrast to the neutrons emitted

by the fragments which tend to be peaked in the recoil direction of those fragments. Scission neutrons were first identified by their angular distributions [42], but the neutron energy spectrum may also be affected by their presence [43]. However, a great deal of work has since shown that some scission neutrons could be reabsorbed by the moving fragments, resulting in an anisotropic distribution not so different from that of the neutrons emitted by the fragments themselves [44], thus a word of caution is warranted so that scission neutrons are not automatically equated with an additional isotropic source of neutrons in the data (see also [45]). Finally, when the secondary fragment undergoes beta decay, the resulting nucleus may on rare occasions be left with sufficient excitation energy to emit a neutron. Because they are delayed by the relatively slow beta-decay process, these are known as delayed neutrons [46].

The gamma-ray energies and multiplicities have been recently measured for several fissioning systems [47–49]. The measured properties of these gamma rays can be used to estimate the energy they remove from the excitation energies of the fragments. By adding the energies removed by both neutrons and gammas, the initial excitation energies of the fragments can be reconstructed. Because they also carry away angular momentum, the prompt gammas can be used to deduce the initial angular momentum of the fragments [50].

3 Fission Theory and Modeling

The liquid-drop model (LDM) was the first approach used to describe the fission process [8, 9]. The LDM has since evolved into the macroscopic-microscopic model that is widely used today [51, 52]. The remarkable success of the LDM can be attributed to the fact that it gives a good description of the bulk behavior of the nucleus (i.e., the properties that vary smoothly with the number of nucleons), and any deviations from this bulk behavior are due primarily to the contribution from nucleons in the thin surface region of the nucleus [53]. The macroscopic-microscopic model starts from a family of curves that describe the surface of the nucleus as a geometrical object. The total energy of the nucleus is then obtained as the sum of a macroscopic energy, a shell correction, and a pairing correction. The macroscopic contribution often consists primarily of a surface energy, proportional to the surface integral of the nuclear shape, and a Coulomb energy calculated as the volume integral of the inverse-distance potential inside the nucleus, assuming a uniform charge distribution [53, 54]. There are additional terms that can be added to improve the accuracy of the macroscopic-energy term, and various liquid-drop prescriptions have been developed depending on which terms are included, such as the standard LDM [55], the generalized liquid-drop model [56, 57], the Lublin-Strasbourg liquid drop [58], and the finite-range liquid-drop model [51, 52]. The shell correction term was introduced by Strutinsky [59, 60] to account for quantum effects. In order to calculate this correction, it is necessary to construct a potential function that can be used in the Schrödinger equation to calculate a set of single-

particle states. From there, the “shell energy” can be calculated as the sum of single-particle energies over the occupied states. The difference between this shell energy and one calculated using a continuous smoothed density of states gives the shell correction energy [54, 61]. A similar approach gives the pairing correction as the difference in pairing correlation energy (the difference in ground-state energies of the nucleus with and without pairing) using the actual single-particle states and a smooth density of states [54, 61]. There are several methods to generate the potential function needed for the shell and pairing corrections, but the method of folded potentials [53, 54] is especially well adapted to the wide range of shapes encountered in fission.

The macroscopic-microscopic model gives the energy of the nucleus as a function of its shape, and this can be used to generate a potential energy surface (PES) as a function of shape parameters. The PES can then be used to locate fission barriers [62] and extract their properties, which in turn can provide estimates of fission rates [56, 57]. More importantly, the PES is a fundamental ingredient in dynamical (i.e., time-dependent) calculations of the fission process. One way to model fission dynamics is by performing a random walk across the PES. Ward et al. [63] adopted this approach, using a Metropolis algorithm with transition rates across the PES determined by level densities obtained with a combinatorial technique.

Another approach is to solve the classical Langevin equation for the system [64]. The Langevin approach essentially models the evolution of the system as that of a Brownian particle coupled to a heat bath. The Langevin approach has been coupled to statistical particle emission models at each time step to predict properties of particles emitted before scission [65], and has been successfully used to calculate fission-fragment mass, charge, and angular distributions, as well as fission probabilities and cross sections [66–68]. A special case of the Langevin method in the strong-damping limit, where inertia can be ignored, has also been successfully applied to the calculation of fragment mass distributions for a wide range of parent nuclei [69].

Scission-point models are another type of approach to fission developed starting in the 1950s [70, 71] to predict fission-fragment properties, and have continued to evolve through the present day [72, 73]. These models use purely statistical arguments at scission, without invoking the dynamical evolution of the parent nucleus up to that point. Scission-point models rely on two critical assumptions: (1) the fission-fragment properties can be determined entirely from an analysis of the system at scission, and (2) a thermodynamic equilibrium exists at scission between the fragments. A probability distribution for the configuration at scission can then be constructed based on the energy of the system in this configuration. Using this probability distribution, average properties of the fragments can be obtained. For example, in recent work by Lemaitre et al. [73], charge yields were calculated for a wide range of actinides using this approach.

Microscopic descriptions of the fission process start from protons, neutrons, and an effective (i.e., in-medium) interaction between them [74, 75]. The Hartree-Fock [76, 77] and Hartree-Fock-Bogoliubov (HFB) approximation can be used

to construct self-consistent configurations of the parent nucleus that are relevant to fission, under the assumption of a solution consisting of independent quasi-particles, by constraining collective parameters of the nucleus (e.g., quadrupole and octupole moments) [61, 78]. This type of approach falls under the larger category of density functional theory (DFT) [79]. There are various ways to extract fission observables using the microscopic method. For example, the set of HFB energies as a function of collective parameters can be used within a scission-point model [73], or to construct a PES as the basic framework for the methods discussed above. Alternately, the time evolution of the system to scission can be treated within the same microscopic framework. The time-dependent Hartree-Fock (TDHF) method is a powerful approach that can describe the evolution of the nucleus to scission [22, 80]. The TDHF approach is limited to the assumption of a single Slater determinant solution at all times, however, it does not require collective-parameter constraints and elementary single-particle degrees of freedom are automatically included [61]. The TDHF approach was applied to the fission problem early on [22], and later extend to include pairing [80, 81]. Recently, Bulgac et al. have developed the time-dependent superfluid local density approximation (TDSLDA) [24, 82, 83], a fully microscopic extension of DFT that includes pairing. In the TDSLDA, all degrees of freedom are treated on an equal footing and all symmetries are correctly implemented. This approach was recently applied to the study of fission dynamics in ^{240}Pu [24].

Other approaches have attempted to go beyond the inherent restriction of the TDHF method to a single determinant through configuration mixing [84]. The mixing can be between microscopic states labeled by continuous parameters, as in the generator coordinate method (GCM) [85, 86], or between microscopic states in a discrete basis (e.g., configuration interaction in the shell model [87]). In the GCM, the wave function of the nucleus is written as a linear superposition of HFB solutions labeled by the relevant collective parameters (see, e.g., section 9.5 in [78]). Because the collective parameters can take on a continuous set of values, the linear superposition takes the form of an integral over these parameters and the unknown weights of the linear expansion are determined by a variational principle [61, 78]. The application of the variational principle with the GCM wave function leads to the so-called Hill-Wheeler equation [85], which is an integro-differential non-local non-linear equation that is very difficult to solve for more than one collective parameter [88]. A more tractable approach is to expand the Hill-Wheeler equation to second order in the non-locality (i.e., the difference in value between the collective parameters). This approximation is often accompanied by the assumption of a Gaussian shape for the overlap between GCM states, known as the Gaussian overlap approximation (GOA). With these simplifications, the Hill-Wheeler equation reduces to a Schrödinger-like equation in the collective coordinates, where the collective inertia tensor and potential are constructed from the underlying single-particle degrees of freedom. The GCM is readily extended to include a time dependence and, as in the static case, can be approximated by a time-dependent collective Schrödinger equation. This time-dependent equation can then

be solved using standard techniques and used to predict fission-fragment properties such as mass distributions, TKE, TXE, etc. [89–92]. The GCM can also be extended to include single-particle degrees of freedom [93] while also eliminating the need for a GOA [94]. The standing challenge for these GCM approaches is to include all relevant collective and single-particle degrees of freedom in a computationally tractable way [94, 95]. Another difficulty in this approach is that the GCM states for different values of the collective parameters are not guaranteed to be orthogonal, which complicates the interpretation of the results [88].

The discrete-basis approach to fission provides an alternative to the GCM by mixing states that are orthogonal from the start, and where single-particle degrees of freedom can be built in explicitly [96–98]. In this method, a set of configurations must first be identified that can be used as a discrete basis to adequately model fission dynamics near scission. Next, the continuum wave functions of post-scission states have to be described, and their coupling to pre-scission states has to be calculated. In this way, the discrete-basis method will be able to describe the latter stages of the fission process, which are especially challenging to model within the GCM framework, because of non-adiabatic behavior [94].

In [96, 97] the construction of a discrete basis for the description of fission dynamics is illustrated by a toy model for the fictitious fission of ^{32}S into two ^{16}O fragments. The ground state of ^{32}S can be constructed simply by filling the lowest shell-model orbitals for the protons and neutrons: $0s_{1/2}$, $0p_{3/2}$, $0p_{1/2}$, $0d_{5/2}$, and $1s_{1/2}$. Identifying the magnetic substate quantum numbers with K , the projection of the angular momentum on the symmetry axis of the nucleus, we define a K^π partition as the number of pairs of nucleons of a given type occupying states with given K quantum number and parity π . For the $^{16}\text{O} + ^{16}\text{O}$ system the K^π partition corresponds to the ground state of a single ^{16}O nucleus and its parity partner, so that their \pm combination has good parity. By comparing K^π partitions of the initial ^{32}S and final $^{16}\text{O} + ^{16}\text{O}$ configurations, the “fission” process can be seen to proceed through a set of intermediate 2p-2h states.

The same principles can be applied to more realistic Hartree-Fock calculations of heavy nuclei [98]. Configurations with a given K partition (here parity is no longer necessarily a good quantum number) can be followed as a function of the quadrupole constraint (Q_{20}) to scission. In some cases, these configurations will display a minimum in energy as a function of Q_{20} just before scission and are labeled as “cliff” states, while others will have no minimum to hold the nucleus back from separating into fragments and are labeled “glider” states. When following the lowest-energy configurations along the fission path for ^{236}U [98], the transitions between different K partitions before scission involve single or double pair jumps, while the transition between glider states at scission can involve significantly more pairs. The major rearrangement of the K partition at scission is not easily described in approaches that rely on shape parameters alone (e.g., the GCM without single-particle extensions), and is more naturally described in a discrete-basis approach [99].

4 Data Evaluation

Fission theory and experiment are brought together in data evaluations. Evaluations are used to fill gaps where data are missing and resolve discrepancies between data sets, with the help of theory and modeling. We will focus on models used in evaluations of: (1) fission cross sections, and (2) properties of fission fragments and of the neutrons and gamma rays they emit. Cross-section evaluations typically rely on Hauser-Feshbach theory [100] and transition-state theory, first introduced by Eyring to describe chemical reaction rates [101] and later adapted to nuclear reactions by Wigner [102]. In the transition-state model, passage over a barrier is mediated by a set of states on top of the barrier. The probability of transmission through these states was formulated by Hill and Wheeler in 1953 [85]. States in the first well of the potential energy surface are called “class-I” states. States in the well separating the two fission barriers are called “class-II” states. Both class-I and class-II states can enter into calculations of the fission cross-section [103]. This basic model has been improved by using barrier properties and level densities calculated within a consistent microscopic framework [104], and through the use of R-matrix theory with Monte-Carlo simulations of class-I and class-II state properties and of their coupling matrix elements [105]. Various models of fission-fragment properties have been incorporated into event-by-event codes such as GEF [106], FIFRELIN [107], CGMF [108], and FREYA [109, 110]. These codes can be used to evaluate fragment yields, TKE, and the spectra and multiplicities of the neutrons and gamma rays they emit. The FREYA code, for example, provides an event-by-event simulation of post-scission physics with full kinematic information for the products and emitted particles [109, 111]. Additional information on event-by-event simulation codes for the evaluation of fission data can be found in the recent review papers by Capote et al. [112] and Talou et al. [113].

5 Conclusion

Nuclear fission remains an active area of study more than 80 years after its discovery. The field has made tremendous strides since the first papers on fission were published in 1939, yet we still lack a predictive theory of this complex phenomenon that follows the fissioning system from its formation to the last decay of the final products, within a single consistent framework. Fission provides a rich choice of measurable quantities to test and refine models with, and very sophisticated descriptions of fission have been developed. Yet, there remain many fundamental questions for experimentalists and theorists, such as: what happens at scission? How do we describe the transition from one to two nuclei within a microscopic framework? what are the appropriate degrees of freedom throughout the fission process? How is the initial energy of the parent nucleus distributed among the final products? These questions can be addressed by theory as its predictive power

improves, but experiments must guide and constrain the theory developments. In particular, theory will greatly benefit from multi-parameter experiments where many fission observables are measured simultaneously on an event-by-event basis. This type of comprehensive measurements can be used to reconstruct the state of the parent nucleus at scission, which is where many theoretical calculations of fission have to stop. Experiments that directly probe pre-scission dynamics are also extremely useful in constraining theory. These types of experiments include the measurement of pre-scission particles, fission time scales, and of exotic processes such as muon-induced fission [114].

References

1. J. Chadwick, *Nature* **129**, 312 (1932)
2. G. Herrmann, *Nucl. Phys.* **A502**, 141 (1989)
3. J.M. Pearson, *Phys. Today* **68**, 40 (2015)
4. J.L. Spradley, *Phys. Teacher* **27**, 656 (1989)
5. I. Noddack, *Z. Angew. Chem.* **47**, 653 (1934)
6. K. Starke, *J. Chem. Ed.* **56**, 771 (1979)
7. O. Hahn, F. Strassmann, *Naturwissenschaften* **27**, 11 (1939)
8. L. Meitner, O. Frisch, *Nature* **143**, 239 (1939)
9. N. Bohr, J.A. Wheeler, *Phys. Rev.* **56**, 426 (1939)
10. G.F. Bertsch, *Nucl. Phys.* **A574**, 169 (1994)
11. H.J. Krappe, K. Pomorski, *Theory of Nuclear Fission: a Textbook* (Springer, New York, 2012)
12. D. Filges, F. Goldenbaum, *Handbook of Spallation Research* (Wiley, Weinheim, 2009)
13. G.J. Russell, ICANS-XI International Collaboration on Advanced Neutron Sources, Tsukuba (1990), p. 291
14. R. Yanez, W. Loveland, J. S. Barrett, L. Yao, B.B. Back, S. Zhu, T.L. Khoo, *Phys. Rev. C* **88**, 014606 (2013)
15. B.B. Back, H. Esbensen, C.L. Jiang, K.E. Rehm, *Rev. Mod. Phys.* **86**, 317 (2014)
16. G.N. Flerov, K.A. Petrzhak, *J. Phys. U.S.S.R.* **3**, 275 (1940)
17. G. Scharff-Goldhaber, G.S. Klaiber, *Phys. Rev.* **70**, 229 (1946)
18. A. Messiah, *Quantum Mechanics* (Dover, Mineola, 1999)
19. A. Baran, *Phys. Lett. B* **76**, 8 (1978)
20. R. Rodríguez-Guzmán, L.M. Robledo, *Phys. Rev. C* **89**, 054310 (2014)
21. J.E. Escher, J.T. Burke, F.S. Dietrich, N.D. Scielzo, I.J. Thompson, W. Younes, *Rev. Mod. Phys.* **84**, 353 (2012)
22. J.W. Negele, S.E. Koonin, P. Möller, J.R. Nix, A.J. Sierk, *Phys. Rev. C* **17**, 1098 (1978)
23. J.F. Berger, M. Girod, D. Gogny, *Nucl. Phys.* **A502**, 85 (1989)
24. A. Bulgac, P. Magierski, K.J. Roche, I. Stetcu, *Phys. Rev. Lett.* **116**, 122504 (2016)
25. H.W. Wilschut, V.L. Kravchuk, *Nucl. Phys.* **A734**, 156 (2004)
26. M. Morjean, J.L. Charvet, M. Chevallier, C. Cohen, D. Dauvergne, R. Dayras, A. Drouart, J.D. Frankland, D. Jacquet, R. Kirsch, M. Laget, P. Lantesse, A. L'Hoir, A. Marchix, L. Nalpas, M. Parlog, C. Ray, C. Schmitt, C. Stodel, L. Tassantog, C. Volant, *Eur. Phys. J. D* **45**, 27 (2007)
27. D.J. Hofman, B.B. Back, I. Diószegi, C.P. Montaya, S. Schadmand, R. Varma, P. Paul, *Phys. Rev. Lett.* **72**, 470 (1994)
28. D.J. Hinde, D. Hilscher, H. Rossner, *Nucl. Phys.* **A538**, 243 (1992)
29. E.A.C. Crouch, *At. Data Nucl. Data Tables* **19**, 417 (1977)
30. P. Talou, T. Kawano, I. Stetcu, J.P. Lestone, E. McKigney, M.B. Chadwick, *Phys. Rev. C* **94**, 064613 (2016)

31. A.C. Wahl, *Physics and Chemistry of Fission*, vol. I (IAEA, Vienna, 1965) , p. 317
32. K.F. Flynn, E.P. Horwitz, C.A.A. Bloomquist, R.F. Barnes, R.K. Sjolblom, P.R. Fields, L.E. Glendenin, *Phys. Rev. C* **5**, 1725 (1972)
33. L.E. Glendenin, J.E. Gindler, D.J. Henderson, J.W. Meadows, *Phys. Rev. C* **24**, 2600 (1981)
34. A.C. Wahl, *At. Data Nucl. Data Tables* **39**, 1 (1988)
35. C. Wagemans, *The Nuclear Fission Process* (CRC Press, Boca Raton, 1991)
36. M. Mirea, *Phys. Rev. C* **83**, 054608 (2011)
37. K.-H. Schmidt, B. Jurado, *Rep. Prog. Phys.* **81**, 106301 (2018)
38. D.G. Madland, *Nucl. Phys.* **A772**, 113 (2006)
39. B.E. Watt, *Phys. Rev.* **87**, 1037 (1952)
40. G.A. Petrov, A.S. Vorobyev, V.E. Sokolov, A.M. Gagarski, I.S. Guseva, O.A. Shcherbakov, V.I. Petrova, T.A. Zavarukhina, G.V. Val'ski, Yu. . Pleva, T.E. Kuzmina, *AIP Conf. Proc.* **1175**, 289 (2009)
41. A.S. Vorobyev, O.A. Shcherbakov, Yu.S. Pleva, A.M. Gagarski, G.V. Val'ski, G.A., Petrov, V.I. Petrova, T.A. Zavarukhina, *Nucl. Instr. Methods Phys. Res. A* **598**, 795 (2009)
42. H.R. Bowman, S.G. Thompson, J.C.D. Milton, W.J. Swiatecki, *Phys. Rev.* **126**, 2120 (1962)
43. N. Kornilov, *Fission Neutrons: Experiments, Evaluation, Modeling and Open Problems* (Springer, Cham, 2015)
44. N. Carjan, M. Rizea, *Phys. Rev. C* **82**, 014617 (2010)
45. A.S. Vorobyev, O.A. Shcherbakov, A.M. Gagarski, G.V. Val'ski, G.A. Petrov, *EPJ Web Conf.* **8**, 03004 (2010)
46. K.D. Talley, Beta-delayed neutron data and models for SCALE, Ph.D. Dissertation, University of Tennessee, Knoxville (2016)
47. A. Chyzh, C.Y. Wu, E. Kwan, R.A. Henderson, T.A. Bredeweg, R.C. Haight, A.C. Hayes-Sterbenz, H.Y. Lee, J.M. O'Donnell, J.L. Ullmann, *Phys. Rev. C* **90**, 014602 (2014)
48. S. Oberstedt, R. Billnert, T. Belgya, T. Bryś, W. Geerts, C. Guerrero, F.-J. Hamsch, Z. Kis, A. Moens, A. Oberstedt, G. Sibbens, L. Szentmiklosi, D. Vanleeuw, M. Vidali, *Phys. Rev. C* **90**, 024618 (2014)
49. A. Oberstedt, R. Billnert, F.-J. Hamsch, S. Oberstedt, *Phys. Rev. C* **92**, 014618 (2015)
50. J.B. Wilhelmy, E. Cheifetz, R.C. Jared, S.G. Thompson, H.R. Bowman, J.O. Rasmussen, *Phys. Rev. C* **5**, 2041 (1972)
51. T. Ichikawa, A. Iwamoto, P. Möller, A. J. Sierk *Phys. Rev. C* **86**, 024610 (2012)
52. P. Möller, A.J. Sierk, T. Ichikawa, A. Iwamoto, M. Mumpower, *Phys. Rev. C* **91**, 024310 (2015)
53. R.W. Hasse, W.D. Myers, *Geometrical Relationships of Macroscopic Nuclear Physics* (Springer, New York, 1988)
54. M. Bolsterli, E.O. Fiset, J.R. Nix, J.L. Norton, *Phys. Rev. C* **5**, 1050 (1972)
55. N. Carjan, F.A. Ivanyuk, Yu. Oganessian, G. Ter-Akopian, *Nucl. Phys.* **A942**, 97 (2015)
56. X. Bao, H. Zhang, G. Royer, J. Li, *Nucl. Phys.* **A906**, 1 (2013)
57. J. Gao, X. Bao, H. Zhang, J. Li, H. Zhang, *Nucl. Phys.* **A929**, 246 (2014)
58. K. Pomorski, J. Dudek, *Phys. Rev. C* **67**, 044316 (2003)
59. V.M. Strutinsky, *Nucl. Phys.* **A95**, 420 (1967)
60. V.M. Strutinsky, *Nucl. Phys.* **A122**, 1 (1968)
61. P. Ring, P. Schuck, *The Nuclear Many-Body Problem* (Springer, Heidelberg, 1980)
62. P. Möller, A.J. Sierk, A. Iwamoto, *Phys. Rev. Lett.* **92**, 072501 (2004)
63. D.E. Ward, B.G. Carlsson, T. Døssing, P. Möller, J. Randrup, S. Åberg, *Phys. Rev. C* **95**, 024618 (2017)
64. P. Fröbrich, L.I. Gontchar, *Phys. Rep.* **292**, 131 (1998)
65. K. Mazurek, C. Schmitt, P.N. Nadochty, A.V. Cheredov, *Phys. Rev. C* **94**, 064602 (2016)
66. A.J. Sierk, *Phys. Rev. C* **96**, 034603 (2017)
67. D.O. Eremenko, V.A. Drozdov, O.V. Fotina, S.Yu. Platonov, O.A. Yuminov, *Phys. Rev. C* **94**, 014602 (2016)

68. E. Vardaci, P.N. Nadtochy, A. Di Nitto, A. Brondi, G. La Rana, R. Moro, P.K. Rath, M. Ashaduzzaman, E.M. Kozulin, G.N. Knyazheva, I.M. Itkis, M. Cinausero, G. Prete, D. Fabris, G. Montagnoli, N. Gelli, *Phys. Rev. C* **92**, 034610 (2015)
69. J. Randrup, P. Möller, A.J. Sierk, *Phys. Rev. C* **84**, 034613 (2011)
70. P. Fong, *Phys. Rev.* **89**, 332 (1953)
71. P. Fong, *Phys. Rev.* **102**, 434 (1956)
72. B.D. Wilkins, E.P. Steinberg, R.R. Chasman, *Phys. Rev. C* **14**, 1832 (1976)
73. J.-F. Lemaître, S. Panebianco, J.-L. Sida, S. Hilaire, S. Heinrich, *Phys. Rev. C* **92**, 034617 (2015)
74. N. Schunck, L.M. Robledo, *Rep. Prog. Phys.* **79**, 116301 (2016)
75. D. Lacroix, arXiv:1001.5001v1 (2010)
76. S.J. Krieger, *Phys. Rev. C* **1**, 76 (1970)
77. M. Harvey, A.S. Jensen, *Nucl. Phys.* **A164**, 641 (1971)
78. W. Greiner, J.A. Maruhn, *Nuclear Models* (Springer, Berlin, 1996)
79. D.M. Brink, *Nucl. Phys. News* **12**, 27 (2002)
80. C. Simenel, A.S. Umar, *Phys. Rev. C* **89**, 031601(R) (2014)
81. G. Scamps, C. Simenel, D. Lacroix, *Phys. Rev. C* **92**, 011602(R) (2015)
82. A. Bulgac, *Ann. Rev. Nucl. Part. Sci.* **63**, 97 (2013)
83. I. Stetcu, A. Bulgac, P. Magierski, K.J. Roche, *Phys. Rev. C* **84**, 051309 (2011)
84. P.-O. Löwdin, *Adv. Chem. Phys.* **2**, 207 (1959)
85. D.L. Hill, J.A. Wheeler, *Phys. Rev.* **89**, 1102 (1953)
86. J.J. Griffin, J.A. Wheeler, *Phys. Rev.* **108**, 311 (1957)
87. E. Caurier, G. Martinez-Pinedo et al., *Rev. Mod. Phys.* **77**, 427 (2005)
88. P. Bonche, J. Dobaczewski, H. Flocard, P.-H. Heenen, J. Meyer, *Nucl. Phys.* **A510**, 466 (1990)
89. J.-F. Berger, M. Girod, D. Gogny, *Comput. Phys. Comm.* **63**, 365 (1991)
90. H. Goutte, J.F. Berger, P. Casoli, D. Gogny, *Phys. Rev. C* **71**, 024316 (2005)
91. D. Regnier, N. Dubray, N. Schunck, M. Verrière, *Phys. Rev. C* **93**, 054611 (2016)
92. W. Younes, D. Gogny, J.-F. Berger, *A Microscopic Theory of Fission Dynamics Based on the Generator Coordinate Method*. Lecture Notes in Physics, vol. 950 (Springer, Cham, 2019)
93. H. Müther, K. Goeke, K. Allaart, A. Faessler, *Phys. Rev. C* **15**, 1467 (1977)
94. R. Bernard, H. Goutte, D. Gogny, W. Younes, *Phys. Rev. C* **84**, 044308 (2011)
95. M. Verrière, N. Dubray, D. Regnier, N. Schunck, *Fission and Properties of Neutron-Rich Nuclei: Proceedings of the Sixth International Conference on ICFN6* (World Scientific, Singapore, 2017), p. 371
96. G.F. Bertsch, J.M. Mehlhaff, *EPJ Web Conf.* **122**, 01001 (2016)
97. G.F. Bertsch, *Int. J. Mod. Phys. E* **26**, 1740001 (2017)
98. G.F. Bertsch, W. Younes, L.M. Robledo, *Phys. Rev. C* **97**, 064619 (2018)
99. G.F. Bertsch, W. Younes, *Ann. Phys.* **403**, 68 (2019)
100. W. Hauser, H. Feshbach, *Phys. Rev.* **87**, 366 (1952)
101. H. Eyring, *J. Chem. Phys.* **3**, 107 (1935)
102. E. Wigner, *Trans. Faraday Soc.* **34**, 29 (1938)
103. J. Lynn, B.B. Back, *J. Phys. A* **7**, 395 (1974)
104. S. Goriely, S. Hilaire, A.J. Koning, *Phys. Rev. C* **78**, 064307 (2008)
105. O. Bouland, J.E. Lynn, P. Talou, *Phys. Rev. C* **88**, 054612 (2013)
106. K.-H. Schmidt, B. Jurado, C. Amouroux, C. Schmitt, *Nucl. Data Sheets* **131**, 107 (2016)
107. O. Litaize, O. Sérot, L. Berge, *Eur. Phys. J A* **51**, 177 (2015)
108. T. Kawano, P. Talou, M.B. Chadwick, T. Watanabe, *J. Nucl. Sci. Tech.* **47**, 462 (2010)
109. J. Randrup, R. Vogt, *Phys. Rev. C* **80**, 024601 (2009)
110. J.M. Verbeke, J. Randrup, R. Vogt, *Comput. Phys. Comm.* **222**, 263 (2018)

111. M.J. Marath, R.C. Haight, R. Vogt, M. Devlin, P. Talou, I. Stetcu, J. Randrup, P.F. Schuster, S.D. Clarke, S.A. Pozzi, *Phys. Rev. C* **97**, 044622 (2018)
112. R. Capote, Y.-J. Chen, F.-J. Hamsch, N.V. Kornilov, J.P. Lestone, O. Litaize, B. Morillon, D. Neudecker, S. Oberstedt, T. Ohsawai, N. Otuka, V.G. Pronyaev, A. Saxena, O. Serot, O.A. Shcherbakov, N.-C. Shu, D.L. Smith, P. Talou, A.S. Vorobyev, *Nucl. Data Sheets* **131**, 1 (2016)
113. P. Talou, R. Vogt, J. Randrup, M.E. Rising, S.A. Pozzi, J. Verbeke, M.T. Andrews, S.D. Clarke, P. Jaffke, M. Jandel, T. Kawano, M.J. Marath, K. Meierbachtol, L. Nakae, G. Rusev, A. Sood, I. Stetcu, C. Walker, *Eur. Phys. J. A* **54**, 9 (2018)
114. V.E. Oberacker, A.S. Umar, J.C. Wells, C. Bottcher, M.R. Strayer, J.A. Maruhn, *Phys. Rev. C* **48**, 1297 (1993)

Microscopic Calculation of Fission Fragment Mass Distributions at Increasing Excitation Energies



Nicolas Schunck, Zachary Matheson, and David Regnier

1 Introduction

In spite of numerous practical applications, e.g., for energy production, a comprehensive understanding of nuclear fission based on our best knowledge of nuclear forces and quantum many-body methods remains elusive. In recent years, increases in computational power have triggered a renaissance of microscopic fission theory [1]. A lot of emphasis has been put on the calculation of spontaneous fission half-lives, which are key to predicting the stability of superheavy elements [2–6]. Several groups have also developed tools to compute primary charge and mass distributions (before the prompt neutron emission from the fragments) [7–12]. With the recent exception of [13], most of these applications have been restricted to the low-energy regime where the fissioning nucleus is assumed to be well-described by a zero-temperature formalism. Recent precision measurements, however, point to a subtle and non-trivial dependence of the fission product yields on the excitation

N. Schunck (✉)

Nuclear and Chemical Science Division, Lawrence Livermore National Laboratory, Livermore, CA, USA

e-mail: schunck1@llnl.gov

Z. Matheson

Department of Physics and Astronomy and FRIB Laboratory, Michigan State University, East Lansing, MI, USA

e-mail: matheson@nscl.msu.edu

D. Regnier

Institut de Physique Nucléaire, IN2P3-CNRS, Université Paris-Sud, Université Paris-Saclay, Orsay Cedex, France

e-mail: regnier@ipno.in2p3.fr

© This is a U.S. government work and not under copyright protection in the U.S.; foreign copyright protection may apply 2021

J. Escher et al. (eds.), *Compound-Nuclear Reactions*, Springer Proceedings in Physics 254, https://doi.org/10.1007/978-3-030-58082-7_35

energy [14]. In this contribution, we discuss briefly some of the challenges for a microscopic description of such a phenomenon.

2 Energy Density Functional Theory

The energy density functional (EDF) approach to nuclear structure is based on mapping the original many-body problem of A interacting particles into an effective one-body problem that is computationally tractable [15]. In practice, it implies defining a reference state, or vacuum, $|\Phi\rangle$ which has a well-defined mathematical form. For example, in applications of the EDF approach in electronic structure theory, $|\Phi\rangle$ is a Slater determinant of single particle wave functions. In nuclear physics, $|\Phi\rangle$ is most often taken as a Bogoliubov vacuum of the kind

$$|\Phi(\mathbf{g})\rangle = \prod_{\mu} \beta_{\mu}^{(\mathbf{g})} |-\rangle, \quad (1)$$

where $|-\rangle$ is the particle vacuum and the β_{μ} are quasiparticle annihilation operators. The latter are related to the particle operators via the Bogoliubov transformation

$$\beta_{\mu}^{(\mathbf{g})} = \sum_i U_{i\mu}^{(\mathbf{g})*} c_i + \sum_i V_{i\mu}^{(\mathbf{g})*} c_i^{\dagger} \quad (2a)$$

$$\beta_{\mu}^{(\mathbf{g})\dagger} = \sum_i V_{i\mu}^{(\mathbf{g})} c_i + \sum_i U_{i\mu}^{(\mathbf{g})} c_i^{\dagger}. \quad (2b)$$

In the single-reference version of the EDF approach, the energy is taken as a functional $\mathcal{E} \equiv \mathcal{E}[\rho^{(\mathbf{g})}, \kappa^{(\mathbf{g})}, \kappa^{(\mathbf{g})*}]$ of the one-body density matrix $\rho^{(\mathbf{g})}$ and anomalous density $\kappa^{(\mathbf{g})}$, which are given by

$$\rho_{ij}^{\mathbf{g}} \equiv \frac{\langle \Phi(\mathbf{g}) | c_j^{\dagger} c_i | \Phi(\mathbf{g}) \rangle}{\langle \Phi(\mathbf{g}) | \Phi(\mathbf{g}) \rangle} \quad \kappa_{ij}^{\mathbf{g}} \equiv \frac{\langle \Phi(\mathbf{g}) | c_j c_i | \Phi(\mathbf{g}) \rangle}{\langle \Phi(\mathbf{g}) | \Phi(\mathbf{g}) \rangle} \quad \kappa_{ij}^{\mathbf{g}*} \equiv \frac{\langle \Phi(\mathbf{g}) | c_i^{\dagger} c_j^{\dagger} | \Phi(\mathbf{g}) \rangle}{\langle \Phi(\mathbf{g}) | \Phi(\mathbf{g}) \rangle}. \quad (3)$$

The coefficients $U^{(\mathbf{g})}$ and $V^{(\mathbf{g})}$ of the Bogoliubov transformations are variational parameters. The minimization of the energy with respect to them gives rise to the Hartree-Fock-Bogoliubov (HFB) equation. Solving it determines the actual densities $\rho^{(\mathbf{g})}$ and $\kappa^{(\mathbf{g})}$ of the system.

In all these expressions, the label $\mathbf{g} \equiv |g|e^{i\varphi_{\mathbf{g}}}$ refers to the fact that densities are allowed to spontaneously break the symmetries of the nuclear Hamiltonian. Examples of such symmetry breaking are the particle number, which explains pairing correlations, and rotational invariance, which implies that the nucleus can be deformed (in the intrinsic frame of reference).

The mathematical form of the energy functional \mathcal{E} is dictated by physics arguments. It is customary to break the energy functional into a part that only

depends on $\rho^{(g)}$ (the particle-hole channel) and another one that also depends on $\kappa^{(g)}$ (the particle-particle channel). Standard examples of functionals in the p.h. channel are the Skyrme and Gogny functionals; in the pairing channel, energy functionals are often derived from simple density-dependent, zero-range two-body potentials.

The nuclear EDF approach can be extended to describe systems at finite temperature. At $T > 0$, a quantum-mechanical system is not described by some ket $|\Phi\rangle$ but by a density operator $\hat{D} = e^{\beta\hat{H}}/Z$ where \hat{H} is the exact Hamiltonian of the system, $Z = \text{Tre}^{-\beta\hat{H}}$ the partition function and $\beta = 1/kT$. Determining the density operator is a formidable task; in practice, the HFB approximation consists in replacing it with a specific, quadratic form of creation and annihilation operators, $\hat{H} \rightarrow \hat{K}$. Using the statistical Wick theorem, it is then possible to show that there is a one-to-one correspondence between the generalized density of the HFB theory and the operator \hat{K} ; we refer to [15, 16] for details about the formalism. In practice, solving the finite-temperature HFB equation only requires modifying the expression for the one-body density matrix and anomalous density according to

$$\rho_{kl} = \left(V^*(1-f)V^T \right)_{kl} + \left(UfU^\dagger \right)_{kl} \quad (4a)$$

$$\kappa_{kl} = \left(V^*(1-f)U^T \right)_{kl} + \left(UfV^\dagger \right)_{kl}, \quad (4b)$$

where $f_\mu = 1/(1 + e^{\beta E_\mu})$ is the Fermi-Dirac statistical occupation of the quasiparticle with energy E_μ .

3 Large-Amplitude Collective Motion

The description of nuclear fission within the nuclear EDF approach often begins with the introduction of collective variables q_μ that are supposed to drive the fission process.¹ Following the intuition of Meitner, Bohr, etc., we view fission as an extreme deformation process: the collective variables are thus the parameters that characterize the nuclear shape. In the EDF picture, these are typically the expectation value on the reference state (1) of suitable operators such as, e.g., the mass multipole moments. By solving the HFB equation under constraints on the expectation value of such operators, one can construct a potential energy surface (PES) which shows how the energy of the nucleus changes as a function of the collective variables \mathbf{q} . An example of such a PES for ^{236}U is shown in Fig. 1.

¹This is in fact not necessary in the time-dependent DFT approach to fission, where all degrees of freedom encapsulated in the (now time-dependent) generalized density are treated on the same footing [17–19].

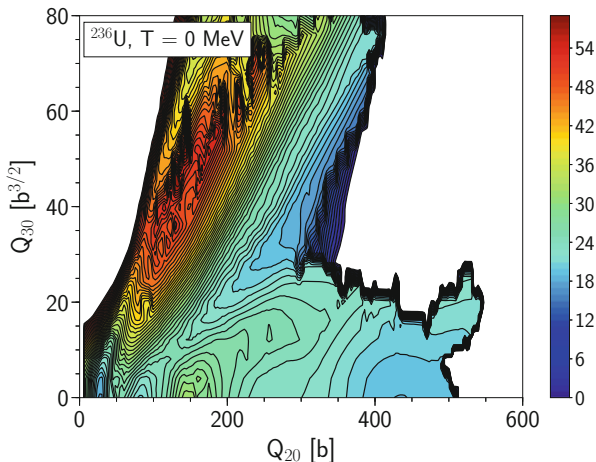


Fig. 1 Potential energy surface of ^{236}U for the SkM* Skyrme functional as a function of the axial quadrupole and octupole moments. Technical details of the calculations are identical to those in [20]

The PES encodes a lot of information about the fission process. In particular, it is possible to identify regions of the PES at large elongation that correspond to nuclear configurations where the two fragments have split.² It is often possible, although not always easy, to partition the collective space in two regions separated by a scission line (in 2D collective spaces) or hypersurface (in N-D spaces). Along the scission line, the nucleus is extremely deformed and it is possible to identify prefragments separated by a thin neck. The actual shape of the nucleus, hence the characteristics of the prefragments (charge and mass in particular), is different at each point along the scission line. Therefore, a PES encodes a large number of possible fragmentations and could, in principle, allow the determination of fission fragment properties. However, it says nothing of the probability to populate any particular configuration.

The time-dependent generator coordinate method (TDGCM) provides a rigorous method to compute such a probability [7, 8, 10, 23, 24]. Given a set of coordinate variables and a set of generator states (typically HFB solutions) $|\Phi(\mathbf{q})\rangle$, we assume that the many-body wave function of the fissioning nucleus reads

$$|\Psi\rangle(t) = \int d^N \mathbf{q} f(\mathbf{q}, t) |\Phi(\mathbf{q})\rangle, \quad (5)$$

where $f(\mathbf{q}, t)$ are unknown, time-dependent weight functions. Inserting this ansatz into the time-dependent, many-body Schrödinger equation yields the famous Hill-

²The very concept of scission configuration is in fact one of the major limitations of the static EDF treatment of fission as discussed extensively in [1, 20–22].

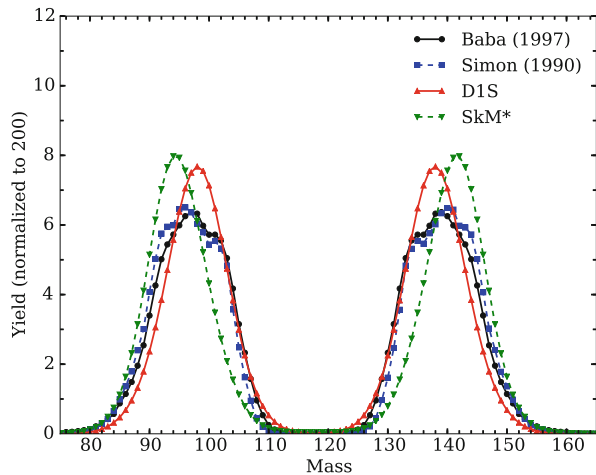
Wheeler (HW) equation. The HW equation is an integral equation that is not solvable analytically. The Gaussian overlap approximation (GOA) allows converting it into a collective, Schrödinger-like equation for a function $g(\mathbf{q}, t)$ that plays the role of the probability amplitude,

$$i\hbar \frac{\partial g(\mathbf{q}, t)}{\partial t} = \left[-\frac{\hbar^2}{2} \sum_{ij} \frac{\partial}{\partial q_i} B_{ij}(\mathbf{q}) \frac{\partial}{\partial q_j} + V(\mathbf{q}) \right] g(\mathbf{q}, t), \quad (6)$$

where $B \equiv B_{ij}(\mathbf{q})$ is the collective inertia tensor, and $V(\mathbf{q})$ the collective potential. The latter contains zero-point energy corrections [12]. We refer to [1] for additional discussion about the calculation of the collective inertia. From the solution of (6), we can extract the flux of probability through the scission line, which allows to compute charge or mass distributions [9]. An example of such a calculation for the primary fragment mass distribution of ^{236}U is shown in Fig. 2. Quantitatively, calculations based on non-relativistic [9, 11] or covariant energy density functionals [13] can reproduce the main features of the fragment charge and mass distributions to within 25% at best. However, subtle qualitative effects such as the very rapid structural change of the mass distributions in Fermium isotopes can also be predicted rather well [25].

Solving (6) requires setting an initial energy E_0 for the collective wave packet. This energy is conserved throughout the time evolution and can be related to the energy of the compound nucleus in neutron-induced fission. By varying E_0 , one can in principle calculate the evolution of fission fragment mass distributions as a function of excitation energy [26]. However, doing so does not incorporate the effect of the excitation energy on the potential energy.

Fig. 2 Primary fission fragment mass distributions for $^{235}\text{U}(n, f)$ for thermal fission. Calculations were performed with the code FELIX [12] based on a set of two potential energy surfaces, one with the Skyrme SkM* parametrization, the other with the D1S parametrization of the Gogny force; see [10] for additional technical details



4 Open Problems

It is straightforward to solve the finite-temperature HFB equation and compute a PES at finite temperature. This provides an appealing template to describe fission at increasing excitation energies. However, several problems appear in such an approach. First, the connection between the experimental value of the excitation energy and the actual value of the temperature T that one must set to solve the finite-temperature HFB equation is ill-defined. This problem was first discussed qualitatively in [20]. Following several studies [27, 28] that showed that fission is an example of over-damped collective motion, it has been argued in [28] that the collective motion is entropy-driven and that the effective potential energy surface should be $F(\mathbf{q}) = E_{\text{int}}(\mathbf{q}, T) - T(\mathbf{q})S(\mathbf{q})$ with the deformation-dependent temperature adjusted so that the intrinsic energy matches the experimental value. The resulting potential energy curve is shown on the right-hand side of Fig. 3 and compared with the “traditional” free energy curve at constant temperature in the left-hand side. The fact that, in the entropy-driven scenario, the fission barriers tend to increase as the excitation energy increases does not seem to be consistent with experimental evidence that fission fragment distributions become symmetric as excitation energy increases.

Another problem of the finite-temperature approach is the fact that the ansatz (5) breaks down at $T > 0$. This is simply a consequence of the fact that a quantum many-body system at $T > 0$ is not described by a single ket $|\Psi\rangle$, but by a density operator associated with a given statistical ensemble. Extending the framework of the generator coordinate method (GCM) (or TDGCM) to such statistical ensembles has been attempted in [29] and leads to coupled equations of motion. To the best of our knowledge, the conclusions of this isolated work have never been tested in an actual implementation.

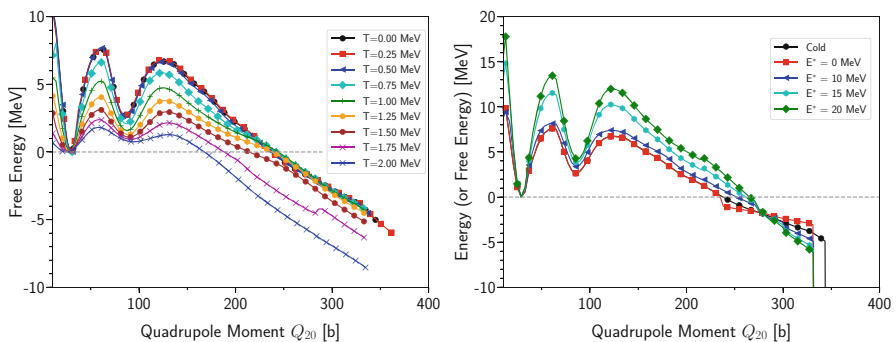


Fig. 3 Left: Free energy as a function of the axial quadrupole moment for different values of the nuclear temperature T for $^{239}\text{Pu}(n,f)$; see [20] for technical details. Right: Entropy-driven potential energy surface for the same nucleus; see text for details

One may adopt a pragmatic approach and assume that one could simply retain the TDGCM collective equation (6) and simply adapt its two main ingredients, the collective inertia and potential.³ In this case, one could choose the collective potential to be the free energy $F(\mathbf{q}; T)$. The calculation of the collective inertia is a little more problematic. It is possible to extract a formula by following the reasoning employed in the adiabatic time-dependent HFB theory—only by starting the derivations not from the time-dependent HFB equation but from the Liouville equation for the density operator. In this case, one can show that the collective mass tensor $\mathbf{M} \equiv \mathbf{B}^{-1}$ becomes

$$\mathbf{M} = 2\hbar^2[\mathbf{M}^{(1)}]^{-1}\mathbf{M}^{(3)}[\mathbf{M}^{(1)}]^{-1}$$

with the energy moments $\mathbf{M}^{(K)}$ given by

$$M_{ab}^{(K)} = \sum_{\mu < \nu} \left(F_{a,\mu\nu}^{11*} \frac{f_\nu - f_\mu}{(E_\nu - E_\mu)^K} F_{b,\mu\nu}^{11} + F_{a,\mu\nu}^{12*} \frac{1 - f_\mu - f_\nu}{(E_\mu + E_\nu)^K} F_{b,\mu\nu}^{12} \right. \\ \left. + F_{a,\mu\nu}^{21*} \frac{1 - f_\mu - f_\nu}{(E_\mu + E_\nu)^K} F_{b,\mu\nu}^{21} + F_{a,\mu\nu}^{22*} \frac{f_\nu - f_\mu}{(E_\nu - E_\mu)^K} F_{b,\mu\nu}^{22} \right),$$

where $f_\mu = 1/(1 + \exp \beta E_\mu)$ is the Fermi-Dirac occupation of the quasiparticle μ . To avoid singularities at quasiparticle crossings, we add a regulator

$$\frac{1}{x^K} \rightarrow R_K(x) = \left\{ \frac{1}{x^{Kn}} \left(1 - e^{-\left(\frac{x}{\Lambda}\right)^{Kn}} \right) \right\}^{\frac{1}{n}}$$

which, by construction, converges to $1/\Lambda^K$ for $x \rightarrow 0$ and to $1/x^K$ for $x \rightarrow +\infty$. For $n = 2$ and $\Lambda = 0.2$, the cut-off region is such that $|E_\mu - E_\nu| \leq 0.16$ MeV for the moment of order $K = 3$. Figure 4 shows the impact of different ranges Λ ($n = 2$) for the collective mass along the least-energy path in ^{240}Pu . While the regulator fulfills its role of filtering out non-physical values of the inertia, we emphasize that it is merely a patch that reflects the breakdown of the theory at quasiparticle crossings. Such a trick was employed in [30, 31].

5 Conclusions

We have briefly reviewed the state of the art in predicting fission fragment distributions with a quantum theory of large-amplitude collective motion coupled with nuclear density functional theory. Currently, existing methods seem to be

³An illustration of such a pragmatic approach is solving (6) with the ATDHFB inertia tensor instead of the GCM one.

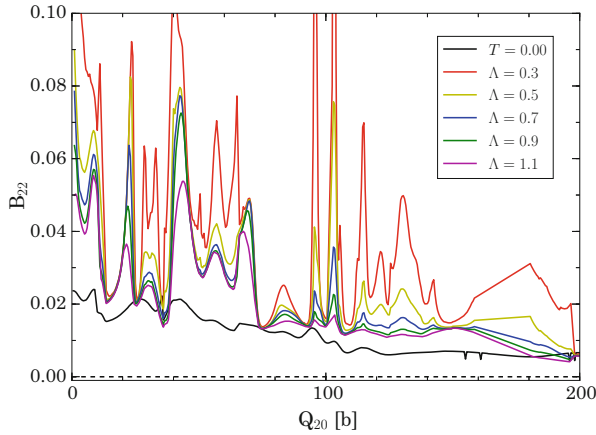


Fig. 4 Collective inertia tensor $B(q_{20})$ along the least-energy fission pathway of ^{240}Pu at $T = 0.5$ MeV for different values of the regulator; see text for details

capable of reproducing fission fragment distributions to within about 20–30% (in the best cases). Ongoing work on building more predictive energy functionals, see, e.g., [32, 33] for two recent examples; progress in removing some of the approximations in computing the collective inertia [34]; and constant increase in computing power, which could allow performing calculations in $N > 2$ collective spaces, all of this suggest that this accuracy may be substantially improved in the near future.

However, being able to predict the evolution of fission fragment distributions at higher excitation energies will most likely require work of a more fundamental nature. Because of the very high level density of states at excitation energies of 10–20 MeV, an approach based on formulating a theory of collective motion with quasiparticle excitations such as in [35] seems unpractical. In this respect, a finite-temperature approach may be more promising, but it is currently plagued by a number of uncertainties related to the definition of said temperature, the calculation of collective inertia at non-zero temperature and, more generally, the fact that all information about the system is now encoded in a density operator.

Acknowledgments Support for this work was partly provided through the U.S. Department of Energy (DOE) Office of Science Graduate Student Research (SCGSR) Program. It was partly performed under the auspices of the US Department of Energy by the Lawrence Livermore National Laboratory under Contract DE-AC52-07NA27344. Computing support for this work came from the Lawrence Livermore National Laboratory (LLNL) Institutional Computing Grand Challenge program.

References

1. N. Schunck, L.M. Robledo, Microscopic theory of nuclear fission: a review. *Rep. Prog. Phys.* **79**(11), 116301 (2016). <https://doi.org/10.1088/0034-4885/79/11/116301>
2. M. Warda, J.L. Egido, Fission half-lives of superheavy nuclei in a microscopic approach. *Phys. Rev. C* **86**(1), 014322 (2012). <https://doi.org/10.1103/PhysRevC.86.014322>
3. A. Staszczak, A. Baran, W. Nazarewicz, Spontaneous fission modes and lifetimes of super-heavy elements in the nuclear density functional theory. *Phys. Rev. C* **87**(2), 024320 (2013). <https://doi.org/10.1103/PhysRevC.87.024320>
4. J. Sadhukhan et al., Spontaneous fission lifetimes from the minimization of self-consistent collective action. *Phys. Rev. C* **88**(6), 064314 (2013). <https://doi.org/10.1103/PhysRevC.88.064314>
5. J. Zhao et al., Multidimensionally-constrained relativistic mean-field study of spontaneous fission: coupling between shape and pairing degrees of freedom. *Phys. Rev. C* **93**(4), 044315 (2016). <https://doi.org/10.1103/PhysRevC.93.044315>
6. R. Rodríguez-Guzmán, L.M. Robledo, Microscopic description of fission in odd-mass uranium and plutonium nuclei with the Gogny energy density functional. *Eur. Phys. J. A* **53**(12), 245 (2017). <https://doi.org/10.1140/epja/i2017-12444-9>
7. H. Goutte, P. Casoli, J.-F. Berger, Mass and kinetic energy distributions of fission fragments using the time dependent generator coordinate method. *Nucl. Phys. A* **734**, 217 (2004). <https://doi.org/10.1016/j.nuclphysa.2004.01.038>
8. H. Goutte et al., Microscopic approach of fission dynamics applied to fragment kinetic energy and mass distributions in ^{238}U . *Phys. Rev. C* **71**(2), 024316 (2005). <https://doi.org/10.1103/PhysRevC.71.024316>
9. D. Regnier et al., FELIX-1.0: A finite element solver for the time dependent generator coordinate method with the Gaussian overlap approximation. *Comput. Phys. Commun.* **200**, 350 (2016). <https://doi.org/10.1016/j.cpc.2015.11.013>
10. D. Regnier et al., Fission fragment charge and mass distributions in $^{239}\text{Pu}(n,f)$ in the adiabatic nuclear energy density functional theory. *Phys. Rev. C* **93**(5), 054611 (2016). <https://doi.org/10.1103/PhysRevC.93.054611>
11. A. Zdeb, A. Dobrowolski, M. Warda, Fission dynamics of Cf 252. *Phys. Rev. C* **95**(5), 054608 (2017). <https://doi.org/10.1103/PhysRevC.95.054608>
12. D. Regnier et al., FELIX-2.0: New version of the finite element solver for the time dependent generator coordinate method with the Gaussian overlap approximation. *Comput. Phys. Commun.* **225**, 180 (2018). <https://doi.org/10.1016/j.cpc.2017.12.007>
13. J. Zhao et al., Microscopic self-consistent description of induced fission dynamics: finite-temperature effects. *Phys. Rev. C* **99**(1), 014618 (2019). <https://doi.org/10.1103/PhysRevC.99.014618>
14. M.E. Gooden et al., Energy dependence of fission product yields from ^{235}U , ^{238}U and ^{239}Pu for incident neutron energies between 0.5 and 14.8 MeV. *Nucl. Data Sheets* **131**, 319 (2016). <https://doi.org/10.1016/j.nds.2015.12.006>. Special Issue on Nuclear Reaction Data
15. N. Schunck, *Energy Density Functional Methods for Atomic Nuclei*. IOP Expanding Physics (IOP Publishing, Bristol, 2019). OCLC: 1034572493
16. J.-P. Blaizot, G. Ripka. *Quantum Theory of Finite Systems* (The MIT Press, Cambridge, 1985). ISBN: 978-0262022149
17. J.W. Negele et al., Dynamics of induced fission. *Phys. Rev. C* **17**(3), 1098 (1978). <https://doi.org/10.1103/PhysRevC.17.1098>
18. C. Simenel, A.S. Umar, Formation and dynamics of fission fragments. *Phys. Rev. C* **89**(3), 031601(R) (2014). <https://doi.org/10.1103/PhysRevC.89.031601>
19. A. Bulgac et al., Induced fission of ^{240}Pu within a real-time microscopic framework. *Phys. Rev. Lett.* **116**(12), 122504 (2016). <https://doi.org/10.1103/PhysRevLett.116.122504>

20. N. Schunck, D. Duke, H. Carr, Description of induced nuclear fission with Skyrme energy functionals. II. Finite temperature effects. *Phys. Rev. C* **91**(3), 034327 (2015). <https://doi.org/10.1103/PhysRevC.91.034327>
21. W. Younes, D. Gogny, Nuclear scission and quantum localization. *Phys. Rev. Lett.* **107**(13), 132501 (2011). <https://doi.org/10.1103/PhysRevLett.107.132501>
22. N. Schunck et al., Description of induced nuclear fission with Skyrme energy functionals: Static potential energy surfaces and fission fragment properties. *Phys. Rev. C* **90**(5), 054305 (2014). <https://doi.org/10.1103/PhysRevC.90.054305>
23. J.F. Berger, Quantum dynamics of wavepackets on two-dimensional potential energy surfaces governing nuclear fission, in *Dynamics of Wave Packets in Molecular and Nuclear Physics.*, ed. by J. Broeckhove, L. Lathouwers, P. van Leuven. Lecture Notes in Physics, vol. 256 (Springer, Berlin, 1986), p. 21
24. J.F. Berger, M. Girod, D. Gogny, Time-dependent quantum collective dynamics applied to nuclear fission. *Comput. Phys. Commun.* **63**(1), 365 (1991)
25. D. Regnier, N. Dubray, N. Schunck, From asymmetric to symmetric fission in the fermium isotopes within the time-dependent generator-coordinate- method formalism. *Phys. Rev. C* **99**(2), 024611 (2019). <https://doi.org/10.1103/PhysRevC.99.024611>
26. W. Younes, D. Gogny, Fragment yields calculated in a time-dependent microscopic theory of fission. Tech. rep. LLNL-TR-586678. Lawrence Livermore National Laboratory (LLNL), Livermore, CA, 2012
27. Y. Tanimura, D. Lacroix, G. Scamps, Collective aspects deduced from time-dependent microscopic mean-field with pairing: Application to the fission process. *Phys. Rev. C* **92**(3), 034601 (2015). <https://doi.org/10.1103/PhysRevC.92.034601>
28. A. Bulgac et al., Fission Dynamics (2018). <http://arxiv.org/abs/1806.00694>
29. K. Dietrich, J.-J. Niez, J.-F. Berger, Microscopic transport theory of nuclear processes. *Nucl. Phys. A* **832**(3), 249 (2010). <https://doi.org/10.1016/j.nuclphysa.2009.11.004>
30. V. Martin, L.M. Robledo, Fission barriers at finite temperature: a theoretical description with the Gogny force. *Int. J. Mod. Phys. E* **18**(04), 861 (2009). <https://doi.org/10.1142/S0218301309012963>
31. Y. Zhu, J.C. Pei, Thermal fission rates with temperature dependent fission barriers. *Phys. Rev. C* **94**(2), 024329 (2016). <https://doi.org/10.1103/PhysRevC.94.024329>
32. A. Bulgac et al., Minimal nuclear energy density functional. *Phys. Rev. C* **97**(4), 044313 (2018). <https://doi.org/10.1103/PhysRevC.97.044313>
33. R. Navarro Pérez et al., Microscopically based energy density functionals for nuclei using the density matrix expansion. II. Full optimization and validation. *Phys. Rev. C* **97**(5), 054304 (2018). <https://doi.org/10.1103/PhysRevC.97.054304>
34. J. Sadhukhan et al., Pairing-induced speedup of nuclear spontaneous fission. *Phys. Rev. C* **90**(6), 061304 (2014). <https://doi.org/10.1103/PhysRevC.90.061304>
35. R. Bernard et al., Microscopic and nonadiabatic Schrödinger equation derived from the generator coordinate method based on zero- and two-quasiparticle states. *Phys. Rev. C* **84**(4), 044308 (2011). <https://doi.org/10.1103/PhysRevC.84.044308>

Microscopic Description of Fission for the r-Process in Neutron Star Mergers



J.-F. Lemaître, S. Goriely, S. Hilaire, and N. Dubray

1 Introduction

The fission process represents a key physical quantity of interest in fundamental nuclear physics as well as in many nuclear applications. In particular, it plays a key role in nucleosynthesis applications and more specifically in our understanding of the rapid neutron-capture process, or r-process, called for to explain the origin of about half of the elements heavier than iron in the Universe [1].

In the now well-documented r-process scenario of neutron star mergers, the number of free neutrons per seed nuclei can reach a few hundred [1–3]. With such a neutron richness, heavy fissioning nuclei can be produced. In this case, fission plays a fundamental role, more particularly by (1) recycling the matter during the neutron irradiation, (2) shaping the r-abundance distribution in the $110 \leq A \leq 170$ mass region at the end of the neutron irradiation, (3) defining the residual production of some specific heavy stable nuclei, more specifically Pb and Bi, but also the long-lived cosmochronometers Th and U, and (4) heating the environment through the energy released and consequently impacting the observed light curve of the astronomical event [2, 3]. For a review on the role of fission during the r-process nucleosynthesis in neutron star mergers, see Ref. [4].

More specifically, fission probabilities and fission yields are two key quantities to predict r-abundance distributions. Fission probabilities and yields for a few thousands nuclei, especially heavy exotic neutron-rich nuclei that cannot be produced in the laboratory, are needed to determine which nuclei are produced or recycled

J.-F. Lemaître (✉) · S. Goriely

Institut d’Astronomie et d’Astrophysique, Université Libre de Bruxelles, Brussels, Belgium

S. Hilaire · N. Dubray

CEA, DAM, DIF, Arpajon, France

© This is a U.S. government work and not under copyright protection in the U.S.; foreign copyright protection may apply 2021

J. Escher et al. (eds.), *Compound-Nuclear Reactions*, Springer Proceedings in Physics 254, https://doi.org/10.1007/978-3-030-58082-7_36

by fission during the neutron irradiation. Phenomenological models are not suited to determine such quantities due to the exotic nature of the nuclei involved and the low reliability of such models far away from the experimentally known region. The importance of reliable predictions is discussed in Refs. [5, 6].

Detailed fission paths, from which fission probability can be deduced, can be determined on the basis of the Hartree–Fock–Bogoliubov (HFB) model which has proven its capacity to estimate the potential energy surface (PES), hence the static fission barrier heights and widths, with a relatively high degree of accuracy [4]. In this case, the static aspect of fission is treated via the least-energy path (LEP) where from the fission barrier is deduced, while the dynamical approach can be described through the least-action path (LAP) taking into account the inertia tensor.

Fission yields of the heavy neutron-rich elements are also fundamental ingredients in r-process calculations. Microscopic approaches, like the Scission Point Yield (SPY) model [7], may predict eventually new fission modes such as the doubly asymmetric fission of the nuclei in the region of ^{278}Cf which impacts the final abundances of rare-earth elements [2]. In addition, the SPY model provides the mean number of evaporated neutrons per fissioning nucleus which may also affect the neutron flux, especially during the late neutron irradiation.

Our latest effort to improve the prediction of fission paths, spontaneous fission half-lives, and fission yields are described in the next sections.

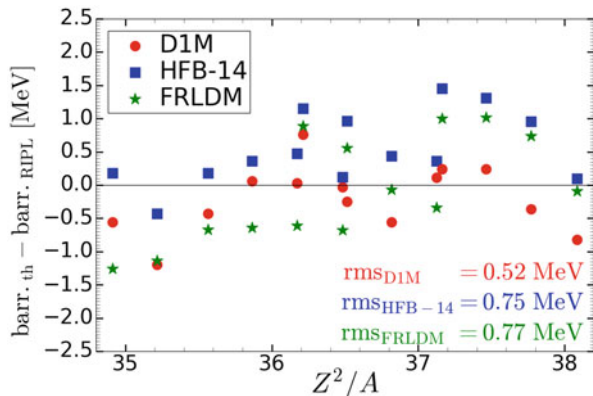
2 Potential Energy Surface and Fission Path

The PES is explored in the deformation space by imposing constraints to the standard HFB variational procedure with respect to the axial quadrupole deformation Q_{20} related to nucleus elongation and the octupole deformation Q_{30} related to the mass (or left-right) asymmetry. All calculations in the present study are performed with the Gogny DIM interaction. The final PES in the (Q_{20}, Q_{30}) plane is constructed by correcting the mean-field energy E_{HFB} for the triaxiality degree of freedom at small deformations and for the collective correlation effects beyond mean field. All details concerning the HFB calculations with the Gogny interaction including the basis expansion, convergence criteria, the variational procedure, and corrections of the mean field can be found in Ref. [8] and references therein. For the time being, only PES for even–even nuclei has been estimated.

2.1 Least-Energy Fission Path and Fission Barriers

The method used to determine the LEP of a PES is inspired from the flooding method. It is based on a comprehensive approach, proceeding by dichotomy, to determine the LEP using a binary search tree to store information about the saddle

Fig. 1 (Color online)
Comparison of DIM, Skyrme-BSk14 [9], and FRLDM [10] primary fission barrier heights with empirical values [11] as a function of the fissibility parameter Z^2/A



points and their neighboring wells. More details can be found in [8] and references therein.

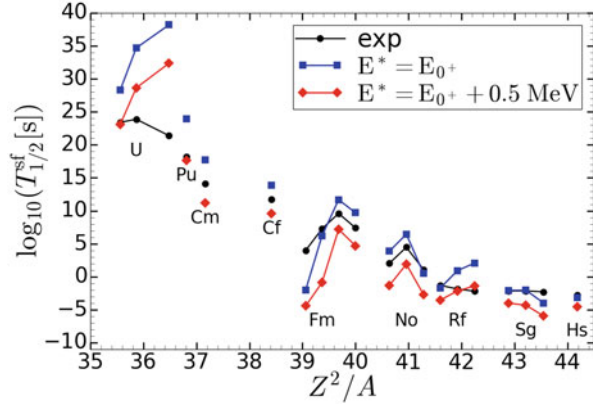
The highest (or primary) fission barrier, which is crucial for the calculation of fission probabilities, can directly be extracted from the LEP. It corresponds to the difference between the energy of the highest saddle point and the ground-state 0^+ level energy of the even–even fissioning nuclei. In Fig. 1, we compare the primary barrier height of the 14 even–even nuclei for which empirical values have been extracted from fission cross section measurements [11]. A good agreement is found with empirical data with the root-mean-square (rms) deviation of 0.52 MeV. The agreement is particularly good for ^{232}U , ^{234}U , ^{236}U , and ^{238}Pu . DIM fission barrier heights are in better agreement with the empirical values than the ones obtained with the Skyrme-HFB calculations based on the BSk14 force [9] (rms = 0.75 MeV) as well as with the finite-range liquid-drop model (FRLDM) [10] (rms = 0.77 MeV).

2.2 Least-Action Fission Path: Fission Lifetime

The Dijkstra’s algorithm [13] is used to minimize the action of the fission path. The action depends on the inertia tensor, the potential energy of the system (i.e. the PES), the total energy of the system (which depends on its excitation energy), and the trajectory of the LAP. The inner turning point is close to the ground-state well while the outer turning point is located in the high Q_{20} region of the PES. More details can be found in Ref. [8] and references therein. The spontaneous fission half-life can be obtained within the WKB formalism as

$$T_{1/2}^{\text{sf}}[\text{s}] = 2.86 \times 10^{-21} (1 + e^{2S(E^*)/\hbar}) \quad (1)$$

Fig. 2 (Color online)
Spontaneous fission half-lives $T_{1/2}^{\text{sf}}$ as a function of the fissibility parameter Z^2/A for $E^* = E_{0^+}$ (squares) and $E^* = E_{0^+} + 0.5$ MeV (diamonds). Theoretical results are compared with experimental data (dots) [12]



where S is the action along the LAP computed at an excitation energy equal to the energy of the ground-state level, since nuclei are expected to fission spontaneously from their fundamental 0^+ level.

The resulting half-lives are compared with experimental data in Fig. 2. Experimental half-lives are fairly well reproduced, though systematically overestimated. The short half-lives (typically $T_{1/2}^{\text{sf}} \lesssim 1$ y) for nuclei with $Z \gtrsim 100$ are satisfactorily estimated. It is well known that fission half-lives are extremely sensitive to the adopted zero-point energy E^* . To test this sensitivity, half-lives are also computed assuming the excitation energy of the 0^+ level has been underestimated by 0.5 MeV, i.e. $E^* = E_{0^+} + 0.5$ MeV. The corresponding predictions are shown in Fig. 2. Half-lives vary by two to three orders of magnitude for heavy nuclei and up to five orders of magnitude for U isotopes.

3 Fission Fragments and SPY Model

3.1 SPY Model

The SPY model is a static and statistical scission point model [7, 14] that assumes a thermodynamic equilibrium at scission, hence neglects the evolution between the saddle and the scission points. The model is based on two pillars, namely the absolute available energy balance at the scission configurations and the statistical description of the available phase space.

The available energy balance is performed for all energetically possible fragmentations of a fissioning system at scission as a function of the deformation of both fragments. The available energy is defined as the difference between the potential energy of the fissioning system at scission and the energy of the excited compound nucleus where both nascent fragments are supposed to be at rest. The potential energy of the fissioning system at scission is obtained as the sum of the

individual binding energies of the two fragments and the interaction energy between the fragments composed of the Coulomb repulsion and the nuclear attraction. The system at scission is treated as a microcanonical ensemble where all available states are equiprobable. In this framework, the number of available states of a given fragmentation is the product of the state densities of the two isolated fragments. The yield of a fragmentation is the number of available states associated with this fragmentation whatever the deformation of the fragments.

The new version of the SPY model, called SPY2 [14], is based on fully microscopic nuclear ingredients to describe the fragments properties at the scission point. The scission configuration of the fissioning nucleus is no more defined by two uniformly charged fragments without diffusivity separated by a scission distance, like in the original version SPY1 [7], but rather on the basis of the fragments' proton density derived from HFB proton spatial distributions. The proton density at the scission neck is used as a separation criterion for the nascent fragments which is the same whatever the fissioning system. The Coulomb repulsion is numerically computed from the HFB proton spatial distributions of the fragments. The state densities are no more described in the framework of a Fermi gas but in the framework of the statistical BCS model of nuclear state densities on the basis of the discrete single-particle level scheme obtained in the same microscopic framework as the one used to estimate individual binding and Coulomb energies, which takes pairing and shell effects coherently into account on the basis of the same nuclear structure properties.

All SPY2 inputs are computed within the same self-consistent microscopic HFB framework on the basis of the BSk27 Skyrme interaction [15].

3.2 Fission of ^{236}U , ^{240}Pu , and ^{252}Cf

We compare in Fig. 3 the experimental yield distributions of the three fissioning systems ^{236}U , ^{240}Pu , and ^{252}Cf with those predicted by SPY1 and SPY2. With SPY1 (Fig. 3a–c, blue dashed lines), the yield distribution is peaked around $A_1 = 132$ and $A_2 = A_{\text{CN}} - 132$, particularly for U and Pu. These peaked distributions can be explained by the high sensitivity to the fragments shell effect, in particular to the doubly magic nucleus $^{132}_{50}\text{Sn}_{82}$ which is associated with the soft fragment $^{104}_{42}\text{Mo}_{62}$ in the ^{236}U case. Compared to SPY1, the SPY2 yield distributions (Fig. 3a–c, green thin lines) are much wider and also in better agreement with experimental data but present strong staggering patterns. To compare the overall structure with experimental data, the yield distributions are smoothed by a normalized Gaussian function.

In the U case (Fig. 3a, red line), the symmetric part of the distribution is overestimated compared to experimental data. This is partially due to an underestimate of the highly asymmetric part of the yields distribution, which, in turn, is due to an overestimate of the kinetic energy (KE) for asymmetric fragments. A lower

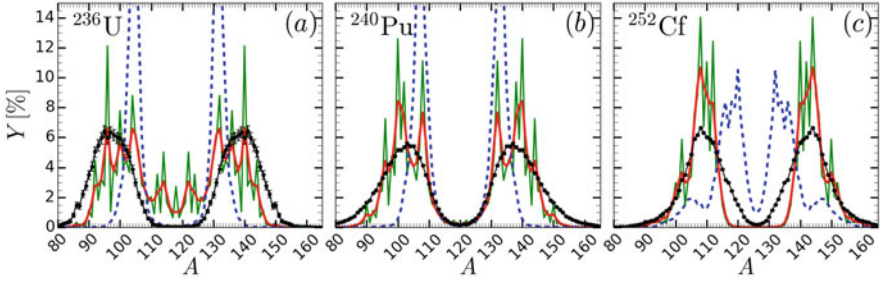


Fig. 3 (Color online) The black dotted lines represent experimental (pre-neutron-emission) fission yields for thermal neutron-induced fission of ^{235}U (a) [16], ^{239}Pu (b) [17], and the spontaneous fission of ^{252}Cf (c) [18]. The green (red) lines correspond to SPY2 raw (smoothed) fission yields and the blue dashed line to SPY1 yields

KE of these asymmetric fragments would increase their available energy, hence their number of available states. An increase of the number of available states of highly asymmetric fragmentations, for a fixed number of available states of other ones increase the probability of these asymmetric fragmentations, and consequently decrease the symmetric contribution. Pu mass distribution (Fig. 3b, red line) matches fairly well experimental data. Like in the U case, yields of the high asymmetric fragmentations are underestimated due to an overestimate of the KE of the highly asymmetric fragmentations. In the Cf case (Fig. 3c), the peak around $A = 132$ completely disappears with respect to SPY1. The slightly asymmetric yields are underestimated due to an overestimate of the peaks height, i.e. an underestimate of the KE for these slightly asymmetric fragments.

3.3 Systematic

SPY2 is now used to calculate systematically the fission yields for about 2000 heavy nuclei (Fig. 4) which allows us to study the impact of fragments shell effects on the fission mode. Using the same peak analysis as in Ref. [7], it is possible to estimate the peak multiplicity corresponding to the number of significant humps characterizing the isobaric yield distribution.

The peak multiplicity is rather sensitive to the neutron number of the compound nucleus responsible for the vertical transitions seen in Fig. 4. The fission of light nuclei $N_{\text{CN}} \leq 100$ is found to be asymmetric (2 peaks); this is consistent with the asymmetric mode of ^{180}Hg [19, 20]. The symmetric fission region (1 peak) with $100 < N_{\text{CN}} \leq 140$ is more extended with SPY2 than with SPY1 where the neutron-rich limit is obtained around $N_{\text{CN}} \approx 132$ [7]. According to experimental data [21], the transition from symmetric to asymmetric modes is located around $N_{\text{CN}} \approx 136$. The late transition predicted by the SPY2 model is responsible for the non-negligible symmetric component found for $^{236}_{92}\text{U}_{144}$, as illustrated in Fig. 3a.

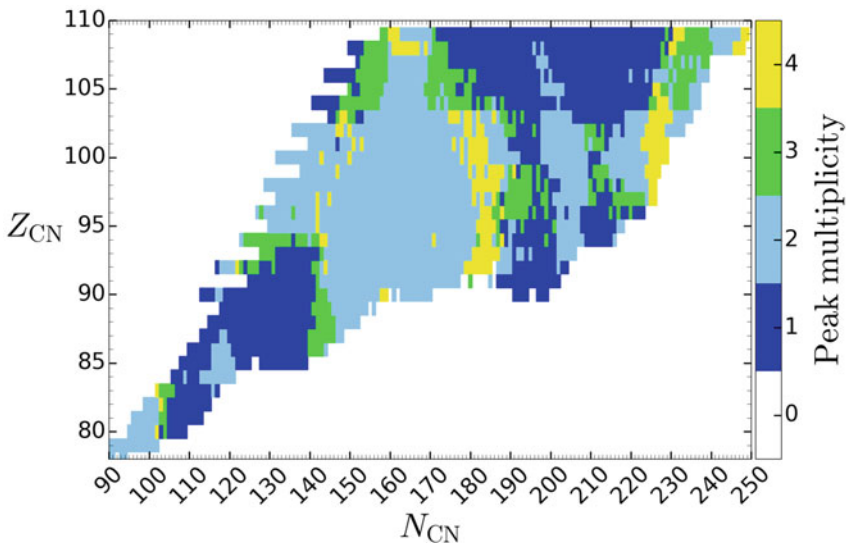


Fig. 4 (Color online) Systematics in the (N, Z) plane of the peak multiplicity in the isobaric yields for some 2000 nuclei for an initial excitation energy of $Q = 8$ MeV

The transition between symmetric to asymmetric fission and the asymmetric fission mode of some nuclei are complex problems which have been extensively studied for the last decades, especially since the discovery of the mass asymmetry feature characterizing the U fission. It remains an open problem which has been mainly studied from different aspects, in particular considering the saddle or scission points configuration of the fissioning system.

A doubly asymmetric fission (4 peaks) is still predicted (yellow region in Fig. 4). These nuclei play a key role in explaining the origin of the rare-earth elements ($A \simeq 165$) during the r-process nucleosynthesis occurring in collapsing neutron stars [2]. Our new SPY2 version of the model confirms the conclusions of Ref. [2].

4 Conclusion

LEP and LAP have been obtained for a large number of even–even nuclei using Gogny DIM PES. The fission barriers deduced from LEP are in good agreement with evaluated data. Spontaneous fission half-lives deduced from LAP fairly well reproduced experimental data, though the predictions remain very sensitive to the excitation energy of the fissioning nucleus. It is planned to extend the PES, LEP, and LAP calculations systematically to odd- A and odd-odd nuclei.

The updated version of the SPY model is based on the mean-field proton density at the scission neck and assumes that the Coulomb repulsion between nascent

fragments drives the evolution of the fissioning system between the saddle and scission points. The fission yields calculation has been significantly improved, in particular by predicting relatively wide peaks, as observed experimentally. Our systematic study of the fission mode for some 2000 heavy nuclei with $78 \leq Z \leq 110$ shows that the fission mode is mainly determined by the neutron number.

References

1. M. Arnould et al., *Phys. Rep.* **450**, 97–213 (2007)
2. S. Goriely et al., *Phys. Rev. Lett.* **111**, 242502 (2013)
3. O. Just et al., *MNRAS* **448**, 541–567 (2015)
4. S. Goriely, *Eur. Phys. J. A* **51**, 22 (2015)
5. S. Goriely, *Eur. Phys. J. A* **51**, 172 (2015)
6. S. Hilaire et al., *Eur. Phys. J. A* **52**, 336 (2016)
7. J.F. Lemaître et al., *Phys. Rev. C* **92**, 034617 (2015)
8. J.F. Lemaître et al., *Phys. Rev. C* **98**, 024623 (2018)
9. S. Goriely et al., *Phys. Rev. C* **75**, 064312 (2007)
10. P. Möller et al., *Phys. Rev. C* **79**, 064304 (2009)
11. R. Capote et al., *Nucl. Data Sheets* **110**, 3107–3214 (2009)
12. N.E. Holden et al., *Pure Appl. Chem.* **72**, 1525–1562 (2000)
13. E.W. Dijkstra, *Numer. Math.* **1**, 269–271 (1959)
14. J.F. Lemaître et al., *Phys. Rev. C* **99**, 034612 (2019)
15. S. Goriely et al., *Phys. Rev. C* **88**, 061302 (2013)
16. C. Romano et al., *Phys. Rev. C* **81**, 014607 (2010)
17. C. Tsuchiya et al., *J. Nucl. Sci. Technol.* **37**, 941–948 (2000)
18. S. Zeynalov et al., *J. Korean Phys. Soc.* **59**, 1396–1399 (2011)
19. A.N. Andreyev et al., *Phys. Rev. Lett.* **105**, 252502 (2010)
20. S. Panebianco et al., *Phys. Rev. C* **86**, 064601 (2012)
21. K.H. Schmidt et al., *Nucl. Phys. A* **665**, 221–267 (2000)

Event-by-Event Fission Modeling with FREYA



R. Vogt, J. Randrup, J. T. Van Dyke, and L. A. Bernstein

1 Overview

Nuclear fission has made a significant impact on society even though the physical mechanisms behind the process are still not understood in detail. While great strides have been made in theoretical many-body calculations of fission, see e.g. the talks by W. Younes and N. Schunck in these proceedings, a comprehensive model of the phenomenon, including neutron and photon emission, based on these theories is still in the future. There is thus a need for more phenomenological approaches that can model complete fission events. Such codes implement a physically consistent description of fission and allow studies of correlations among fragments, neutrons, and photons with full kinematic information.

R. Vogt (✉)

Nuclear and Chemical Sciences Division, Lawrence Livermore National Laboratory, Livermore, CA, USA

Physics Department, University of California at Davis, Davis, CA, USA

e-mail: vogt2@llnl.gov

J. Randrup

Nuclear Science Division, Lawrence Berkeley National Laboratory, Berkeley, CA, USA

J. T. Van Dyke

Physics Department, University of California at Berkeley, Berkeley, CA, USA

L. A. Bernstein

Nuclear Science Division, Lawrence Berkeley National Laboratory, Berkeley, CA, USA

Nuclear Engineering Department, University of California at Berkeley, Berkeley, CA, USA

© This is a U.S. government work and not under copyright protection in the U.S.; foreign copyright protection may apply 2021

J. Escher et al. (eds.), *Compound-Nuclear Reactions*, Springer Proceedings in Physics 254, https://doi.org/10.1007/978-3-030-58082-7_37

2 Introduction to FREYA

As input, FREYA requires the mass distribution of the primary fission fragments, $Y(A)$, and the mean total kinetic energy for a given mass split, $\overline{\text{TKE}}(A)$, for the particular excitation considered. (FREYA can simulate both neutron-induced fission and spontaneous fission.)

The initial nucleus A_0 splits into light and heavy fragments, A_L and A_H , respectively. The Q -value for a particular split is $Q = M_0c^2 - M_Lc^2 - M_Hc^2$. The total fragment kinetic energy, TKE, is sampled from $\text{TKE}(A_H)$ and the total excitation energy available for rotational and statistical excitation at scission is $E_{\text{sc}}^* = Q - \overline{\text{TKE}}$. The corresponding ‘‘scission temperature’’ T_{sc} is obtained from $E_{\text{sc}}^* = a(A_0)T_{\text{sc}}^2$ where the scale of the level density parameter $a(A) = A/e_0$ is governed by $e_0 \approx 10$ MeV. This is the first adjustable parameter in FREYA.

In addition to any overall rigid rotation, which imparts mean angular momenta to the two fragments, they also acquire fluctuations around the mean values from the wriggling and bending modes. The magnitude of these spin fluctuations is governed by the ‘‘spin temperature’’ $T_S = c_S T_{\text{sc}}$ which can be adjusted through the second FREYA parameter c_S . The spin fluctuations vanish for $c_S = 0$.

After subtracting the rotational energy of the two fragments, E_{rot} , a total of $E_{\text{stat}} = E_{\text{sc}}^* - E_{\text{rot}}$ is left for statistical excitation which is distributed between the two fragments. A preliminary partition, $E_{\text{stat}} = \acute{E}_L^* + \acute{E}_H^*$, is made according to the heat capacities of the fragments, which in turn is assumed to be proportional to the level density parameters, i.e. $\acute{E}_L^* : \acute{E}_H^* = a_L : a_H$. If the shell corrections are negligible, or the available energy is large, $a_i \approx A_i/e_0$. Because the observed neutron multiplicities for known nuclei at low energies suggest that the light fragments tend to be disproportionately excited, the light fragment is given a larger excitation energy by the third parameter x , $\overline{E}_L^* = x\acute{E}_L^*$, $\overline{E}_H^* = E_{\text{stat}} - \overline{E}_L^*$, where $x > 1$.

After the mean fragment excitation energies have been assigned, FREYA considers thermal fluctuations in the statistical excitation. The mean fragment excitation is related to its temperature T_i by $\overline{E}_i^* = a_i T_i^2$ with associated variance $\sigma_{E_i^*}^2 = 2\overline{E}_i^* T_i$. An energy fluctuation δE_i^* is sampled from a truncated normal distribution of variance $2c\overline{E}_i^* T_i$ and the fragment excitations are adjusted accordingly, $E_i^* = \overline{E}_i^* + \delta E_i^*$, $i = L, H$. Energy is conserved by making a compensating opposing fluctuation in TKE, $\text{TKE} = \overline{\text{TKE}} - \delta E_L^* - \delta E_H^*$. The factor c multiplying the variance is the fourth FREYA parameter. It compensates for the truncation of the normal distribution due to energy conservation. Finally, TKE may be adjusted by the fifth and final FREYA parameter, $d\text{TKE}$, to reproduce the average neutron multiplicity, $\overline{\nu}$.

The neutrons are evaporated isotropically in the frame of the emitting fragment, apart from a slight flattening due to the nuclear rotation. Their energy is sampled from a black-body energy spectrum, $dN_n/dE_n \sim E_n \exp(-E_n/T_{\text{max}})$, where T_{max} is the maximum possible temperature in the daughter nucleus. FREYA generally assumes that neutron evaporation continues until the nuclear excitation energy is

below the neutron separation energy S_n , so that neutron evaporation continues as long as energetically possible.

After neutron evaporation has ceased, the excited product nucleus emits photons. First, statistical photons are emitted isotropically with an energy distribution sampled from a black-body spectrum modulated by a giant-dipole resonance form factor. When the nuclear excitation energy enters the regime of the tabulated decays from the RIPL-3 compilation [1], FREYA switches to a discrete cascade which is continued until the half-life exceeds a specified value, t_{\max} , based on the detector response time, or until the nucleus is in its ground state. The average photon energy and photon multiplicity depend on t_{\max} as well as the minimum photon energy measurable in the detectors, denoted in FREYA as g_{\min} . While the photon observables depend on both t_{\max} and g_{\min} , these quantities are not parameters but depend on specific experimental details.

3 Recent Results on Photon Emission

The detector-dependent quantities g_{\min} and t_{\max} were added to FREYA in Ref. [2] when the RIPL lines were introduced. We studied the effect of changing g_{\min} on the calculated average E_γ and M_γ . If g_{\min} is on the order of a few hundred keV, the total energy emitted in photons does not change much. Increasing g_{\min} to 1–2 MeV would correspondingly reduce the measured photon energy by a similar amount. There is a stronger dependence of M_γ on g_{\min} . A 1 MeV cutoff energy reduces the photon multiplicity by a factor of three or more, depending on c_S . (A larger c_S results in the emission of more soft photons. See Ref. [2] for details.)

The effects of t_{\max} on E_γ and N_γ are more subtle. Increasing t_{\max} is more likely to increase the photon multiplicity from some individual long-lived isomers but the changes are generally on the percent level [2].

We compare our calculated prompt fission photon spectrum to the results of Oberstedt et al. [3]. The measured high-energy slope of the photon energy spectrum is in good agreement with the FREYA calculation, even without including the experimental uncertainties. The peaks observed in the low-energy part of the photon spectrum, shown in Fig. 1b, arising from the inclusion of the RIPL transitions, also agree well with FREYA. The peaks in the data are somewhat above our calculation, leading to a discrepancy between our calculated multiplicity and the data using the same g_{\min} and t_{\max} . Oberstedt et al. measured $\langle M_\gamma \rangle = 8.19 \pm 0.11$, $\langle E_\gamma \rangle = 6.92 \pm 0.09$ MeV, and $\langle E_\gamma/M_\gamma \rangle = 0.85 \pm 0.02$ MeV while, for the same cutoffs, we find $\langle M_\gamma \rangle = 6.93$, $\langle E_\gamma \rangle = 6.48$ MeV, and $\langle E_\gamma/M_\gamma \rangle = 0.93$ MeV.

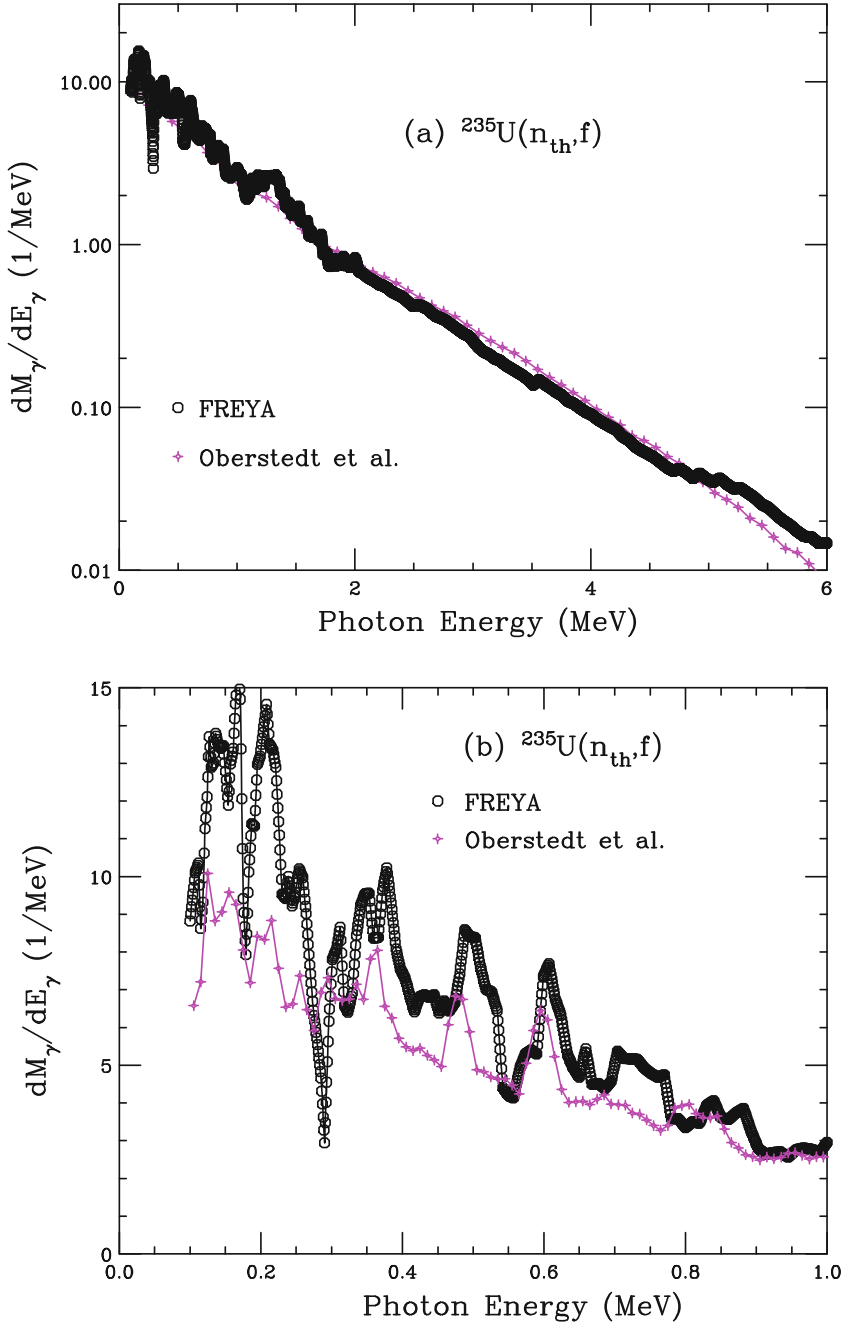


Fig. 1 (Color online) The photon energy spectrum calculated for $^{235}\text{U}(n_{\text{th}}, f)$ (magenta points) compared to data from Oberstedt et al. [3] (black points). The total photon spectrum is shown in (a) while the low-energy spectrum is shown in (b)

4 Parameter Optimization for Spontaneous Fission

The five FREYA parameters, e_0 , c_S , x , c , and $dTKE$, are all physics-based and affect some observables directly without having any significant effect on others. For example, c_S , the parameter related to spin fluctuations, controls the photon energy and multiplicity but has a negligible effect on the neutron observables. (The only effect of c_S on neutron emission comes from the fact that it controls the division of the total excitation energy into rotational and statistical excitation. Giving more energy to rotation by a large c_S reduces the energy available for neutron emission.) The parameter x controlling the excitation energy advantage given to the light fragment has a direct effect on the neutron multiplicity as a function of fragment mass, $\nu(A)$, while, e.g. having no effect on the neutron multiplicity distribution $P(\nu)$. The parameter x is also the only parameter to have a strong effect on the neutron–neutron angular correlations, as will be discussed later. The parameter controlling the width of the thermal fluctuations, c , conversely, has a strong effect on $P(\nu)$ and its moments but no effect on $\nu(A)$. All the parameters, however, have some effect on the prompt fission neutron spectrum because all affect the energy available for neutron emission, either directly, as through c_S and $dTKE$, or indirectly, through the excitation energy sharing via x or the fluctuations controlled by c . Indeed, the only observable that is affected by e_0 is the neutron spectrum. See Refs. [2, 4] for more discussion on how the parameter choices affect observables.

A first attempt to make a global fit of the five FREYA parameters was made in Ref. [5] using a grid search method. More recently an optimization using simulated annealing was able to generally reproduce these results as well as provide variances and covariance on the parameter values [6]. Similar studies were carried out for all spontaneous fission isotopes in FREYA.

Techniques such as a brute force grid search are computationally intensive and, in order to avoid local minima, which are not the global minimum and thus not physically relevant, it is necessary to move away from simpler optimization schemes like gradient descent. Optimized parameters were determined for FREYA using the simulated annealing method [7] in Ref. [6] which injects a certain randomness into the process to allow for the procedure to occasionally jump in a seemingly “worse” direction in order to move out of a potential local minimum and eventually find the global solution. The general flow of such an algorithm is to first generate a random solution, calculate its cost using some objective function, generate a random neighboring solution, calculate the cost of this new solution with the same objective function, and then compare these costs using an acceptance probability function. This acceptance probability is calculated by comparing the difference of the two costs with the so-called temperature. This is a parameter which is initially equal to unity and is decreased to a new value, T' , after each iteration of the algorithm employing a scale factor α , generally between 0.8 and 1, allowing the algorithm to become less stochastic as the number of iterations is increased. This procedure helps prevent the algorithm from sinking into a local minimum. In the FREYA

Table 1 Results of the optimization for all spontaneously fissioning isotopes which are modeled by FREYA. The best fit values of the five parameters, y , and their associated variances, σ_y , are given for each isotope. In addition, the number of data sets and evaluations used for each isotope are indicated. The evaluations of Ref. [8], available for all isotopes, provide multiple observables: the neutron multiplicity distribution $P(\nu)$ and its first three moments: $\bar{\nu}$, ν_2 , and ν_3

	e_0 (MeV ⁻¹)	x	c	c_S	$dTKE$ (MeV)	# Sets
²³⁸ U(sf)						
y	10.391	1.220	0.939	0.899	-1.375	1
σ_y	±0.124	±0.005	±0.080	±0.078	±0.528	-
²³⁸ Pu(sf)						
y	10.521	1.232	1.968	0.893	-1.408	1
σ_y	±0.337	±0.049	±0.005	±0.005	±17.679	-
²⁴⁰ Pu(sf)						
y	10.750	1.307	3.176	0.908	-3.219	2
σ_y	±0.019	±0.005	±0.126	±8.374 × 10 ⁻⁵	±0.015	-
²⁴² Pu(sf)						
y	10.018	1.144	3.422	0.911	-1.662	3
σ_y	±3.238	±0.0232	±0.116	±0.066	±0.014	-
²⁴⁴ Cm(sf)						
y	10.488	1.239	1.391	0.906	-4.494	3
σ_y	±2.306	±0.022	±0.339	±0.104	±0.028	-
²⁵² Cf(sf)						
y	10.429	1.274	1.191	0.875	0.525	6
σ_y	±1.189	±0.035	±0.131	±0.040	±1.918 × 10 ⁻⁶	-

optimization, the solutions are values of the 5 parameters and the objective function is the χ^2 uncertainty.

The results for all isotopes undergoing spontaneous fission in FREYA are given in Table 1. Note that in some cases only a single data set or evaluation is available for optimization. In general, however, the single set is an evaluation of the neutron multiplicity distribution and its first three moments, providing multiple observables. However, these observables are directly associated with the parameter c , affecting the width of $P(\nu)$, and indirectly to $dTKE$ through the value of the neutron multiplicity $\bar{\nu}$.

Some general trends can be observed in the results. The asymptotic value of the level density parameter e_0 , the excitation energy sharing parameter x , and the scale factor of the scission temperature setting the photon energy and multiplicity c_S all are equivalent within the uncertainties with $\langle e_0 \rangle \sim 10.2/\text{MeV}$, $\langle x \rangle \sim 1.2$, and $\langle c_S \rangle \sim 0.89$, respectively. Thus these quantities are rather isotope independent. One might expect that e_0 , regulating the temperature of the fragment, as well as the spontaneously fissioning nucleus itself, for neutron emission has a universal value since it is related to the asymptotic level density parameter. However, it is the least constrained of all the parameters because no observables are directly sensitive to e_0 except the prompt fission neutron spectrum and it is sensitive to all five parameters.

The parameters c and $dTKE$ are strongly isotope dependent. In some cases, where c is large, the neutron multiplicity is close to 2 and FREYA would produce a rather narrow $P(\nu)$ without increasing c . Interestingly, the multiplicity distribution for $^{238}\text{U}(\text{sf})$ is so narrow that it forces $c < 1$ in this case. The values of $dTKE$ are strongly correlated with c (positive correlation) as well as e_0 and c_S (negative correlation) because these parameters are more directly related to $\bar{\nu}$ than x is since changing x can change $\nu(A)$ while keeping $\bar{\nu}$ fixed. See Ref. [6] for more details and for comparison to data. This study is being followed by parameter optimization for neutron-induced fission.

Acknowledgments The work of R.V. was performed under the auspices of the U.S. Department of Energy by Lawrence Livermore National Laboratory under Contract DE-AC52-07NA27344. The work of J.R. and L.A.B. was performed under the auspices of the U.S. Department of Energy by Lawrence Berkeley National Laboratory under Contract DE-AC02-05CH11231. This work was supported by the Office of Defense Nuclear Nonproliferation Research & Development (DNN R&D), National Nuclear Security Administration, U.S. Department of Energy.

References

1. R. Capote et al., RIPL – reference input parameter library for calculations of nuclear reactions and nuclear data evaluations. Nucl. Data Sheets **110**, 3107 (2009)
2. R. Vogt, J. Randrup, Improved modeling of photon observables with FREYA. Phys. Rev. C **96**, 064620 (2017)
3. A. Obersted, et al.: Improved values for the characteristics of prompt-fission γ -ray spectra from the reaction $^{235}\text{U}(n_{\text{th}},f)$, Phys. Rev. C **87**, 051602(R) (2013)
4. R. Vogt, J. Randrup, Neutron angular correlations in spontaneous and neutron-induced fission. Phys. Rev. C **90**, 064623 (2014)
5. R. Vogt, A. Nicholson, J. Randrup, I. Gauld, S. Croft, Uncertainty quantification with the event-by-event fission model FREYA, in *Proceedings 1st ANS Advances in Nuc. Nonpro. Tech. and Policy, Santa Fe, NM* (2016). Technical Report: LLNL-CONF-690741
6. J. Van Dyke, L.A. Bernstein, R. Vogt, Parameter optimization and uncertainty analysis of FREYA for spontaneous fission (2018). arXiv:1809.05587
7. S. Kirkpatrick, C.D. Gelatt, M.P. Vecchi, Optimization by simulated annealing. Science **220**, 4598 (1983)
8. P. Santi, M. Miller, Reevaluation of prompt neutron emission multiplicity distributions for spontaneous fission. Nucl. Sci. Eng. **160**, 190 (2008)

Capabilities of the NIFFTE FissionTPC



R. J. Casperson

1 Introduction

Accurate neutron-induced fission cross section measurements are crucial for nuclear reactor design and stockpile stewardship. Future nuclear reactors may use fast neutrons, which would require higher precision measurements at higher incident neutron energies [1–3]. Fission cross section measurements are often performed in ratio, with ^{238}U or ^{235}U used as a reference reaction, and many of these past measurements were performed with parallel-plate ionization chambers [4]. The stacks of actinide foils are spaced close together to emphasize the large specific ionization of fission fragments relative to α particles from the decay of the target material.

Twin Frisch-grid ionization chambers [5, 6] go beyond conventional ionization chambers, using multiple signals to enable a determination of the charged-particle track angle. The detected angle contains information about the amount of actinide target material traversed, and can be included in the estimation of fission fragment detection efficiency.

The fission Time Projection Chamber (fissionTPC) was designed for full three-dimensional charge cloud reconstruction by the NIFFTE (Neutron-Induced Fission Fragment Tracking Experiment) Collaboration, applying technologies that have been used since the 1970s for high-energy physics to low-energy nuclear physics challenges. The fissionTPC has a two volume drift chamber with MICROMEAS of 2 mm pitch, typically operated with a blend of argon and isobutane [7]. Tracking algorithms allow for vertexing of the charge cloud, providing a mass distribution for actinide target, as well as angle and energy information of detected particles.

R. J. Casperson for the NIFFTE Collaboration (✉)
Lawrence Livermore National Laboratory, Livermore, CA, USA
e-mail: casperson1@llnl.gov

© This is a U.S. government work and not under copyright protection in the U.S.; foreign copyright protection may apply 2021
J. Escher et al. (eds.), *Compound-Nuclear Reactions*, Springer Proceedings in Physics 254, https://doi.org/10.1007/978-3-030-58082-7_38

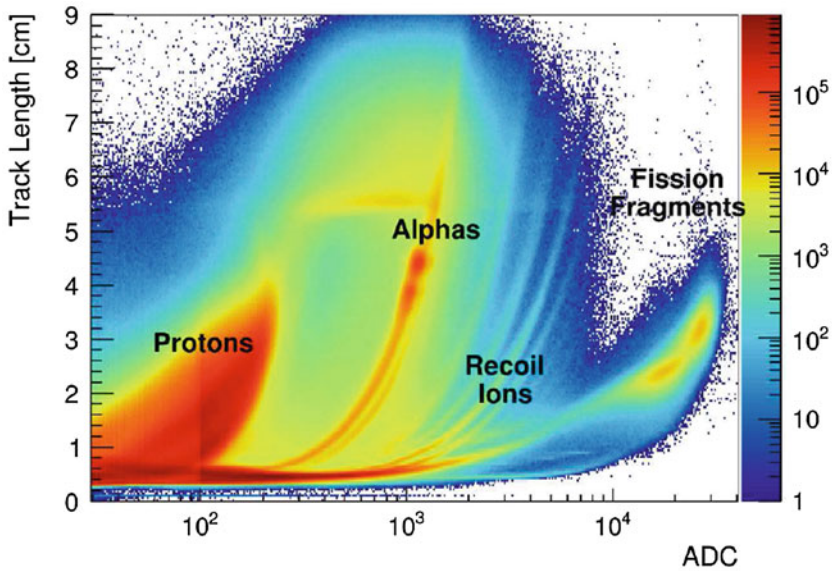


Fig. 1 Joint length and energy distribution adapted from [8]. Various particle types have been labeled. ADC is the integrated signal strength and is proportional to the particle energy

A measurement of the normalized cross section ratio of $^{238}\text{U}/^{235}\text{U}$ was recently measured by the NIFFTE Collaboration [8], using angle and energy information for sophisticated efficiency modeling, and position information to identify the source of detected fission fragments from side-by-side actinide deposits. The particle identification used was relatively simple, and an energy cut alone was applied to select fission fragments. The joint distribution of length and energy can be seen in Fig. 1, where ADC is the integrated signal strength and is proportional to the particle energy. A wealth of additional information is available in the three-dimensional charge cloud data, and the following sections describe how this information can be used.

2 Stopping Power Model

Reconstructed tracks from the fissionTPC have start and end vertices that define the track direction. The cloud of charge recorded by the detector can be projected along this axis to define a one-dimensional distribution of ionization density. This distribution can then be fit with a stopping power model to determine the atomic number and atomic mass of the detected particle. A phenomenological global function was defined that describes a wide range of stopping powers for argon +

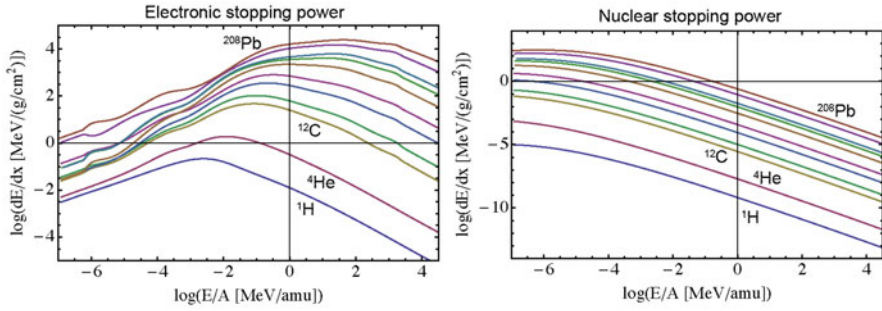


Fig. 2 Electronic and nuclear stopping power of argon + 5% isobutane calculated using SRIM [9]

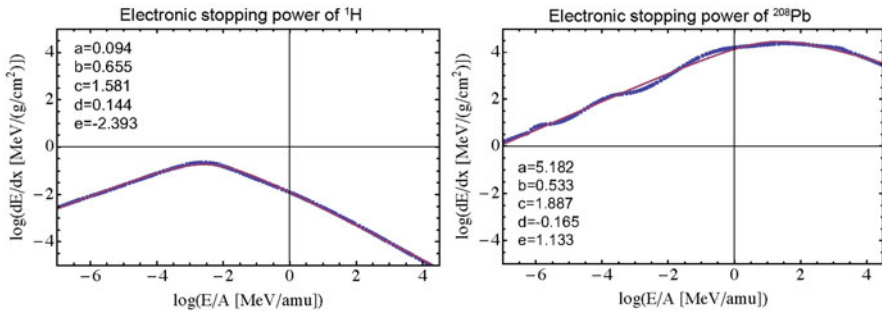


Fig. 3 Fits to ^1H and ^{208}Pb SRIM stopping powers using five-term function

5% isobutane calculated in SRIM [9], where the input data for the fit can be seen in Fig. 2.

The local electronic stopping power fit function for a single particle has the form $f(x) = a - b\sqrt{c + (x - e)^2} + d(x - e)$, which has five free parameters and describes the logarithm of the stopping power vs. the logarithm of the particle energy per amu. Fits to ^1H and ^{208}Pb can be seen in Fig. 3, which have very different parameters, but both describe the stopping power function to $\sim 5\%$ accuracy. The shell effects visible at low energy for ^{208}Pb are smoothed over in the fit, and the oscillations deviate from the fit by up to 15%, but this should not impact the interpretation of fissionTPC data.

With acceptable local fits to SRIM electronic stopping powers, a global fit can be generated by expanding each term into a series of logarithmic powers of the atomic number, where x is $\log(E/A)$:

$$\log\left(\frac{dE_e}{dx}\right) = (a_0 + a_1 \log Z + a_2 \log^2 Z + a_3 \log^3 Z) - b_0 \sqrt{(c_0 + c_1 Z) + (x - (e_0 + e_1 \log Z + e_2 \log^2 Z + e_3 \log^3 Z))^2} + x(d_0 + d_1 \log Z + d_2 \log^2 Z) \tag{1}$$

The nuclear recoil contribution to stopping power is important for slower-moving particles, and can be described with a simpler function:

$$\log\left(\frac{dE_n}{dx}\right) = (a_0 + a_1 \log Z) + x(b_0 + b_1 \log Z) + x^2(c_0 + c_1 \log Z) + x^3(d_0 + d_1 \log Z) \quad (2)$$

The combined stopping power has 24 parameters and is fit to the data shown in Fig. 2. The results shown in the following section use a fit that is only applicable to argon + 5% isobutane, but the same functional form is expected to apply to other materials as well. Future fissionTPC measurements with ratios involving recoils of hydrogen isotopes (e.g. ${}^6\text{Li}(n,t)$ or ${}^1\text{H}(n,el)$) will likely use an alternative gas such as Ar+CO₂, in order to avoid background recoils from hydrogen in the isobutane.

3 Ionization Profile Results

The fit functions defined in Eqs. 1 and 2 contain the atomic mass A and atomic number Z , and these quantities can be fit for each track recorded with the fissionTPC. Figure 4 shows the distribution of A , Z , and energy for in-beam data from ${}^{235}\text{U}$ and ${}^{239}\text{Pu}$ targets. ADC again refers to the integrated track signal, and is proportional to energy.

The upper two plots show the heavy and light fragment distributions from fission, but the two distributions appear to be skewed relative to one another. One possibility is that the SRIM stopping powers for fission fragments have systematic errors. Past work on ${}^{252}\text{Cf}$ fission fragments traveling through a mylar foil found the SRIM stopping power to be $\sim 15\%$ low for light fragments and $\sim 25\%$ low for heavy fragments, making this interpretation likely [10]. Another possibility is that the digital threshold for recording points of charge in the fissionTPC requires a stopping power dependent correction. The diagonal line of events at $Z=20$ and $A=40$ represents argon recoils, and should be a localized point. This indicates that the determination of Z and A is energy dependent and will require some correction.

Comparisons of SRIM stopping powers to experiment can guide corrections to the stopping power model (e.g. a linear correction as a function of mass or energy), but calibrations using the fissionTPC data itself will be important for validating such a model. Argon and carbon recoils are straightforward examples for an argon isobutane drift gas, but the addition of krypton or xenon to the gas would be useful calibrations for light and heavy fragments, respectively. Measuring ${}^{252}\text{Cf}(sf)$ could be a useful validation for the distribution as a whole.

The lower two plots in Fig. 4 show fits to the lower-energy distribution of events. The α particles are clearly localized, although not precisely at $Z=2$ and $A=4$, and the proton distribution is distorted. The halo of events surrounding the α -peak is most likely due to pile-up and fragmentation of tracks from the high decay-rate of

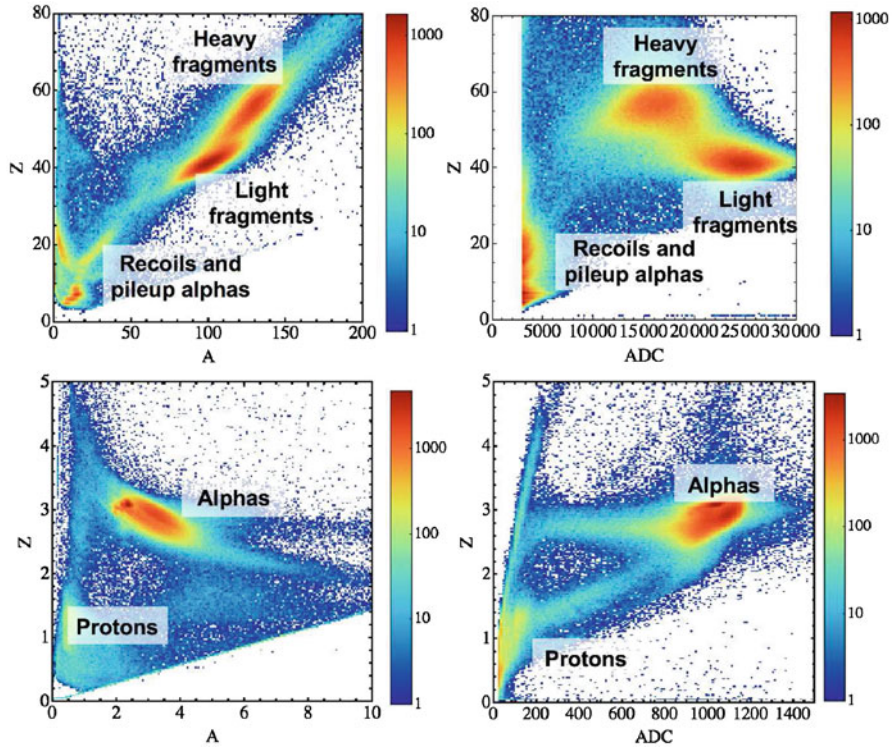


Fig. 4 Fits to combined ^{235}U and ^{239}Pu in-beam data, for two different energy ranges

the ^{239}Pu target. The ionization density of the recorded protons is very low, which indicates that attempts to distinguish hydrogen isotopes will require larger signals, and therefore higher MICROMEGAS gain.

4 Discussion

Applying particle identification algorithms to the ionization profiles of fissionTPC data is the logical next step in future experiments, and would leverage one of the strengths of time projection chambers. The stopping power distributions in Fig. 2 showed that there are a small number of distinct features in the stopping power of a given particle. Fitting with a full stopping power model is one approach, but other parameterizations could include initial charge density, maximum charge density, and relative position of the maximum charge density. Future work will consider the most effective approach to fitting the ionization profiles.

A few new types of experiments become accessible with true particle identification. Fitting prompt fission product yield distributions would be useful, but requires

a better understanding of the stopping power bias, and would benefit from a few calibration experiments (e.g. ^{252}Cf and various drift gas recoils). Light ion reactions (e.g. $n+\text{Li}$) require distinguishing hydrogen isotope recoils, as would multi-particle breakup reactions.

Acknowledgments This work is performed under the auspices of the U.S. Department of Energy by Lawrence Livermore National Laboratory under Contract DE-AC52-07NA27344. The neutron beam for this work was provided by LANSCE, which is funded by the U.S. Department of Energy and operated by Los Alamos National Security, LLC, under contract DE-AC52-06NA25396.

References

1. G. Aliberti, G. Palmiotti, M. Salvatores, T. Kim, T. Taiwo, M. Anitescu, I. Kodeli, E. Sartori, J. Bosq, J. Tommasi, *Ann. Nucl. Energy* **33**(8), 700 (2006). <https://doi.org/10.1016/j.anucene.2006.02.003>. <http://www.sciencedirect.com/science/article/pii/S0306454906000296>
2. G. Aliberti, W. Yang, R. McKnight, *Nucl. Data Sheets* **109**(12), 2745 (2008). <https://doi.org/10.1016/j.nds.2008.11.004>. <http://www.sciencedirect.com/science/article/pii/S0090375208000926>
3. M. Salvatores, G. Palmiotti, G. Aliberti, H. Hiruta, R. McKnight, P. Obložinský, W. Yang, *Nucl. Data Sheets* **109**(12), 2725 (2008). <https://doi.org/10.1016/j.nds.2008.11.001>. <http://www.sciencedirect.com/science/article/pii/S0090375208000896>
4. S.A. Wender, S. Balestrini, A. Brown, R.C. Haight, C.M. Laymon, T.M. Lee, P.W. Lisowski, W. McCorkle, R.O. Nelson, W. Parker, N.W. Hill, *Nucl. Instrum. Methods Phys. Res. A Accel. Spectrom. Detect. Assoc. Equip.* **336**(12), 226 (1993). [https://doi.org/10.1016/0168-9002\(93\)91102-S](https://doi.org/10.1016/0168-9002(93)91102-S). <http://www.sciencedirect.com/science/article/pii/016890029391102S>
5. P. Salvador-Castiñeira, T. Bryś, R. Eykens, F.J. Hamsch, A. Göök, A. Moens, S. Oberstedt, G. Sibbens, D. Vanleeuw, M. Vidali, C. Pretel, *Phys. Rev. C* **92**, 014620 (2015). <https://doi.org/10.1103/PhysRevC.92.014620>. <http://link.aps.org/doi/10.1103/PhysRevC.92.014620>
6. P. Salvador-Castiñeira, T. Bryś, R. Eykens, F.J. Hamsch, A. Göök, A. Moens, S. Oberstedt, G. Sibbens, D. Vanleeuw, M. Vidali, C. Pretel, *Phys. Rev. C* **92**, 044606 (2015). <https://doi.org/10.1103/PhysRevC.92.044606>. <http://link.aps.org/doi/10.1103/PhysRevC.92.044606>
7. M. Heffner, D. Asner, R. Baker, J. Baker, S. Barrett, C. Brune, J. Bundgaard, E. Burgett, D. Carter, M. Cunningham, et al., *Nucl. Instrum. Methods Phys. Res. A Accel. Spectrom. Detect. Assoc. Equip.* **759**, 50 (2014). <https://doi.org/10.1016/j.nima.2014.05.057>. <http://www.sciencedirect.com/science/article/pii/S0168900214005890>
8. R.J. Casperson, et al., *Phys. Rev. C* **97**, 034618 (2018). <https://doi.org/10.1103/PhysRevC.97.034618>. <https://link.aps.org/doi/10.1103/PhysRevC.97.034618>
9. J.F. Ziegler, M. Ziegler, J. Biersack, *Nucl. Instrum. Methods Phys. Res. B Beam Interactions Mater. Atoms* **268**(1112), 1818 (2010). <https://doi.org/10.1016/j.nimb.2010.02.091>. <http://www.sciencedirect.com/science/article/pii/S0168583X10001862>. 19th International Conference on Ion Beam Analysis
10. G. Knyazheva, S. Khlebnikov, E. Kozulin, T. Kuzmina, V. Lyapin, M. Mutterer, J. Perkowski, W. Trzaska, *Nucl. Instrum. Methods Phys. Res. B Beam Interactions Mater. Atoms* **248**(1), 7 (2006). <https://doi.org/10.1016/j.nimb.2006.04.071>. <http://www.sciencedirect.com/science/article/pii/S0168583X06000543>

Part X
Experimental Techniques and Facilities

Resonance Measurements at Rensselaer Polytechnic Institute



Ezekiel Blain, Devin Barry, Greg Leinweber, Michael Rapp,
and Yaron Danon

1 Introduction

The Gaertner Linear Accelerator (LINAC) Center houses a 60 MeV electron linear accelerator located at Rensselaer Polytechnic Institute (RPI). The LINAC is primarily used for cross-section measurements and provides accurate nuclear data from the thermal region up to 20 MeV. These measurements are a combination of transmission, capture, scattering, and fission measurements. The time-of-flight (ToF) technique is used to obtain the cross section as a function of the incident neutron energy. Flight paths exist at a range of detector locations from 15 m out to 250 m which can provide excellent energy resolution for a wide range of experiments. The accelerator operates at pulse widths down to 8 ns and can operate at peak currents as high as 3 A. This results in a neutron flux of approximately 4×10^{13} neutrons per second. Additionally, an upgrade is currently underway for the facility which will greatly increase the neutron flux from the facility allowing for more sophisticated measurements to be performed. An overview of some of the experimental detector systems as well as recent measurement results are as follows.

E. Blain (✉) · Y. Danon
Rensselaer Polytechnic Institute, Troy, NY, USA
e-mail: blaine2@rpi.edu

D. Barry · G. Leinweber · M. Rapp
Naval Nuclear Laboratory, Schenectady, NY, USA

© This is a U.S. government work and not under copyright protection in the U.S.; foreign copyright protection may apply 2021
J. Escher et al. (eds.), *Compound-Nuclear Reactions*, Springer Proceedings in Physics 254, https://doi.org/10.1007/978-3-030-58082-7_39

2 Transmission Measurements

Some of the most common measurements performed at the RPI LINAC facility are transmission measurements which are used to measure total cross section. These measurements involve a detector located in the neutron beam which measures the transmission through a sample material. The ratio of the counts with and without the sample can be used to determine the total cross section of the sample material. These measurements are particularly useful since the ratio method eliminates the need to know the specific detector efficiency and neutron flux since they cancel out in the calculation. There are several transmission detector setups which span a broad energy range from thermal up to 20 MeV. The detectors in the thermal to keV region all employ ^6Li glass. The thermal detector is located at a flight path of 15 m and has a thickness of 3 mm which allows for excellent energy resolution while maintaining a high counting rate. Two mid-energy transmission detectors are located at 31 and 100 m, respectively. These 0.5 in. detectors are used to accurately measure the resonances to higher energy in an attempt to extend the resolved resonance region. There is an additional EJ-301 detector array at 250 m that is used to measure total cross section for the neutron energy range from 0.5 to 20 MeV.

Recent transmission results have been achieved for measurements of separated isotopes of Mo. These measurements combined data taken with both the 31 m transmission detector and the 100 m transmission detector. These measurements resulted in new measured resonances from all isotopes that could be used to extend the resolved resonance region. Additionally, new fits were obtained for the unresolved resonance region (URR). More detailed results for these Mo measurements can be found in the following references [1, 2].

3 Capture Measurements

In combination with the transmission measurements, capture measurements are also performed in order to provide a more complete set of experimental data to be used in evaluations. By simultaneously measuring the capture and transmission the resonance widths for the neutron and gamma can be fit together to allow for more accurate resonance parameters. At RPI capture measurements can be performed from thermal energies up to the low MeV region utilizing one of two capture detection systems described in the following sections.

3.1 Low Energy Capture

For low energy capture measurements in the thermal to low keV region a capture multiplicity detector is used. This is a 16-segment NaI(Th) detector which provides

almost a total 4π detection coverage with a capture sample located in the center of the detector. A liner of B_4C with enriched ^{10}B is used to absorb scattered neutrons which could cause capture in the detector crystals and be mistaken for a capture event. The detector is located at a flight path of ~ 25.6 m which provides excellent resolution up to a neutron energy of several keV. A recent measurement was performed measuring the capture yield of several separated Gd isotopes. This new measurement identified several new resonances in the measured Gd isotopes; particularly 169 new resonances in ^{155}Gd and 96 new resonances in ^{157}Gd . This showcases the ability of the RPI low energy capture detector to provide high quality capture data on separated isotopes which can extend the resolved resonance region of isotopes. A full analysis of the Gd results can be found in reference [3].

Using this detector the total energy deposited in the detector can be measured as a function of the ToF. This is of particular value when measuring isotopes which have both capture and fission. A recent measurement was performed at RPI using this detector which measured the capture and fission from a sample of ^{235}U . By only looking at events which deposited a greater energy than the binding energy from capture, a selection of events only from fission could be obtained. This allowed for the separation of the fission signal from the capture signal at all energies. The results were typically in agreement with previous evaluations; however, the new measurement suggested a lower cross section in the range from 0.6 to 2.25 keV compared to the ENDF 7.1 evaluation. The measurement was used in the new evaluation of ^{235}U for ENDF 8.0, and the new evaluation agrees much better with this measurement. A full analysis of the measurement and techniques used can be found in reference [4].

3.2 Mid-Energy Capture

A detector array was recently built at RPI at a 45 m flight path in order to perform capture measurements in the mid-energy region. This region extends from the end of the resolved resonance region into the unresolved resonance region. The array consists of four C_6D_6 detectors mounted in a low mass system centered around a capture sample. C_6D_6 was chosen for the detector material due to its very low capture cross section limiting the probability for false capture detection. A B_4C sample is used in order to obtain the neutron flux shape at low energies in order to calculate the capture yields. To measure the flux shape at higher energies, a thin plastic beam monitor was created and placed behind the detection system [5]. The array utilizes the combination of the total detection method with a pulse weighting criteria in order to obtain the capture yields.

A recent measurement was done on a sample of isotopic ^{56}Fe in order to measure the capture yield at higher energies. The measured yield was higher than the ENDF 7.1 evaluation but lower than the JEFF 3.3 evaluation. These results were sent to the International Atomic Energy Agency (IAEA) for their new evaluation of ^{56}Fe . Figure 1 shows the comparison of the data with the previous ENDF 7.1 and JEFF 3.3

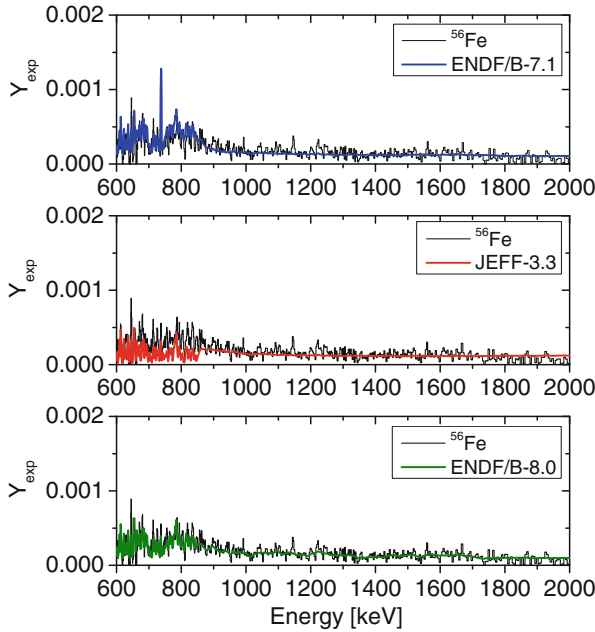


Fig. 1 A comparison of the experimental capture yield found using the RPI mid-energy capture detector with the ENDF 7.1, JEFF 3.3, and ENDF 8.0 evaluation. The ENDF 7.1 is shown to be higher than the experimental yield and JEFF 3.3 is lower; however, the new evaluation from ENDF 8.0 which utilizes the data is in much better agreement

evaluations, and the new ENDF 8.0 evaluation which uses the IAEA evaluation. This shows that the data provided from this measurement were helpful in constraining the new evaluation of ^{56}Fe . Further information on this measurement can be found in the following reference [6].

4 Fission Measurements

Fission measurements investigating aspects of the resonance region have previously been performed at RPI utilizing the Lead Slowing Down Spectrometer (LSDS). The LSDS is a 1.8 m cube of high purity lead which incorporates the high neutron scattering and low absorption cross section of lead to increase the neutron flux locally within the cube. This allows for neutron fluxes several orders of magnitude higher than traditional ToF measurements. The fission measurements use a double Frisch gridded ionization chamber to measure the fission fragment mass and charge distribution as a function of neutron ToF. The LSDS uses a modified ToF equation which takes into account the slowing down spectrum of the neutrons in the lead and can be seen below in Eq. (1) where $k = 165,000 \text{ eV } \mu\text{s}$, E is in eV, and

t is in μs . This slowing down in the lead broadens the energy resolution of the measurement and makes direct resonance measurements difficult. However, resonance information can still be obtained through looking at the change in fission fragment mass distribution looking at specific energy regions corresponding to resonance clusters. This work has been previously performed for neutron induced fission on ^{235}U and ^{239}Pu and the results can be seen in full in reference [7]. These results highlight the ability to utilize the LSDS for fission measurements in the resonance region which provide meaningful results regardless of the resolution of the system.

$$E(t) = \frac{k}{(t + 0.3)^2} \quad (1)$$

5 Conclusions

The RPI LINAC is one of the leading experimental facilities for neutron cross-section measurements using the ToF technique. Its many detector arrays and flight-path locations allow for various types of measurements to be performed spanning from thermal energy up to 20 MeV. Particularly, in the resonance region, the ability to simultaneously measure the capture and transmission allows for the extraction of the neutron and gamma resonance parameters providing a more complete view of the resolved resonance region. Many of the measurements have already been used for new evaluations, recently ^{56}Fe and ^{235}U which have impacted the new ENDF 8.0 evaluations. Additionally, with the new facility upgrade scheduled to complete in 2021, the LINAC facility will offer higher neutron fluxes and energies than were previously achievable allowing for more accurate measurements to be performed in the future.

References

1. R. Bahran, D. Barry, G. Leinweber, M. Rapp, R. Block, A. Daskalakis, B. McDermott, S. Piela, E. Blain, Y. Danon, Isotopic Mo neutron total cross section measurements in the energy range 1 to 620 keV. *Nucl. Data Sheets* **119**, 137–139 (2014)
2. K.E. Remley, G. Leinweber, D.P. Barry, R.C. Block, M.J. Rapp, Y. Danon, R.M. Bahran, Transmission measurements and resonance parameter analysis for Mo-98 and Mo-100. *Ann. Nucl. Energy* **122**, 23–36 (2018)
3. Y.-R. Kang, M.W. Lee, G.N. Kim, T.-I. Ro, Y. Danon, D. Williams, G. Leinweber, R.C. Block, D.P. Barry, M.J. Rapp, Neutron capture measurements and resonance parameters of gadolinium. *Nucl. Sci. Eng.* **180**(1), 86–116 (2015)
4. Y. Danon, D. Williams, R. Bahran, E. Blain, B. McDermott, D. Barry, G. Leinweber, R. Block, M. Rapp, Simultaneous measurement of ^{235}U fission and capture cross sections from 0.01 eV to 3 keV using a gamma multiplicity detector. *Nucl. Sci. Eng.* **187**(3), 291–301 (2017)

5. E. Blain, Y. Danon, B. McDermott, A. Youmans, J. Brown, N. Thompson, A. Weltz, K. Mohindroo, G. Leinweber, R. Block, M. Rapp, D. Barry, Development of an in-beam neutron flux monitor for time of flight capture measurements. *Trans. Am. Nucl. Soc.* **115**, 640–642 (2016)
6. B. McDermott, E. Blain, N. Thompson, A. Weltz, A. Youmans, Y. Danon, D. Barry, R. Block, A. Daskalakis, B. Epping, G. Leinweber, M. Rapp, ^{56}Fe capture cross section experiments at the RPI LINAC Center, in *EPJ Web Conf.*, vol. 146 (2017), p. 11038
7. C. Romano, Y. Danon, R. Block, J. Thompson, E. Blain, E. Bond, Fission fragment mass and energy distributions as a function of neutron energy measured in a lead slowing down spectrometer. *Phys. Rev. C* **81**, 014607 (2010)

Experimental Facilities at iThemba LABS and Measurements to Constrain Astrophysical Processes



Mathis Wiedeking

1 Introduction

The iThemba LABS $K = 200$ separated sector cyclotron (SSC) has been utilized for nuclear physics research since its commissioning in the mid-1980s. In the past 30 years, beam time has been divided between three programs (nuclear physics, hadron therapy, and isotope production), which limited the competitiveness of the nuclear physics research program. While beam time for nuclear physics research is not limited to weekends any longer, it will be increased significantly when the laboratory starts operations of the 70 MeV accelerator for radioisotope production (South African Isotope Facility—SAIF).

Subatomic Physics research will continue to play a major part of research at iThemba LABS. The research programs will focus on niche areas where iThemba LABS will complement the research carried out at cognate laboratories around the world [1]. The research infrastructure is in the progress to be significantly improved and the human resources will be supplemented to enable the laboratory to deliver on its research and training/education mandates.

The nuclear physics research topics at iThemba LABS are broadly classified into Nuclear Reaction, Nuclear Structure, and Applications of Nuclear Physics.

Over the last few years the benefits and possibilities of combining research equipment to perform cutting edge measurements have been realized and implemented. The merging of the K600 magnetic spectrometer with the AFRODITE Clover detectors is a prime example of a powerful setup and is shown in Fig. 1. New silicon particle arrays have also been developed over the last few years and can be coupled to AFRODITE and the K600 spectrometer. Several major experimental capabilities

M. Wiedeking (✉)
iThemba LABS, Cape Town, South Africa
e-mail: wiedeking@tlabs.ac.za



Fig. 1 Coupling Clover γ -ray detectors to the K600 magnetic spectrometer. Visible on the left are Clover detectors around the scattering chamber and on right is the first of two dipole magnets of the K600

have been or are in the process of being implemented. These include an electron spectrometer, fast-timing and large-volume LaBr₃:Ce detectors, a tape station, and a Doppler Shift Attenuation Method setup. These and other developments, together with the existing infrastructure will lay the foundation for research efforts during the coming years and will enable exciting nuclear physics measurements to be carried out.

One of the main research efforts focus on measurements to unravel the structure of the Giant Electric Dipole Resonance (GEDR) and resonances on its low-energy tail (e.g., Pygmy Dipole Resonance (PDR)), as well as the related photon strength function (PSF) and nuclear level density (NLD) below the particle threshold.

A selected number of the facility developments are detailed in sect. 2, which have been taken from iThemba LABS 2018 Long Range Plan [1] and elaborated on, while sect. 3 focuses on interesting measurements in particular those related to PSF and NLD measurements at iThemba LABS and examples of measurements that place constraints on astrophysical processes.

2 Experimental Facilities and Developments

2.1 K600 Magnetic Spectrometer

The $K = 600$ magnetic spectrometer (K600) at iThemba LABS is a high-resolution magnetic spectrometer for light ions. It has the capability to measure light-charged

particles from scattering or direct reactions at extreme forward angles, including zero degrees. This makes it one of only two facilities worldwide, the other being at RCNP Japan, with the capability of combining high-energy resolution with zero degree measurements at medium beam energies.

Accurate scattering angle information is imperative to allow for the necessary corrections of the first- and second-order dependence of the focal plane position on the horizontal scattering angle at the K600 spectrometer. This capability is critical and essential to exploit the high-resolution capabilities of the K600.

The K600 experimental program is increasingly dependent on the horizontal and vertical drift chambers and one additional drift chamber will be manufactured to provide the much needed redundancy for the focal plane detector setup. A new focal plane is currently being designed to further allow for the detection of heavier ions or lower excitation energies.

2.2 *AFRODITE*

AFRODITE (AFRican Omnipurpose Detector for Innovative Techniques and Experiments) is a γ -ray detector array with the capability of detecting both high- and low-energy photons with a reasonably high efficiency by combining Compton Suppressed HPGe detectors (CLOVERS) with Low-Energy Photon Spectrometer (LEPS) detectors. A range of ancillary detectors can be combined with AFRODITE, such as silicon or CsI charged-particle detectors, recoil detectors, and fast neutron detectors for time-of-flight discrimination for neutron reaction channels. The fast-timing array of eight $2'' \times 2''$ LaBr₃:Ce detectors can also be added to AFRODITE.

The upgrade of the nine Compton suppressed Clover detector array, AFRODITE, includes doubling the number of Clover detectors, which will provide the capability to improve on high-resolution measurements with double the efficiency, and a factor of ~ 4 increase in the doubles coincidence rate and a factor of ~ 10 for triples coincidences. At the end of 2018, a total of 14 Compton suppressed Clover detectors are available with four additional detectors expected to be available by the end of 2019, with funding through the GAMKA consortium which consists of five institutes: University of the Witwatersrand, University of the Western Cape, University of Zululand, Stellenbosch University, and iThemba LABS.

In addition to the detectors, a nitrogen liquefier will be procured through the GAMKA consortium to provide sufficient liquid nitrogen to operate the full array throughout the year.

2.3 *ALBA*

ALBA (African LaBr₃:Ce Array) with large-volume high-efficiency LaBr₃:Ce detectors will cover approximately $\frac{1}{2}$ of a sphere and consist of a total of 23

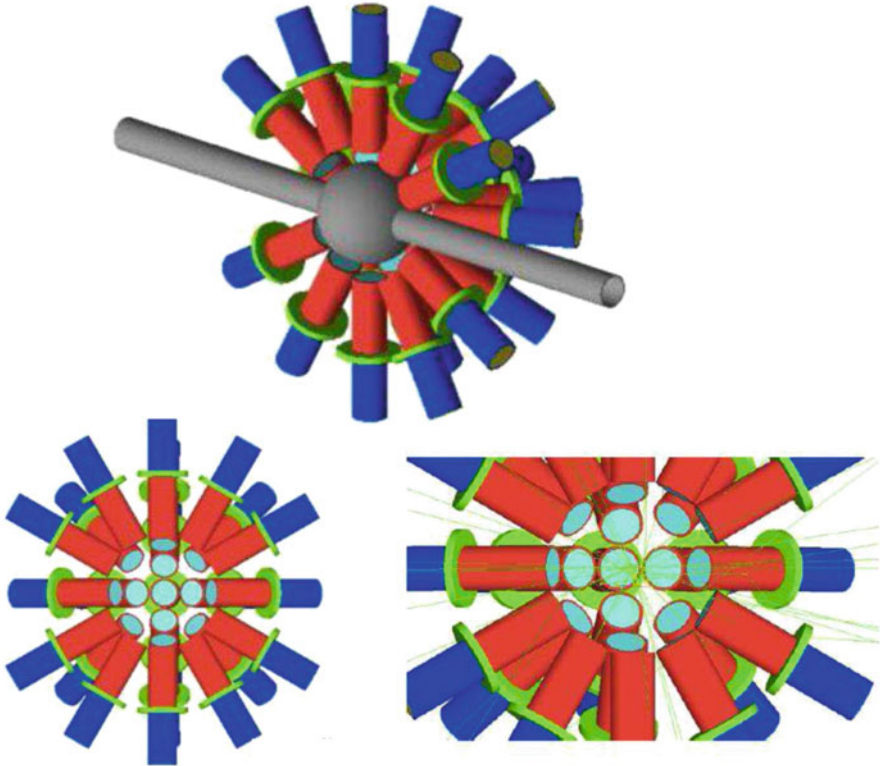


Fig. 2 Schematic arrangement of the African LaBr₃:Ce Array (ALBA) with 23 large-volume detectors [1]

large-volume ($89 \times 203\text{mm}$) LaBr₃:Ce detectors. Coupling these detectors to the K600, other particle detection devices and/or AFRODITE, will provide a unique combination with each detector type capable of probing a different aspect of the nuclear response. ALBA's efficiencies (for 20 detectors) are calculated to be 18.9%, 7.8%, and 4.5% at γ -ray energies of 1, 5, and 10 MeV, respectively. This will provide a significant increase in efficiencies for new and cutting edge research, in particular for measurements of the PSF, PDR, and γ -ray decay of the GEDR, which are not feasible with Clover detectors alone. Currently, six ALBA detectors are already available for measurements. Another 17 detectors are funded through GAMKA funds and are expected to be delivered in 2019 and the first half of 2020. A schematic arrangement of the ALBA array is shown in Fig. 2.

2.4 *Fast Neutron Beams*

The iThemba LABS fast neutron beam facility can provide quasi-mono-energetic neutron beams of energies between 30 and 200 MeV, using the (p,n) reaction on thin Li and Be targets. The neutron beam line is currently one of the few facilities in the world that can provide quasi-mono-energetic neutron beams up to 200 MeV.

The neutron beam line is currently undergoing significant upgrades with the goal of reducing neutron backgrounds to further improve conditions for metrology and neutron physics measurements. The improvements include an enhancement of available beam diagnostics, improved target system, beam dump, extension of the 16 degree flight path, as well as the rearrangement of shielding blocks. The upgrade is expected to be completed in 2019.

3 Experimental Measurements

Two of the main experimental projects focus on the development of innovative techniques for characterizing the quasi-continuum through the measurement of the PSF, NLD, and the PDR which will provide new opportunities for nuclear structure and astrophysics studies. The significant developments of new and existing experimental infrastructure with the addition of new detector technologies at iThemba LABS (see sect. 2) make it possible to embark on research programs with impact on the fields of nuclear structure and astrophysics. Results from measurements of the NLD and PSF (together with its resonances) allow for interesting investigations into the nucleosynthesis processes and can provide constraints of processes for the production of individual nuclei. Some examples of key experimental measurements, results, and conclusions are now summarized.

3.1 *PSF and NLD from Inverse Kinematic Reactions*

iThemba LABS in collaboration with other institutes has conceived and developed a novel technique to extract the shape of the PSF which relies on the combined detection of particles, primary high-energy as well as low-energy discrete γ -ray transitions [2, 3]. This initial effort to fully characterize the PSF was recently enhanced at iThemba LABS through the first measurement of the NLD and PSF using inverse kinematics with the $^{86}\text{Kr}(d,p)$ reaction and analyzed with the Oslo Method [4]. The success of this Inverse-Oslo approach makes it possible to measure the NLD and PSF of nuclei, which were previously inaccessible, either due to their chemical or physical properties or their radioactive character, and provides complementary access and information to other methods.

3.2 *Pygmy Dipole Resonance*

Studies of the PSF and NLD are mainly concerned with determining the overall electromagnetic decay (and excitation) properties of a nucleus, but researchers at iThemba LABS are also interested in understanding particular nuclear structure aspects, such as the GEDR and the PDR, that define the structure of the PSF. While the PDR has been studied for a range of nuclei, spanning several mass regions, its nature and evolution with deformation is not understood. While the PDR has been studied in ^{74}Ge with a combination of particle telescopes and AFRODITE [5], the available equipment is ideally suited for an experimental investigation of the PDR with the use of the K600 magnetic spectrometer at zero degrees, coupled to an array of γ -ray detectors, and an experimental program is underway to study the PDR in deformed nuclei (L. Pellegrini, private communications).

3.3 ^{138}La

Researchers at iThemba LABS have measured the PSFs and NLDs for $^{138,139,140}\text{La}$ at the Oslo Cyclotron Laboratory (OCL) [6]. The Maxwellian-averaged cross sections (MACS) were calculated and from these the (γ, n) production rates were found. The results show that the $^{139}\text{La}(\gamma, n)^{138}\text{La}$ production rate is smaller than the $^{138}\text{La}(\gamma, n)^{137}\text{La}$ destruction rate. Through this new determination of the reaction rates the conclusion is made that ^{138}La cannot be produced by photoreactions during the p-process and instead the neutrino process is the dominant production process for ^{138}La [7].

3.4 ^{180}Ta

The PSFs and NLDs were measured for $^{180,181,182}\text{Ta}$ [8] at the OCL and used as input parameters in the TALYS reaction code [9] to calculate (n, γ) cross sections. From these the MACS and reaction rates of astrophysical interest are obtained. The latter is used in s-process calculations and p-process simulations to re-estimate the nucleosynthesis of ^{180}Ta in light of the new experimental data [10]. The results show that the s-process contribution in the production of ^{180}Ta is negligible and instead the p-process is the primary production mechanism of nature's rarest stable isotope.


Acknowledgements Support from the National Research Foundation (South Africa) and the IAEA under Research Contract 20454 is greatly appreciated.

References

1. iThemba LABS, Long range plan (2018), http://www.tlabs.ac.za/wp-content/uploads/pdf/finalLRP_may2018c.pdf
2. M. Wiedeking et al., Phys. Rev. Lett. **108**, 162503 (2012)
3. M. Krtička et al., Phys. Rev. **C93**, 054311 (2016)
4. V. W. Ingeberg et al., Eur. Phys. J. A **56**, 68 (2020)
5. D. Negi et al., Phys. Rev. C **94**, 024332 (2016)
6. B.V. Kheswa et al., Phys. Rev. C **95**, 045805 (2017)
7. B.V. Kheswa et al., Phys. Lett B **744**, 268 (2015)
8. C.P. Brits et al., Phys. Rev. C **99**, 054330 (2019)
9. A. Koning, D. Rochman, Nucl. Data Sheets **113**, 2841 (2012)
10. K.L. Malatji et al., Phys. Lett. B **791**, 403 (2019)

Late Gamma Rays from Neutron-Induced Fission and Capture from ^{235}U



G. Rusev, J. M. O'Donnell, I. Stetcu, M. Jandel, P. Talou , B. Baramsai, T. A. Bredeweg, E. Bond, A. Couture, S. Mosby, C. J. Prokop, J. L. Ullmann, and C. L. Walker

1 $^{235}\text{U}+n$ Experiment

The late emission γ rays from the $^{235}\text{U}(n, \gamma)$ and $^{235}\text{U}(n, f)$ reactions were studied in an experiment with a 26-mg/cm^2 thick target enriched to ^{235}U . The experiment was performed at flight path 14 of the Lujan Center using neutrons produced via spallation reaction of 800-MeV protons striking a tungsten target with a repetition rate of 20 Hz [1]. A 1 in. thick water moderator increases the neutron flux at low energies. The γ -rays were measured with the DANCE array, which consists of 160 BaF₂ detectors in a 4π configuration [2]. Pictures of DANCE are shown in Fig. 1. DANCE was equipped with the NEUANCE array [3] serving as a fission trigger by measuring the prompt fission neutrons. NEUANCE consists of 21 stilbene detectors in a cylindrical configuration located in the central cavity of DANCE (*cf.* Fig. 1). The signals from all DANCE and NEUANCE detectors were digitized by CAEN VX1730B cards (14-bit, 500 MHz). In offline analysis, coincidence events of detectors fired within 5 ns were built and ordered in time relative to the beginning of the neutron spill (T_0).

G. Rusev (✉) · J. M. O'Donnell · I. Stetcu · P. Talou · T. A. Bredeweg · E. Bond · A. Couture · S. Mosby · C. J. Prokop · J. L. Ullmann · C. L. Walker
Los Alamos National Laboratory, Los Alamos, NM, USA
e-mail: rusev@lanl.gov

M. Jandel
Los Alamos National Laboratory, Los Alamos, NM, USA
University of Massachusetts Lowell, Lowell, MA, USA

B. Baramsai
Los Alamos National Laboratory, Los Alamos, NM, USA
NASA Glenn Research Center, Brook Park, OH, USA

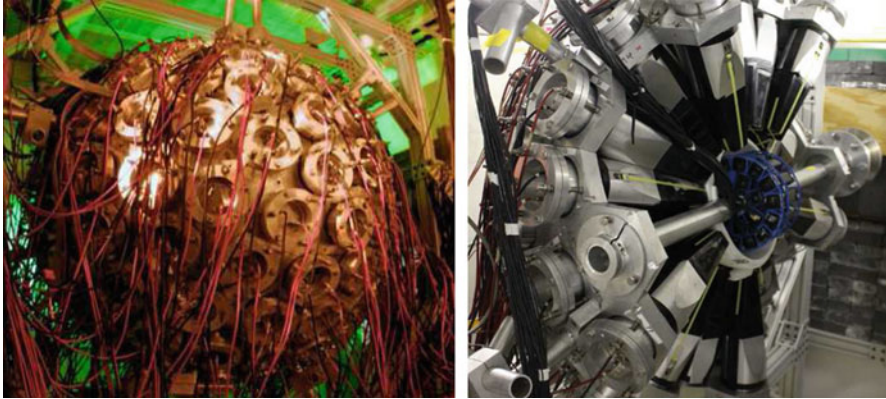


Fig. 1 A photograph of DANCE (left). DANCE consists of 160 BaF₂ detectors in a 4 π configuration. One of the DANCE hemispheres (right) with the beam line and NEUANCE installed in the central cavity

2 Preliminary Results

The train of detector hits for a fission event starts with the detection of at least one neutron by NEUANCE. In the same 5-ns coincidence event, a few DANCE detectors register the prompt fission γ rays (PFG). This event is followed by a long sequence of events containing γ rays from de-excitation of isomeric states in the fission fragments (late γ rays) as well as background events (beam related background, natural background, and cosmic rays). We applied a method, developed for similar experiments, to estimate the background [4]. The method requires three time spectra: PFG relative to T_0 , late γ rays relative to T_0 , and “late-prompt” events. See Appendix B in Ref. [4] for more details. A “late-prompt” spectrum with the estimated background is given in Fig. 2. Time 0 refers to the time of fission while the counts at later times correspond to the detected late γ rays. An energy spectrum of the late γ rays is produced by integrating the “late-prompt” spectrum from 50 ns to 2 μ s. The energy spectrum obtained is shown in Fig. 2 and compared with predictions [5] from the CGMF code [6]. Note, we estimate the background for each energy bin of the spectrum independently.

The product nucleus of the $^{235}\text{U}(n, \gamma)^{236}\text{U}$ reaction exhibits two low-lying isomeric states, one at 687.6 keV ($T_{1/2} = 3.78$ ns) and the other at 1052.4 keV ($T_{1/2} = 100$ ns). A partial level scheme of ^{236}U is shown in Fig. 3. We applied the same method for background estimation to obtain the energy spectrum of the late γ rays. The prompt γ rays, i.e. the γ rays feeding any of the isomers, are selected by the total γ -ray energy (E_{γ}^{total}) measured by DANCE: $E_{\gamma}^{total} = 6545.5 - 687.6$ keV or $6545.5 - 1052.5$ keV, where 6545.5 keV is the Q value of the $^{235}\text{U}(n, \gamma)$ reaction. The late γ rays are selected by the condition $E_{\gamma}^{total} = 687.6$ keV or 1052.5 keV, respectively. A sample γ -ray spectrum is given in Fig. 3.

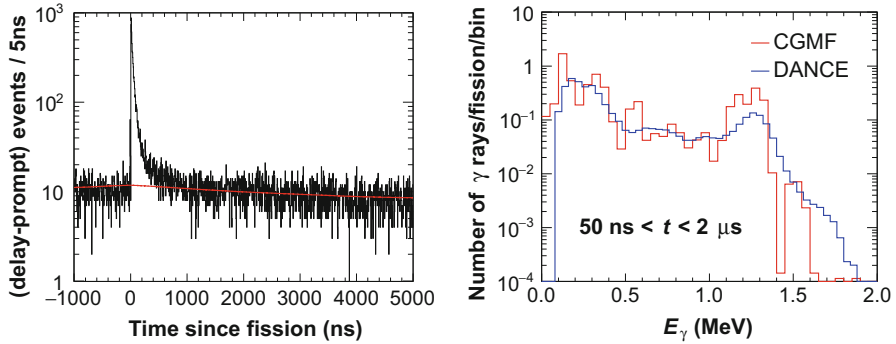


Fig. 2 A spectrum of “late-prompt” events (left) with background estimated using the method from Ref. [4]. Obtained spectrum of late γ rays from fission (right) compared with CGMF predictions from Ref. [5]

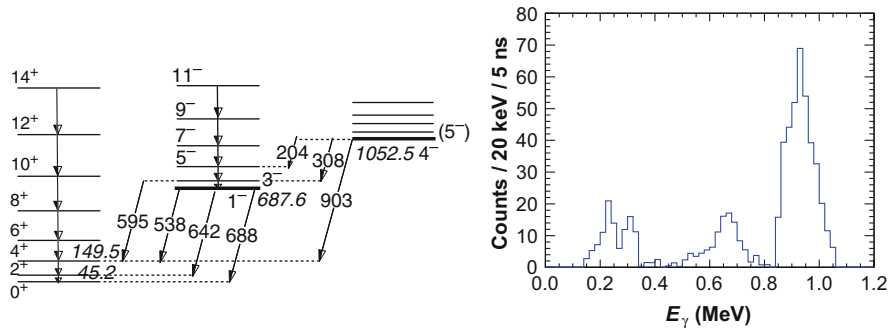


Fig. 3 A partial level scheme of ^{236}U (left). A spectrum of late γ rays (right) de-exciting the isomeric state at 1052.5 keV at 50 ns since the $^{235}\text{U}(n, \gamma)$ reaction occurred

In summary, we presented preliminary results for spectra of late γ rays from fission and neutron capture demonstrating the potential of DANCE to measure isomeric states with half lives from a few ns up to μs .

Acknowledgments This work benefited from the use of the LANSCE facility and the Manuel J. Lujan, Jr. Neutron Scattering Center. The work was performed under the auspices of the National Nuclear Security Administration (NNSA) of the U.S. Department of Energy at Los Alamos National Laboratory under Contract DE-AC52-06NA25396. The work was partly supported by the NNSA Office of Nonproliferation and Verification Research and Development.

References

1. M. Mocko, G. Muhrer et al., Nucl. Instrum. Methods A **704**, 27 (2013)
2. M. Heil et al., Nucl. Instrum. Methods A **459**, 229 (2001)

3. M. Jandel et al., Nucl. Instrum. Methods A **882**, 105 (2018)
4. J.M. O'Donnell, Nucl. Instrum. Methods A **805**, 87 (2016)
5. P. Talou et al., Phys. Rev. C **94**, 064613 (2016)
6. P. Talou et al., Eur. Phys. J. A **54**, 9 (2018)

Index

A

Alhassid, Y., 97
Ari-izumi, T., 165

B

Baramsai, B., 323
Barry, D., 309
Bello Garrote, F.L., 203
Belyshev, S., 165
Bernstein, L., 293
Blain, E., 309
Bond, E.M., 323
Bredeweg, T.A., 323
Brown, D., 57, 133
Brune, C., 45
Bulavin, L., 247
Burke, J., 221

C

Capote, R., 17, 65
Carlson, B.V., 17, 65
Casperson, R., 221, 301
Cherevko, K., 247
Chimanski, E.V., 65
Chiron, T., 209
Cizewski, J., 217
Constantinou, C., 145
Couture, A., 187, 323

D

Danon, Y., 309
Davis, E., 53

Denis-Petit, D., 209
Dickhoff, W., 83
Dietrich, F., 233
Draayer, J., 73
Dubray, N., 285
Dytrych, T., 73

E

Escher, J., 73, 221, 229, 233

F

Fan, G., 165
Filipescu, D., 165
Firestone, R., 179

G

Garland, H., 217
Gaudfroy, L., 209
Gheorghe, I., 165
Glorius, J., 209
Goriely, S., 3, 285
Gorton, O., 229
Grieser, M., 209
Grimes, S., 139
Gueorguiev, V., 233

H

Hagiwara, M., 251, 255
Henriques, A., 209
Herman, M., 57, 133

Herman, M.W., 17
 Hilaire, S., 3, 285
 Holt, J., 91
 Hughes, R., 221

I

Ishkhanov, B., 174

J

Jandel, M., 323
 Jenkovszky, L., 247
 Jurado, B., 209

K

Karampagia, S., 123
 Kawano, T., 27
 Koehler, P., 187
 Koning, A., 65
 Kunz, P., 233

L

Langer, C., 209
 Larsen, A.-C., 165, 203
 Launey, K., 73
 Leinweber, G., 309
 Lemaître, J.-F., 285
 Lepailleur, A., 217
 Lim, Y., 91
 Lima, E., 203
 Litvinov, Y.A., 209
 Loveland, W., 239
 Lui, Y.-W., 174

M

Mamun, M.A.A., 145
 Matheson, Z., 275
 Mathieu, L., 209
 Méot, V., 209
 Mercenne, A., 73
 Midtbø, J., 203
 Miyamoto, S., 165
 Mosby, S., 323

N

Nobre, G., 57, 133

O

O'Donnell, J.M., 323

P

Pain, S., 217
 Pérez-Sánchez, R., 209
 Pibernat, J., 209
 Prakash, M., 145
 Prokop, C.J., 323

R

Randrup, J., 293
 Rapp, M., 309
 Ratkiewicz, A., 217
 Regnier, D., 275
 Reifarth, R., 209
 Renstrom, T., 165
 Renstrøm, T., 230
 Roig, O., 209
 Rusev, G., 323

S

Sanami, T., 251, 255
 Schunck, N., 275
 Scielzo, N., 221
 Siem, S., 165
 Sims, H., 185
 Sin, M., 17
 Stetcu, I., 323
 Stopani, K., 165
 Sysoev, V., 247

T

Talou, P., 323
 Thomas, B., 209
 Thomas, B.A., 209
 Thomas, J.C., 209
 Thompson, I., 37
 Trkov, A., 17
 Tsekhanovich, I., 209
 Tveten, G., 165

U

Ullmann, J., 173, 187
 Ullmann, J.L., 323
 Utsunomiya, H., 165

V

Van Dyke, J., 293
 Varlamov, V., 165
 Vogt, R., 293

Voinov, A., 113
von Neumann-Cosel, P., 155

W

Walker, C.L., 323
Walter, D., 185
Wang, H., 165
Whitehead, T., 91
Wiedeking, M., 315

Y

Yashima, H., 251, 255
Yonai, S., 251, 255
Younes, W., 261

Z

Zeiser, F., 195
Zelevinsky, V., 123